Design and optical characterization of anisotropic plasmonic metamaterials at visible and infrared wavelengths

Vasilantonakis, Nikolaos

Awarding institution:
King's College London

King's College London

Design and optical characterization of anisotropic plasmonic metamaterials at visible and infrared wavelengths

Thesis submitted for the degree of

Doctor of Philosophy (PhD)

In the Department of Physics

By

Nikolaos Vasilantonakis

2015

Design and optical characterization of anisotropic plasmonic metamaterials at visible and infrared wavelengths

By

Nikolaos Vasilantonakis

What we are trying in all these discussions and talks here is to see if we cannot radically bring about a transformation of the mind. Not accept things as they are [...] *but to understand it, to go into it, to examine it, give your heart and your mind with every thing that you have to find out, a way of living differently. But, that depends on you and not somebody else, because in this there is no teacher...*

– J. Krishnamurti –

Abstract

The field of plasmonics studies the interaction of light and free electrons in metals, giving rise to excitation of surface waves, on a metallodielectric interface. One branch of plasmonics is the design of metamaterials in visible and infrared spectral range which are artificial structures designed to manipulate the propagation of light in a way not possible with conventional materials.

This thesis is categorized in 3 main parts. The first part examines the effects of waveguided modes in Au nanorod metamaterial waveguides. It shows, both theoretically and experimentally, that these materials can be designed to control the sign and magnitude of modal group velocity depending on the geometry and polarization chosen exhibiting high effective refractive indices (up to 10) and have an unusual cut-off from the high-frequency side, providing deep-subwavelength ($\lambda_0/6$ – $\lambda_0/8$ waveguide thickness) single-mode guiding. This allows slow light to exist in such waveguides in a controllable environment which is a critical factor for nonlinear and active nanophotonic devices, quantum information processing, buffering and optical data storage components. The second part discusses, analytically and numerically, strategies for biosensing and nonlinearity enhancement with hyperbolic nanorod metamaterials. It shows how the sensitivity of unbound, leaky as well as waveguided modes can be enhanced based on geometrical considerations. Additionally, refractive index variation of the host medium produces 2 orders of magni-

tude higher sensitivity compared to nanorod or superstrate refractive index changes. In certain configurations, both TE and TM-modes of the metamaterial transducer have comparable sensitivities opening up opportunities for polarization multiplexing in sensing experiments. The figure of merit of the aforementioned structure is one order of magnitude higher than surface plasmon polariton and localized surface plasmon sensors making it ideal for sensitive-dependant applications such as chemo- and biosensors and nonlinear photonic devices. The third part investigates Strontium Ruthenate thin films as a new material for near-IR plasmonic applications. It is demonstrated that their plasmonic behavior can be optimized by their deposition conditions leading to a selective and tunable plasma frequency in 324 - 392 nm range and epsilon-near-zero wavelength in 1.11 – 1.47 μm range. Applications of these films range from heat-generating nanostructures in the near-IR spectral range, to metamaterial-based ideal absorbers and epsilon-near-zero components, where the interplay between real and imaginary parts of the permittivity in a given spectral range is needed for optimizing the spectral performance.

Contents

List of Figures

Acknowledgements

I am grateful to my advisers, Prof. Anatoly V. Zayats and Dr. Gregory A. Wurtz, for their patience and guidance throughout the duration of my PhD. My sincere appreciation goes to all the group members at King's College London and Imperial College with whom I had the honour to work with. I would especially like to thank my life companion, Katerina, for all the psychological support.

Chapter 1

Introduction

1.1 From optics to nano-optics: A historical overview

The term "optics" is widely used not only for scientific reasons but also in our daily experiences. Sentences that contain "optical field of view", "optical communications" or "optical signals" are mere examples of the catholic usage of this word. From the physical point of view, optics is a branch of physics that investigates the properties of light, such as light-light and light-matter interactions, along with the fabrication of instruments for the detection of it.

The history of optics goes back to ancient times where many Greek scientists and philosophers, like Ptolemy, Euclid and Empedocles, cogitated about the properties and nature of light. During the 9^{th}, 10^{th} and 11^{th} century optics were also developed in the Islamic world from the contributions of Al-Kindi, Ibn Sahl and Avicenna. A few centuries later in the medieval Europe, Robert Grosseteste, Roger Bacon and Witelo tried to give a better insight on light based on the work of the aforementioned scientists. However,

the advent of optics started in the beginning of the 17^{th} century where the first optical device was introduced. Galileo Galilei is credited to be the first who constructed telescope a in 1609 and a microscope in 1610 [1]. It is worth mentioning two more pioneers in microscope development, Robert Hooke and Antony van Leeuwenhoek. The resolution of their microscope was so high for that period, that allowed them to observe the first blood cells and plant tissues along with microscopic organisms, such as bacteria and protozoans, initiating a new field known today as biology. During the same century, Johannes Kepler [2] derived the *Kepler's laws of planetary motion* from the astronomical observations of Tycho Brahe, Willebrord Snellius expressed the mathematical *law of refraction*[1] in 1621 and Renè Descartes had independently found the law of reflection [3]. Francesco Maria Grimaldi was first to coin the term *diffraction* (from the Latin word "diffringere" meaning "to break into pieces") marking the beginning of diffractive optics. At the start of the 18^{th} century Isaac Newton published "Opticks" [4] one of the most recognized book to date, in which he developed the corpuscular theory of light. A century later (1803), Thomas Young did the famous double slit interferometer experiment observing the interference pattern that emerges from two closely spaced slits. The results supported his previous work [5] stating that light has wavelike properties and was further enhanced by Augustin-Jean Fresnel [6]. This raised a great dilemma of whether light should be considered a particle, according to Newtonian theory, or a wave. Regardless of the answer, all these developments towards the theory of light had a drastic impact in the advancement of optical technology. A few decades later, Abbe

[1]This law was first introduced by Ibn Sahl in 984. It was also examined by Ptolemy and Witelo but due to luck of mathematical tools (absence of trigonometry) their results were written in tables instead of equations.

[7] and Rayleigh [8], showed that microscope resolution is strongly connected with the diffraction limit, a limit that does not depend only on wavelength but also on the numerical aperture of the objective. To give a typical example, a high resolution objective has numerical aperture of about 1.4 giving a diffraction limit of about $\lambda/3$, which means that no resolution smaller the one third of the wavelength can be obtained. As a consequence, the question whether or not the diffraction limit could be overcome was raised. This was the incentive for the invention of various techniques that allowed this limit to be stretched propelling the field of nano-optics.

The field of nano-optics concentrates on sizes in the nm-scale, this is the reason why high resolution is critical. One of the first techniques that tried to stretch the diffraction limit (known as *Abbe's limit*) was confocal microscopy [9] first patented by Marvin Minsky in 1957 [10]. This led to the invention of confocal fluorescent microscopy which proved a unique tool for biomedical studies [10]. Pulsed laser radiation was the spark for the creation of nonlinear optics which led to the invention of coherent anti-Stokes Raman scattering microscopy [11] and multiphoton excitation [12] that increased even more spatial resolution. Near field optical microscopy offered a great alternative for high resolution imaging. It was first proposed by Synge [13] in 1928 and the main idea was to exploit the properties of evanescent waves on the vicinity of the specimen surface instead of acquiring the far field domain spectra. This can be achieved by placing a detector with a minute aperture (probe) very close to the surface of the sample (a distance much smaller than the incident wavelength). To acquire a topological image of the sample, the aperture scans the sample's surface in small increments. This technique allows the resolution of the image to depend only on the numerical aperture and not the incoming wavelength. Due to experimental

limitations at that time, Synge's idea was soon forgotten and needed many decades for the experimental confirmation [14] that showed sub-wavelength imaging resolution as high as $\lambda/60$. Additionally, the invention of scanning probe microscopy [15] further enhanced near-field imagining techniques since it allowed high accuracy control between the distance of the probe and the sample. To achieve high resolution images at optical wavelengths, Massey [16] suggested that a piezoelectric device could be used for positioning the probe. Soon after, the first experimental sub-wavelength resolution images at optical frequencies were independently realized by Pohl *et al.* [17] and Lewis *et al.* [18]. Today all these techniques and slight variations of them, such as scanning near field optical microscopy, near-field reflection microscope, photon scanning tunneling microscope and so on, are used in a plethora of applications in different fields [19–22] affirming that nano-optics are here to stay.

1.2 Basis of nano-optics

The aim of the current Section is to briefly describe the very basics of nano-optics and show that, even at such small sizes, no fundamental physical law is violated. *Heisenberg's uncertainty principle* states that the uncertainty in the spatial position of a particle along a direction multiplied by the uncertainty of momentum (p) along the *same* direction cannot be smaller than $\hbar/2$, where $\hbar$ is the reduced Planck constant. If we choose direction to be x-axis, it can be written as

$$\Delta p_x \cdot \Delta x \geq \hbar/2 \tag{1.1}$$

If the particle is replaced by a photon, the momentum will be $\mathbf{p} = \hbar\mathbf{k}$, where

k is photon's wavevector. Substituting to Eq. (1.1) and rearranging the terms we get

$$\Delta x \geq \frac{1}{2\Delta k_x} \tag{1.2}$$

which means that as Δx decreases, the magnitude of wavevector along the x direction must be increased (spread) for the inequality to hold. To give a better insight of the physical significance of Eq. (1.2) let us consider a photon which is travelling in 2D space. If we mesh space in such a way that photon's position is very accurately known (left image of Fig. 1.1), it is impossible to find its momentum since direction cannot be determined. Similarly, if the mesh block is big enough for momentum measurement, the location uncertainty increases since photon can be anywhere inside the meshed block (right image of Fig. 1.1). An immediate consequence of this observation is that a balance between the size of mesh (Δx) and photon's momentum is required. This requirement is given from Eq. (1.2) and represents not only a physical law but a fundamental property of universe.

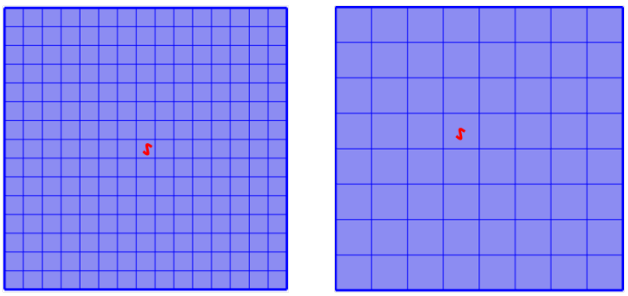

Figure 1.1: Heisenberg's uncertainty principle for a photon. In the left image the photon's position is accurately known but momentum cannot be measured while in the right, there is enough space to measure momentum, but this creates an uncertainty of photon's exact location inside the meshed block.

The spread of wavevector plays a central point in nano-optics and can be realized in various ways such as sending a light beam in a closely spaced slit or focusing a ray of light in a focal spot using lens. In any case, the spatial uncertainty must be small enough for a wide spread of **k**. The maximum spread in a given direction, say x, cannot exceed the total length of **k** in vacuum (i.e. $k = 2\pi/\lambda$). Using this result, Eq. (1.2) becomes

$$\Delta x \geq \frac{\lambda}{4\pi} \tag{1.3}$$

showing the proportionality of spatial uncertainty and wavelength. This result is very similar to Rayleigh's and Abbe's diffraction limit. An emerging query is how it is possible to maximize **k**-spread without breaking Heisenberg's uncertainty principle. To answer this, let us assume a photon travelling in xz-plane. The total wavevector will be $k = \sqrt{k_x^2 + k_z^2}$ and its magnitude should not exceed $k = 2\pi/\lambda$. The main idea is to increase k_x even above threshold and simultaneously introduce a purely imaginary k_z in order to retain a total length of $2\pi/\lambda$. In this case, the wavevector spread along the x-direction will also be enhanced and will not be strictly restricted from Eq. (1.2). However, due to the purely imaginary k_z, waves along this direction are doomed to exponentially decay with distance due to the $\exp(ik_z z) = \exp(-|k_z|z)$ term. These type of waves are called *evanescent waves*. On the other hand, the exponential term along x-direction is increased with distance, since k_x is real, leading to non-physical electromagnetic fields. So it appears the aforementioned strategy is a mere mathematical trick with no physical meaning, however all these results are correct for light travelling in an infinite 2D space. If we add a different material (two semi-infinite media or an inhomogeneity for example) then it might be feasible to have decaying fields in one direction without the need of exponentially increasing fields on the

other. In this case Rayleigh limit is not a limit any more and extreme field confinement is possible. In this principle lies the heart of nano-optics and the main challenge is to find the right conditions (material properties, structure shape and so on) to achieve high field confinement.

1.3 Introduction to metamaterials

The vast majority of optical device functionality is based on interactions between the incident waves and the materials used. Every year there are numerous publications from scientists and engineers who propose a plethora of different structures with novel properties. Nevertheless, the capability and applicability of these devices is highly confined due to the available materials used for fabrication. As a consequence, the need of synthetic or artificial materials is imperative.

One way to approximate this problem is by structuring subwavelength composite inclusions. Due to the small size of the inclusions, compared to the incident wavelength, the macroscopic electromagnetic response can be expressed in terms of the "effective" dielectric properties, that is a material that combines the properties of the inclusions and the host environment together. Since these materials are man-made and fabricated in a way to achieve specific optical response at specific frequencies, they are called *metamaterials*. The prefix "meta" comes from the Greek dictionary (μετα) which means "beyond". It states that this category of materials exhibit properties that are *beyond* the conventional materials that nature provide us. It is a fairly new field in science since the first appearance of the term "metamaterial" was in 2000 by Smith *et al.* [23].

To give a specific terminology of what a metamaterial is, we will use

the definition from W. Cai and V. Shalaev that states [24]: *A metamaterial is an artificially structured material which attains its properties from the unit structure rather than the constituent materials. A metamaterial has an inhomogeneity scale that is much smaller than the wavelength of interest, and its electromagnetic response is expressed in terms of homogenized material parameters.* It should be noted that the wavelength of interest corresponds to free space wavelength and, for the purpose of this thesis, the inhomogeneity scale takes place at energies where non-local effects can be neglected. Based on this definition, the current thesis can also be included in the metamaterial field. Nevertheless, this field is so broad that a more compact classification is needed which is the scope of the next Section.

1.3.1 Categorization based on the effective parameters

Although metamaterial is a modern word, it includes material properties that has been described almost 50 years ago like Veselago's manuscript on left-handed materials back in 1968 [25]. With the rapid growth of optical metamaterials, especially during the last decade, a variety of research fields has been emerged such as optical nonlinearity in metamaterials [26–28], extreme chirality [29, 30], optical magnetism [31, 32], super resolution [33–36] and invisibility cloaking [37–39]. It is thus mandatory to even further categorize the current thesis. This can be achieved through the usage of permittivity (ε) and permeability (μ) since both parameters are used to describe the macroscopic overall response of a material as a concrete medium[2]. Of course, from the microscopic point of view, each atom or molecule can excite small dipoles when an external field is applied. As a result, a periodic metamaterial has a

[2]In this case, ε and μ are called *effective* permittivity and permeability respectively but for simplicity the current Section omits the "effective" term.

periodic local field inside the unit cell and the field distribution cannot be considered uniform. Nevertheless, because the incident light has large wavelengths compared to inhomogeneities' size, it does not feel the local changes of field distribution. Instead of that, the local optical response of each inhomogeneity is averaged ending up to a macroscopic uniform field distribution. Due to this uniformity, there is a linear response of the electric field (E) with the magnetic displacement (D) and similarly, the magnetic field (H) with magnetic flux density (B). The ratio of these two pairs is the origin of permittivity and permeability (i.e. $\varepsilon = D/E$, $\mu = B/H$). It should be noted that all materials, even dielectrics, exhibit absorption which makes the effective parameters to be complex valued. In most cases, dielectrics have a negligible absorption and thus their permittivity and permeability is considered purely real. However, in general, different symbolism is used to distinguish the real and imaginary parts.

The classification of materials can be achieved through the real permittivity (ε_r) and permeability (μ_r) as seen in Fig. 1.2 [40]. Typical materials like transparent dielectrics have a positive set of ε_r and μ_r (grey quadrant). They are often called *real materials* due to the negligible imaginary part meaning that the effective parameters are equal to their real counterparts. Most materials that nature provide us are in this branch and used in our every day's life. When ε_r and μ_r are negative, the direction of the induced electromagnetic field is opposite compared to the incident one. These are artificial media called *negative index materials* (yellow quadrant) and have some peculiar properties since they reverse physical phenomena such as electromagnetic propagation, Snell's law or Cherenkov radiation. In both combinations propagation is allowed since the refractive index is positive ($\varepsilon_r\mu_r > 0$). When the product of $\varepsilon_r\mu_r$ is negative, refractive index becomes imaginary hence no

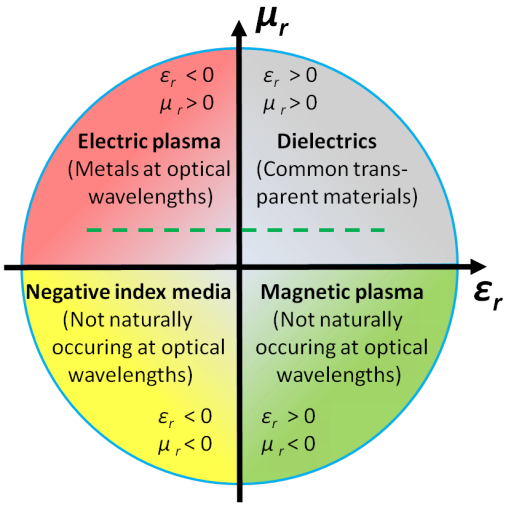

Figure 1.2: Categorization of materials based on their effective parameters. The axes depict the real part of permittivity (ε_r) and permeability (μ_r). The grey quadrant corresponds to conventional dielectric materials while the yellow one to artificial negative index materials. In both cases propagation is allowed since the refractive index is positive. For the other two cases (red and green quadrants) ε_r and μ_r have opposite signs leading to purely imaginary refractive index. No propagation is allowed and evanescent waves are formed. Optical materials have a very narrow permeability range close to 1 (green dashed line).

propagation is allowed leading to the formation of evanescent waves. Depending on whether ε_r or μ_r is negative, materials are categorized in the *electric plasma* (red quadrant) or the *magnetic plasma* (green quadrant) field, respectively. For noble metals, like Gold and Silver, the electric field is anti-parallel to the displacement vector above the plasma frequency leading to $\varepsilon_r < 0$, and similarly, in materials such as Cobalt and Nickel, the magnetic field is anti-parallel to the magnetic induction exhibiting $\mu_r < 0$ at certain wavelengths. In the field of optics (mainly visible and IR region), metals exhibit non-magnetic behaviour and so $\mu_r \cong 1$ (green dashed line).

The main scope in metamaterial research is to fabricate synthetic materials with the ability to enter regions of the effective parameter space (Fig. 1.2) that is impossible with any conventional medium and at the same time without violating Maxwell's equations. Due to the extra effective parameter space, a better control of the optical response is possible. One way to tailor the electromagnetic response is via the use of *plasmonic metamaterials* where this thesis is dedicated. Although such materials can be created from the electric or magnetic plasma quadrants (Fig. 1.2), the former is more commonly used in optics since it exhibits better optical properties. As a consequence, the thesis is placed in the red quadrant where $\varepsilon_r < 0$ and $\mu_r > 0$. Before examining such structures, a description on plasmonic metamaterials is needed. Questions such as "what are plasmons and surface plasmon polaritons?" or "what are the properties and the excitation conditions of plasmonic media?" are important in the field of plasmonics and will be discussed in the next Chapter.

1.4 Structure of thesis

This thesis consists of the following parts:

- **Chapter 1: Introduction** (this Chapter), started with a historical overview of optics as a general term, and continued with the fundamental principles of nano-optics introducing the metamaterials as an effective way to approach nano-scale applications. It ended with the classification of materials based on their effective parameters defining the effective parameter space where the current thesis is dedicated.

- **Chapter 2: Nanoplasmonics**, introduces two core excitations in plasmonics, namely bulk and surface plasmons, and focuses on a particular

surface excitation, known as surface plasmon polariton, along with its main applications. The dielectric function of metallic media is discussed next; which provides an accurate theoretical description of the dispersive nature of such materials. Finally, the basic properties and excitation conditions of surface plasmons polaritons are shown together with the experimental configuration that was used here.

- **Chapter 3: Light propagation in uniaxial anisotropic media and principles of ellipsometry**, introduces the metallic nanorod metamaterials as a way to achieve hyperbolic dispersion, and explains why hyperbolicity is critical. Light propagation in indefinite media is discussed next and the effective medium theory is developed based on the transfer matrix and Maxwell Garnett methods. The aforementioned theory is then compared with numerical simulations to test its validity. Lastly, the principles of spectroscopic ellipsometry are described along with the experimental setup used in this thesis.

- **Chapter 4: Designing guided modes of hyperbolic metamaterial slab waveguides**, demonstrates, theoretically and experimentally, the waveguiding properties and mode structure of planar anisotropic metamaterial waveguides. It starts with a short introduction regarding elliptic and hyperbolic regimes in metamaterials and continues with the analytical and numerical examination of the mode structure of each case for a slab waveguide geometry. We show that negative (positive) group velocity can be achieved only when the waveguide is in the hyperbolic (elliptic) regime specified by a particular polarization of the incident light. Next, we demonstrate the impact of the effective plasma frequency in the mode dispersion and explain the non-monotonous pat-

tern observed at increasing concentrations for the hyperbolic scenario. Finally, the impact of a porous alumina layer on top of the waveguide is presented. We describe how slow light can be achieved by carefully structuring the porous alumina layer followed with the experimental confirmation.

- **Chapter 5: Refractive index sensing with hyperbolic metamaterials**, examines, analytically and numerically, the dependence of the optical response of metallic nanorod metamaterials on refractive index variations in commonly used experimental sensing configurations, including transmission, reflection, and total internal reflection. The main purpose is to develop a general strategy for maximising refractive index sensitivity for different configurations, taking into account contributions from the superstrate, embedding matrix, and the metal itself. Firstly, it shows how sensing can be increased for higher-order modes and decreasing thickness of the transducer. Secondly, it demonstrates how the sensitivity to changes in the refractive index of a host medium is much stronger with respect to the superstrate or metal refractive indices. Finally, it compares the figure of merit with conventional sensing geometries and shows one order of magnitude higher sensing capabilities when the hyperbolic metamaterial geometry is considered.

- **Chapter 6: Optimizing Strontium Ruthenate thin films for near-infrared plasmonic applications**, investigates how the deposition pressure of $SrRuO_3$ thin films grown on MgO (001) substrate can be modulated to achieve the best response for plasmonic applications. It begins with the structural characterization of the films based on atomic force microscopy and X-ray diffraction techniques. It contin-

ues with the electrical and optical examination for the determination of carrier density, carrier mobility, plasma frequency and epsilon-near-zero frequency at different oxygen pressures. Additionally, to understand the nature of the optical properties, the measured optical constants are compared with a Drude-Lorentz model. Finally, the properties of $SrRuO_3$ are compared with conventional plasmonic metals to dictate the advantages/disadvantages of each one with emphasis on the field of plasmonics.

References

[1] M. Born and E. Wolf, *Principles of Optics*, 6th ed. Oxford: Pergamon, (1970).

[2] C. Murray and S. Dermott, *Solar System Dynamics*. Cambridge University Press, (1999).

[3] D. M. Clarke, *Descartes: A Biography*. Cambridge University Press, (2006).

[4] I. Newton, *Opticks*. Dover Publications, (1979).

[5] T. Young, "The bakerian lecture: On the theory of light and colours," *Philosophical Transactions of the Royal Society of London*, vol. **92**, pp. 12–48, (1802).

[6] H. Crew, C. Huygens, T. Young, A. Fresnel, and F. Arago, *The Wave Theory of Light: Memoirs of Huygens, Young and Fresnel*. American Book Company, (1900).

[7] E. Abbe, "Beiträge zur theorie des mikroskops und der mikroskopischen wahrnehmung," *Archiv f. Miroskop. Anat.*, vol. **9**, p. 413, (1873).

[8] L. Rayleigh, "Investigations in optics, with special reference to the spectroscope," *Phil. Mag.*, vol. **8**, pp. 261–274/403–411/477–486, (1879).

[9] M. Minsky, "Memoir on inventing the confocal scanning microscope," *Scanning*, vol. **10**, pp. 128–138, (1988).

[10] J. Pawley, *Handbook of Biological Confocal Microscopy.* Springer, (2006).

[11] A. Zumbusch, G. R. Holtom, and X. S. Xie, "Three-dimensional vibrational imaging by coherent anti-stokes raman scattering," *Phys. Rev. Lett.*, vol. **82**, pp. 4142–4145, (1999).

[12] W. Denk, J. H. Strickler, and W. W. Webb, "2-photon laser scanning fluorescence microscopy," *Science*, vol. **248**, pp. 73–76, (1990).

[13] E. H. Synge, "A suggested model for extending microscopic resolution into the ultra-microscopic region," *Phil. Mag.*, vol. **6**, pp. 356–362, (1928).

[14] E. A. Ash and G. Nicholls, "Super-resolution aperture scanning microscope," *Nature*, vol. **237**, pp. 510–513, (1972).

[15] G. Binnig, H. Rohrer, C. Gerber, and E. Weibel, "Tunneling through a controllable vacuum gap," *Appl. Phys. Lett.*, vol. **40**, pp. 178–180, (1982).

[16] G. A. Massey, "Microscopy and pattern generation with scanned evanescent waves," *Appl. Opt.*, vol. **23**, pp. 658–660, (1984).

[17] D. W. Pohl, W. Denk, and M. Lanz, "Optical stethoscopy: image recording with resolution $\lambda/20$," *Appl. Phys. Lett.*, vol. **44**, pp. 651–653, (1984).

[18] A. Lewis, M. Isaacson, A. Harootunian, and A. Muray, "Development of a 500 Å spatial resolution light microscope," *Ultramicroscopy*, vol. **13**, pp. 227–231, (1984).

[19] M. Hausmann, B. Perner, A. Rapp, L. Wollweber, H. Scherthan, and K. Greulich, "Near-field scanning optical microscopy in cell biology and cytogenetics," *Methods Mol. Biol.*, vol. **319**, pp. 275–294, (2006).

[20] D. A. Bonnell and S. V. Kalinin, *Scanning Probe Microscopy for Energy Research.* World Scientific, (2013).

[21] E. Betzig and R. J. Chichester, "Single molecules observed by near-field scanning optical microscopy," *Science*, vol. **262**, pp. 1422–1425, (1993).

[22] J. Cheng and X. S. Xie, *Coherent Raman Scattering Microscopy.* Taylor & Francis Group, (2013).

[23] D. Smith, W. Padilla, D. Vier, S. Nemat-Nasser, and S. Schultz, "Composite medium with simultaneously negative permeability and permittivity," *Phys. Rev. Lett.*, vol. **84**, pp. 4184–4187, (2000).

[24] W. Cai and V. Shalaev, *Optical Metamaterials - Fundamentals and Applications.* Springer, (2010).

[25] V. Veselago, "Electrodynamics of substances with simultaneously negative values of sigma and mu," *Sov. Phys. Usp.*, vol. **10**, pp. 509–514, (1968).

[26] M. Klein, C. Enkrich, M. Wegener, and S. Linden, "Second-harmonic generation from magnetic metamaterials," *Science*, vol. **313**, pp. 502–504, (2006).

[27] M. Klein, M. Wegener, N. Feth, and S. Linden, "Experiments on second- and third-harmonic generation from magnetic metamaterials," *Opt. Express*, vol. **15**, pp. 5238–5247, (2007).

[28] A. Popov and V. Shalaev, "Compensating losses in negative-index metamaterials by optical parametric amplification," *Opt. Lett.*, vol. **31**, pp. 2169–2171, (2006).

[29] E. Plum, V. Fedotov, A. Schwanecke, N. Zheludev, and Y. Chen, "Giant optical gyrotropy due to electromagnetic coupling," *Appl. Phys. Lett.*, vol. **90**, no. 223113, (2007).

[30] M. Decker, M. Klein, M. Wegener, and S. Linden, "Circular dichroism of planar chiral magnetic metamaterials," *Opt. Lett.*, vol. **32**, pp. 856–858, (2007).

[31] S. Zhang, W. Fan, B. Minhas, A. Frauenglass, K. Malloy, and S. Brueck, "Midinfrared resonant magnetic nanostructures exhibiting a negative permeability," *Phys. Rev. Lett.*, vol. **94**, no. 037402, (2005).

[32] W. Cai, U. Chettiar, H. Yuan, V. de Silva, A. Kildishev, and V. Shalaev, "Metamagnetics with rainbow colors," *Opt. Express*, vol. **15**, pp. 3333–3341, (2007).

[33] N. Fang, H. Lee, C. Sun, and X. Zhang, "Sub-diffraction-limited optical imaging with a silver superlens," *Science*, vol. **308**, pp. 534–537, (2005).

[34] T. Taubner, D. Korobkin, Y. Urzhumov, G. Shvets, and R. Hillenbrand, "Near-field microscopy through a sic superlens," *Science*, vol. **313**, p. 1595, (2006).

[35] Z. Liu, H. Lee, Y. Xiong, C. Sun, and X. Zhang, "Far-field optical hyperlens magnifying subdiffraction-limited objects," *Science*, vol. **315**, p. 1686, (2007).

[36] Z. Liu, S. Durant, H. Lee, Y. Pikus, N. Fang, Y. Xiong, C. Sun, and X. Zhang, "Far-field optical superlens," *Nano Lett.*, vol. **7**, pp. 403–408, (2007).

[37] J. Pendry, D. Schurig, and D. Smith, "Controlling electromagnetic fields," *Science*, vol. **312**, pp. 1780–1782, (2006).

[38] D. Schurig, J. Mock, B. Justice, S. Cummer, J. Pendry, A. Starr, and S. Smith, "Metamaterial electromagnetic cloak at microwave frequencies," *Science*, vol. **314**, pp. 977–980, (2006).

[39] W. Cai, U. Chettiar, A. Kildishev, and V. Shalaev, "Optical cloaking with metamaterials," *Nat. Photonics*, vol. **1**, pp. 224–227, (2007).

[40] J. Pendry, "Focus issue: negative refraction and metamaterials – introduction," *Opt. Express*, vol. **11**, p. 639, (2003).

Chapter 2

Nanoplasmonics

In this Chapter we introduce the bulk and surface plasmon oscillations of metals along with two dielectric function models for the realization of them, namely Drude-Sommerfeld and Lorentz. We then focus our attention on a specific surface charge oscillation called surface plasmon polariton and discuss its fundamental properties for the simplest case of a planar metallodielectric interface with anisotropic or isotropic characteristics. The excitation conditions along with their limitations are also discussed for these type of waves. Lastly, the localized surface plasmon polaritons are defined and examined for an isolated ellipsoid based on the quasi-static approximation.

2.1 Plasmons and surface plasmon polaritons

Although there are many ways to classify a material by its properties, in physics it is often categorized by the characteristic electron bandgap regime. As a result there are three main types; materials with large (dielectrics), low (semiconductors) and no (metals) bandgap. Since the valence and conduction band for metals overlaps, electrons are not tightly bounded with the

ion core (nucleus) and are *almost* free to travel inside the metal. As a consequence they exhibit very high conductivity and the interaction with the electromagnetic radiation is closely connected by the free electrons in the metal. There are various theoretical models describing the dielectric function of metals (Section 2.2). For the simplest case where electrons are completely unbounded from the nucleus, they oscillate 180° out of phase relative to the incident electric field. This is the physical meaning of dielectric's function negative sign which is the root of high reflectivity of metals in the visible spectrum.

The free electron model for metals allows volume (bulk) and surface charge oscillations known as *plasmons* and *surface plasmon polaritons* (SPPs). The term "plasmon" comes from "plasma" which is considered a state of matter where the negative ions (charges) are free to move around without interacting with the positive ion cores. This condition is automatically satisfied in metals, due to the absence of bandgap, but for non-metallic media an external source is required to overcome the bandgap threshold (for instance through heating). The existence of plasmons (both volume and surface) is strongly connected with the interaction of metallic features with light. Although plasmonic effects can appear from ultraviolet all the way up to microwave frequencies, the most commonly studied regime is the visible one due to the plethora of nanoscale applications. The research field of optical phenomena related to the electromagnetic behaviour of metals in the visible regime is named *nanoplasmonics*.

Surface plasmons were first introduced by Ritchie [1] in 1957 and experimentally observed by Powell and Swan [2, 3] in 1959. In the following decades, they were extensively studied by many scientists such as Otto [4], Kretschmann [5] and Raether [6], making plasmonics a fundamental research

area in nano-optics. Although SPPs can be excited through electron bombardment in a metallodielectric interface the most common way is via optical illumination. Electron-based techniques produce very high energy electrons that are difficult to couple with SPPs due to very large momentum leading to broad coupling regime. On the other hand, a light source produces photons of specific energies and in more controllable environment ending up to well defined spectral features. In its most basic form, an SPP propagates along a metallodielectric interface in a wave-like fashion [7, 8] and decays exponentially fast as we move away from the interface (Section 1.2). As a result, SPPs are highly confined near the vicinity of the interface as will be shown in Section 2.3. The subwavelength confinement leads to an enhancement of the electromagnetic fields making them extremely sensitive to surface conditions (such as the morphology of the interface). This is a key property in some applications based on extraordinary sensitivity boundary conditions, such as chemo- and biosensors [9, 10]. Apart from the aforementioned, the 2D nature of SPPs provides a plethora of applications such as optical computing and signal processing [11–13], subwavelength waveguiding [14], near field imaging [15], plasmonic light sources [16] and plasmonic nanolithography [17].

Manipulating highly confined SPPs on an interface, it is possible to scale down photonic and optoelectronic devices to nanometric dimensions which can greatly improve the energy consumption, lifetime and efficiency of them. Due to the exponential decay of the normal to the interface electromagnetic fields they cannot be observed directly with conventional far-field experiments unless SPPs interact with a surface defect and couple into light. In the past, it was possible to measure only the far field scattered light (due to the interaction of the SPPs with boundary inhomogeneities) and examine the SPP properties based on the scattering process [8], that was based on

many assumptions. The reason for these assumptions was due to the uncertainty of the microscopic structure of the surface. However, the development of near field techniques such as near field optical microscopy (SNOM) [18], energy electron loss spectroscopy (EELS) [19] and cathodoluminescence (CL) [20], gave the chance to directly probe the SPP field over the surface they are excited, with a lateral resolution of only 20 nm [21]. These discoveries revolutionized the surface polariton examination [22–24], and many of their properties (localization, backscattering, interference and so on) have been thoroughly investigated directly on the surface [25, 26].

2.2 Dielecric function of metals

The optical properties of noble metals have been extensively studied by many authors [27, 28]. The scope of this Section is to give a short overview of the physical process involved in such media and derive the theoretical formulas for the examination of them. Since metals are absorbent and dispersive, the dielectric function is complex valued and expressed in terms of frequency, thus $\varepsilon = \varepsilon(\omega)$. Note that, as discussed in Section 1.3.1, metals have permeability near unity for the visible-IR regime so the challenge is to derive an expression for $\varepsilon(\omega)$. There are mainly two contributing factors (a) the conduction electrons can freely move inside the metal and (b) when the incident photons have higher energies than metal's interband transition threshold, interband transitions can occur.

2.2.1 Drude–Sommerfeld model

In the case where electrons are completely unbounded from nucleus, the dielectric response is given from the Drude–Sommerfeld model (commonly

known as *Drude* model). Based on Newton's second law, the motion of an electron at position $\mathbf{r}$ and time t is given [29]

$$m_e \frac{\partial^2 \mathbf{r}}{\partial t^2} + m_e \Gamma \frac{\partial \mathbf{r}}{\partial t} = e\mathbf{E}_0 e^{-i\omega t} \tag{2.1}$$

where m_e and e are the mass and charge of free electrons, while $\mathbf{E}_0$ and ω are the amplitude and angular frequency of the driving electric field. The symbol Γ is the damping term which is proportional to υ_F/l where υ_F is the Fermi velocity (i.e. the velocity of electrons when their kinetic energy is equal to the Fermi energy) and l is the electron's mean free path between two consecutively scattering events. The solution of Eq. (2.1) (read Appendix A) gives

$$\varepsilon_{Drude}(\omega) = 1 - \frac{\omega_p^2}{\omega^2 + i\Gamma\omega} \tag{2.2}$$

where $\omega_p = \sqrt{\frac{n_e e^2}{\varepsilon_0 m_e}}$ is the *free* plasma frequency, with n_e and ε_0 being the number of free electrons per unit volume and permittivity of vacuum, respectively. It is also useful to separate the real and imaginary parts of the above expression as it will be insightful when time comes to examine the dispersion relation for some simple paradigms (for more information read Section 2.3)

$$\varepsilon_{Drude}(\omega) = 1 - \frac{\omega_p^2}{\omega^2 + \Gamma^2} + i\frac{\Gamma\omega_p^2}{\omega(\omega^2 + \Gamma^2)} \tag{2.3}$$

The plasma frequency is a very important parameter for metals since above that frequency they cease to have metallic behaviour (i.e. the permittivity becomes positive).

2.2.2 Lorentz model

As we will soon see the Drude–Sommerfeld model produces accurate results for most metals in the IR spectrum or above. For frequencies where inter-band transitions occur the aforementioned model starts to fail. A method to overcome this discrepancy is by introducing a restoration force to make the modelled electrons bounded even though they are not connected to a nucleus. Based on the same principle as in Section 2.2.1 the equation of motion now becomes

$$m_e^* \frac{\partial^2 \mathbf{r}}{\partial t^2} + m_e^* \gamma \frac{\partial \mathbf{r}}{\partial t} + m_e^* \omega_0^2 \mathbf{r} = e\mathbf{E}_0 e^{-i\omega t} \tag{2.4}$$

where m_e^* is now the *effective* electron mass and γ is the damping coefficient expressing the radiative damping of bound electrons. The extra term $m_e^* \omega_0^2 \mathbf{r}$ comes from the spring-like connection of electrons with the nucleus based on Hooke's law. The solution leads to (read also Appendix A)

$$\varepsilon_{Lor}(\omega) = 1 - \frac{\omega_p^{*2}}{\omega^2 - \omega_0^2 + i\gamma\omega} \tag{2.5}$$

Here $\omega_p^* = \sqrt{\frac{n_e^* e^2}{\varepsilon_0 m_e^*}}$ is the *effective* plasma frequency with n_e^* to be the volume density of bound electrons. The resonant frequency of the spring is $\omega_0 = \sqrt{k/m_e^*}$ with k to be the spring constant. Separating again the real and imaginary parts we find

$$\varepsilon_{Lor}(\omega) = 1 + \frac{\omega_p^{*2}(\omega_0^2 - \omega^2)}{(\omega_0^2 - \omega^2)^2 + \gamma^2\omega^2} + i\frac{\gamma\omega_p^{*2}\omega}{(\omega_0^2 - \omega^2)^2 + \gamma^2\omega^2} \tag{2.6}$$

In order to test the validity of Eq. (2.2) and (2.5), a comparison with the experimental permittivity of Au taken from [30] is shown in Fig. 2.1. From Fig. 2.1(a) and especially from Fig. 2.1(b) we observe that the Lorentz model fits well only in the regime where electron transitions occur (< 600

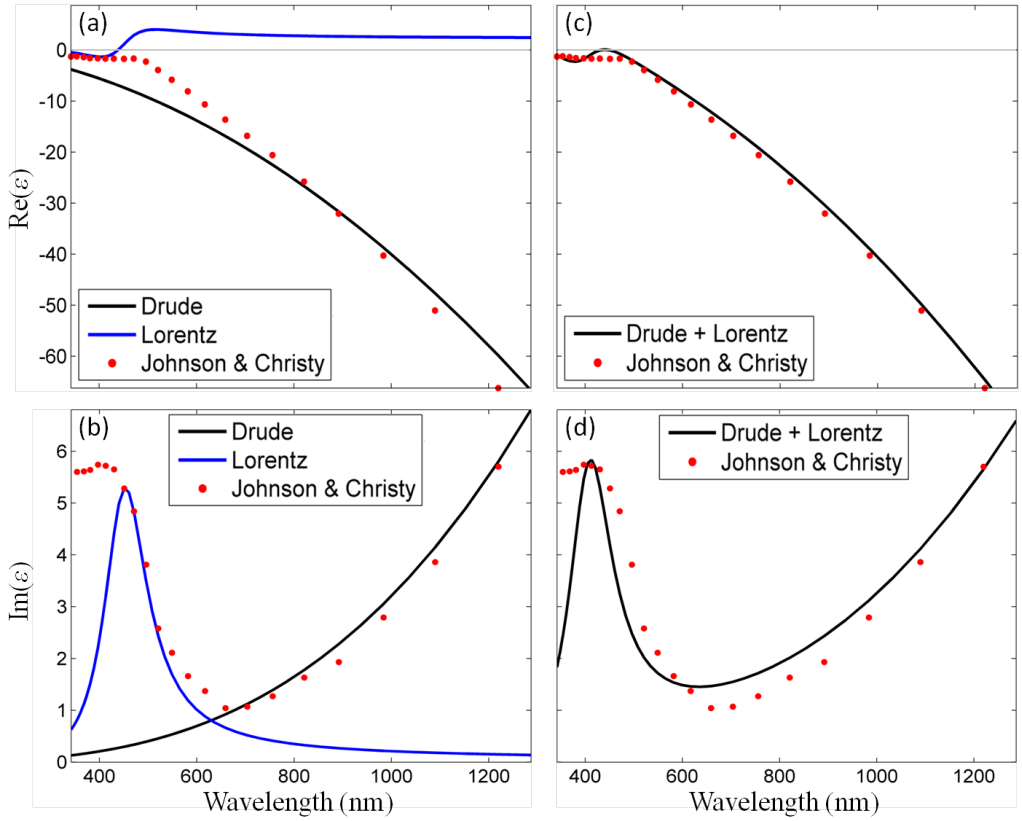

Figure 2.1: Comparison of the real (a) and imaginary (b) permittivity of Au, based on the Drude and Lorentz models, with the experimental data taken from [30]. The Lorentz model agrees well below 600 nm while the Drude one for greater wavelengths. (c),(d) Same case as before, but adding the contribution of both models ($\varepsilon_{Drude}(\omega) + \varepsilon_{Lor}(\omega)$).

nm), while for greater wavelengths the Drude model dominates. The electron transitions of noble metals and especially for Au considered here, are due to d and s-p conduction electrons [31]. Additionally, the surface plasmon resonance of Au is close to 2.38 eV (520 nm) meaning that both mechanisms contribute to absorption. Consequently to make a dielectric function that fits well through the whole spectral range a sum of these two models is necessary. A very simple example is shown in Fig. 2.1(c) and 2.1(d) where

the sum of $\varepsilon_{Drude}(\omega)$ and $\varepsilon_{Lor}(\omega)$ is taken as the dielectric permittivity of Au. It is obvious that this combined model has better agreement than its individual counterparts alone. However, in order to improve the fitting, a constant $\varepsilon_\infty = 6$ offset was inserted which expresses the total contribution of all higher-energy electronic polarizability. It should be noted that below a free space wavelength of about 500 nm, the model still deviates from the experimental data since only one oscillator is accounted. To improve the agreement even further, more oscillators of the form of Eq. (2.5) can be introduced.

2.3 Basic properties of surface plasmon polaritons

In the previous Section we explained how the dielectric function of metals can be modelled for a broad range of wavelengths inside and outside the interband transition regime. Here, we explain some basic properties of surface plasmon polaritons based on some simple paradigms. We consider the case of an electromagnetic wave in two half-space planar media. Although it is not mandatory for the explanation of the fundamental physical properties of SPPs, we take one of the two semi-infinite media to be anisotropic. The reason for this choice will become apparent in the following Sections.

There are two possible configurations of the electromagnetic wave. The first one is to have the magnetic field perpendicular to the **k**-plane, known as TM- or p-polarization, and the other to have the electric field, known as TE- or s-polarization. The later one is not used for the excitation of SPPs because metals are non-magnetic since their permeability is close to unity for all frequencies of interest (see Fig. 1.2). The only way to excite SPPs via

TE-polarization is to use materials with negative permeability in order to get a real solution of the SPP wavevector. However, this is outside the scope of the current thesis and will not be discussed further, the reader can read through Appendix B.2 for more information.

Let us consider the case of TM-polarized waves in 2 half-space media as shown in Fig. 2.2. The material (ε_1, μ_1) is isotropic with $\mu_1 = 1$, while the material $(\widetilde{\varepsilon}_2, \mu_2)$ is anisotropic of the form $\widetilde{\varepsilon}_2 = (\varepsilon_{xx}, \varepsilon_{yy}, \varepsilon_{zz})^\intercal$ and $\mu_2 = 1$. The permittivity tensor has zero off-diagonal elements. The electromagnetic fields for the two media, namely $j = 1$ and $j = 2$, can be written as

$$\mathbf{E}_j = (E_{xj}, 0, E_{zj})^\intercal e^{i(k_{xj}x \mp k_{zj}z - \omega t)}, \quad j = 1, 2 \tag{2.7}$$

$$\mathbf{H}_j = (0, H_{yj}, 0)^\intercal e^{i(k_{xj}x \mp k_{zj}z - \omega t)}, \quad j = 1, 2 \tag{2.8}$$

where the $\mp k_{zj}z$ term corresponds to the lower $(z < 0)$ or upper $(z > 0)$ material.

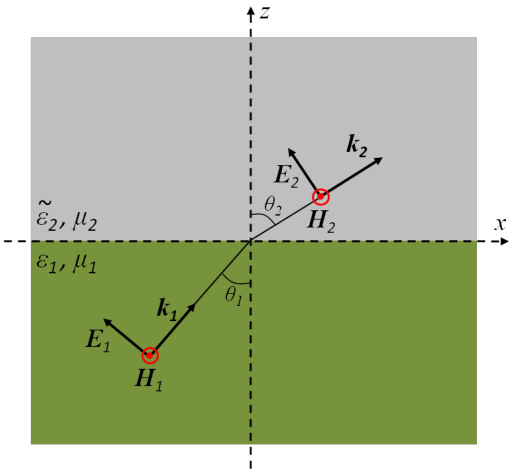

Figure 2.2: TM-polarized waves inside a material (ε_1, μ_1) and a material $(\widetilde{\varepsilon}_2, \mu_2)$. Both media are considered semi-infinite.

The main target is to derive the dispersion relation of SPPs and for that the wavevector parallel to x-direction needs to be calculated. The macroscopic Maxwell's equations with no net charge ($\rho = 0$) or current densities ($\mathbf{J} = 0$) for the Fig. 2.2 scenario take the form

$$\nabla \cdot (\varepsilon_j \mathbf{E}_j) = 0, \quad j = 1, 2 \tag{2.9}$$

$$\nabla \times \mathbf{E}_j = -\frac{\mu_j}{c}\frac{\partial \mathbf{H}_j}{\partial t} = \frac{i\omega\mu_j}{c}\mathbf{H}_j, \quad j = 1, 2 \tag{2.10}$$

$$\nabla \cdot \mathbf{B}_j = 0, \quad j = 1, 2 \tag{2.11}$$

$$\nabla \times \mathbf{H}_j = -\frac{\varepsilon_j}{c}\frac{\partial \mathbf{E}_j}{\partial t} = -\frac{i\omega}{c}\varepsilon_j \mathbf{E}_j, \quad j = 1, 2 \tag{2.12}$$

and the boundary conditions at the interface ($z = 0$)

$$(\mathbf{D}_2 - \mathbf{D}_1) \cdot \hat{n} = 0 \tag{2.13}$$

$$\hat{n} \times (\mathbf{E}_2 - \mathbf{E}_1) = 0 \tag{2.14}$$

$$\hat{n} \times (\mathbf{H}_2 - \mathbf{H}_1) = 0 \tag{2.15}$$

where $\hat{n}$ is the unit vector normal to the interface. Applying Eq. (2.9)-(2.15) we can find (read Appendix B) the following set of equations that connect the wavevector components of the two materials

$$\frac{k_{z1}}{k_{z2}} = -\frac{\varepsilon_1}{\varepsilon_{xx}} \tag{2.16}$$

$$k_{z1}^2 + k_x^2 = \left(\frac{\omega}{c}\right)^2 \varepsilon_1 \tag{2.17}$$

$$k_{z2}^2 + \frac{\varepsilon_{xx}}{\varepsilon_{zz}} k_x^2 = \left(\frac{\omega}{c}\right)^2 \varepsilon_{xx} \tag{2.18}$$

Dividing Eq. (2.17) with Eq. (2.18) and based on the result of Eq. (2.16) we can find the *anisotropic SPP dispersion* between two semi-infinite media

$$k_x = \frac{\omega}{c}\sqrt{\frac{\varepsilon_{zz}\varepsilon_1(\varepsilon_{xx}-\varepsilon_1)}{\varepsilon_{xx}\varepsilon_{zz}-\varepsilon_1^2}} > k_0 \tag{2.19}$$

and also the dispersion of the wavevector components normal to the interface for each material

$$k_{z1} = \frac{\omega\varepsilon_1}{c}\sqrt{\frac{\varepsilon_{zz}-\varepsilon_1}{\varepsilon_{xx}\varepsilon_{zz}-\varepsilon_1^2}} \tag{2.20}$$

$$k_{z2} = \frac{\omega\varepsilon_{xx}}{c}\sqrt{\frac{\varepsilon_{zz}-\varepsilon_1}{\varepsilon_{xx}\varepsilon_{zz}-\varepsilon_1^2}} \tag{2.21}$$

Since the wavevectors are derived, the SPP excitation conditions can now be investigated. For simplicity, let us assume that all permittivities have high real parts compared to their imaginary counterparts. This practically means that the SPP damping is negligible and the modes can propagate along the interface for long distances. Nevertheless, this has no connection with the excitation conditions which means that the imaginary parts can be safely ignored. In order to have propagating waves along the interface we need k_x to be real valued and thus the normal components must be purely imaginary. If k_{z1} and k_{z2} are imaginary, their ratio must be positive. Inspecting Eq. (2.16) we see that this holds only when ε_1 and ε_{xx} are opposite in sign [32]. As a consequence, excitation of SPPs can *only* be realized when one medium has dielectric properties and the other metallic. If for example the isotropic dielectric medium has $\varepsilon_1 > 0$, then the SPP excitation conditions require the $\varepsilon_{xx} < 0$ and from Eq. (2.19)-(2.21) the $\varepsilon_{zz} > \varepsilon_1$ if ε_{zz} is positive, or $\varepsilon_{xx}\varepsilon_{zz} > \varepsilon_1^2$ if ε_{zz} is negative. The main outcome from the above paradigm is the requirement of *at least* one component of the permittivity tensor to be negative.

For the specific case where the anisotropic medium becomes isotropic we have $\varepsilon_{xx} = \varepsilon_{zz} = \varepsilon_2$ and Eq. (2.19)-(2.21) simplify to the well known *isotropic*

SPP dispersion

$$k_x = \frac{\omega}{c}\sqrt{\frac{\varepsilon_1\varepsilon_2}{\varepsilon_1+\varepsilon_2}} \tag{2.22}$$

and the normal to the interface wavevector components

$$k_{zj} = \frac{\omega}{c}\sqrt{\frac{\varepsilon_j^2}{\varepsilon_1+\varepsilon_2}}, \quad j = 1,2 \tag{2.23}$$

In order to get a real k_x we need the sum and the product of permittivities to be either both positive or both negative. Inspecting Eq. (2.23) we observe that k_{zj} can become imaginary only when the sum of permittivities is negative, leading to $\varepsilon_1\varepsilon_2 < 0$ for k_x to be real. We thus conclude to a fundamental property of SPPs: The only way for surface plasmon polaritons to exist is by having a metallodielectric interface regardless the anisotropy of the material.

Based on the results we have derived so far, we will examine a few more physical properties of SPPs. To keep the examples simple, we consider only isotropic materials. The only difference using anisotropic materials is the different response at various directions, however the basic principles governing SPPs are still the same. Based on Fig. 2.2, let us assume that ε_1 is a lossless dielectric and ε_2 a metal. If we write $\varepsilon_2 = \varepsilon_2' + i\varepsilon_2''$ where ε_2' and ε_2'' are real quantities then the SPP wavevector will be $k_x = k_x' + ik_x''$, where k_x' and k_x'' are also real. The k_x' part represents the SPP wavelength while the k_x'' is damping of the surface wave as it propagates along the interface due to ohmic losses. To calculate the real and imaginary part of k_x we need to insert the complex ε_2 into Eq. (2.22). Under the assumption $|\varepsilon_2''| \ll |\varepsilon_2'|$, which is correct for most noble metals in the visible spectrum and above, we get

$$k_x' \approx \frac{\omega}{c}\sqrt{\frac{\varepsilon_2'\varepsilon_1}{\varepsilon_2'+\varepsilon_1}} \tag{2.24}$$

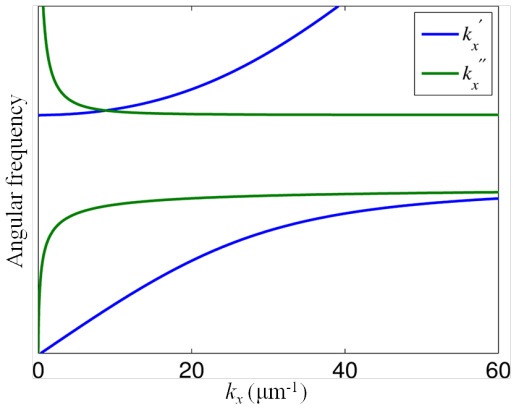

Figure 2.3: Isotropic SPP dispersion showing the real (k_x') and imaginary (k_x'') components of the wavevector. The frequency gap distinguishes the dispersion into a lower and higher frequency branch. Notice in the lower frequency part how the damping term sharply increases as the SPP reaches higher wavevectors.

$$k_x'' \approx \frac{\omega}{c}\sqrt{\frac{\varepsilon_2'\varepsilon_1}{\varepsilon_2'+\varepsilon_1}}\frac{\varepsilon_2''\varepsilon_1}{2\varepsilon_2'(\varepsilon_2'+\varepsilon_1)} \tag{2.25}$$

Fig. 2.3 illustrates the aforementioned expressions for a SPP on a metal, with a Drude-Sommerfeld permittivity, and air. A frequency gap is observed where both components become purely imaginary meaning that no SPP can exist. Notice also how in the lower frequency branch the damping term precipitously increases as the SPP approaches higher wavevectors. All these phenomena will be discussed in the next Section. From Eq. (2.24) we can directly measure the SPP wavelength

$$\lambda_{SPP} = \frac{2\pi}{k_x'} \approx \lambda\sqrt{\frac{\varepsilon_2'+\varepsilon_1}{\varepsilon_2'\varepsilon_1}} \tag{2.26}$$

where λ is the wavelength of light in vacuum. For example, if a wave with $\lambda = 700$ nm is in vacuum ($\varepsilon_1 = 1$) and approaches a Au interface with [30] $\varepsilon_2 = -16.8 + 1.07i$ the SPP wavelength will be approximately 680 nm. Since

ohmic losses are present, it is reasonable to examine how far the surface wave can travel. The *propagation length* (L_p) is defined as the distance a wave can travel before its electromagnetic components are decreased by $1/e$ compared to the initial ones. The reason why the value $1/e$ is used has to do with the exponential nature of the fields. If we replace the $k_x = k'_x + ik''_x$ in Eq. (2.7) and (2.8) we can directly observe the exponential decay ($e^{-|k''_x|x}$) of the fields along the interface due to damping. The $1/e$ decay length happens when $L_p = 1/k''_x$. For the same wavelength and permittivities as before, the SPP propagation length is around 54 μm.

Another interesting parameter, is the decay length at directions normal to the interface. Since the wavevector along the z-axis is purely imaginary, there is no propagation and the fields start to decay immediately away from the surface. For that reason, the characteristic decay where the fields are decreased by $1/e$ is called *skin depth* (L_s). Based on the same assumption as the one we did for Eq. (2.24) and (2.25), we can replace $\varepsilon_2 = \varepsilon'_2 + i\varepsilon''_2$ in Eq. (2.23) and get

$$k_{1z} \approx \frac{\omega}{c}\sqrt{\frac{\varepsilon_1^2}{\varepsilon'_2 + \varepsilon_1}}\left[1 - i\frac{\varepsilon''_2}{2(\varepsilon'_2 + \varepsilon_1)}\right] \tag{2.27}$$

$$k_{2z} \approx \frac{\omega}{c}\sqrt{\frac{\varepsilon'^2_2}{\varepsilon'_2 + \varepsilon_1}}\left[1 + i\frac{\varepsilon''_2}{2\varepsilon'_2}\right] \tag{2.28}$$

Notice in the above expressions when $|\varepsilon''_2| \ll |\varepsilon'_2|$ the imaginary parts are very small. For instance, if $|\varepsilon'_2|/|\varepsilon''_2| = 10$ then $k'_{1z}/k''_{1z} = 22$ and $k'_{2z}/k''_{2z} = 20$. Using the same permittivities as before and neglecting the imaginary part for the k_z terms, we find the skin depth to be $1/k_{z1} \approx 443$ nm and $1/k_{z2} \approx 26$ nm. This means that the electromagnetic fields decay much faster inside the metal than into the dielectric.

2.4 Excitation of surface plasmon polaritons

The excitation of surface plasmon polaritons requires energy and momentum conservation along the interface. Since energy is given from $E = \hbar\omega$ and momentum along a given direction from $p_x = \hbar k_x$, the dispersion relation of the SPP wavevector at different angular frequencies needs to be analysed. We will examine the dispersion of a SPP in an isotropic metallodielectric interface. The anisotropic scenario is thoroughly discussed in Section 5.2. Let assume that the dielectric is air ($\varepsilon_1 = 1$) and the dielectric function of metal ($\varepsilon_2(\omega)$) follows either the Drude-Sommerfeld model (Eq. (2.2)) or the Lorentz model (Eq. (2.5)). If we plug these two cases in Eq. (2.22) we can plot the dispersion of a surface plasmon polariton in terms of the angular frequency as shown in Fig. 2.4.

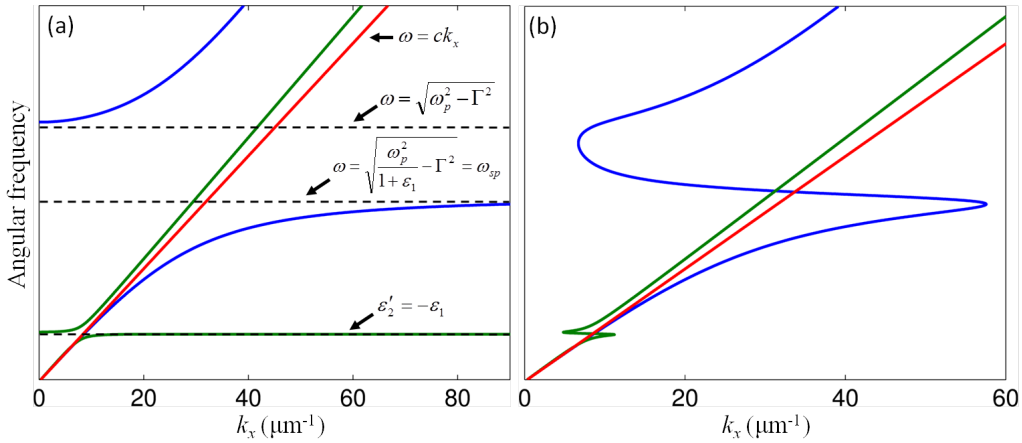

Figure 2.4: SPP dispersion relation for a semi-infinite air/metal interface without (a) and with (b) ohmic losses. The green curve takes into account the interband transitions while the blue one (Drude-Sommerfeld model) does not. The red line is the light line in air. Figure (a) also shows the asymptotic lines for some characteristic frequencies (black dashed lines).

The green and blue curves show the SPP dispersion when the Lorentz or the Drude-Sommerfeld model is taken into account, respectively. The light line in air is also apparent for guidance (red line). There are also some characteristic asymptotic dashed lines that mark some important frequencies around which a drastic change of the dispersion is observed. The only difference between the two graphs is that in Fig. 2.4(a) both models are considered lossless (i.e. the imaginary part is zero for all frequencies) while in Fig. 2.4(b) losses are also accounted. From both images, especially from Fig. 2.4(a), we see that the dispersion is separated into a low-frequency and a high-frequency part. The high-frequency branch is not a real SPP because the k_z component in metal is not purely imaginary any more. These are volume plasmons that exist *inside* the metal due to electron oscillations (read Section 2.1). Conversely, the low-frequency branch corresponds to a real SPP since it satisfies all the wavevector conditions for a surface mode to exist. For the Lorentz model (green curve), the critical point where the two branches separate is when $\varepsilon_2' = -\varepsilon_1$. Since ε_1 is positive then ε_2' should be negative which means that the angular frequency must always be greater than the resonant frequency (ω_0). This can be easily checked from Eq. (2.6). For the Drude-Sommerfeld model we see two asymptotic lines. The one that is closer to the low-frequency branch is observed when $k_x \to \infty$ which is true when $\varepsilon_2' \to -\varepsilon_1$ (See Eq. (2.24)). This corresponds to the critical frequency $\omega^2 = \omega_p^2/(1+\epsilon_1) - \Gamma^2$ (Eq. (2.3)) also known as surface plasmon frequency (ω_{sp}). For the asymptotic line closer to the upper frequency branch, we have $k_x \to 0$ which is true when $\varepsilon_2' \to 0$. From the same equation as before, this is valid when $\omega^2 = \omega_p^2 - \Gamma^2$. Considering the lossy case of Fig. 2.4(b), We observe that the dispersion can not become infinite or zero no matter which dielectric function model is used. On the contrary there is finite continuous

transition that connects the low- and high-frequency parts. As the frequency approaches the transition regime the losses increase dramatically and prevent any further increase of k_x. This is the reason why the SPP dispersion can not extend to very high wavevectors and experimentally is always finite.

Another interesting feature with practical significance, is the larger SPP wavevector than the wavevector of light in vacuum. Only for low energies the light line asymptotically starts to approach the SPP dispersion. The physical explanation for the increased momentum of SPPs is due to the strong coupling of the electromagnetic field with the surface electrons. A forthcoming dilemma is how a SPP can be excited if there is always momentum mismatch.

The simplest way to overcome this obstacle is by adding a dielectric medium with refractive index $n > 1$. In this case, the slope of the light line will be tilted by a factor of n since $\omega = ck/n$. A simple paradigm that shows the crossing of a higher index dielectric light line and the SPP dispersion based on Eq. (2.2) is shown in Fig. 2.5(a). One of the first experimental demonstrations, known as Otto configuration [4], is depicted in Fig. 2.5(b). In this arrangement, an evanescent wave is formed in the prism/air surface and through tunneling it couples to the air/metal surface that can support SPPs. Since $k_{SPP} = k_{prism} \sin\theta$, where k_{prism} is the total wavevector inside the prism, the momentum matching can be satisfied by tuning the angle of incidence (θ). When the angle of incidence becomes equal to the critical angle where a SPP is excited a minima in the reflection spectrum is observed (more will be discussed in next Chapter). The major barrier of the previous method was the difficult control of the air gap. To overcome this, a slightly modified method was proposed a few years later, known as Kretschmann configuration (Fig. 2.5(c)). Here, the air gap is replaced by a metal and the evanescent fields in the prism/metal interface can tunnel through the metal

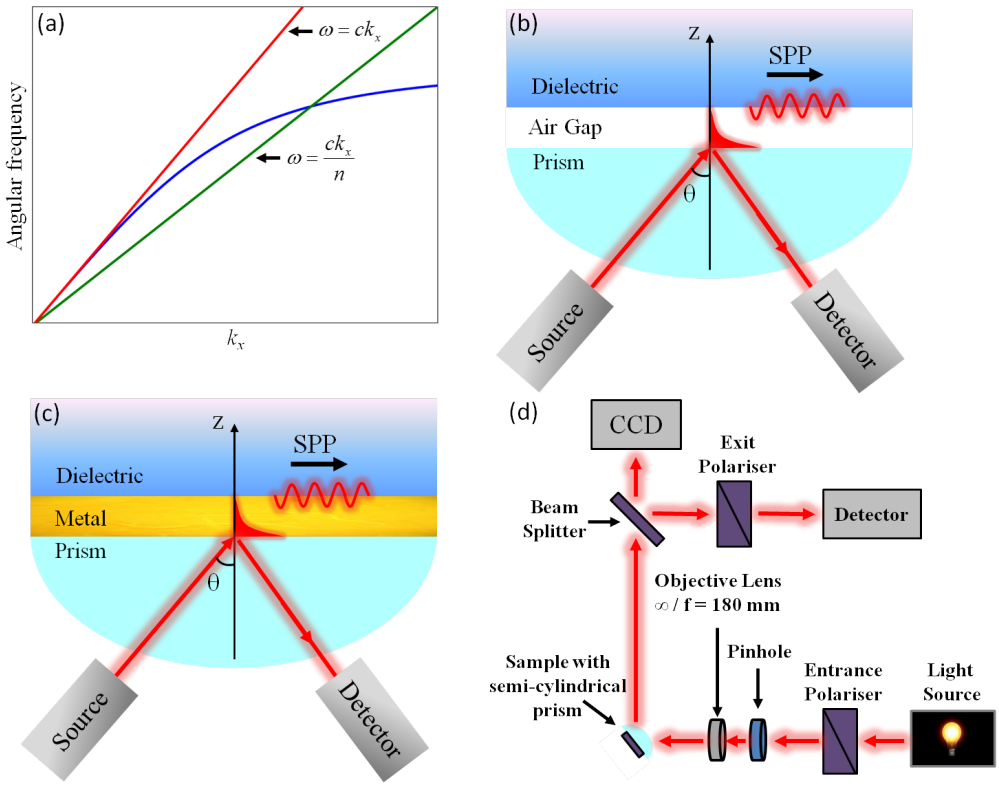

Figure 2.5: Experimental excitation of SPPs. (a) When $n > 1$ the light line is tilted by c/n and can couple to the SPP at the crossing point where both energy and momentum are conserved. One common way to experimentally achieve this is through the Otto (b) or Kretschmann (c) configurations. (d) Experimental setup based on Kretschmann configuration.

slab and couple to surface waves in the metal/dielectric interface. It should be noted that careful inspection of metal's thickness is required. If the metal is very thin the radiation damping of SPPs will be very intense due to the radiation damping into the dielectric. On the other hand, if it is too thick the evanescent waves will be absorbed and no SPPs will be excited. However, it is easier to control the thickness of the metal rather than the air gap in Otto's method.

In the current thesis the angular resolved spectroscopy was done based on the Kretschmann configuration. Fig. 2.5(d) depicts the experimental setup. The source, which is a typical white light lamp, creates a light beam that passes through a polariser (entrance polariser) in order to specify the incident polarisation (either TE- or TM-). The polarised beam then passes through a $\infty/f = 180$ mm objective lens and reaches the sample area. It should be noted that a pinhole with a 0.5 mm diameter aperture is placed just before the lens in order to minimize the spread of the beam so that the sample is under plane wave illumination at a single angle of incidence. The measured wavelengths range from 400 nm to 900 nm giving a minimum angle spread of $\delta\theta_{min} = \pm 0.056^{\circ}$ and maximum $\delta\theta_{max} = \pm 0.126^{\circ}$. Afterwards, the beam approaches the interface of a semi-cylindrical prism of the same refractive index as the sample's substrate (Fig. 2.5(d)). The semi-cylindrical shape guarantees that the incident light will always be normal to the prism's interface *regardless* the rotation angle of the source. An index matching fluid is used to mount the sample on the flat interface of the prism (Nikon NF immersion oil). After light is reflected from the sample, it enters a beam splitter and 50% of light's intensity goes to a visualization CCD and the rest passes through a second polariser (exit polariser) and is directed to the detection system. This system comprises of a spectrometer (Triax 322 from HORIBA Yobin Yvon) coupled to LH2 cooled CCD.

Apart from the aforementioned methods there are a few other ways to excite SPPs. One way is via the scanning near-field optical microscopy (SNOM) on the interface of a metallodielectric pair as shown in Fig. 2.6(a). The main advantage of this technique is that light in its apex is confined to a single spot acting as a point source. This allows selective illumination of structure at a tiny point of interest making it ideal for the examination of surface plas-

mon interactions since they remain unperturbed by the scattered wavelets produced by a bigger size illumination spot [25]. The SNOM's tip acts as a scatterer and provides momentum matching meaning that the evanescent component of the source can achieve in-plane wavevectors of any magnitude and thus excite SPPs [25]. However, due to the fact these waves decay exponentially fast as we move away from the interface, the probe must be on subwavelength distance from the interface.

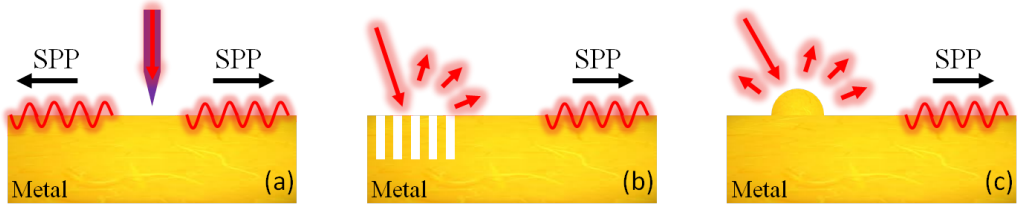

Figure 2.6: Experimental configurations for the excitation of SPPs. Excitation with a SNOM probe (a) a periodic grating (b) and surface features (c).

Another method that can support momentum conservation for the SPP excitation is light diffraction on periodic gratings [7] (Fig. 2.6(b)). If a smooth metal film is grated, the incident light can be diffracted along the grating directions. The diffracted light whose wavevector matches the corresponding one of the SPP can couple and excite it. Depending on various parameters such as the thickness of the metal layer or the depth of the grating, SPPs can be excited on both surfaces of the metallic layer outside the grating area [33]. In general, when a surface has random roughness the excitation requirements can be satisfied without any special configuration. The reason is that all wavevectors are present on the vicinity of the surface [7, 8]. The main obstacle in this scenario is the low SPP coupling due to the randomness of wavevectors. The non-resonant excitation result in a low efficiency of SPP

and high reflectivity. The momentum is also conserved because here $k_{SPP} \rightarrow k_{SPP} \pm n\frac{2\pi}{\alpha}$, where n is a natural number and α is the lattice constant of grating. The extra term $n\frac{2\pi}{\alpha}$, also known as grating wavevector, adds the extra momentum needed.

A third method, similar to the grating one, is the use of surface features such as small nanoparticles shown in Fig. 2.6(c). Features of any shape can be used for the SPP excitation as long as their size remain small compared to wavelength. All the configurations of Fig. 2.6 has been proved valuable for different kind of experiments, however they will not be discussed further since the Kretschmann configuration was used for the current thesis. The reader can refer to [34] or [35] for more information.

2.5 Localized surface plasmons

In the previous Sections we discussed about the properties of surface plasmon polaritons along with their excitation conditions. Here we introduce another fundamental excitation of plasmonics tightly connected with the shape of the (nano)particle. These modes arise from the coherent charge density oscillations due to the spatial confinement of the particle. Since the size of the particle is considered a lot smaller than a planar interface where SPPs exist, the excited modes are non-propagating and are thus localized, hence the term *localized surface plasmons* (LSPs). An immediate consequence of spatial confinement of the particle is that LSPs can be excited by direct illumination without the need of momentum matching methods (see Section 2.4).

For Ag and Au nanoparticles the LSP falls into the visible spectrum. For this reason colloidal Au was, for many centuries, a fascinating material commonly used in the medieval cathedral windows or ornamental cups since it

provided different colors based on the size and shape of nanoparticles. Over the last years there has been a significant growth in the exploitation of colloidal Au for biological labels or markers in microscopic techniques [36]. The intense light absorption and scattering of nanoparticles at their resonance, the so-called localized surface plasmon resonance (LSPR), has found many potential applications ranging from photovoltaics [37] to imaging, sensing and photothermal therapy [38]. The strong confinement of the near-field at the LSP resonance is used for surface-enhanced Raman scattering [39], nanophotonic functionality [40], and as a chemo- or biosensor [41, 42] among others. For an in-depth discussion regarding the biosensing capabilities of LSPs read Chapter 5.

If an isolated spherical particle of size d and permittivity ε interacts with an external electromagnetic field of wavelength $\lambda \gg d$ in a medium of permittivity ε_m, then the phase of this field can be considered constant over the particle volume. In this scenario the time-derivatives in Maxwell's equations can be neglected leading to the *quasi-static approximation*. The solution to this problem is known as *Laplace equation* for the potential $\nabla^2\Phi = 0$. The electric field can then be found through $E = -\nabla\Phi$. The general solution to this problem can be found in standard textbooks, such as [43], leading to

$$\Phi_{in} = -\frac{3\varepsilon_m}{\varepsilon + 2\varepsilon_m} E_0 r cos(\theta) \tag{2.29}$$

$$\Phi_{out} = -E_0 r cos(\theta) + \frac{\mathbf{p} \cdot \mathbf{r}}{4\pi\varepsilon_0\varepsilon_m r^3} \tag{2.30}$$

$$\mathbf{p} = 4\pi\varepsilon_0\varepsilon_m R^3 \frac{\varepsilon - \varepsilon_m}{\varepsilon + 2\varepsilon_m} \mathbf{E}_0 \tag{2.31}$$

where Φ_{in}, Φ_{out} are the potentials inside and outside the particle of radius R, r is the space position, and θ is the angle between the external electric field,

$\mathbf{E}_0$, and the induced dipole moment, $\mathbf{p}$. Defining the polarizability g through $\mathbf{p} = \varepsilon_0 \varepsilon_m g \mathbf{E}_0$, we find that

$$g = 4\pi R^3 \frac{\varepsilon - \varepsilon_m}{\varepsilon + 2\varepsilon_m} \tag{2.32}$$

The above expression clearly shows a resonant behaviour when $|\varepsilon + 2\varepsilon_m|$ minimizes. This minimization corresponds to an LSP with a dipolar resonance at $\mathrm{Re}(\varepsilon) = -2\varepsilon_m$ assuming that the $\mathrm{Im}(\varepsilon)$ is small. It is thus clear that if ε_m is dielectric ε must be metal for the resonance to exist.

We now turn our attention to a slightly more general case closer to the shape of the structures where this thesis is focused. The spherical particle is now converted to an ellipsoid with semi-axes c_x, c_y, c_z along the x-, y- and z-directions, respectively. The scattering problem for an isolated ellipsoid can be treated in a similar way as before leading to the following polarizability expression [28]

$$g_i = 4\pi c_x c_y c_z \frac{\varepsilon - \varepsilon_m}{3\varepsilon_m + 3N_i(\varepsilon - \varepsilon_m)}, \quad i = x, y, z \tag{2.33}$$

where N_i is the depolarization factor (more information can be found in Section 3.5). For the case where $c_x = c_y = c_z = R$ we get $N_x = N_y = N_z = 1/3$ and Eq. (2.33) simplifies to (2.32). The polarizability plays a crucial role in the efficiency with which a particle scatters and absorbs light; this can be directly observed in the scattering cross sections for the scattering, C_{sca}, and absorption, C_{abs}, given from [28]

$$C_{sca} = \frac{k_0^4}{6\pi} |g_i|^2 \tag{2.34}$$

$$C_{abs} = k_0 \mathrm{Im}(g_i) \tag{2.35}$$

A particular class of ellipsoids are the *prolate ellipsoids* which are a good approximation of the nanorod metamaterials which the current thesis mainly investigates. In this scenario we have $c_x = c_y < c_z$, so the aspect ratio, namely c_z/c_x, can change drastically. Fig. 2.7(a) shows the impact of aspect ratio on particle's shape when varying it from 1 (sphere) to 10. When aspect ratio becomes greater than unity two types of LSPs can be distinguished, one is excited along the short axis of the ellipsoid, known as transverse mode, and the other along the long axis, known as longitudinal mode. To see the optical importance of the aspect ratio, the extinction cross section, defined as $C_{ext} = C_{sca} + C_{abs}$, for various aspect ratios is depicted in Fig. 2.7(b) and Fig. 2.7(c) for the transverse and longitudinal modes respectively. The nanoparticle is Au taken from [30] while the surrounding medium has $\varepsilon_m = 1.5^2$. In both cases C_{ext} increases with aspect ratio which is due to the increased volume of the nanoparticle (Fig. 2.7(a)). At the same time there is a slight blue-shift of the transverse mode and a drastic red-shift of the longitudinal mode. The reason for this is the actual change of the short and long semi-axes; the short semi-axis changes only a little when the aspect ratio goes from 1 to 10, while in the long semi-axis it increases sharply. To better visualize the mode-shift, Fig. 2.7(d) demonstrates the resonant wavelength shift of the longitudinal and transverse modes in terms of the aspect ratio. It is clear that controlling aspect ratio it is possible to set the longitudinal mode position anywhere from visible to infrared. Notice also how the two modes converge to a single wavelength as the aspect ratio becomes unit. It should be emphasized that at all times the condition $\lambda \gg c_{x,y,z}$ must hold. For Fig. 2.7 the short semi-axis was kept fixed at 5 nm while the long semi-axis was varied from $5 - 50$ nm so even at the extreme case where $c_z = 50$ nm the minimum wavelength (450 nm) was still significantly higher.

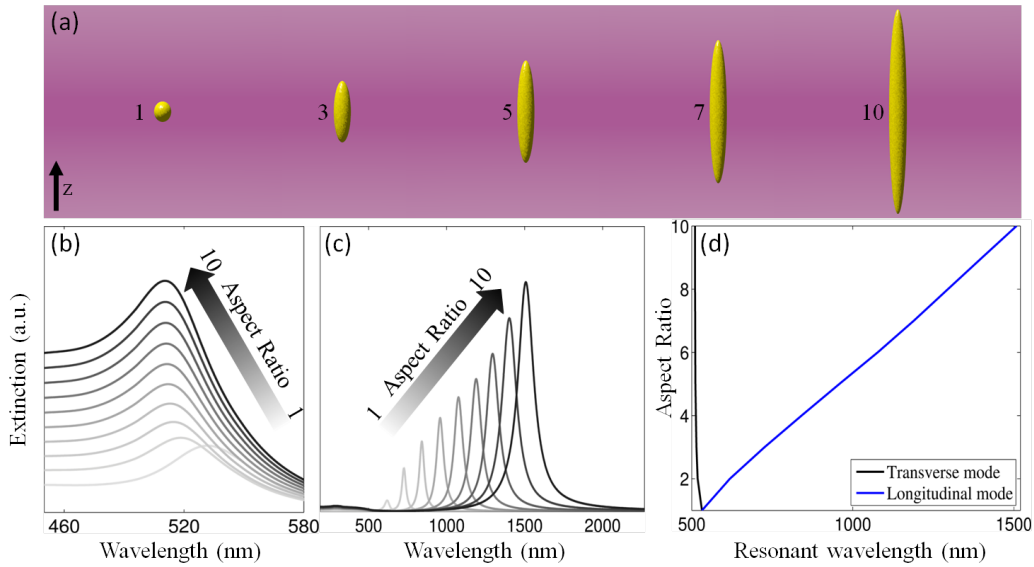

Figure 2.7: (a) Schematics of prolate ellipsoids at different aspect ratios shown with numbers. Extinction cross sections of the (b) transverse and (c) longitudinal modes with aspect ratio ranging from 1 to 10. (d) Resonant wavelength of the transverse and longitudinal modes for the same aspect ratio range as before. Notice the drastic (slight) red-shift (blue-shift) of the longitudinal mode (transverse mode).

To conclude, in this Chapter the fundamental excitations in plasmonics were introduced along with the properties and excitation conditions of surface plasmon polaritons. Nevertheless the anisotropic material used was indefinite. In order to realize the actual structures examined in this thesis, a better understanding of the theoretical tools is required; this is the scope of the next Chapter.

References

[1] R. H. Ritchie, "Plasma losses by fast electrons in thin films," *Phys. Rev.*, vol. **106**, pp. 874–881, (1957).

[2] C. J. Powell and J. B. Swan, "Origin of the characteristic electron energy losses in aluminum," *Phys. Rev.*, vol. **115**, pp. 869–875, (1959).

[3] C. J. Powell and J. B. Swan, "Origin of the characteristic electron energy losses in magnesium," *Phys. Rev.*, vol. **116**, pp. 81–83, (1959).

[4] A. Otto, "Excitation of nonradiative surface plasma waves in silver by the method of frustrated total reflection," *Z. Physik*, vol. **216**, pp. 398–410, (1968).

[5] E. Kretschmann and H. Raether, "Radiative decay of non radiative plasmons excited by light," *Z. Naturforsch. A*, vol. **23**, pp. 2135–2136, (1968).

[6] H. Raether, *Excitation of Plasmons and Interband Transitions by Electrons.* Springer, (1980).

[7] H. Raether, *Surface Plasmons on Smooth and Rough Surfaces and on Gratings.* Springer, (1988).

[8] V. M. Agranovich and D. L. Mills, *Surface Polaritons.* North-Holland, (1982).

[9] G. Boisde and A. Harmer, *Chemical and Biochemical Sensing with Optical Fibers.* Arthech House, (1996).

[10] J. N. Anker, W. P. Hall, O. Lyandres, N. C. Shah, J. Zhao, and R. P. V. Duyne, "Biosensing with plasmonic nanosensors," *Nat. Mat.*, vol. **7**, pp. 442–453, (2008).

[11] G. A. Wurtz and A. V. Zayats, "Nonlinear surface plasmon polaritonic crystals," *Las. & Phot. Rev.*, vol. **2**, pp. 125–135, (2008).

[12] W. L. Barnes, A. Dereux, and T. W. Ebbesen, "Surface plasmon subwavelength optics," *Nature*, vol. **424**, pp. 824–830, (2003).

[13] A. V. Zayats and I. I. Smolyaninov, "Near-field photonics: surface plasmon polaritons and localized surface plasmons," *J. Opt. A: Pure Appl. Opt.*, vol. **5**, pp. S16–S50, (2003).

[14] T. W. Ebbesen, C. Genet, and S. I. Bozhevolnyi, "Surface-plasmon circuitry," *Phys. Today*, vol. **61**, pp. 44–50, (2008).

[15] W. Nomura, M. Ohtsu, and T. Yatsui, "Nanodot coupler with a surface plasmon polariton condenser for optical far/near-field conversion," *Appl. Phys. Lett.*, vol. **86**, p. 181108, (2005).

[16] S. Nakamura and G. Fasol, *The Blue Laser Diode: GaN-Based Light Emitting Diode and Lasers.* Springer, (1997).

[17] W. Srituravanich, N. Fang, C. Sun, Q. Luo, and X. Zhang, "Plasmonic nanolithography," *Nano Lett.*, vol. **4**, pp. 1085–1088, (2004).

[18] D. W. Pohl and D. Courjon, *Near Field Optics*. Kluwer, (1993).

[19] J. Hillier and R. F. Baker, "Microanalysis by means of electrons," *J. Appl. Phys.*, vol. **15**, pp. 663–675, (1944).

[20] J. Gotze, M. Plotze, and D. Habermann, "Origin, spectral characteristics and practical applications of the cathodoluminescence (cl) of quartz – a review," *Min. and Petr.*, vol. **71**, pp. 225–250, (2001).

[21] Y. Oshikane, T. Kataoka, M. Okuda, S. Hara, H. Inoue, and M. Nakano, "Observation of nanostructure by scanning near-field optical microscope with small sphere probe," *Sci. Tech. Adv. Mat.*, vol. **8**, pp. 181–185, (2007).

[22] P. M. Adam, L. Salomon, F. de Fornel, and J. P. Goudonnet, "Determination of the spatial extension of the surface-plasmon evanescent field of a silver film with a photon scanning tunneling microscope," *Phys. Rev. B*, vol. **48**, pp. 2680–2683, (1993).

[23] P. Dawson, F. de Fornelc, and J. P. Goudonnet, "Imaging of surface plasmon propagation and edge interaction using a photon scanning tunneling microscope," *Phys. Rev. Lett.*, vol. **72**, pp. 2927–2930, (1994).

[24] D. P. Tsai, J. Kovasc, Z. Wang, M. Moskovits, V. M. Shalaev, J. S. Suh, and R. Botet, "Photon scanning tunneling microscopy images of optical excitations of fractal metal colloid clusters," *Phys. Rev. Lett.*, vol. **72**, pp. 4149–4152, (1994).

[25] B. Hecht, H. Bielefeldt, L. Novotny, Y. Inouye, and D. W. Pohl, "Local excitation, scattering, and interference of surface plasmons," *Phys. Rev. Lett.*, vol. **77**, pp. 1889–1892, (1996).

[26] S. I. Bozhevolnyi, B. Vohnsen, and A. V. Zayats, *Optics at the Nanometer Scale*. Kluwer Acad. Publ., (1996).

[27] M. Born and E. Wolf, *Principles of Optics*, 6th ed. Cambridge University Press, (1980).

[28] C. F. Bohren and D. R. Huffman, *Absorption and Scattering of Light by Small Particles*. John Wiley & Sons, (1983).

[29] N. W. Ashcroft and N. D. Mermin, *Solid State Physics*. Saunders College Publishing, (1976).

[30] P. B. Johnson and R. W. Christy, "Optical constants of the noble metals," *Phys. Rev. B*, vol. **6**, pp. 4370–4379, (1972).

[31] N. E. Christensen and B. O. Seraphin, "Relativistic band calculation and the optical properties of Gold," *Phys. Rev. B*, vol. **4**, pp. 3321–3344, (1971).

[32] M. Kadic, S. Guenneau, and S. Enoch, "Transformational plasmonics: cloak, concentrator and rotator for spps," *Opt. Express*, vol. **18**, pp. 12 027–12 032, (2010).

[33] L. Salomon, G. Bassou, H. Aourag, J. P. Dufour, F. de Fornel, F. Carcenac, and A. V. Zayats, "Local excitation of surface plasmon polaritons at discontinuities of a metal film: Theoretical analysis and optical near-field measurements," *Phys. Rev. B*, vol. **65**, p. 125409, (2002).

[34] A. V. Zayats, I. I. Smolyaninov, and A. A. Maradudin, "Nano-optics of surface plasmon polaritons," *Phys. Reports*, vol. **408**, pp. 131–314, (2005).

[35] S. A. Maier, *Plsmonics: Fundamental and Applications.* Springer, (2007).

[36] M. Matsumoto, H. Yoshimura, V. S. Kulkarni, and K. Nagayama, "Surfacant monolayers on a clean mercury surface: apparatus and experiments," *Colloid Polym. Sci.*, vol. **1990**, pp. 1174–1178, (1990).

[37] H. A. Atwater and A. Polman, "Plasmonics for improved photovoltaic devices," *Nature Mater.*, vol. **9**, pp. 205–213, (2010).

[38] P. K. Jain, X. Huang, I. El-Sayed, and M. El-Sayed, "Noble metals on the nanoscale: Optical and photothermal properties and some applications in imaging, sensing, biology, and medicine." *Acc. Chem. Res.*, vol. **41**, pp. 1578–1586, (2008).

[39] K. Kneipp, Y. Wang, H. Kneipp, L. T. Perelman, I. Itzkan, R. R. Dasari, and M. S. Feld, "Single molecule detection using surface-enhanced Raman scattering (SERS)," *Phys. Rev. Lett.*, vol. **78**, pp. 1667–1670, (1997).

[40] E. Hutter and J. H. Fendler, "Exploitation of localized surface plasmon resonance," *Adv. Mater.*, vol. **16**, pp. 1685–1706, (2004).

[41] A. V. Kabashin, P. Evans, S. Pastkovsky, W. Hendren, G. A. Wurtz, R. Atkinson, R. Pollard, V. A. Podolskiy, and A. V. Zayats, "Plasmonic nanorod metamaterials for biosensing," *Nat. Mat.*, vol. **8**, pp. 867–871, (2009).

[42] K. A. Willets and R. P. Van Duyne, "Localized surface plasmon resonance spectroscopy and sensing," *Annu. Rev. Phys. Chem.*, vol. **58**, pp. 267–297, (2007).

[43] J. D. Jackson, *Classical Electrodynamics*. John Wiley & Sons, (1999).

Chapter 3

Light propagation in uniaxial anisotropic media and principles of ellipsometry

Here the main theoretical formulas, used for the experimental analysis, are extracted. We start with a short overview of hyperbolic metamaterials and introduce the metallic nanorod arrays as a specific type of hyperbolic metamaterial which waveguiding properties are the core of this thesis. To rationalize this behaviour we present an approximate semi-analytical formulation of that particular structure to calculate the optical response of the system. We begin with the examination of the propagation of light in an infinite uniaxial anisotropic medium and derive the basic dispersion relation of wavevector components along with the expression of the effective refractive index in terms of the ordinary and extraordinary components. Based on the transfer matrix method, the Fresnel coefficients and field distributions for an isotropic multilayer system are expressed for both normal and oblique angle of incidence. These results from the infinite uniaxial anisotropic material are

used in combination with the Maxwell Garnett formalism to generalise the transfer matrix method to support anisotropic layers as well. The resulting semi-analytical model is then tested against numerical simulations to verify its validity. Finally, the main theoretical framework of ellipsometry is presented in order to gather a better understanding of one of the experimental instruments (ellipsometer) used in this thesis for the determination of a new material in the field of plasmonics.

3.1 Metallic nanorods as hyberbolic metamaterials

In the previous Chapter we discussed some basic properties of anisotropy in metamaterials and compared them with their isotropic counterparts. There is yet another fundamental characteristic of anisotropy that defines the shape of the isofrequency surface. Let us consider a material represented by a diagonal permittivity tensor expressed as $\varepsilon = (\varepsilon_\perp, \varepsilon_\perp, \varepsilon_\parallel)$ and $\mu = 1$. The subscripts $\perp$ and $\parallel$ represent the perpendicular and parallel permittivity components with respect to the optical axis, respectively. The wavevector isofrequency surface for the ordinary and extraordinary modes is then expressed by

$$k_x^2 + k_y^2 + k_z^2 = \varepsilon_\perp \left(\frac{\omega}{c}\right)^2 \tag{3.1}$$

$$\frac{k_x^2 + k_y^2}{\varepsilon_\parallel} + \frac{k_z^2}{\varepsilon_\perp} = \left(\frac{\omega}{c}\right)^2 \tag{3.2}$$

where k_x, k_y and k_z are the wavevector components along the x-, y- and z-axes, ω is the angular frequency of the wave and c the speed of light in free space.

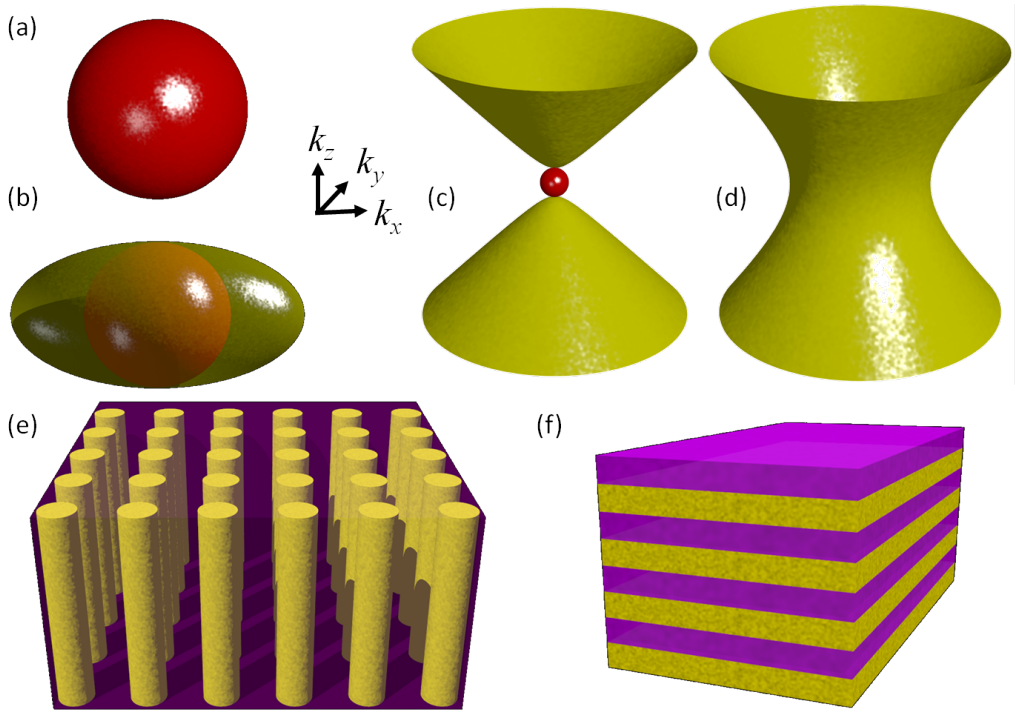

Figure 3.1: Isofrequency surfaces of typical dielectric materials (a, b) and hyperbolic metamaterials (c, d). (a) Spherical (isotropic) and (b) elliptical (anisotropic) isofrequency for a medium with $\varepsilon_\perp = \varepsilon_\parallel > 0$ and $\varepsilon_\perp \neq \varepsilon_\parallel$, respectively. Type I (c) and type II (d) hyperbolic metamaterial with $\varepsilon_\perp > 0$, $\varepsilon_\parallel < 0$ for the type I case and $\varepsilon_\perp < 0$, $\varepsilon_\parallel > 0$ for type II. Note how the k_z wavevector component can be extended to infinity due to the hyperbolic nature of such material affirming that infinite field confinement can be achieved along that direction. The red and gold colors in (a)-(c) correspond to the ordinary and extraordinary isofrequencies. Fabricating metallic nanowire arrays (e) or layered metal-dielectric structures (f) it is possible to achieve type I and II hyperboloidal dispersion, respectively. Images were constructed via POV-Ray imaging software.

Depending on the combination of $\varepsilon_\perp$ and $\varepsilon_\parallel$ various isofrequency surfaces can be produced. At frequencies where $\varepsilon_\perp = \varepsilon_\parallel > 0$ (isotropic case) Eq. (3.2) has spherical shape (Fig. 3.1(a)) and elliptical when $\varepsilon_\perp \neq \varepsilon_\parallel$ (Fig.

3.1(b)). On the other hand, Eq. (3.1) always exhibits spherical isofrequency since it depends only on $\varepsilon_\perp$. Regardless the case, these shapes correspond to dielectric materials since both permittivities are positive. At frequencies for which $\varepsilon_\perp > 0$, $\varepsilon_\parallel < 0$ or $\varepsilon_\perp < 0$, $\varepsilon_\parallel > 0$, type I and type II hyperbolic isofrequencies are formed as depicted in Fig. 3.1(c), (d), respectively. The hyperbolic pattern then has a unique property compared to the spherical or elliptical cases; it is unbounded, supporting modes with infinite momenta. This means that a wavevector component can reach very high values making extreme wavelength confinement possible along a given direction. It is one of the major properties that make hyperbolic metamaterials (HMMs) such an active research area [1]. A plethora of different fields, from spontaneous emission enhancement [2] and acoustics [3] to heat transfer [4] and analogue cosmology [5, 6], have shown great interest to this phenomenon. More precisely HMMs, such as nanowire arrays (type I HMMs) shown in Fig. 3.1(e) or layered metal-dielectric structures (type II HMMs) shown in Fig. 3.1(f), have been fabricated and numerous peculiar properties have been realized including subwavelength imaging [7–9] and focusing [10, 11], biosensing techniques [12–14] and lifetime engineering [15–17].

In this thesis periodic[1] Au nanorod arrays were structured and investigated, we thus limit our discussion to type I HMMs. The choice was solely due to fabrication reasons with the experimental work focusing on these HMMs. Each structure has its own favoured properties, for instance metal-dielectric layers can be used for hyperlensing [2] or enhanced photon density of states with indefinite cavities [16] while an array of nanorods can be ap-

[1]Please note that there is no actual periodicity in neither the experimental structures nor the effective medium approximation. A more accurate term could be “average periodicity” or “pseudo-periodicity”. However, for the sake of simplicity we call it “periodicity”.

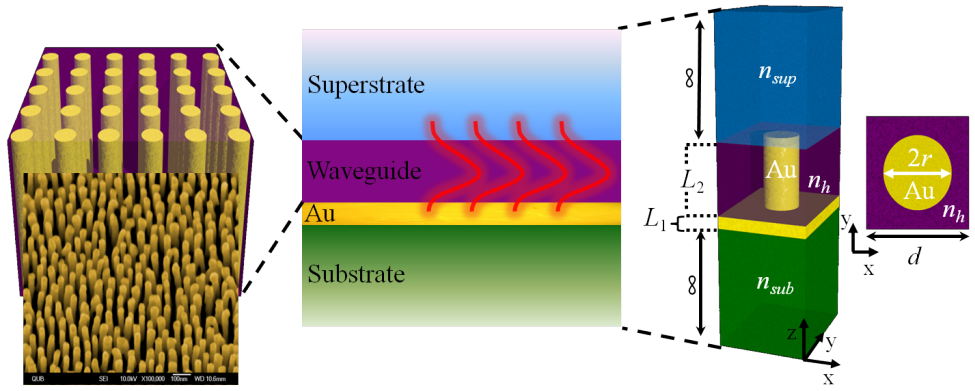

Figure 3.2: Schematics of a hyperbolic metamaterial waveguide geometry consisting of an array of Au nanorods. Middle-Right: Geometry and cross-section taken across the rod of the unit cell. Left: Schematic of a Au nanorod metamaterial array along with a typical SEM perspective view. The waveguide is sandwiched between semi-infinite substrate and superstrate media of refractive index n_{sub} and n_{sup}, respectively. A Au underlayer is usually present for fabrication reasons. The refractive index of the matrix embedding the nanorods is n_h. The thickness of the Au underlayer film and nanorods are L_1 and L_2, respectively. The unit cell has period d and radius r.

plied for optical data storage [18] or as nonlinear nanophotonic component [19]. A general geometry of a hyperbolic waveguide made of Au nanorods is depicted in Fig. 3.2. The structures are grown on cover slips meaning that the refractive index of the substrate is similar to that of glass ($n_{sub} \approx 1.5$). For the measurements the optical response of the system is collected in air, thus $n_{sup} = 1$. Between the waveguide and the substrate, a thin underlayer film of Au is deposited to provide enough conductivity for the growth of the nanorods. Since the nanorods are formed in a periodic fashion, the unit cell can be defined with period d and nanorod radius r.

To experimentally fabricate the structure of Fig. 3.2 the following proce-

dure is required: a) A 10 nm film of Ta_2O_5, acting as an adhesion layer for the following multilayer deposition, is grown on a 200 μm cover slip followed by the growth on a thin Au layer ($L_1 \approx 10$ nm). The reason why Ta_2O_5 is used on top of glass is to keep Au from peeling off. Since it is only 10 nm thick it does not affect the optical measurements. b) Next is the growth of a homogeneous aluminium layer several hundreds of nanometres thick ($L_2 \approx 500 - 800$ nm) via magnetron sputtering. c) Lastly, the aluminium is anodized and periodic pores are formed which can then be filled via electrochemical growth. The anodization of aluminium, an in-house process called *two-step anodization*, is an electrochemical process in which the metal is oxidized in an electrolytic solution (here sulphuric acid was used) via chemical etching [20]. A great effort has been made over the years towards the control and understanding of the porous patterning in which the reader can refer to [21–29].

3.2 Light propagation in an anisotropic permittivity medium

Anisotropic materials have the property to decompose a propagating light beam due to the optical birefringence along different directions. As a consequence the propagation of a plane wave becomes more complex since the Poynting vector is not always parallel to the wavevector and the electric-magnetic-wavevector triplet is not orthogonal any more[2]. In this Section we derive the dispersion and field expressions in an infinite uniaxial anisotropic medium. The resulted expressions will be of assistance later when the generalized transfer matrix method will be formulated.

[2]However the electric displacement remains orthogonal to the magnetic field and wavevector.

Let us assume a plane wave of wavevector $\mathbf{k}$ travelling in a non-magnetic infinite biaxial anisotropic medium. We set the Cartesian axes to coincide with the principal dielectric axes in order to have only diagonal components of the permittivity tensor. For the case of non-zero off-diagonal elements the reader can refer to [30], however for the current scope this is not needed. Then the electric field displacement can be written as

$$\begin{bmatrix} D_x \\ D_y \\ D_z \end{bmatrix} = \begin{bmatrix} \varepsilon_{xx} & 0 & 0 \\ 0 & \varepsilon_{yy} & 0 \\ 0 & 0 & \varepsilon_{zz} \end{bmatrix} \begin{bmatrix} E_x \\ E_y \\ E_z \end{bmatrix} = \varepsilon_0 \begin{bmatrix} n_{xx}^2 & 0 & 0 \\ 0 & n_{yy}^2 & 0 \\ 0 & 0 & n_{zz}^2 \end{bmatrix} \begin{bmatrix} E_x \\ E_y \\ E_z \end{bmatrix} \tag{3.3}$$

where ε_i, $i = xx, yy, zz$ is the permittivity along the x, y, z directions and $n_i = \sqrt{\varepsilon_i/\varepsilon_0}$ is the respective refractive index. For the uniaxial scenario we set the ordinary axes to $\varepsilon_{xx} = \varepsilon_{yy}$ and the extraordinary axis to ε_{zz}. Thus, uniaxiality requires the determination of only two wavevector components, namely k_x and k_z, to fully solve the electromagnetic problem. If $\mathbf{k}$ forms an angle θ from the optical axis z, then TM- and TE-polarization configurations[3] can be drawn as in Fig. 3.3. From this scheme we can write the following relation for wavevector

$$\mathbf{k} = k\hat{\boldsymbol{e}} = k(\hat{\boldsymbol{i}}\sin\theta + \hat{\boldsymbol{k}}\cos\theta) = \hat{\boldsymbol{i}}k_x + \hat{\boldsymbol{k}}k_z \tag{3.4}$$

where $\hat{\boldsymbol{i}}$, $\hat{\boldsymbol{k}}$ are the unit vectors for the x and z directions respectively, and $\hat{\boldsymbol{e}}$ is the unit vector parallel to $\mathbf{k}$.

As always, we start from the source free Maxwell's equations assuming a harmonic time dependence

[3]Please note that in an infinite medium there are no polarization configurations but rather ordinary and extraordinary solutions. However, for consistency with the following Sections, the symbolism is retained.

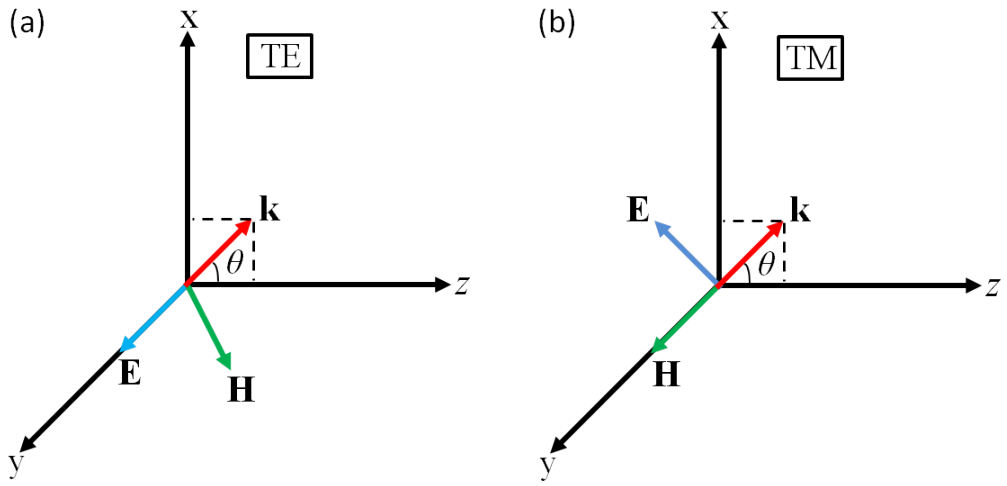

Figure 3.3: TE (a) and TM (b) configurations for a uniform plane wave travelling inside an infinite anisotropic medium.

$$\nabla \times \mathbf{E} = i\omega\mu_0\mathbf{H} \tag{3.5}$$

$$\nabla \times \mathbf{H} = -i\omega\mathbf{D} \tag{3.6}$$

$$\nabla \cdot \mathbf{D} = 0 \tag{3.7}$$

$$\nabla \cdot \mathbf{H} = 0 \tag{3.8}$$

Since we have plane waves, we are looking for Bloch type solutions of the form $\mathbf{E}(\mathbf{r}) = \mathbf{E}_0 e^{i\mathbf{k}\cdot\mathbf{r}}$ and $\mathbf{H}(\mathbf{r}) = \mathbf{H}_0 e^{i\mathbf{k}\cdot\mathbf{r}}$ so applying the permutation $\nabla \to i\mathbf{k}$ we get

$$\mathbf{k} \times \mathbf{E} = \omega\mu_0\mathbf{H} \tag{3.9}$$

$$\mathbf{k} \times \mathbf{H} = -\omega\mathbf{D} \tag{3.10}$$

$$\mathbf{k} \cdot \mathbf{D} = 0 \tag{3.11}$$

$$\mathbf{k} \cdot \mathbf{H} = 0 \tag{3.12}$$

The last two equations are not needed since they can immediately be extracted from Eq. (3.9) and (3.10) by dotting both sides with $\mathbf{k}$. In analogy with the isotropic case where $k = nk_0 = n\omega/c$, it is convenient to define the *effective permittivity* (ε_{eff}) and *effective refractive index* (n_{eff}) so that a similar expression can also be used for anisotropic materials. Of course here the effective parameters can not be trivially expressed since permittivity is a tensor. So Eq. (3.4) can be re-written as

$$\mathbf{k} = \frac{\omega}{c} n_{eff} \hat{\boldsymbol{e}} = \frac{\omega}{c} \sqrt{\varepsilon_{eff}} \hat{\boldsymbol{e}} \tag{3.13}$$

The main target now is to find a suitable expression for n_{eff} which satisfies all Maxwell's equations. Substituting Eq. (3.13) to (3.9) and (3.10) and rearranging the terms we get

$$\mathbf{H} = \frac{n_{eff}}{\mu_0 c} \hat{\boldsymbol{e}} \times \mathbf{E} \tag{3.14}$$

$$\mathbf{E} - \frac{\mathbf{D}}{\varepsilon_0 n_{eff}^2} = \hat{\boldsymbol{e}}(\hat{\boldsymbol{e}} \cdot \mathbf{E}) \tag{3.15}$$

Since the electric displacement is linearly connected with the electric field the determinant of Eq. (3.15) must vanish in order to avoid trivial solutions. To calculate the determinant, it will first be easier to examine the field components. Analysing each component of the electric field we end up with the following three expressions

$$E_x \left(1 - \frac{n_{xx}^2}{n_{eff}^2}\right) = \sin\theta (E_x \sin\theta + E_z \cos\theta) \tag{3.16}$$

$$E_y \left(1 - \frac{n_{yy}^2}{n_{eff}^2}\right) = 0 \tag{3.17}$$

$$E_z \left(1 - \frac{n_{zz}^2}{n_{eff}^2}\right) = \cos\theta (E_x \sin\theta + E_z \cos\theta) \tag{3.18}$$

The above relations are general due to the fact that no condition on polarization was chosen. The next step is to solve the appropriate determinant for each polarization.

For the TE-polarization $E_x = E_z = 0$ and $E_y \neq 0$ (Fig. 3.3(a)). From Eq. (3.17) we can immediately see that the determinant vanishes only when $n_{eff} = n_{yy}$. This means that although light is inside an anisotropic medium, it propagates as if the medium was isotropic because the electric field has only one component along one of the principal directions of the crystal, namely the y direction. Since the wavevector is known, the plane wave electromagnetic response can be calculated leading to

$$\mathbf{E}(\mathbf{r},t) = \hat{\boldsymbol{j}} E_0 e^{i(\mathbf{k}\cdot\mathbf{r}-\omega t)} \tag{3.19}$$

$$\mathbf{H}(\mathbf{r},t) = \frac{E_0}{Z_0} n_{yy} \left(-\hat{\boldsymbol{i}}\cos\theta + \hat{\boldsymbol{k}}\sin\theta\right) e^{i(\mathbf{k}\cdot\mathbf{r}-\omega t)} \tag{3.20}$$

$$\mathbf{k}\cdot\mathbf{r} = k_0 n_{yy}(x\sin\theta + z\cos\theta) \tag{3.21}$$

where E_0 is the initial magnitude of the electric field which is considered a known parameter and Z_0 is the impedance in vacuum.

TM-polarization (Fig. 3.3(b)) is a little bit more complicated but the fundamental steps remain the same. Here we have $E_x \neq 0$, $E_z \neq 0$ and $E_y = 0$. Rearranging the terms of Eq. (3.16) and (3.18) we can bring them to the following eigenvalue form

$$\begin{bmatrix} \cos^2\theta - \frac{n_{xx}^2}{n_{eff}^2} & -\cos\theta\sin\theta \\ -\cos\theta\sin\theta & \sin^2\theta - \frac{n_{zz}^2}{n_{eff}^2} \end{bmatrix} \begin{bmatrix} E_x \\ E_z \end{bmatrix} = 0 \tag{3.22}$$

Setting the determinant to zero we find the relation that connects the angle-dependent effective refractive index with the refractive index along the x and z directions

$$\frac{1}{n_{eff}^2} = \frac{\cos^2\theta}{n_{xx}^2} + \frac{\sin^2\theta}{n_{zz}^2} \tag{3.23}$$

In order to check the validity of the expression we can multiply it by k^2 and, knowing that $k_z = k\cos\theta$ and $k_x = k\sin\theta$, we find

$$\frac{k_z^2}{n_{xx}^2} + \frac{k_x^2}{n_{zz}^2} = \left(\frac{\omega}{c}\right)^2 \tag{3.24}$$

which is exactly the same expression as the one derived in Eq. (2.18). Yet another check can be made by calculating the group velocity since we know the wavevector dispersion from the aforementioned expression. Based on the definition of group velocity, namely $\boldsymbol{\upsilon}_g \equiv \partial\omega/\partial\mathbf{k}$, we can find υ_{gx} and υ_{gz} for the x and z directions, respectively

$$\upsilon_{gx} = \frac{\partial\omega}{k_x} = \frac{cn_{eff}}{n_{zz}^2}\sin\theta \tag{3.25}$$

$$\upsilon_{gz} = \frac{\partial\omega}{k_z} = \frac{cn_{eff}}{n_{xx}^2}\cos\theta \tag{3.26}$$

Then the group velocity angle, θ_g, will be given from $\tan\theta_g = \upsilon_{gx}/\upsilon_{gz}$ resulting in

$$\tan\theta_g = \frac{n_{xx}^2}{n_{zz}^2}\tan\theta \tag{3.27}$$

From the above, it is clear that group velocity will not have the same direction with the wavevector because $\theta_g \neq \theta$ supporting the non-orthogonality of the $\mathbf{E}-\mathbf{H}-\mathbf{k}$ triplet due to anisotropy. Note that the angles become the same for the case of isotropic medium where $n_{xx} = n_{zz}$.

Let us now continue with the calculation of the electromagnetic field. Since we are looking for solutions of the form $\{\mathbf{E}(\mathbf{r}), \mathbf{H}(\mathbf{r})\} = \{\mathbf{E}_0, \mathbf{H}_0\}e^{i\mathbf{k}\cdot\mathbf{r}}$

and $\mathbf{k}$ has been derived (Eq. (3.23)), our only concern is to find the appropriate $(\mathbf{E}_0, \mathbf{H}_0)$ set. Substituting Eq. (3.23) to (3.16) we can connect the E_x and E_z components via

$$E_x = -\frac{n_{zz}^2 \cos\theta}{n_{xx}^2 \sin\theta} E_z \tag{3.28}$$

Using the relation $E_0^2 = E_x^2 + E_z^2$ we can find E_x, E_z in terms of the (known) initial magnitude of the electric field

$$E_x = \frac{n_{zz}^2 \cos\theta}{\sqrt{n_{xx}^4 \sin^2\theta + n_{zz}^4 \cos^2\theta}} E_0 \tag{3.29}$$

$$E_z = -\frac{n_{xx}^2 \sin\theta}{\sqrt{n_{xx}^4 \sin^2\theta + n_{zz}^4 \cos^2\theta}} E_0 \tag{3.30}$$

Having derived the electric field, the magnetic field can be simply calculated from Eq. (3.9). Writing the total fields in vector form we finally get

$$\mathbf{E}(\mathbf{r}, t) = \frac{E_0}{\sqrt{n_{xx}^4 \sin^2\theta + n_{zz}^4 \cos^2\theta}} (n_{zz}^2 \cos\theta \hat{\boldsymbol{i}} - n_{xx}^2 \sin\theta \hat{\boldsymbol{k}}) e^{i(\mathbf{k}\cdot\mathbf{r} - \omega t)} \tag{3.31}$$

$$\mathbf{H}(\mathbf{r}, t) = \hat{\boldsymbol{j}} \frac{E_0}{Z_0} \frac{n_{xx} n_{zz} \sqrt{n_{xx}^2 \sin^2\theta + n_{zz}^2 \cos^2\theta}}{\sqrt{n_{xx}^4 \sin^2\theta + n_{zz}^4 \cos^2\theta}} e^{i(\mathbf{k}\cdot\mathbf{r} - \omega t)} \tag{3.32}$$

$$\mathbf{k} \cdot \mathbf{r} = k_0 n_{eff} (x \sin\theta + z \cos\theta) \tag{3.33}$$

Although the expressions seems to be complicated, we can confirm their validity for the limiting case of the anisotropic material, i.e. $n_{xx} = n_{zz} = n$. Then the TM-fields will become $\mathbf{E}(\mathbf{r}, t) = E_0(\cos\theta \hat{\boldsymbol{i}} + \sin\theta \hat{\boldsymbol{k}}) e^{i(\mathbf{k}\cdot\mathbf{r} - \omega t)}$ and $\mathbf{H}(\mathbf{r}, t) = \hat{\boldsymbol{j}}(nE_0/Z_0) e^{i(\mathbf{k}\cdot\mathbf{r} - \omega t)}$. Note how the magnetic field becomes independent of the angle since it always remains oriented along the ordinary axis.

3.3 Transfer matrix method for multiple planar interfaces at normal incidence

Here we derive some of the fundamental theoretical tools based on the transfer matrix method. This formalism allow us to analytically calculate the optical response of a multilayer system of arbitrary thickness and constitutes the core numerical component for almost all structures examined in this thesis. The transfer matrix method is completed in two steps: At first we examine the normal wavevector scenario (i.e. normal angle of incidence) and in the next Section we generalize it to support oblique propagation.

From now on we omit the time dependence ($e^{-i\omega t}$) of the electromagnetic field and focus only on the *space dependence* unless otherwise specified. Consider a plane wave propagating along z-direction with the electric field parallel to x-direction. We can then write the electromagnetic field as $\mathbf{E}(z) = \hat{\boldsymbol{i}} E_x(z) = \hat{\boldsymbol{i}} E(z)$ and $\mathbf{H}(z) = \hat{\boldsymbol{j}} H_y(z) = \hat{\boldsymbol{j}} H(z)$. At the moment, let us assume an infinite lossless and isotropic dielectric. The wave can travel along either the z or the -z axis thus, without loss of generality, we can write the fields as the sum of a forward-moving and a backward-moving wave

$$\mathbf{E}(z) = \mathbf{E}_{0+} e^{ikz} + \mathbf{E}_{0-} e^{-ikz} = \mathbf{E}_{+}(z) + \mathbf{E}_{-}(z) \tag{3.34}$$

$$\mathbf{H}(z) = \frac{1}{Z} \hat{\boldsymbol{k}} \times \mathbf{E}(z) \tag{3.35}$$

where $\mathbf{E}_{0+}$ and $\mathbf{E}_{0-}$ is the *initial electric field* in the positive and negative direction respectively, and Z is the impedance of the material. Based on the above, we can define the *reflection coefficient* as the portion of the electric field that is reflected back over the field that is transmitted

$$\Gamma(z) \equiv \frac{E_{-}(z)}{E_{+}(z)} \tag{3.36}$$

We now want to calculate the reflection coefficient at two distinct points *inside* the same material. If these points are z_1 and z_2, we can simplify the notation by substituting $\{E(z_1), H(z_1), E_{\pm}(z_1), \Gamma(z_1)\} \rightarrow \{E_1, H_1, E_{1\pm}, \Gamma_1\}$ for point z_1, and similarly for z_2. If we set $L = |z_2 - z_1|$ the forward $\{E_{1+}, E_{2+}\}$ and backward $\{E_{1-}, E_{2-}\}$ electric fields can be expressed in a matrix form known as *propagation matrix*

$$\begin{bmatrix} E_{1+} \\ E_{1-} \end{bmatrix} = \begin{bmatrix} e^{-ikL} & 0 \\ 0 & e^{ikL} \end{bmatrix} \begin{bmatrix} E_{2+} \\ E_{2-} \end{bmatrix} \tag{3.37}$$

Applying Eq. (3.36) at points z_1 and z_2 one can connect Γ_1 and Γ_2 with the help of Eq. (3.37). This leads to the following expression known as *reflection coefficient propagation*

$$\Gamma_1 = \Gamma_2 e^{2ikL} \tag{3.38}$$

This basically shows that the reflection coefficient inside the same material will be phase shifted by e^{2ikL} between two points at distance L. Substituting Eq. (3.37) to Eq. (3.34) and (3.35) we can derive the total electromagnetic field between points z_1 and z_2. After some calculations we obtain the following matrix

$$\begin{bmatrix} E_1 \\ H_1 \end{bmatrix} = \begin{bmatrix} \cos(kL) & -iZ\sin(kL) \\ -iZ^{-1}\sin(kL) & \cos(kL) \end{bmatrix} \begin{bmatrix} E_2 \\ H_2 \end{bmatrix} \tag{3.39}$$

Since we examined the optical behaviour *inside* an infinite medium, we can continue by adding an interface. So now we consider the case of two half-space isotropic and lossless media where a plane wave approaches the surface at normal incidence. Based on the previous notation, we set the first medium (incident medium) to have the set of $\{E, H, E_+, E_-, Z\}$ parameters while the second one (transmitted medium) to have $\{E', H', E'_+, E'_-, Z'\}$.

The main scope again is to connect the backward and forward fields. For normal incidence, both the electric and magnetic fields are tangential to to the surface thus the boundary conditions require $E = E'$ and $H = H'$. Using Eq. (3.34) and (3.35) we can express the forward and backward waves via $E_+ + E_- = E'_+ + E'_-$ and $Z^{-1}(E_+ + E_-) = Z'^{-1}(E'_+ + E'_-)$. Solving them we arrive to the expression

$$\begin{bmatrix} E_+ \\ E_- \end{bmatrix} = \frac{1}{\tau} \begin{bmatrix} 1 & \rho \\ \rho & 1 \end{bmatrix} \begin{bmatrix} E'_+ \\ E'_- \end{bmatrix} \tag{3.40}$$

$$\tau = \frac{2n}{n + n'} \tag{3.41}$$

$$\rho = \frac{n - n'}{n + n'} \tag{3.42}$$

where n and n' is the refractive index of each medium. The ρ and τ are the famous Fresnel coefficients that describe the elementary transmission and reflection between the two media, respectively. It is noteworthy to mention that in case it is required to find these coefficients from the n' to the n material, we can simply swap the primes in Eq. (3.41) and (3.42). From the definition of Γ and with the assistance of Eq. (3.40) we can express the reflection coefficient for each material as

$$\Gamma = \frac{\rho + \Gamma'}{1 + \rho\Gamma'} \tag{3.43}$$

Since we have an interface, it is also convenient to define the *transmission coefficient* as the portion of the electric field that is transmitted in the second medium over the initial transmitted field

$$T \equiv \frac{E'_+}{E_+} \tag{3.44}$$

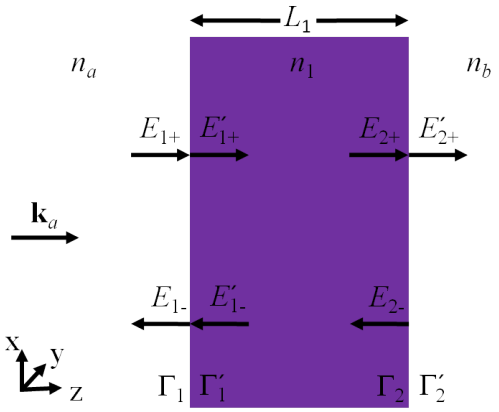

Figure 3.4: Single dielectric slab between two semi-infinite media at normal incidence. Note that the arrows indicate the reflected and transmitted waves, not the actual direction of the electric field.

So far we examined the case between two semi-infinite dielectrics. Let us now turn our attention to a finite layer sandwiched between these media as depicted in Fig. 3.4. Since now there are two interfaces, the subscripts 1 and 2 indicate the first and second interface, respectively. As before, the "+" and "−" represent the forward (transmitted) and backward (reflected) waves, while the non-prime and prime notations dictate the optical response just before and after the corresponding interface. Note that since the n_b medium is infinite there is no backward wave in this medium, which means that $\Gamma'_2 = 0$. Similarly to the previous case, we need to find the reflection and transmission coefficient along with the matrix that connects the backward and forward waves at each interface. However, since now we have two boundaries, we care about finding the *overall* transmission response into the n_b medium, which is E'_{2+}/E_{1+} (in accordance with Eq. (3.44)). Generally, the overall transmission and reflection response are the most critical factors since these are measured during the experimental characterization.

To calculate Γ_1 we do the following: First we apply Eq. (3.42) on each

interface, then we use the propagation matrix based on Eq. (3.38) to relate Γ_1' with Γ_2, and finally we apply Eq. (3.43) for each surface to connect them all together. The final result is

$$\Gamma_1 = \frac{\rho_1 + \rho_2 e^{2ik_1 L_1}}{1 + \rho_1 \rho_2 e^{2ik_1 L_1}} \tag{3.45}$$

$$\rho_1 = \frac{n_a - n_1}{n_a + n_1} \tag{3.46}$$

$$\rho_2 = \frac{n_1 - n_b}{n_1 + n_b} \tag{3.47}$$

which expresses the total reflection response in terms of the refractive index of each material, the thickness of the layer and the wavevector inside it.

Similarly, for the calculation of the overall transmission response (T_1), E_{1+} must be expressed in terms of E'_{2+}. Via Eq. (3.40), $\{E_{1+}, E_{1-}\}$ can be related with $\{E'_{1+}, E'_{1-}\}$. Applying the propagation matrix (Eq. (3.37)) for medium n_1, we can connect $\{E'_{1+}, E'_{1-}\}$ with $\{E_{2+}, E_{2-}\}$ and re-evaluating Eq. (3.40) on the second interface $\{E_{2+}, E_{2-}\}$ can be expressed in terms of $\{E'_{2+}, 0\}$ leading to

$$\begin{bmatrix} E_{1+} \\ E_{1-} \end{bmatrix} = \frac{1}{\tau_1} \begin{bmatrix} 1 & \rho_1 \\ \rho_1 & 1 \end{bmatrix} \begin{bmatrix} e^{-ik_1 L_1} & 0 \\ 0 & e^{ik_1 L_1} \end{bmatrix} \frac{1}{\tau_2} \begin{bmatrix} 1 & \rho_2 \\ \rho_2 & 1 \end{bmatrix} \begin{bmatrix} E'_{2+} \\ 0 \end{bmatrix} \tag{3.48}$$

The same principle can be applied for multiple layers. In that case we need to apply Eq. (3.37) and (3.40) for each slab. Since the heart of these calculations is matrices multiplication, the process is called *transfer matrix method* (TMM) and was first introduced by Abelès back in 1950 [31]. Solving the aforementioned expression we get

$$\begin{bmatrix} E_{1+} \\ E_{1-} \end{bmatrix} = \frac{e^{-ik_1 L_1}}{\tau_1 \tau_2} \begin{bmatrix} 1 + \rho_1 \rho_2 e^{2ik_1 L_1} & \rho_2 + \rho_1 e^{2ik_1 L_1} \\ \rho_1 + \rho_2 e^{2ik_1 L_1} & \rho_1 \rho_2 + e^{2ik_1 L_1} \end{bmatrix} \begin{bmatrix} E'_{2+} \\ 0 \end{bmatrix} \tag{3.49}$$

Thus the overall transmission response will be

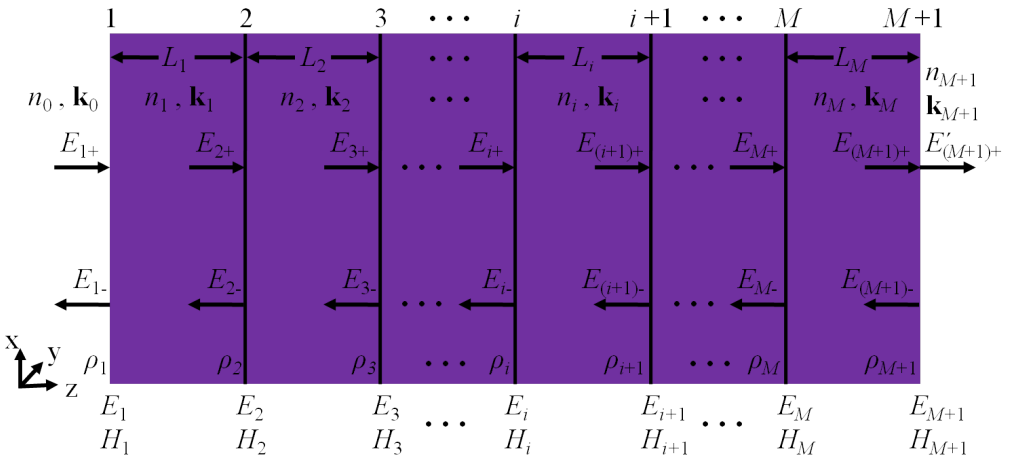

Figure 3.5: Multilayer dielectric between two semi-infinite media at normal incidence. Only the backward and forward fields for the left side of each layer are shown. Note that the arrows under them indicate the reflected and transmitted waves, not the actual direction of the electric field.

$$T_1 = \frac{\tau_1 \tau_2 e^{ik_1 L_1}}{1 + \rho_1 \rho_2 e^{2ik_1 L_1}} \tag{3.50}$$

$$\rho_1 = \frac{n_a - n_1}{n_a + n_1} \quad , \quad \rho_2 = \frac{n_1 - n_b}{n_1 + n_b} \tag{3.51}$$

$$\tau_1 = \frac{2n_a}{n_a + n_1} = 1 + \rho_1 \quad , \quad \tau_2 = \frac{2n_1}{n_1 + n_b} = 1 + \rho_2 \tag{3.52}$$

Since the total electromagnetic fields are continuous across the interfaces, it is straight forward to write $\{E_1, H_1\}$ in terms of $\{E_2, H_2\}$. The calculations are exactly the same as the derivation of Eq. (3.39) with the substitutions $\{k, L, Z\} \rightarrow \{k_1, L_1, Z_1\}$.

We now have all the required knowledge to expand the TMM formalism for the multilayer scenario as the one demonstrated in Fig. 3.5. The main scope is to calculate the overall reflection (E_{1-}/E_{1+}) and transmission (E'_{M+1}/E_{1+}) response based on the TMM formalism. Similarly to the dis-

cussed single layer scenario, the generalized elementary reflection coefficients for the left (ρ_i) and right (ρ'_i) side of each layer will have the form

$$\rho_i = \frac{n_{i-1} - n_i}{n_{i-1} + n_i} = -\rho'_i \quad , i = 1, 2, 3..., M+1 \tag{3.53}$$

and the elementary transmission coefficients

$$\tau_i = \frac{2n_{i-1}}{n_{i-1} + n_i} = 1 + \rho_i \quad , i = 1, 2, 3..., M+1 \tag{3.54}$$

$$\tau'_i = \frac{2n_i}{n_{i-1} + n_i} = 1 + \rho'_i \quad , i = 1, 2, 3..., M+1 \tag{3.55}$$

Repeating the same steps as the one in Eq. (3.49), we can express the backward and forward propagating electric fields between the i^{th} and $(i+1)^{th}$ layer as

$$\begin{bmatrix} E_{i+} \\ E_{i-} \end{bmatrix} = \frac{1}{\tau_i} \begin{bmatrix} e^{-ik_iL_i} & \rho_i e^{ik_iL_i} \\ \rho_i e^{-ik_iL_i} & e^{ik_iL_i} \end{bmatrix} \begin{bmatrix} E_{(i+1)+} \\ E_{(i+1)-} \end{bmatrix} \quad , i = M, M-1, ..., 1 \tag{3.56}$$

From the above the reflection response at the i^{th} layer can be found leading to an expression similar to Eq. (3.45)

$$\Gamma_i = \frac{\rho_i + \Gamma_{i+1} e^{2ik_iL_i}}{1 + \rho_i \Gamma_{i+1} e^{2ik_iL_i}} \quad , i = M, M-1, ..., 1 \tag{3.57}$$

Note that since there is no backward wave at the right side of the $(M+1)^{th}$ layer (See Fig. 3.5), it follows that $\Gamma_{M+1} = \rho_{M+1}$. The transmission response can also be calculated for the i^{th} layer leading to

$$T_i = \frac{\tau_i T_{i+1} e^{ik_iL_i}}{1 + \rho_i \Gamma_{i+1} e^{2ik_iL_i}} \quad , i = M, M-1, ..., 1 \tag{3.58}$$

where again for the $(M+1)^{th}$ layer we have $T_{M+1} = \tau_{M+1}$. It is worth mentioning that finding the overall transmission (E'_{M+1}/E_{1+}) is equal to calculating T_1 since Eq. (3.58) is recursive and thus stores the information

of all higher layers. Finally, we can generalize Eq. (3.39) to extract the total electromagnetic fields for the i^{th} layer

$$\begin{bmatrix} E_i \\ H_i \end{bmatrix} = \begin{bmatrix} \cos(k_i L_i) & -iZ_i \sin(k_i L_i) \\ -iZ_i^{-1} \sin(k_i L_i) & \cos(k_i L_i) \end{bmatrix} \begin{bmatrix} E_{i+1} \\ H_{i+1} \end{bmatrix} \quad , i = M, M-1, ..., 1 \tag{3.59}$$

with the conditions $E_{M+1} = E'_{M+1}$ and $H_{M+1} = Z_{M+1}^{-1} H'_{M+1}$ for the final layer.

All the calculations we have done so far are based on Fig. 3.5. However it is not obvious from that sketch whether it takes into account the realistic case where multiple reflections and transmissions occur inside each layer. The short answer is yes, all the expressions derived so far are rigorous. The reader can refer to Appendix C for an in-depth investigation.

3.4 Transfer matrix method for multiple planar interfaces at oblique incidence

Here we generalize the previous Section and examine the case of light propagation in a multilayer system at any angle of incidence. Additionally, light propagation in lossy (e.g. metal) multilayer systems is discussed. We will see that many equations derived at normal incidence retain the same form at oblique incidence.

Let us assume that we have two dielectric isotropic materials of refractive index n and n'. A plane wave propagating in n approaches the interface at an angle θ. To keep it as general as possible, we assume a reflected wave in both media as sketched in Fig. 3.6 for both polarizations. Generally, we can write the incident and reflected wavefronts for the n medium as $\mathbf{k}_{\pm} = \hat{\boldsymbol{i}} k_{x\pm} + \hat{\boldsymbol{j}} k_{y\pm} + \hat{\boldsymbol{k}} k_{z\pm}$ and similarly for $\mathbf{k}'_{\pm}$. According to the boundary conditions,

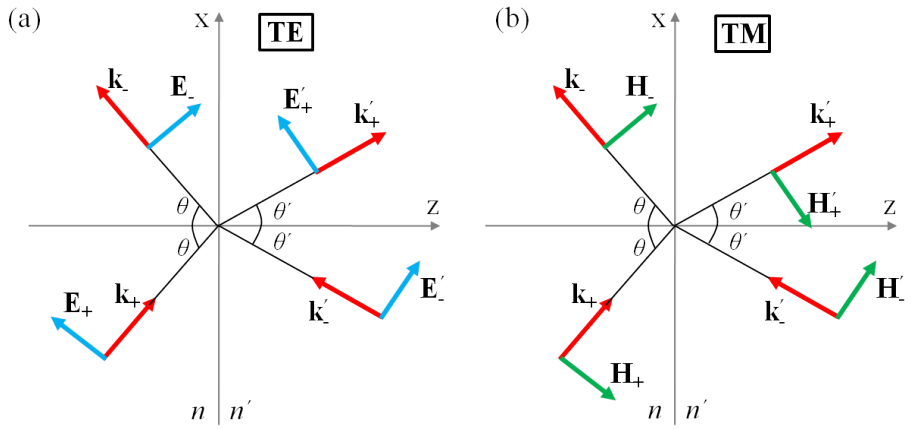

Figure 3.6: General scheme of forward and backward electromagnetic waves at an interface for oblique incidence. Light propagates from material n to material n' at an angle θ being either TE- (a) or TM-polarized (b).

the tangential components of the electric field must be continuous across the interface. If we assume that the interface corresponds to $z = 0$ we can write a condition that is valid for both polarizations

$$\mathbf{E}_{\mathrm{T}+}e^{i\mathbf{k}_+\cdot\mathbf{r}} + \mathbf{E}_{\mathrm{T}-}e^{i\mathbf{k}_-\cdot\mathbf{r}} = \mathbf{E}'_{\mathrm{T}+}e^{i\mathbf{k}'_+\cdot\mathbf{r}} + \mathbf{E}'_{\mathrm{T}-}e^{i\mathbf{k}'_-\cdot\mathbf{r}} \tag{3.60}$$

where the "T" subscript denotes the transverse part of the electric fields with respect to z-direction, i.e. $\mathbf{E}_{\mathrm{T}} = \hat{\boldsymbol{k}} \times (\mathbf{E} \times \hat{\boldsymbol{k}}) = \mathbf{E} - \hat{\boldsymbol{k}}E_z$ (for both polarizations). Using the general form of $\{\mathbf{k}_\pm, \mathbf{k}'_\pm\}$ and setting $z = 0$ at the interface, Eq. (3.60) becomes

$$\mathbf{E}_{\mathrm{T}+}e^{i(k_{x+}x+k_{y+}y)} + \mathbf{E}_{\mathrm{T}-}e^{i(k_{x-}x+k_{y-}y)} = \mathbf{E}'_{\mathrm{T}+}e^{i(k'_{x+}x+k'_{y+}y)} + \mathbf{E}'_{\mathrm{T}-}e^{i(k'_{x-}x+k'_{y-}y)} \tag{3.61}$$

for the expression to be valid the propagation phase factors must be the same for *any* $\{x, y\}$ point along the interface, leading to the conservation of wavevector components for that direction, namely

$$k_{x+} = k_{x-} = k'_{x+} = k'_{x-} \tag{3.62}$$

$$k_{y+} = k_{y-} = k'_{y+} = k'_{y-} \tag{3.63}$$

If there is propagation only in the xz-plane, such as in Fig. 3.6, then $k_{y+} = 0$ (and so every k_y component) and the planes of incidence and reflection will coincide with xz-plane. This is valid for our case, because the actual geometry of the structures characterized in the current thesis have the same symmetry along the x- and y-axes. So even though 3D geometries are investigated, the physical problem can be approximated in two dimensions.

Having derived all these expressions, we can simplify the notations for the wavevectors as follows

$$\mathbf{k} = \mathbf{k}_+ = \hat{\boldsymbol{\imath}} k_x + \hat{\boldsymbol{k}} k_z = \hat{\boldsymbol{\imath}} k \sin\theta + \hat{\boldsymbol{k}} k \cos\theta \tag{3.64}$$

$$\mathbf{k}_- = \hat{\boldsymbol{\imath}} k_x - \hat{\boldsymbol{k}} k_z = \hat{\boldsymbol{\imath}} k \sin\theta - \hat{\boldsymbol{k}} k \cos\theta \tag{3.65}$$

$$\mathbf{k}' = \mathbf{k}'_+ = \hat{\boldsymbol{\imath}} k'_x + \hat{\boldsymbol{k}} k'_z = \hat{\boldsymbol{\imath}} k' \sin\theta' + \hat{\boldsymbol{k}} k' \cos\theta' \tag{3.66}$$

$$\mathbf{k}'_- = \hat{\boldsymbol{\imath}} k'_x - \hat{\boldsymbol{k}} k'_z = \hat{\boldsymbol{\imath}} k' \sin\theta' - \hat{\boldsymbol{k}} k' \cos\theta' \tag{3.67}$$

Using Eq. (3.64) and (3.65) we can decouple the contribution of the transverse electric field along the x- and z-directions so that $\mathbf{E}_{\mathrm{T}}(x,z) = \mathbf{E}_{\mathrm{T}}(z)E_{\mathrm{T}}(x)$ with $\mathbf{E}_{\mathrm{T}}(z) = \mathbf{E}_{\mathrm{T}+}e^{ik_z z} + \mathbf{E}_{\mathrm{T}-}e^{-ik_z z}$ and $E_{\mathrm{T}}(x) = e^{ik_x x}$. Since the x-component of wavevector is conserved (Eq. (3.62)), we have $E_{\mathrm{T}}(x) = E'_{\mathrm{T}}(x)$. Thus, in order to examine the response of $\mathbf{E}_{\mathrm{T}}$ we only need to calculate $\mathbf{E}_{\mathrm{T}}(z)$ since $E_{\mathrm{T}}(x)$ will simply cancel. The transverse part of the electric field in both media can then be written as

$$\mathbf{E}_{\mathrm{T}}(z) = \mathbf{E}_{\mathrm{T}+}e^{ik_z z} + \mathbf{E}_{\mathrm{T}-}e^{-ik_z z} \tag{3.68}$$

$$\mathbf{E}'_{\mathrm{T}}(z) = \mathbf{E}'_{\mathrm{T}+}e^{ik'_z z} + \mathbf{E}'_{\mathrm{T}-}e^{-ik'_z z} \tag{3.69}$$

The main target then is to calculate $\{\mathbf{E}_{\mathrm{T}\pm}, \mathbf{E}'_{\mathrm{T}\pm}\}$. Generally, for oblique moving waves both TE and TM waves can exist at the same time, meaning that the *total* electromagnetic fields will be

$$\mathbf{E}(\mathbf{r}) = \mathbf{E}_{TM}(\mathbf{r}) + \mathbf{E}_{TE}(\mathbf{r}) \tag{3.70}$$

$$\mathbf{H}(\mathbf{r}) = \mathbf{H}_{TM}(\mathbf{r}) + \mathbf{H}_{TE}(\mathbf{r}) \tag{3.71}$$

Each term can be further analysed into backward and forward fields leading to

$$\mathbf{E}_i(\mathbf{r}) = \mathbf{E}_{i+}(\mathbf{r}) + \mathbf{E}_{i-}(\mathbf{r}) \quad , i = TE, TM \tag{3.72}$$

$$\mathbf{H}_i(\mathbf{r}) = \mathbf{H}_{i+}(\mathbf{r}) + \mathbf{H}_{i-}(\mathbf{r}) \quad , i = TE, TM \tag{3.73}$$

The above expressions are of course valid for the n' medium by adding a prime to all symbols. Let $\{A_+, A_-\}$ be the amplitude of the initial backward and forward electric field for TM-polarization and $\{B_+, B_-\}$ for TE-polarization. Then with the assistance of Fig. 3.6 we can write $\mathbf{E}_{TE+} = \hat{\boldsymbol{j}}B_+e^{i\mathbf{k}_+\cdot\mathbf{r}}$, $\mathbf{E}_{TM+} = (\hat{\boldsymbol{i}}A_+\cos\theta - \hat{\boldsymbol{k}}A_+\sin\theta)e^{i\mathbf{k}_+\cdot\mathbf{r}}$. The respective magnetic fields can be trivially found from Eq. (3.35). Applying Eq. (3.70) and (3.71) for the forward wave case in medium n we find

$$\mathbf{E}_+(\mathbf{r}) = [(\hat{\boldsymbol{i}}\cos\theta - \hat{\boldsymbol{k}}\sin\theta)A_+ + \hat{\boldsymbol{j}}B_+]e^{i\mathbf{k}_+\cdot\mathbf{r}} \tag{3.74}$$

$$\mathbf{H}_+(\mathbf{r}) = \frac{1}{Z}[(-\hat{\boldsymbol{i}}\cos\theta + \hat{\boldsymbol{k}}\sin\theta)B_+ + \hat{\boldsymbol{j}}A_+]e^{i\mathbf{k}_+\cdot\mathbf{r}} \tag{3.75}$$

So the transverse components will be

$$\mathbf{E}_{\mathrm{T}+}(\mathbf{r}) = (\hat{\boldsymbol{i}}A_+\cos\theta + \hat{\boldsymbol{j}}B_+)e^{i\mathbf{k}_+\cdot\mathbf{r}} \tag{3.76}$$

$$\mathbf{H}_{\mathrm{T}+}(\mathbf{r}) = \frac{1}{Z}(-\hat{\boldsymbol{i}}B_+\cos\theta + \hat{\boldsymbol{j}}A_+)e^{i\mathbf{k}_+\cdot\mathbf{r}} \tag{3.77}$$

Following the same steps for the reflected wave we have

$$\mathbf{E}_-(\mathbf{r}) = [(\hat{\boldsymbol{i}}\cos\theta + \hat{\boldsymbol{k}}\sin\theta)A_- + \hat{\boldsymbol{j}}B_-]e^{i\mathbf{k}_-\cdot\mathbf{r}} \tag{3.78}$$

$$\mathbf{H}_-(\mathbf{r}) = \frac{1}{Z}[(\hat{\boldsymbol{i}}\cos\theta + \hat{\boldsymbol{k}}\sin\theta)B_- - \hat{\boldsymbol{j}}A_-]e^{i\mathbf{k}_-\cdot\mathbf{r}} \tag{3.79}$$

and the transverse components become

$$\mathbf{E}_{\mathrm{T}-}(\mathbf{r}) = (\hat{\boldsymbol{i}}A_-\cos\theta + \hat{\boldsymbol{j}}B_-)e^{i\mathbf{k}_-\cdot\mathbf{r}} \tag{3.80}$$

$$\mathbf{H}_{\mathrm{T}-}(\mathbf{r}) = \frac{1}{Z}(\hat{\boldsymbol{i}}B_-\cos\theta - \hat{\boldsymbol{j}}A_-)e^{i\mathbf{k}_-\cdot\mathbf{r}} \tag{3.81}$$

Note that all the aforementioned expressions can also be applied for material n' by adding a prime to all symbols.

There are two more points we need to clarify before we can derive the overall expression for the transverse electromagnetic fields. Firstly, the $A_\pm$ and $B_\pm$ amplitudes correspond to the total fields so we need to find the appropriate expressions for their transverse counterparts. Secondly, the transverse impedance should also be calculated for both polarizations. Inspecting Fig. 3.6(a) we observe that $A_{\mathrm{T}\pm} = A_\pm\cos\theta$ and from Fig. 3.6(b) $B_{\mathrm{T}\pm} = B_\pm$. The transverse impedance is defined as the ratio of the transverse components (with respect to z-axis) of the electric and magnetic field. Therefore, for TE-polarization we have $Z_{TE} = -E_y/H_x = Z/\cos\theta$ while for TM-polarization $Z_{TM} = E_x/H_y = Z\cos\theta$. Summarizing all the expressions

$$A_{\mathrm{T}\pm} = A_\pm\cos\theta \tag{3.82}$$

$$B_{\mathrm{T}\pm} = B_\pm \tag{3.83}$$

$$Z_{TE} = \frac{Z}{\cos\theta} \tag{3.84}$$

$$Z_{TM} = Z\cos\theta \tag{3.85}$$

So now Eq. (3.76), (3.77) and (3.80), (3.81) can be fully written in terms of the transverse components only

$$\mathbf{E}_{\mathrm{T}+}(\mathbf{r}) = (\hat{\boldsymbol{i}}A_{\mathrm{T}+} + \hat{\boldsymbol{j}}B_{\mathrm{T}+})e^{i\mathbf{k}_+\cdot\mathbf{r}} \tag{3.86}$$

$$\mathbf{H}_{\mathrm{T}+}(\mathbf{r}) = (-\hat{\boldsymbol{i}}\frac{B_{\mathrm{T}+}}{Z_{TE}} + \hat{\boldsymbol{j}}\frac{A_{\mathrm{T}+}}{Z_{TM}})e^{i\mathbf{k}_+\cdot\mathbf{r}} \tag{3.87}$$

$$\mathbf{E}_{\mathrm{T}-}(\mathbf{r}) = (\hat{\boldsymbol{i}}A_{\mathrm{T}-} + \hat{\boldsymbol{j}}B_{\mathrm{T}-})e^{i\mathbf{k}_-\cdot\mathbf{r}} \tag{3.88}$$

$$\mathbf{H}_{\mathrm{T}-}(\mathbf{r}) = (\hat{\boldsymbol{i}}\frac{B_{\mathrm{T}-}}{Z_{TE}} - \hat{\boldsymbol{j}}\frac{A_{\mathrm{T}-}}{Z_{TM}})e^{i\mathbf{k}_-\cdot\mathbf{r}} \tag{3.89}$$

Adding up Eq. (3.86)-(3.89) and omitting the common phase factor $e^{ik_x x}$ we can calculate the *total* transverse fields for the n medium (and similarly for the n')

$$\mathbf{E}_{\mathrm{T}}(z) = \hat{\boldsymbol{i}}E_{TM}(z) + \hat{\boldsymbol{j}}E_{TE}(z) \tag{3.90}$$

$$\mathbf{H}_{\mathrm{T}}(z) = -\hat{\boldsymbol{i}}H_{TE}(z) + \hat{\boldsymbol{j}}E_{TM}(z) \tag{3.91}$$

where

$$E_{TM}(z) = A_{\mathrm{T}+}e^{ik_z z} + A_{\mathrm{T}-}e^{-ik_z z} \tag{3.92}$$

$$H_{TM}(z) = \frac{1}{Z_{TM}}(A_{\mathrm{T}+}e^{ik_z z} - A_{\mathrm{T}-}e^{-ik_z z}) \tag{3.93}$$

$$E_{TE}(z) = B_{\mathrm{T}+}e^{ik_z z} + B_{\mathrm{T}-}e^{-ik_z z} \tag{3.94}$$

$$H_{TE}(z) = \frac{1}{Z_{TE}}(B_{\mathrm{T}+}e^{ik_z z} - B_{\mathrm{T}-}e^{-ik_z z}) \tag{3.95}$$

A reasonable question that emerges is why we did all these calculations for the simple scheme of Fig. 3.6. The answer is the importance of Eq. (3.92)-(3.95). If we compare them with Eq. (3.34) and (3.35) for the normal incidence case, we will notice that they have exactly the same form with the

substitutions $Z \to Z_{\mathrm{T}}$ and $e^{\pm ikz} \to e^{\pm ik_z z} = e^{\pm ikz\cos\theta}$. This means that many definitions and derivations for normal incidence will be exactly the same for oblique incidence too. Based on Eq. (3.36), the *transverse reflection coefficient* at a position z will be

$$\Gamma_{\mathrm{T}}(z) \equiv \frac{E_{\mathrm{T}-}(z)}{E_{\mathrm{T}+}(z)} \tag{3.96}$$

From Eq. (3.37), the *transverse propagation matrix* for the forward and backward transverse electric fields for two points at a distance $L = |z_2 - z_1|$ in the same medium n will be

$$\begin{bmatrix} E_{\mathrm{T}1+} \\ E_{\mathrm{T}1-} \end{bmatrix} = \begin{bmatrix} e^{-ik_z L} & 0 \\ 0 & e^{ik_z L} \end{bmatrix} \begin{bmatrix} E_{\mathrm{T}2+} \\ E_{\mathrm{T}2-} \end{bmatrix} \tag{3.97}$$

From Eq. (3.38) we can find the *transverse reflection coefficient propagation*

$$\Gamma_{\mathrm{T}1} = \Gamma_{\mathrm{T}2} e^{2ik_z L} \tag{3.98}$$

The *overall transverse electromagnetic fields* can be found from Eq. (3.39)

$$\begin{bmatrix} E_{\mathrm{T}1} \\ H_{\mathrm{T}1} \end{bmatrix} = \begin{bmatrix} \cos(k_z L) & -iZ_{\mathrm{T}}\sin(k_z L) \\ -iZ_{\mathrm{T}}^{-1}\sin(k_z L) & \cos(k_z L) \end{bmatrix} \begin{bmatrix} E_{\mathrm{T}2} \\ H_{\mathrm{T}2} \end{bmatrix} \tag{3.99}$$

From Eq. (3.41) and (3.42) we can also write the *transverse Fresnel coefficients* on the left and right side of the interface

$$\tau_{\mathrm{T}} = \frac{2n_{\mathrm{T}}}{n_{\mathrm{T}} + n'_{\mathrm{T}}} \tag{3.100}$$

$$\rho_{\mathrm{T}} = \frac{n_{\mathrm{T}} - n'_{\mathrm{T}}}{n_{\mathrm{T}} + n'_{\mathrm{T}}} \tag{3.101}$$

where n_{T} and n'_{T} are the transverse refractive indices on the left and right side of the interface, respectively. The expressions $\rho_{\mathrm{T}} = -\rho'_{\mathrm{T}}$ and $\tau'_{\mathrm{T}} = 1 +$

$\rho'_{\mathrm{T}} = 1 - \rho_{\mathrm{T}}$ are also valid here. The previous equations are correct for both polarizations. We can verify the validity of Eq. (3.101) (and similarly for Eq. (3.100)), by distinguishing the TE- and TM-case leading to the well known elementary Fresnel reflection coefficients for oblique incidence

$$\rho_{TM} = \frac{n\cos\theta' - n'\cos\theta}{n\cos\theta' + n'\cos\theta} \tag{3.102}$$

$$\rho_{TE} = \frac{n\cos\theta - n'\cos\theta'}{n\cos\theta + n'\cos\theta'} \tag{3.103}$$

For $\theta = \theta' = 0$ they both reduce to the reflection coefficient for normal incidence (Eq. (3.42)).

We now have all the required tools to examine the dielectric multilayer scenario for arbitrary angle of incidence as sketched in Fig. 3.7. Similarly to the normal incidence, case we assume no reflected waves from the $(M+1)^{th}$ medium. All the incident angles in each medium are related via *Snell's law of refraction*

$$n_0 \sin\theta_0 = n_i \sin\theta_i = n_{M+1}\sin\theta_{M+1} \quad , i = 1, 2, 3, ..., M \tag{3.104}$$

Thus, by knowing the initial angle, θ_0, it is possible to find all the remaining angles if the materials $n_0, n_1, ..., n_{M+1}$ are given. The *phase thickness* will now be

$$\delta_i = k_{zi} L_i = \frac{\omega}{c} n_i L_i \cos\theta_i \quad , i = 1, 2, 3, ..., M \tag{3.105}$$

The *transverse refractive indices* for each medium will be

$$n_{\mathrm{T}i} = \begin{cases} n_i \cos\theta_i & (TE) \\ n_i / \cos\theta_i & (TM) \end{cases} \quad , i = 0, 1, 2, ..., M+1 \tag{3.106}$$

From Eq. (3.53)-(3.55) we can write the elementary transverse reflection and transmission coefficients for each layer

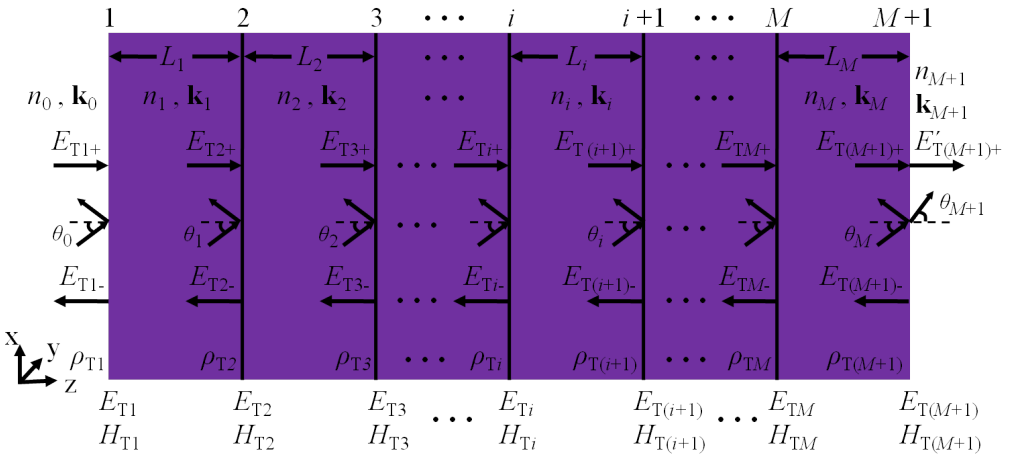

Figure 3.7: Oblique propagation through a dielectric multilayer placed between two semi-infinite media. Only the transverse backward and forward fields for the left side of each interface are shown. The arrows under them indicate the reflected and transmitted waves, not the actual direction of the electric field.

$$\rho_{\mathrm{T}i} = \frac{n_{\mathrm{T}(i-1)} - n_{\mathrm{T}i}}{n_{\mathrm{T}(i-1)} + n_{\mathrm{T}i}} = -\rho'_{\mathrm{T}i} \quad , i = 1, 2, 3..., M+1 \tag{3.107}$$

$$\tau_{\mathrm{T}i} = \frac{2n_{\mathrm{T}(i-1)}}{n_{\mathrm{T}(i-1)} + n_{\mathrm{T}i}} = 1 + \rho_{\mathrm{T}i} \quad , i = 1, 2, 3..., M+1 \tag{3.108}$$

$$\tau'_{\mathrm{T}i} = \frac{2n_{\mathrm{T}i}}{n_{\mathrm{T}(i-1)} + n_{\mathrm{T}i}} = 1 + \rho'_{\mathrm{T}i} \quad , i = 1, 2, 3..., M+1 \tag{3.109}$$

The transverse backward and forward electric fields can be calculated from Eq. (3.56)

$$\begin{bmatrix} E_{\mathrm{T}i+} \\ E_{\mathrm{T}i-} \end{bmatrix} = \frac{1}{\tau_{\mathrm{T}i}} \begin{bmatrix} e^{-ik_{zi}L_i} & \rho_{\mathrm{T}i}e^{ik_{zi}L_i} \\ \rho_{\mathrm{T}i}e^{-ik_{zi}L_i} & e^{ik_{zi}L_i} \end{bmatrix} \begin{bmatrix} E_{\mathrm{T}(i+1)+} \\ E_{\mathrm{T}(i+1)-} \end{bmatrix} \quad , i = M, M-1, ..., 1 \tag{3.110}$$

Of course for the $(M+1)^{th}$ layer there is no backward wave so the limit

condition is

$$\begin{bmatrix} E_{\mathrm{T}(M+1)+} \\ E_{\mathrm{T}(M+1)-} \end{bmatrix} = \frac{1}{\tau_{\mathrm{T}(M+1)}} \begin{bmatrix} 1 & \rho_{\mathrm{T}(M+1)} \\ \rho_{\mathrm{T}(M+1)} & 1 \end{bmatrix} \begin{bmatrix} E'_{\mathrm{T}(M+1)+} \\ 0 \end{bmatrix} \quad , i = M, M-1, ..., 1 \tag{3.111}$$

To calculate the reflection and transmission response of the system we can use Eq. (3.57) and (3.58) to get

$$\Gamma_{\mathrm{T}i} = \frac{\rho_{\mathrm{T}i} + \Gamma_{\mathrm{T}(i+1)} e^{2ik_{zi}L_i}}{1 + \rho_{\mathrm{T}i}\Gamma_{\mathrm{T}(i+1)} e^{2ik_{zi}L_i}} \quad , i = M, M-1, ..., 1 \tag{3.112}$$

$$T_{\mathrm{T}i} = \frac{\tau_{\mathrm{T}i} T_{\mathrm{T}(i+1)} e^{ik_{zi}L_i}}{1 + \rho_{\mathrm{T}i}\Gamma_{\mathrm{T}(i+1)} e^{2ik_{zi}L_i}} \quad , i = M, M-1, ..., 1 \tag{3.113}$$

with the same limit conditions as for the normal incidence case, $\Gamma_{\mathrm{T}(M+1)} = \rho_{\mathrm{T}(M+1)}$ and $T_{\mathrm{T}(M+1)} = \tau_{\mathrm{T}(M+1)}$. Finally, to find the total transverse electromagnetic fields we can use Eq. (3.59) to get

$$\begin{bmatrix} E_{\mathrm{T}i} \\ H_{\mathrm{T}i} \end{bmatrix} = \begin{bmatrix} \cos(k_{zi}L_i) & -iZ_{\mathrm{T}i}\sin(k_{zi}L_i) \\ -iZ_{\mathrm{T}i}^{-1}\sin(k_{zi}L_i) & \cos(k_{zi}L_i) \end{bmatrix} \begin{bmatrix} E_{\mathrm{T}(i+1)} \\ H_{\mathrm{T}(i+1)} \end{bmatrix} \quad , i = M, M-1, ..., 1 \tag{3.114}$$

with the limit condition for the $(M+1)^{th}$ layer $E_{\mathrm{T}(M+1)} = E'_{\mathrm{T}(M+1)}$ and $H_{\mathrm{T}(M+1)} = Z^{-1}_{\mathrm{T}(M+1)} H'_{\mathrm{T}(M+1)}$. The validity of the previous expression can additionally be verified from [32] and [33].

So far we have examined dielectric materials only. However, as we have discussed in the previous Chapters, lossy materials are of fundamental importance in the plasmonics field. Their two main characteristics are their dispersive (i.e. the frequency dependence) and absorptive (i.e. non-zero imaginary part of refractive index) behaviour. Thus for the case of Fig. 3.7, the complex permittivity and refractive index can be written as

$$\varepsilon_i(\omega) = \varepsilon_i^R(\omega) + i\varepsilon_i^I(\omega) \quad , i = 0, 1, 2, ..., M+1 \tag{3.115}$$

$$n_i(\omega) = \sqrt{\frac{\varepsilon_i(\omega)}{\varepsilon_0}} = n_i^R(\omega) + in_i^I(\omega) \quad , i = 0, 1, 2, ..., M+1 \tag{3.116}$$

where $\{\varepsilon_i^R(\omega), n_i^R(\omega)\}$ and $\{\varepsilon_i^I(\omega), n_i^I(\omega)\}$ correspond to the real and imaginary part of the permittivity and refractive index, respectively. Snell's law from Eq. (3.104) is still valid but now the angles θ_i are complex because the refractive indices are. The transverse refractive indices are again given by Eq. (3.106) but with n_i and θ_i complex. The $\cos\theta_i$ can be calculated from

$$\cos\theta_i = \sqrt{1 - \sin^2\theta_i} = \sqrt{1 - \frac{n_0^2 \sin^2\theta_0}{n_i^2}} \quad , i = 1, 2, 3, ..., M \tag{3.117}$$

If we know $n_{\mathrm{T}i}$ we can find the complex elementary transverse reflection and transmission coefficients from Eq. (3.107)-(3.109). The next step is to find the phase thickness which will now be complex due to the complex nature of the wavevector. Since we have isotropic media, we can calculate k_{zi} knowing that $k_{xi} = k_{x0} = (\omega/c)n_0 \sin\theta_0$ and $k_{zi}^2 + k_{xi}^2 = \omega\mu_0\varepsilon_i$. So the complex phase thickness can be expressed as

$$\delta_i = k_{zi}L_i = \frac{\omega L_i}{c}\sqrt{n_i^2 - n_0^2 \sin^2\theta_0} \quad , i = 1, 2, 3, ..., M \tag{3.118}$$

Since we know $n_{\mathrm{T}i}$ and δ_i we can use Eq. (3.112)-(3.114) to find everything else. We thus conclude that all the equations we derived for the multilayer dielectric scenario are also correct for lossy media.

Recapitulating, the TMM allows us to analytically calculate the optical response for the case of a multilayer system of a) arbitrary thickness L_i, b) for any material combination (lossy, lossless or dispersive), c) for any angle of incidence θ_i and for d) TE- or TM-polarization. However, all the above work is valid for the case of *isotropic* media. Since the core of this thesis is connected with highly anisotropic metamaterials (read Section 5.2

for instance), the method needs to be extended to account for anisotropy too. This is the scope of the next Section.

3.5 Maxwell Garnett rule for multiphase mixtures

In this Section we apply an effective medium approach, called Maxwell Garnett formalism, to derive the effective optical constants for a two-phase mixture. We then combine the resulted expressions with the TMM method discussed previously, in order to have a fast semi-analytical method for the determination of the optical response for a given system.

The scientific interest for the optical properties of inhomogeneous multiphase media mainly started from the second half of the 19^{th} century. The main aim of the developed theories is to derive the dielectric constant, usually referred as *effective dielectric constant*, from the knowledge of the dielectric constant of the ingredients and the filling factor of them. For that reason, all these methods are usually called *effective medium theories* (EMT). A fundamental assumption of EMT is that the inhomogeneity is macroscopically uniform. For the case of particles in metal-dielectric composites for instance, this condition holds under the quasi-static limit by assuming that all particles are much smaller than the wavelength in the medium. When the size of the particles starts to become comparable to the wavelength, EMT fails to predict the correct response and only numerical models can be used.

The two most broadly used effective theories are the Maxwell Garnett (MG) [34] and Bruggeman (BG) [35] theories developed in 1904 and 1935, respectively. Their distinct difference is related to the way they treat the medium's constituents. The MG model treats them in an asymmetric way

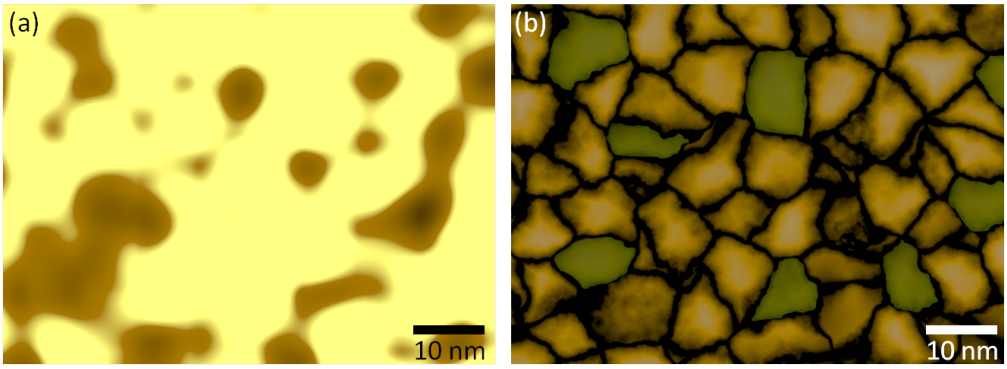

Figure 3.8: Effective medium treatment of a two-phase mixture via the Maxwell Garnett (a) and the Bruggeman (b) methods. The Maxwell Garnett approximation distinguishes the inclusions from the host environment, while the Bruggeman model treats all the constitutes in an equal (symmetrical) way. Images were constructed via POV-Ray imaging software.

so that the inclusions always have a smaller volume fraction compared to the host medium, while the BG model treats the constituents in a symmetric way by introducing grains (Fig. 3.8). This leads the MG model to be accurate for inclusions with small volume fractions but becomes inaccurate when they become comparable to the volume of the host medium. On the other hand, the BG model may be accurate when the volume fractions of the constituents become comparable. For fluid or semi-fluid mixtures, BG theory is the preferred method because it can predict the percolation threshold when the volume of one constituent is increased leading to the formation of grain boundaries. However, it fails to predict optical features when the host medium (high volume fraction) is clearly separated from the inclusions (low volume fraction). For the scope of this thesis, there is a clear volume fraction difference between the constituents (typically the host medium occupies 3 - 4 times more volume compared to inclusions), thus the MG theory is the recommended method. Additionally, the MG model can predict local features

(like the surface plasmon frequency in metallic particles) which are of high importance here.

Let us assume we have an inhomogeneous two-phase mixture as depicted in Fig. 3.8(a). The host medium has permittivity ε_h and the inclusions ε_i. Since it is a two-phase system, all the inclusions have the same permittivity but their shape could in general be arbitrary. The mean electric field over a volume V around a point $\mathbf{r}$ is defined as [36]

$$\langle \mathbf{E}(\mathbf{r}) \rangle = \frac{1}{V} \int_V \mathbf{E}(\mathbf{r} + \mathbf{r}') \mathrm{d}\mathbf{r}' \tag{3.119}$$

If the number of inclusions in volume V is j, the average electric field can be expressed as

$$\langle \mathbf{E}(\mathbf{r}) \rangle = (1 - f) \langle \mathbf{E}_h(\mathbf{r}) \rangle + f \sum_j w_j \langle \mathbf{E}_i(\mathbf{r}) \rangle \tag{3.120}$$

$$\langle \mathbf{E}_h(\mathbf{r}) \rangle = \frac{1}{V_h} \int_{V_h} \mathbf{E}(\mathbf{r} + \mathbf{r}') \mathrm{d}\mathbf{r}' \tag{3.121}$$

$$\langle \mathbf{E}_j(\mathbf{r}) \rangle = \frac{1}{V_j} \int_{V_j} \mathbf{E}(\mathbf{r} + \mathbf{r}') \mathrm{d}\mathbf{r}' \tag{3.122}$$

where V_h is the volume of the host medium, V_j is the volume of the j^{th} inclusion, $f = \sum_j V_j / V$ is the total volume fraction of the inclusions and $w_j = f_j / f$ with $f_j = V_j / V$. The $\langle \mathbf{E}_h(\mathbf{r}) \rangle$ and $\langle \mathbf{E}_j(\mathbf{r}) \rangle$ are the mean electric fields for the host medium and the j^{th} inclusion respectively.

Similarly to Eq. (3.120), the average polarization can be written as

$$\langle \mathbf{P}(\mathbf{r}) \rangle = (1 - f) \langle \mathbf{P}_h(\mathbf{r}) \rangle + f \sum_j w_j \langle \mathbf{P}_i(\mathbf{r}) \rangle \tag{3.123}$$

where again $\langle \mathbf{P}_h(\mathbf{r}) \rangle$ and $\langle \mathbf{P}_j(\mathbf{r}) \rangle$ correspond to the host medium and the j^{th} inclusion. For the case of linear polarisation we have

$$\langle \mathbf{P}_h(\mathbf{r}) \rangle = \varepsilon_0 \chi_h \langle \mathbf{E}_h(\mathbf{r}) \rangle \tag{3.124}$$

$$\langle \mathbf{P}_j(\mathbf{r}) \rangle = \varepsilon_0 \chi_j \langle \mathbf{E}_j(\mathbf{r}) \rangle \tag{3.125}$$

where $\chi_h = \varepsilon_h - 1$ and $\chi_j = \varepsilon_j - 1$ are the linear susceptibilities of the host medium and inclusions respectively. In a similar way, we can define the effective susceptibility (χ_{eff}) that represents the whole structure (host medium + inclusions) as a single unit

$$\langle \mathbf{P}(\mathbf{r}) \rangle = \varepsilon_0 \chi_{eff} \langle \mathbf{E}(\mathbf{r}) \rangle \tag{3.126}$$

Note here that $\chi_{eff} = \varepsilon_{eff} - 1$ is, in general, a tensor since the effective permittivity is not always the same along different directions. Substituting Eq. (3.124)-(3.126) in Eq. (3.123) we obtain the following master equation

$$(1-f)(\varepsilon_{eff} - \varepsilon_h \bar{\bar{\delta}}) \langle \mathbf{E}_h(\mathbf{r}) \rangle + f \sum_j w_j (\varepsilon_{eff} - \varepsilon_j \bar{\bar{\delta}}) \langle \mathbf{E}_j(\mathbf{r}) \rangle = 0 \tag{3.127}$$

where $\bar{\bar{\delta}}$ is the unit diagonal tensor. This is a general expression valid for linear polarization (i.e. linear optical measurements) but with no assumption on either the shape or the orientation of the inclusions.

Since we have a general enough equation to begin with, we will now slowly start to approximate the actual geometry of the structures investigated in the current thesis. Let us consider the scenario of an isolated ellipsoid in a uniform external field $\mathbf{E}_h$. The field inside the ellipsoid will also be uniform and can be linearly connected with the external via $\mathbf{E}_j = \alpha_{jk} \mathbf{E}_h$ where α_{jk} is the electric field tensor[4] which, for the ellipsoidal case, is given by

[4]Not to be confused with the polarizability tensor.

$$\alpha_{jk} = \frac{\varepsilon_h}{\varepsilon_h + N_k(\varepsilon_j - \varepsilon_h)} \quad , k = x, y, z \tag{3.128}$$

The j represent the number of inclusion (here the ellipsoid is isolated so $j = 1$, but we will soon extend it to many so we keep it for consistency) and k is the electric field tensor along a given direction. The N_k is the depolarization factor which measures how much the electric field inside the ellipsoid is decreased due to polarization. For an ellipsoid with semi-axes c_x, c_y, c_z along the x-, y- and z-directions, the depolarization factor along the x-axis takes the form [37], [38]

$$N_x = \frac{c_x c_y c_z}{2} \int_0^\infty \frac{\mathrm{d}s}{(s + c_x^2)\sqrt{(s + c_x^2)(s + c_y^2)(s + c_z^2)}} \tag{3.129}$$

For the depolarization factors N_y and N_z, the semi-axis c_x needs to be interchanged with c_y and c_z, respectively. For the case where many ellipsoids (inclusions) are counted, MG theory cannot continue analytically unless a major assumption is made: The average electric fields inside and outside the inclusions are also linearly connected similarly to the isolated scenario. This means that $\langle \mathbf{E}_j(\mathbf{r}) \rangle = \alpha_{jk} \langle \mathbf{E}_h(\mathbf{r}) \rangle$ which is correct only when the ellipsoids are not interacting with each other. Thus, any interaction between the inclusions cannot be observed from MG theory and needs to be calculated numerically. If we accept this hypothesis, we can replace it with Eq. (3.127) and get

$$(1 - f)(\varepsilon_{eff} - \varepsilon_h \bar{\bar{\delta}}) + f(\varepsilon_{eff} - \varepsilon_j \bar{\bar{\delta}}) \sum_j w_j \alpha_{jk} = 0 \tag{3.130}$$

So the main task now is to calculate $\sum_j w_j \alpha_{jk}$ which, depending on the geometry (size, shape, orientation and so on), could be easy or difficult to find. Solving for ε_{eff} we find

$$\varepsilon_{eff} = \frac{(1-f)\varepsilon_h\bar{\bar{\delta}} + f\varepsilon_j\bar{\bar{\delta}}\sum_j w_j\alpha_{jk}}{1-f+f\sum_j w_j\alpha_{jk}} \tag{3.131}$$

We are now ready to approximate the case of a periodic array of cylindrical nanorods which is the main backbone of this thesis. The cylinder can be approximated to an ellipsoid with one axis (long semi-axis) always greater than the other two. If we take the z-axis to be the long one, we have $c_z \gg c_x = c_y$. Since the cylinders are periodically aligned and they do not interact with each other, we choose a unit cell of volume V and period d in the xy plane with only a single inclusion inside (ε_j). As a consequence we have $\sum_j w_j = 1$, thus $\sum_j w_j\alpha_{jk} \to \alpha_{jk}$. Eq. (3.131) is then simplified to

$$\varepsilon_{eff} = \frac{(1-f)\varepsilon_h\bar{\bar{\delta}} + f\varepsilon_j\bar{\bar{\delta}}\alpha_{jk}}{1-f+f\alpha_{jk}} \tag{3.132}$$

The above expression is valid when $r, d \ll \lambda_0$ (λ_0 being the free space wavelength) so that the effective medium can be considered homogeneous. It should also be stated that when the cylinder has metallic properties ($\varepsilon_h < 0$), the radius should also be smaller than the skin depth to avoid non-uniformities of the field distribution inside the cylinder. However, this requires a Generalized Maxwell-Garnett (GMG) approach which is not considered here; the reader can look at reference [39] for more information. The volume of the unit cell is $V = d^2l$ where l is the length of the z-semi-axis while the volume of the cylinder is $V_c = \pi r^2 l$ with r corresponding to the rod radius. Thus $f = V_c/V = \pi(r^2/d^2) = \pi p^2$ where p is the porosity defined as the radius, r, over the period, d. Porosity plays a crucial role in the optical response of the system and will be of great importance throughout this thesis. Applying all the above to Eq. (3.132) we end up with

$$\varepsilon_{eff} = \frac{(1-\pi p^2)\varepsilon_h\bar{\bar{\delta}} + \pi p^2\varepsilon_j\bar{\bar{\delta}}\alpha_{jk}}{1-\pi p^2+\pi p^2\alpha_{jk}} \tag{3.133}$$

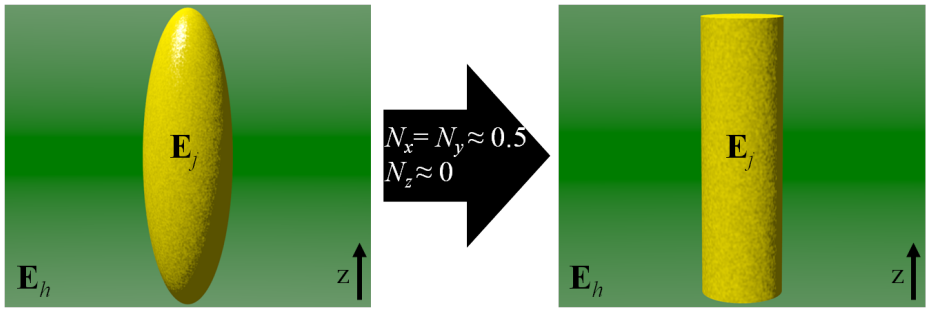

Figure 3.9: A cylinder is an approximate case of an ellipsoid with one of its semi-axes, here the z-axis, a lot greater than the other two. The depolarization factor is then simplified to $N_z \approx 0$ and $N_x = N_y \approx 0.5$. The electric fields inside ($\mathbf{E}_j$) and outside ($\mathbf{E}_h$) the cylinder are linearly connected through the electric field tensor.

So our only concern now is to calculate the electric field tensor which means that the depolarization factor must be found along each semi-axis. Since $c_z \gg c_x = c_y$, Eq. (3.129) can be calculated numerically by setting the appropriate semi-axes values. The long semi-axis for a typical structure here is around 10 times larger than the short ones. Setting $c_z = 10$ and $c_x = c_y = 1$ we get $N_z \approx 0$ and $N_x = N_y \approx 0.5$ (Fig. 3.9). As a result, the electric field tensor for each direction will be

$$\alpha_z = 1 \tag{3.134}$$

$$\alpha_x = \alpha_y = \frac{\varepsilon_h}{\varepsilon_h + 0.5(\varepsilon_j - \varepsilon_h)} \tag{3.135}$$

Substituting Eq. (3.134) and (3.135) to Eq. (3.133), the effective permittivities ε_{effz} and $\varepsilon_{effx} = \varepsilon_{effy}$ can be derived leading to

$$\varepsilon_{effz} = \pi p^2 \varepsilon_j + (1 - \pi p^2)\varepsilon_h \tag{3.136}$$

$$\varepsilon_{effx} = \varepsilon_{effy} = \varepsilon_h \frac{2p^2\varepsilon_j + (\pi^{-1} - p^2)(\varepsilon_h + \varepsilon_j)}{2p^2\varepsilon_h + (\pi^{-1} - p^2)(\varepsilon_h + \varepsilon_j)} \tag{3.137}$$

The above relations express the effective permittivity for an array of cylindrical rods in terms of the permittivities of its constituents and geometry. It should be noted that the expressions are still valid when the period along the xy plane is asymmetrical. In that scenario we should replace $p^2 \rightarrow p_x p_y$, where p_x and p_y are the porosities for the x- and y-directions respectively.

In order to combine the MG theory with the TMM, a final step is required. Each layer in TMM is characterized by a unique permittivity tensor. However, due to the symmetry of the cylindrical rods, two effective permittivities are needed. To calculate the *total* effective permittivity in an uniaxial anisotropic medium Eq. (3.23) in Section 3.2 will be of assistance. It is trivial to solve it and find ε_{eff} in terms of ε_{effx} and ε_{effy}, but it should be noted that the angle θ is the one *inside* the anisotropic layer. It is convenient for calculations to have the substrate angle of incidence as the input one. Applying Snell's law between the substrate and the anisotropic layer we eventually get

$$\varepsilon_{eff} = \varepsilon_{effx} + \left(1 - \frac{\varepsilon_{effx}}{\varepsilon_{effz}}\right) \varepsilon_{sub} \sin^2 \theta \tag{3.138}$$

where ε_{sub} and θ correspond to the permittivity and angle of incidence of the substrate respectively. Eq. (3.138) allows us to treat an anisotropic array of cylindrical rods as an effective medium with a single permittivity fully compatible with the TMM. In the following Section we put all the calculations we have done so far into test and compare them with numerical simulations. At the same time we will discuss some useful quantities for the physical understating of the periodic nanorod array examined here.

Summarizing, the MG approximation allows the determination of the effective dielectric constant in terms of the dielectric function of the constituents and the filling factor (porosity) of them. The limitations of the effective medium approximation considered here, are the following: a) The

volume of the host medium needs to be significantly higher than the volume of inclusions. b) The mean electric fields inside and outside the inclusions are linearly connected. For cylindrical arrays, c) both the radius and the period should be smaller than the free space wavelength and, d) the field distribution inside the cylinders is considered uniform even for metallic rods.

3.6 Comparison between EMT with numerical simulations and effects of the geometry on the optical response

The scope of this Section is to compare the semi-analytical theory, developed in the previous Section, and compare it with 3D numerical models. The results are then analysed and useful physical quantities are defined. Lastly, the effect of geometry on the optical response of the nanorod metamaterial is examined based on the effective medium approximation.

Let us first start with the minimalistic scenario of a thin Au film sandwiched between an isotropic substrate (n_{sub}) and superstrate (n_{sup}). We consider this for two reasons: Firstly, the transfer matrix method (TMM) can be directly compared with numerical simulations without the need of the Maxwell-Garnett (MG) approximation since the structure has no anisotropy and secondly, important physical quantities can be observed and defined that will be of assistance in more complex structures.

The TM-polarized angular spectrum of reflectance and transmittance between TMM and finite element method (FEM) is depicted in Fig. 3.10(a). The thickness of the Au film is 50 nm with permittivity -12.10 $+i1.19$ [40] for $\lambda = 637$ nm. Substrate and superstrate have permittivity 1.5^2 and 1 re-

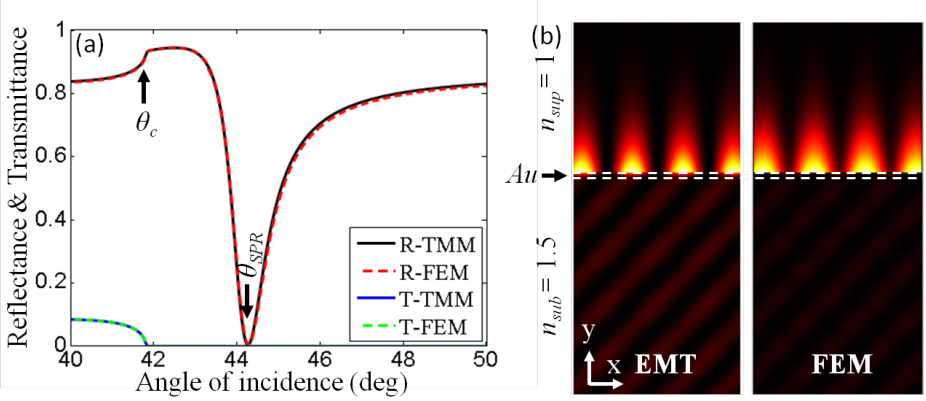

Figure 3.10: (a) Angular dependence of reflectance and transmittance between TMM and FEM for a 50 nm Au film at $\lambda = 637$ nm. The permittivity of the substrate and superstrate is 1.5^2 and 1, respectively, while for Au is -12.10 + i1.19 taken from [40]. The critical angle (θ_c) is at 41.8° and the surface plasmon polariton resonance angle (θ_{SPR}) at 44.3°. TM-polarization is considered with the magnetic field along the z-axis. (b) Surface plot of $\mathrm{Re(E)}^2 = \mathrm{Re(E}_x)^2 + \mathrm{Re(E}_y)^2$ between TMM and FEM at the θ_{SPR} angle. Both images are in good agreement and show a SPP excited along the Au / superstrate interface.

spectively. There is an excellent agreement of the optical response between the TMM and FEM which is expected because TMM is explicit theory (read Appendix C).

For angles below 41°, reflection losses are caused by the absorption of Au and the simultaneous transmission into the superstrate. As the angle approaches the critical value (θ_c) a phenomenon called *total internal reflection* (TIR) occurs and reflectance approaches unity. At this point onwards, almost all light is reflected back and a discontinuity in reflectance is observed because transmittance suddenly becomes zero. The critical angle is given from $\sin\theta_c = n_{sub}/n_{sup}$ which is approximately 41.8° for the structure of Fig. 3.10. Note that only the real parts must be taken into account when complex valued

refractive index materials are considered. Due to the TIR condition, the fields inside the Au layer is a combination of two evanescent fields; one on the substrate / Au interface and the other on the Au / superstrate interface [33]. For angles slightly above TIR, there is a small reflection loss because of the absorption of the metal film. As the angle of incidence further increases, a strong dip in the reflectivity is observed due to the *surface plasmon resonance* (SPR) phenomenon. At this stage, the momentum of the incident wavevector matches the one of a surface wave, affirming the excitation of a SPP on the Au / superstrate interface (Fig. 3.10(b)) explaining the reflectance minimum. Reflectance however cannot become zero since, even at the SPR, there is still some light the leaks out of the metal layer and into the substrate as Fig. 3.10(b) depicts. These modes are known as *leaky modes*. Finally, as the angle of incidence is further increased, the reflectance increases rapidly until it reaches unity at the extreme of 90°.

Since the TMM for the isotropic homogeneous material is in excellent agreement with numerical models, we can continue by comparing the EMT as well. Let us first consider an alumina waveguide as shown in Fig. 3.2 but with pores instead of Au rods. The energy range is 1.4 - 3.1 eV ($\sim$ 400 - 900 nm) which corresponds mainly to visible wavelengths. The refractive indices are $n_{sub} = 1.5$, $n_h = 1.6$, $n_{sup} = 1$ and pores are made of air. Setting $L_1 = 50$ nm, $L_2 = 300$ nm, $r = 25$ nm and $d = 60$ nm, the reflectance dispersion along the waveguide interface ($k_x = \beta$) can be evaluated (Fig. 3.11(a), (b)) for the case of TM-polarization. The agreement between EMT and FEM is very good and they both reveal two optical modes. Although they look the same their nature is different. The high energy mode which is excited just after the light line in the superstrate (dashed line, also named air line since the superstrate is air), represents a propagating mode (leaky mode) which

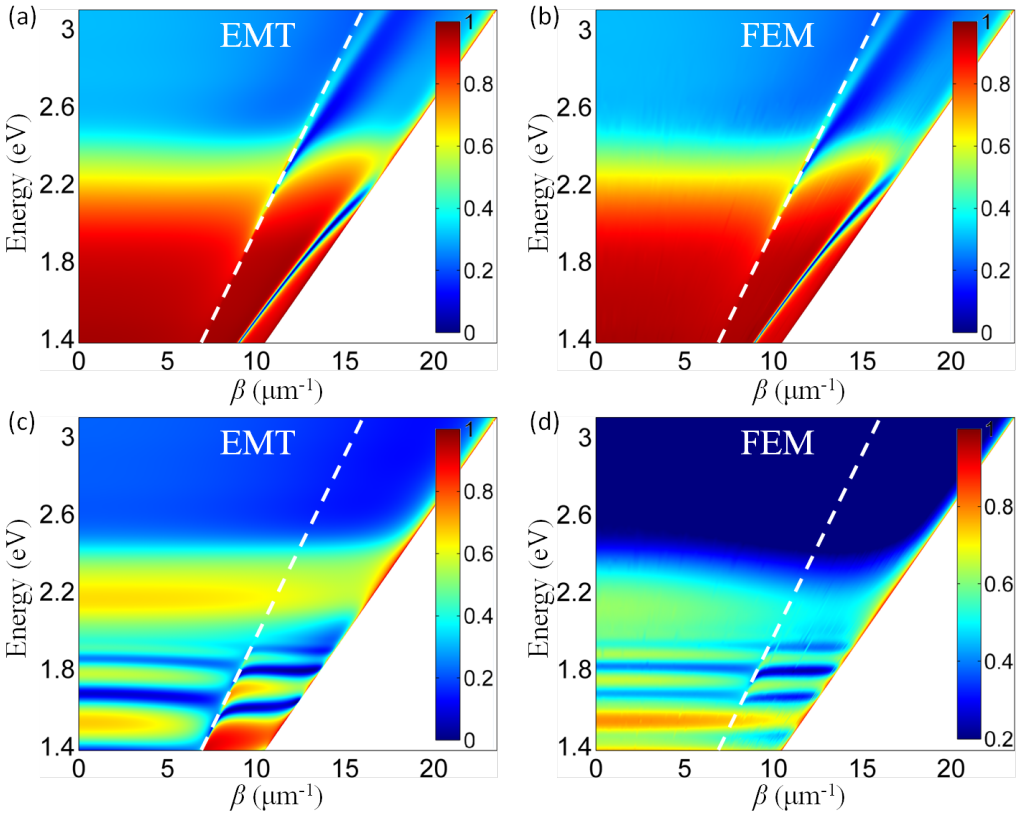

Figure 3.11: (a),(b) Reflectance dispersion between EMT and FEM for the structure of Fig. 3.2 with $L_1 = 50$ nm, $L_2 = 300$ nm, $r = 25$ nm and $d = 60$ nm. The waveguide consists of air pores instead of Au rods (porous alumina). Refractive indices are $n_{sub} = 1.5$, $n_h = 1.6$ and $n_{sup} = 1$. The agreement between EMT and FEM is very good with both methods showing a high energy leaky mode on the right side of the TIR angle (dashed line). The lower energy mode is a SPP excited on the Au / waveguide surface. (c),(d) Same as before but pores are now filled with Au and $L_1 = 10$ nm. The 3^{rd}, 4^{th} and 5^{th} leaky modes are clearly depicted in both simulations. The 2^{nd} mode is also visible in the FEM dispersion close to 1.42 eV, but not in EMT because it is located just below 1.4 eV. Optical constants of Au are taken from [40] and only TM-polarization is considered.

exists inside the waveguide but part of its electromagnetic field leaks out in the substrate. For conventional dielectric waveguides, the reader can refer to standard waveguide theory textbooks [41–43]. The low energy mode far from the TIR line is a SPP excited on the Au / waveguide interface.

Let us now fill the pores with Au and recalculate dispersion. Using the same refractive indices and geometrical parameters as before (apart from L_1 which is now 10 nm), the EMT and FEM result in the dispersions of Fig. 3.11(c), (d) respectively. The agreement is still qualitatively good but now small deviations start to occur. For instance, both figures show the 3^{rd}, 4^{th} and 5^{th} order waveguided modes but at shifted energies. The cut-off frequency (i.e. the mode frequency when $\beta = 0$) for these modes is 1.65 eV, 1.85 eV and 1.95 eV based on the EMT while for FEM is 1.67 eV, 1.82 eV and 1.94 eV, respectively. Additionally, the 2^{nd} mode is also visible in the FEM dispersion close to 1.44 eV but not shown in EMT because it is located at 1.36 eV. We can also observe a different shape formation of the modes, especially around the TIR line. Since only the pores are replaced by Au rods, it means that EMT ceases to be very accurate when metallic waveguides are considered but we can still get a dispersion close to the actual 3D model. Discrepancies come from the increased scattering of the Au nanorods that cannot be tracked with EMT. Additionally, the EMT model assumes uniform field distribution inside the metallic nanorods which is not the case here, since the radius is comparable to the skin depth of Au in the visible ($\sim$ 25 nm). Thus from this point onwards the EMT will be used and 3D numerical models will be launched only when required.

Up to this point we showed that EMT is in good agreement with numerical simulations even for the case of metallic waveguides. However, many questions arise such as "how modes can be distinguished or manipulated?"

or "How thin/thick the waveguide should be for efficient mode excitation?". To give some insight into these questions we should examine the connection between geometry and optical response. There are three geometrical parameters that can be varied, the thickness of the Au film, L_1, the thickness of the waveguide, L_2, and porosity, p.

As it is already mentioned the Au underlayer exists to provide enough conductivity for the growth of the nanorods and does not have any additional role. So its thickness is altered based on the coupling efficiency. For example, Fig. 3.11(a) has $L_1 = 50$ nm because the coupling efficiency (i.e. the rate of light that is coupled to the modes over the overall one) of the modes shown, is maximized. If L_1 is thin the SPP will be strongly damped because of radiation damping into the substrate while if it is thick most of light will get absorbed and the SPP or leaky modes will no longer be efficiently excited. Similar arguments apply for the structure of Fig. 3.11(c). We thus turn our attention to the other two remaining parameters.

The variation of waveguide thickness is one way to shift the energy position of optical modes. Fig. 3.12(a) demonstrates the monotonous red-shift of the 2^{nd} and 3^{rd} order leaky modes for small changes of L_2 at an angle of 70° and a porosity of 0.4. It is clear that even a small increase of the thickness can significantly red-shift the excited leaky modes. For example, when L_2 goes from 200 nm to 240 nm, the 2^{nd} order leaky mode shifts from 727 nm to 793 nm while the 3^{rd} one from 645 nm to 678 nm. Fig. 3.12(b)-(d) show the reflectance dispersion for a broader range of waveguide thickness. It is evident that regardless what angle of incidence examined, the 2^{nd} and 3^{rd} order leaky modes tracked by the black and red arrows respectively, show a monotonous red-shift as L_2 varies from 200 nm to 300 nm. The 4^{th} and 5^{th} waveguided modes, tracked by a green and purple arrow respectively, are also

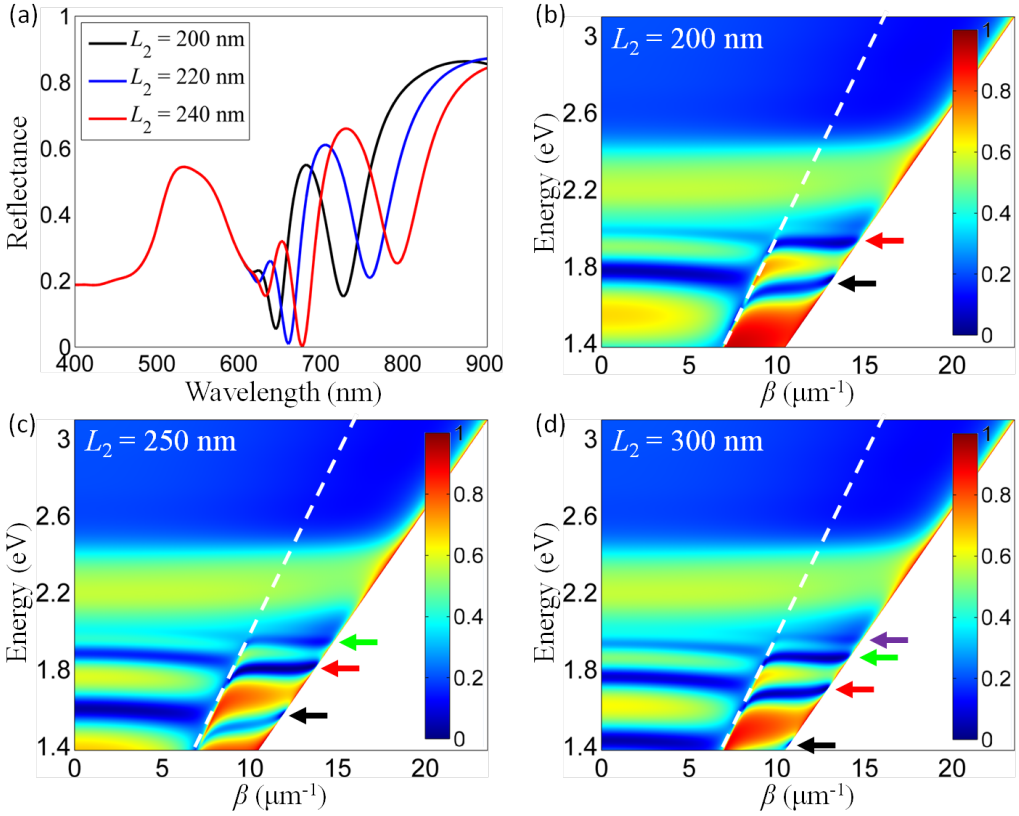

Figure 3.12: Reflectance diagrams for the structure of Fig. 3.2 at various waveguide thicknesses based on EMT. Porosity is 0.4 and L_1 = 10 nm. The dashed line corresponds to the superstrate light line and is there for guidance. Optical constants of Au are taken from [40] and only TM-polarization is considered. (a) Reflectance as L_2 changes for $\theta = 70°$. The monotonous red-shift of the 2^{nd} and 3^{rd} waveguided mode is shown as L_2 increases. (b)-(d) Reflectance dispersion for L_2 = 200 nm, 250 nm and 300 nm, respectively. The black and red arrows track the red-shift of the 2^{nd} and 3^{rd} waveguided mode as thickness increases. The 4^{th} and 5^{th} waveguided modes are also visible at higher L_2, tracked by a green and purple arrow respectively.

visible in Fig. 3.12(c), (d) following the same pattern as discussed. Thus it is possible to control the resonant position of such modes at visible wavelengths

by the appropriate structuring of waveguide thickness.

Considering the thickness of a waveguide for efficient mode excitation, it depends on the actual usage (potential applications) and fabrication limitations. If a use for the waveguide requires a plethora of modes at different energies, L_2 should be thick, typically more than $400-500$ nm, to allow more modes to be excited. On the other hand fabrication conditions may limit the maximum thickness that can be achieved. For example if the template (host medium) of Fig. 3.2 is removed (so we end up in a free-standing array of Au nanorods) the aspect ratio should not exceed 10 otherwise the nanorods might collapse.

The last geometrical parameter is porosity. Because $p = r/d$ it ranges from 0 - 0.5; any higher value has no physical meaning since the diameter of the rods will become higher than the period forcing them to partially merge each other. Fig. 3.13(a) depicts the reflectance diagram when p varies for $L_2 =$ 400 nm at an angle of 70°. In this case a non-monotonous shift of the 3^{rd} and 4^{th} order waveguided mode, tracked by a red and green arrow respectively, is observed. More precisely when porosity is increased from 0.25 to 0.30 and then to 0.35, the 3^{rd} order waveguided mode blue-shifts from 746 nm to 735 nm and then red-shifts to 770 nm while the 4^{th} order waveguided mode goes from 689 nm to 660 nm and back to 680 nm. This behaviour is validated for any angle of incidence as the dispersion graphs in Fig. 3.13(b)-(d) reveal. As a result, the porosity factor allows the non-linear manipulation of the excited optical modes.

From the initial queries, the one about the nature of the optical modes is still not discussed. The standard way to categorize a mode is through the inspection of the electromagnetic fields. The field formation and confinement is usually enough to distinguish them. However, there are other indirect ways

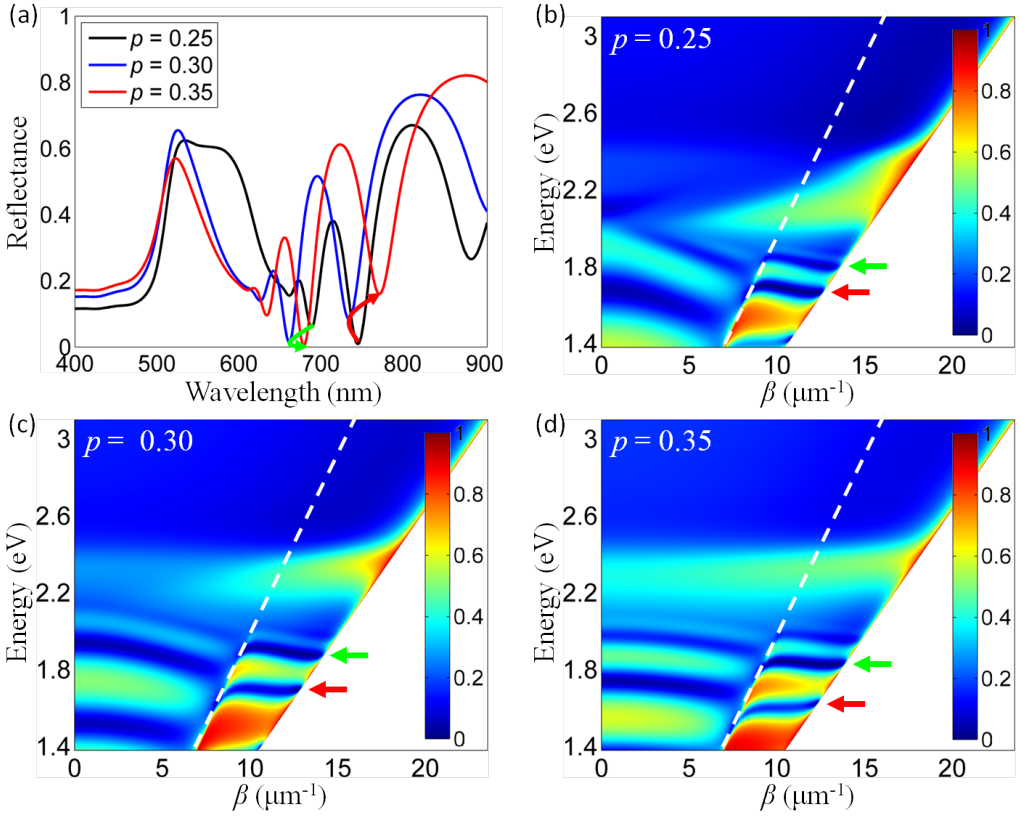

Figure 3.13: Reflectance for the structure of Fig. 3.2 for different porosities. Thickness of the Au underlayer is 10 nm and waveguide 400 nm. The dashed line corresponds to the TIR angle and is there for guidance. Optical constants of Au are taken from [40] and only TM-polarization is considered. (a) Reflectance as p varies for $\theta = 70°$. A non-monotonous shift of the 3^{rd} (red arrow) and 4^{th} (green arrow) waveguided mode is shown as p increases. (b)-(d) Reflectance dispersion for $p = 0.25$, 0.30 and 0.35, respectively, based on EMT. The red and green arrows track the non-monotonous shift of the 3^{rd} and 4^{th} waveguided mode as porosity increases. Similar trend holds for the other modes but is not clearly visible.

to overcome this obstacle. For instance as it is mentioned in Section 2.4, a SPP has a characteristic dispersion so if a mode profile is deviating from it we can safely neglect the SPP nature. For more complicated scenarios where

the mode profiles are similar, like the one in Fig. 3.11(a), the geometry can be of assistance. If we set $L_2 \to 0$ the waveguided mode will vanish while the SPP one will remain in the dispersion diagram.

Although the initial queries have been discussed, new questions emerge from the inspection of the dispersion graphs. a) Why in all dispersions shown, there is a universal cut-off close to 2 eV? b) Why the dispersion diagrams show a negative group velocity contrary to the conventional waveguides? c) Why porosity produces a non-monotonous shift while the thickness of the waveguide does not? All these have an important physical impact and constitute a fundamental backbone of this thesis that is investigated both theoretically and experimentally in Chapter 4.

3.7 Principles of spectroscopic ellipsometry

In this Section the basic principles of ellipsometry are discussed. Up to this point there has been no specific reference to ellipsometry so there is no direct link with the previous Sections. However, the measurements in Chapter 6 were acquired via ellipsometer and is thus important to introduce the main characteristics of it. So the scope here is to explain only the basic theoretical and experimental tools and not to perform a thorough analysis of ellipsometry. For a more detailed overview, the reader can refer to [44] or [45].

3.7.1 Introduction

The first ellipsometer was realized in 1887 by Drude (mostly known from the Drude-Sommerfeld model) [46] but the term "ellipsometer" was used for the first time from Rothen in 1945 [47]. After that, many improvements and modifications were introduced on that field by pioneers such as Paik and

Brockis [48], Aspnes and Studna [49] or Muller and Farmer [50].

Ellipsometry is an optical technique that measures the reflection or transmission of light from a sample [44, 45, 51, 52]. From the measured quantities useful optical characteristics can be extracted such as the (complex) refractive index or thickness of a structure. The reason it is called ellipsometry is due to the change of the polarization state upon reflection (or transmission). The incident light usually has linear polarization but after interaction with sample it becomes elliptical. The physical explanation of the elliptical polarized shape comes from the different reflection/transmission coefficients between TE- and TM-polarization due to the different electric field (see for instance Eq. (3.106)-(3.108) for the multilayer sample case). Thus ellipsometry measures the *change* in the polarization state. During the acquisition two angles, known as ellipsometric angles, are measured. They represent the amplitude ratio (Ψ) and phase difference (Δ) of the TE- and TM-polarized orientations. For spectroscopic acquisitions, where a range of wavelengths is used, a set of $\{\Psi, \Delta\}$ is measured for each wavelength. Most ellipsometers today have a broad wavelength range functionality from the UV to the IR.

In ellipsometry, the appropriate selection of the incident angle is crucial. It is chosen based on the optimum sensitivity of the detected signal. The optimum sensitivity angle varies according to the refractive index of the sample which makes it non-trivial to find. For that reason there are usually tables with various sample characteristics (dielectric to metallic substrates, thin or thick films, isotropic or anisotropic layers and so on) that state the recommended angle to use. In theory any angle can be used from 0° to 90°. However it should be emphasized that normal incidence is not possible unless in-plane anisotropy is introduced. At normal incidence the reflection and transmission coefficients are the same for both polarizations so no phase mismatch

can occur making ellipsometry impossible.

One of the most advantageous properties of ellipsometry is the very high precision of the acquisition that can lead to extremely accurate thickness estimation of up to 0.1 Å [53]. Additionally it is a non-destructive technique that is able to measure not only the optical constants of a material but also its thickness (or thicknesses if a multilayer structure is considered). Moreover, real-time monitoring is possible for instance when real-time growth occurs. One the other hand, a major limitation is the requirement of an optical model for the post-process data analysis which makes ellipsometry an indirect method. Apart from the cases of simplistic structures, the optical models tend to be complicated and it is the user who should accept or reject the ending result. Another limitation is the large illumination spot size which leads to low spatial resolution. As the feature sizes of structures become smaller and smaller, the size of the illumination spot poses a serious problem. It should be noted however that great effort has been made towards the improvement of resolution leading to imaging ellipsometry and resolution as high as 0.5 μm [54].

To date, there is a broad range of applications based on ellipsometry. In the life sciences it is used to measure the adsorption of proteins on surfaces such as TiO_2 [55], tantalum oxide [56] or plasma polymer films [57] and time resolution of 0.1 s has been achieved [58]. Reflection ellipsometry along with the TIR phenomenon explained in Section 3.6 has been employed for biosensing techniques and a range of solutions has been determined from lubricants in water [59] to DNA hybridization [60], sensitivity of proteins in immunoassays [61] or detection of nucleic acid targets [62]. Moreover, imaging ellipsometry has been applied for thickness determination of patterned thin films [63] to roughness and imaging analysis of graphene monolayers [64].

Various types of ellipsometers exist based on the configuration of the constituent parts. At first, ellipsometry was done at a single wavelength with a nulling technique (null ellipsometry) [65]. In this case, measurements were acquired from the minimization of the reflected intensity by rotating a quarter-wave plate until ellipticity was cancelled. However this method was slow and an improved version was introduced named rotating analyser ellipsometer [65]. Here, the quarter-wave plate was at a fixed angle such that the exit light to be circularly polarized. The reflected elliptical light was then passing through a continuously rotating analyser producing a sinusoidal signal which were Fourier analysed for the determination of the ellipsometric angles. There were yet more improvements that led to the spectroscopic ellipsometer that we know today. Many spectroscopic variations exist such as the rotating analyser ellipsometry (PSA_R), rotating compensator ellipsometry (PSC_RA) or rotating analyser ellipsometry with compensator ($PSCA_R$). The reader can refer to [44] for further information. In this thesis a specific spectroscopic method was used named phase modulation ellipsometry (PSMA) which is discussed in the next part.

3.7.2 Ellipsometer configuration

As already mentioned, ellipsometry is based on the phase difference between two polarized waves. There are different methods to obtain polarized light such as dichroism [66] or double refraction with birefringent materials [67]. In ellipsometry, polarization is achieved by reflection and was first explained by Brewster in 1830 [68]. For this thesis the UVISEL 2 spectroscopic ellipsometer from HORIBA Jobin-Yvon was used. Fig. 3.14(a) shows the schematics of the devices integrated in ellipsometer along with the actual experimental instrument.

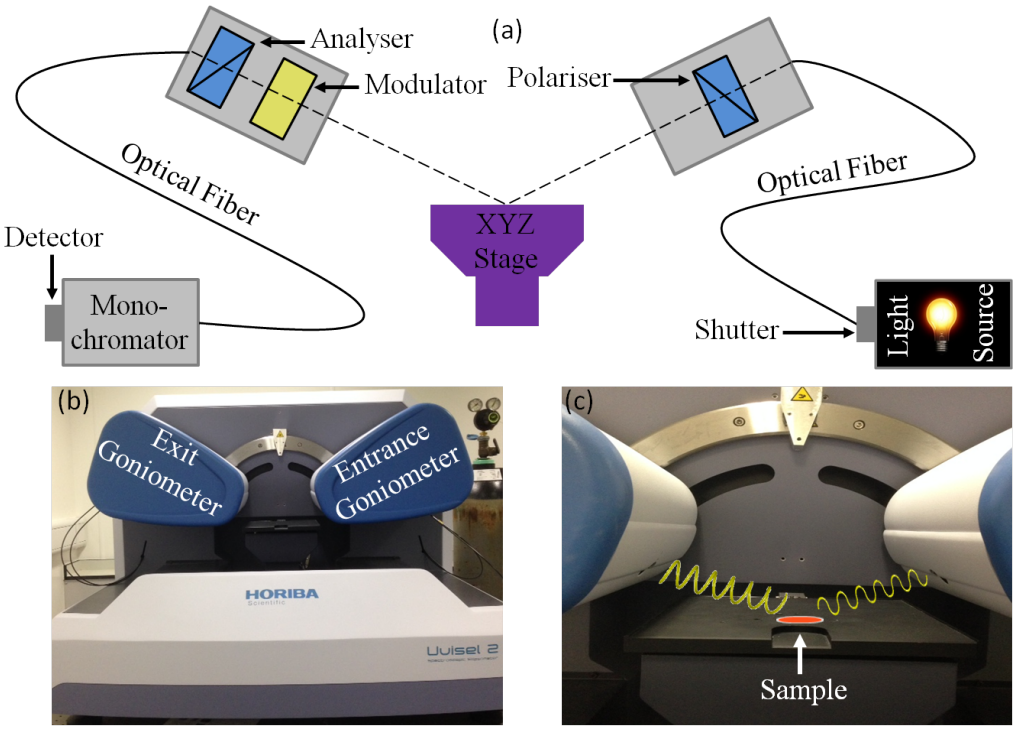

Figure 3.14: (a) Schematics of phase modulated ellipsometer setup. (b) Front view of UVISEL 2 spectroscopic ellipsometer from HORIBA Jobin-Yvon. (c) Closed view of the XYZ stage showing the change from linear to elliptic polarization upon reflection.

Starting from the *light source* there are three main types used in ellipsometry. The tungsten-halogen lamp that functions from VIS to near-IR, the Xenon (Xe) lamp that spans from near-UV to near-IR and the D_2 lamp which mainly extends from deep-UV to near-UV. Due to the broad wavelength range the most common lamp is Xenon. Here a 150 W Xenon light source was used. A *shutter* is located right after the light source in order to control the exposure time (also referred as integration time). An *optical fiber* (1 mm core diameter) is then used to couple light from the output of the source to the input head.

The input head, which is called *entrance goniometer*, is able to move and

thus the angle of incidence can be set. The "goniometer" is the combination of two Greek words, γωνία which means "angle" and μετρώ which means "count". So the device does exactly what the name says; measure angles. A second goniometer (*exit goniometer*) is also placed just after the reflection of light from the sample. The angular range of the UVISEL 2 goniometers is 35° to 90° (Fig. 3.14(b)) and angular resolution as high as 0.01° can be achieved.

In the entrance goniometer there is a *polariser* installed and in the exit goniometer a second polariser, usually referred as *analyser*, is integrated. They have a different designation because the polariser before the sample sets the polarization state of the beam (for example TM-polarization) while the polariser after the sample (analyser) determines the state of polarization after the light has been altered by reflection. One of the first polarisers, known as "Nicol prism", was devised by W. Nicol in 1828 [69]. Other polariser variations were followed such as the "Glan-Thompson prism" designed by P. Glan [70] and improved by S. P. Thompson [71]. Today most ellipsometers, especially the PSMA, use a polariser that is able to retain both polarizations. For this a prism called "Wollaston prism" is integrated in the analyser. Wollaston prism consists of two calcite prisms cemented together. When the elliptical ray of light enters the first part, the ordinary and extraordinary waves propagate undeviated but with not the same speeds. The two parts are at a cleavage angle that does not allow TIR to be reached and thus both waves are able to enter the second part of the prism. The optic axes of the two parts are perpendicular to each other which means that the ordinary wave becomes extraordinary and vice versa. Due to the different optical axis, the two rays are separated and thus polarization can be distinguished. The deviation of the two outgoing beams is usually symmetric to the ingoing one.

As they exit the second part, the two polarizations are further deviated due to Snell's law.

Thus there are two linearly polarized beams that exit the entrance goniometer, but only the one we are interested in is measured at a time. The second spot is several centimetres off the sample and does not affect the acquisition. The sample is placed on a computer controlled 200 mm x 200 mm XYZ *stage* (Fig. 3.14(c)) and a camera is installed for surface analysis of the detection area of the sample. There is also a motorised tilt camera for easy alignment of the tilt angle of the sample.

Upon reflection, the beam enters the *exit goniometer*. Inside the goniometer there are two main instruments; the analyser discussed previously and a *photoelastic modulator* (PEM). The PEM induces a sinusoidal modulation of the phase shift as a function of time. This is obtained by applying a time-varying stress which in turn induces time-varying anisotropy in an although isotropic medium (usually a silica bar is used which is isotropic in its equilibrium). A piezoelectric transducer with resonant frequency at 50 kHz creates a mono-axial stress in the silica bar making it anisotropic. Since the refractive index between the ordinary and extraordinary axes is not the same, light travels at different speeds and the two waves depict an out of phase periodicity.

After the elliptically polarized beam leaves the exit goniometer, it reaches a *monochromator* where light is analysed into its individual spectral components (waves). Finally, the monochromatic wave enters a *detector* where it gets amplified for data acquisition and processing. The UVISEL 2 detection system is composed of a photomultiplier (PMT) for the UV and VIS spectral range and a InGaAs detector for the IR spectral range.

3.7.3 Theory of phase modulation ellipsometry

The main target here is to explain the basic theoretical steps needed for the determination of the ellipsometric angles based on the PSMA configuration of Fig. 3.14. The fundamental equation in ellipsometry connects the $\{\Psi, \Delta\}$ angles with reflection and transmission coefficients as follows

$$\tan \Psi e^{i\Delta} \equiv \frac{\rho_p}{\rho_s} \quad \text{(reflection ellipsometry)} \tag{3.139}$$

$$\tan \Psi e^{i\Delta} \equiv \frac{\tau_p}{\tau_s} \quad \text{(transmission ellipsometry)} \tag{3.140}$$

where $\rho_{s,p}$ and $\tau_{s,p}$ are the reflection and transmission coefficients for TE and TM polarisations, as discussed in Sections 3.3 and 3.4 respectively. As a consequence, the ellipsometer first measures the angles $\{\Psi, \Delta\}$, then the Fresnel coefficients and after that the refractive index or thickness of a material with post-processing models.

Due to the requirement of polariser, analyser and modulator, the polarization coordinate system changes as light travels from the source to the detector. In order to connect the input and output polarized electric fields, a formalism similar to the TMM has been introduced. It is known as Jones matrix if light is fully polarized along a given direction or Muller matrix for random or partially polarized light. The reader can refer to [44, 72, 73] for more details. When the output electric field (E_A) is determined, the detected intensity can be measured from $I = |E_A|^2$. For the PSMA configuration it is given from [74, 75]

$$I(t) = I\left[I_0 + I_s \sin(\delta_0 + B\sin(\omega t)) + I_c \cos(\delta_0 + B\sin(\omega t))\right] \tag{3.141}$$

where I is a pre-factor that depends on the reflectivity of the sample, the transmission of the optical elements and lamp intensity; it is however can-

celled in later calculations. B is the amplitude of the modulated signal of frequency ω and δ_0 is the residual anisotropy in the silica bar of the modulator. Both B and δ_0 are measured during the calibration of the system and are thus considered known. The Fourier coefficients $\{I_0, I_s, I_c\}$ are expressed by the following relations [76]

$$\begin{aligned} I_0 = [1 - \cos(2\Psi)\cos(2A) + \cos(2(P-M))\cos(2M)(\cos(2A) - \cos(2\Psi)) \\ + \sin(2A)\cos\Delta\cos(2(P-M))\sin(2\Psi)\sin(2M)] \end{aligned} \tag{3.142}$$

$$I_s = \sin(2(P-M))\sin(2A)\sin(2\Psi)\sin\Delta \tag{3.143}$$

$$\begin{aligned} I_c = \sin(2(P-M))[\sin(2M)(\cos(2\Psi) - \cos(2A)) \\ + \sin(2A)\cos(2M)\sin(2\Psi)\cos\Delta] \end{aligned} \tag{3.144}$$

So all the coefficients depend on the polariser (P), analyser (A) and modulator (M) angles. For ellipsometry measurements, the two most useful combinations are $P - M = \pm 45°$, $M = 0°$, $A = \pm 45°$ known as configuration II, and $P - M = \pm 45°$, $M = \pm 45°$, $A = \pm 45°$ known as configuration III. The Fourier coefficients for configuration II can be simplified to

$$I_0 = 1 \tag{3.145}$$

$$I_s = \pm\sin(2\Psi)\sin\Delta \tag{3.146}$$

$$I_c = \pm\sin(2\Psi)\cos\Delta \tag{3.147}$$

and for configuration III

$$I_0 = 1 \tag{3.148}$$

$$I_s = \pm\sin(2\Psi)\sin\Delta \tag{3.149}$$

$$I_c = \pm\cos(2\Psi) \tag{3.150}$$

The configuration I represents the case where the analyser is absent [75, 77] but it is generally avoided because the detection system does not depend on the polarization of light.

Since $\{I_0, I_s, I_c\}$ have been expressed in terms of $\{\Psi, \Delta\}$, the next step is to analyse the sine and cosine terms in Eq. (3.141). Setting $\delta = B\sin(\omega t)$ the $\sin\delta$ and $\cos\delta$ can be expanded in the following Bessel series [78]

$$\sin\delta = \sin(B\sin(\omega t)) = 2\sum_{m=0}^{\infty} J_{2m+1}(B)\sin[(2m+1)\omega t] \tag{3.151}$$

$$\cos\delta = \cos(B\sin(\omega t)) = J_0(B) + 2\sum_{m=1}^{\infty} J_{2m}(B)\cos(2m\omega t) \tag{3.152}$$

Because the series is infinite the analysis becomes complicated, thus only the first order terms are kept. Substituting $m = 0$ in Eq. (3.151) and $m = 1$ in Eq. (3.152) we arrive at the following expressions

$$\sin\delta = 2J_1(B)\sin(\omega t) \tag{3.153}$$

$$\cos\delta = J_0(B) + 2J_2(B)\cos(\omega t) \tag{3.154}$$

The intensity can then be rewritten as

$$\begin{aligned} I(t) = I\{&I_0 + I_s[(J_0(B) + 2J_2(B)\cos(\omega t))\sin\delta_0 + 2J_1(B)\sin(\omega t)\cos\delta_0] \\ &+I_c[(J_0(B) + 2J_2(B)\cos(\omega t))\cos\delta_0 - 2J_1(B)\sin(\omega t)\sin\delta_0]\} \end{aligned} \tag{3.155}$$

Although lengthier that Eq. (3.141) the sine and cosine terms are now simplified and will be of assistance for the forthcoming steps. The detected signal can also be written in terms of its harmonic components

$$S(t) = S_0 + S_1 e^{i\omega t} + S_2 e^{2i\omega t} + ... \tag{3.156}$$

where the S_0-S_2 are the coefficients of the first three harmonics. Comparing Eq. (3.155) with Eq. (3.156) these coefficients are equal to

$$S_0 = I[I_0 + J_0(B)(I_s \sin\delta_0 + I_c \cos\delta_0)] \tag{3.157}$$

$$S_1 = I[2J_1(B)(I_s \cos\delta_0 - I_c \sin\delta_0)] \tag{3.158}$$

$$S_2 = I[2J_2(B)(I_c \cos\delta_0 + I_s \sin\delta_0)] \tag{3.159}$$

We can see that the triplet $\{S_0, S_1, S_2\}$ is enough for the determination of the coefficients $\{I_0, I_s, I_c\}$. This is why the higher harmonic terms were omitted in Eq. (3.156). We can further normalise S_1 and S_2

$$S_\omega \equiv \frac{S_1}{S_0} \tag{3.160}$$

$$S_{2\omega} \equiv \frac{S_2}{S_0} \tag{3.161}$$

Finally, we can substitute the above expressions to Eq. (3.157)-(3.159) and solve them to find I_s and I_c

$$I_s = \frac{J_2(B)S_\omega \cos\delta_0 + J_1(B)S_{2\omega}\sin\delta_0}{J_1(B)(2J_2(B) - J_0(B)S_{2\omega})} \tag{3.162}$$

$$I_c = \frac{J_1(B)S_{2\omega}\cos\delta_0 - J_2(B)S_\omega \sin\delta_0}{J_1(B)(2J_2(B) - J_0(B)S_{2\omega})} \tag{3.163}$$

Consequently, the determination of the ellipsometric angles from the detected signal can be summarized in the following way: $\{S_0, S_1, S_2\} \xrightarrow[(3.160),(3.161)]{Eq.} \{S_\omega, S_{2\omega}\} \xrightarrow[(3.162),(3.163)]{Eq.} \{I_s, I_c\} \xrightarrow[(3.143),(3.144)]{Eq.} \{\Psi, \Delta\}$.

References

[1] M. Noginov, M. Lapine, V. Podolskiy, and Y. Kivshar, "Focus issue: hyperbolic metamaterials," *Opt. Express*, vol. **21**, pp. 14 895–14 897, (2013).

[2] Z. Jacob, I. Smolyaninov, and E. Narimanov, "Broadband purcell effect: radiative decay engineering with metamaterials," *Appl. Phys. Lett.*, vol. **100**, p. 181105, (2012).

[3] J. Li, L. Fok, X. Yin, G. Bartal, and X. Zhang, "Experimental demonstration of an acoustic magnifying hyperlens," *Nature Mater.*, vol. **8**, pp. 931–934, (2009).

[4] S. A. Biehs, M. Tschikin, and P. Ben-Abdallah, "Hyperbolic metamaterials as an analog of a blackbody in the near field," *Phys. Rev. Lett.*, vol. **109**, p. 104301, (2012).

[5] I. I. Smolyaninov, Y.-J. Hung, and E. Hwang, "Experimental modeling of cosmological inflation with metamaterials," *Phys. Lett. A.*, vol. **376**, pp. 2575–2579, (2012).

[6] I. I. Smolyaninov and A. V. Kildishev, "Light propagation through random hyperbolic media: from a pile of sand to large scale

structure of present day universe," (2012). [Online]. Available: http://arXiv.org/abs/1202.1993

[7] Z. Liu, H. Lee, Y. Xiong, C. Sun, and X. Zhang, "Far-field optical hyperlens magnifying sub-diffraction-limited objects," *Science*, vol. **315**, p. 1686, (2007).

[8] S. Ishii, A. V. Kildishev, E. Narimanov, V. M. Shalaev, and V. P. Drachev, "Sub-wavelength interference pattern from volume plasmon polaritons in a hyperbolic medium," *Las. Photon. Rev.*, vol. **7**, pp. 265–271, (2013).

[9] J. Rho, Z. Ye, Y. Xiong, X. Yin, Z. Liu, H. Choi, G. Bartal, and X. Zhang, "Spherical hyperlens for two-dimensional sub-diffractional imaging at visible frequencies," *Nat. Commun.*, vol. **1**, p. 143, (2010).

[10] D. R. Smith, D. Schurig, J. J. Mock, P. Kolinko, and P. Rye, "Partial focusing of radiation by a slab of indefinite media," *Appl. Phys. Lett.*, vol. **84**, pp. 2244–2246, (2004).

[11] K. G. Balmain, A. A. Lüttgen, and P. C. Kremer, "Resonance cone formation, reflection, refraction, and focusing in a planar anisotropic metamaterial," *IEEE Ant. Wireless Propag. Lett.*, vol. **1**, pp. 146–149, (2002).

[12] G. Boisde and A. Harmer, *Chemical and Biochemical Sensing with Optical Fibers*. Arthech House, (1996).

[13] J. N. Anker, W. P. Hall, O. Lyandres, N. C. Shah, J. Zhao, and R. P. V. Duyne, "Biosensing with plasmonic nanosensors," *Nat. Mat.*, vol. **7**, pp. 442–453, (2008).

[14] A. V. Kabashin, P. Evans, S. Pastkovsky, W. Hendren, G. A. Wurtz, R. Atkinson, R. Pollard, V. A. Podolskiy, and A. V. Zayats, "Plasmonic nanorod metamaterials for biosensing," *Nat. Mat.*, vol. **8**, pp. 867–871, (2009).

[15] T. Tumkur, G. Zhu, P. Black, Y. A. Barnakov, C. E. Bonner, and M. A. Noginov, "Control of spontaneous emission in a volume of functionalized hyperbolic metamaterial," *Appl. Phys. Lett.*, vol. **99**, p. 151115, (2011).

[16] X. Yang, J. Yao, J. Rho, X. Yin, and X. Zhang, "Experimental realization of three-dimensional indefinite cavities at the nanoscale with anomalous scaling laws," *Nature Photon.*, vol. **6**, pp. 450–454, (2012).

[17] H. N. S. Krishnamoorthy, Z. Jacob, E. Narimanov, I. Kretzschmar, and V. M. Menon, "Topological transitions in metamaterials," *Science*, vol. **336**, pp. 205–209, (2012).

[18] B. Toal, M. McMillen, A. Murphy, W. Hendren, R. Atkinson, and R. Polland, "Tuneable magneto-optical metamaterials based on photonic resonances in nickel nanorod arrays," *Mat. Res. Express*, vol. **1**, p. 015801, (2014).

[19] G. A. Wurtz, R. Polland, W. Hendren, G. P. Wiederrecht, D. J. Gosztola, V. A. Podolskiy, and A. V. Zayats, "Designed ultrafast optical nonlinearity in a plasmonic nanorod metamaterial enhanced by nonlocality," *Nature Nano.*, vol. **6**, pp. 107–111, (2011).

[20] P. G. Sheasby and R. Pinner, *The Surface Treatment and Finishing of Aluminum and its Alloys.* ASM International, (2001).

[21] A. Huczko, "Template-based synthesis of nanomaterials," *Appl. Phys. A*, vol. **70**, pp. 365–376, (2000).

[22] G. Sauer, G. Brehm, S. Schneider, K. Nielsch, R. B. Wehrspohn, J. Choi, H. Hofmeister, and U. Gosele, "Highly ordered monocrystalline silver nanowire arrays," *J. Appl. Phys.*, vol. **91**, pp. 3243–3247, (2002).

[23] M. Hernández-Vélez, "Nanowires and 1D arrays fabrication: An overview," *Thin Solid Films*, vol. **495**, pp. 51–63, (2006).

[24] O. Jessensky, F. Muller, and U. Gosele, "Self-organized formation of hexagonal pore arrays in anodic alumina," *Appl. Phys. Lett.*, vol. **72**, pp. 1173–1175, (1998).

[25] B. Lu, S. Bharathulwar, D. E. Laughlin, and D. N. Lambeth, "Time and orientation dependence of ordering in anodized aluminum for self-organized magnetic arrays," *J. Appl. Phys.*, vol. **87**, pp. 4721–4723, (2000).

[26] A. P. Li, F. Muller, A. Birner, K. Nielsch, and U. Gosele, "Hexagonal pore arrays with a 50–420 nm interpore distance formed by self-organization in anodic alumina," *J. Appl. Phys.*, vol. **84**, pp. 6023–6026, (1998).

[27] N. W. Liu, A. Datta, C. Y. Liu, and Y. L. Wang, "High-speed focused-ion-beam patterning for guiding the growth of anodic alumina nanochannel arrays," *Appl. Phys. Lett.*, vol. **82**, pp. 1281–1283, (2003).

[28] H. Masuda, H. Yamada, M. Satoh, H. Asoh, M. Nakao, and T. Tamamura, "Highly ordered nanochannel-array architecture in anodic alumina," *Appl. Phys. Lett.*, vol. **71**, pp. 2770–2772, (1997).

[29] H. Masuda, Y. Matsui, M. Yotsuya, F. Matsumoto, and K. Nishio, "Fabrication of highly ordered anodic porous alumina using self-organized polystyrene particle array," *Chem. Lett.*, vol. **33**, pp. 584–585, (2004).

[30] S. Visnovský, *Optics in Magnetic Multilayers and Nanostructures.* Taylor & Francis Group, (2006).

[31] F. Abelès, "Recherches sur la propagation des ondes electromagnetiques sinusoidales dans les milieux stratifies," *Ann. Phys.*, vol. **5**, pp. 596–640, (1950).

[32] W. N. Hansen, "Electric fields produced by the propagation of plane coherent electromagnetic radiation in a stratified medium," *Opt. Soc. of America*, vol. **58**, pp. 380–390, (1968).

[33] S. Ekgasit, C. Thammacharoen, and W. Knoll, "Surface plasmon resonance spectroscopy based on evanescent field treatment," *Anal. Chem.*, vol. **76**, pp. 561–568, (2004).

[34] J. C. M. Garnett, "Colours in metal glasses, in metallic films, and in metallic solutions," *Philos. Trans. R. Soc.*, vol. **203**, pp. 385–420, (1904).

[35] D. A. G. Bruggeman, "Berechnung verschiedener physikalischer konstanten von heterogenen substanzen," *Ann. Phys. (Leipz.)*, vol. **24**, pp. 636–679, (1935).

[36] C. F. Bohren and D. R. Huffman, *Absorption and Scattering of Light by Small Particles.* Wiley & Sons, (1983).

[37] L. D. Landau and E. M. Lifshitz, *Electrodynamics of Continuous Media.* Pergamon Press, (1984).

[38] O. D. Kellogg, *Foundations of Potential Theory.* Dover Publications, (1953).

[39] J. Elser, R. Wangberg, V. A. Podolskiy, and E. E. Narimanov, "Nanowire metamaterials with extreme optical anisotropy," *Appl. Phys. Lett.*, vol. **89**, p. 261102, (2006).

[40] P. B. Johnson and R. W. Christy, "Optical constants of the noble metals," *Phys. Rev. B*, vol. **6**, pp. 4370–4379, (1972).

[41] J. D. Jackson, *Classical Electrodynamics*. Wiley & Sons, (1999).

[42] C. A. Balanis, *Advanced Engineering Electromagnetics*. Wiley & Sons, (2012).

[43] A. W. Snyder and J. D. Love, *Optical Waveguide Theory*. Chapman & Hall, (1983).

[44] H. Fujiwara, *Spectroscopic Ellipsometry: Principles and Applications*. Wiley & Sons, (2007).

[45] H. G. Tompkins and E. A. Irene, *Handbook of Ellipsometry*. William Andrew, (2005).

[46] P. Drude, *Ann. Phys.*, vol. **32**, p. 584, (1887).

[47] A. Rothen, "The ellipsometer, an apparatus to measure thicknesses of thin surface films," *Rev. Sci. Instrum.*, vol. **16**, pp. 26–30, (1945).

[48] W. Paik and J. O. Bockris, "Exact ellipsometric measurement of thickness and optical properties of a thin light-absorbing film without auxiliary measurements," *Surf. Sci.*, vol. **28**, pp. 61–68, (1971).

[49] D. E. Aspnes and A. A. Studna, "High precision scanning ellipsometer," *Appl. Opt.*, vol. **14**, pp. 220–228, (1975).

[50] R. H. Muller and J. C. Farmer, "Fast, self-compensating spectral-scanning ellipsometer," *Rev. Sci. Instrum.*, vol. **55**, pp. 371–374, (1984).

[51] H. G. Tompkins and W. A. McGahan, *Spectroscopic Ellipsometry and Reflectometry: A User's Guide.* Wiley & Sons, (1999).

[52] R. M. A. Azzam and N. M. Bashara, *Ellipsometry and Polarized Light.* North-Holland, (1977).

[53] R. W. Collins and Y. T. Kim, "Ellipsometry for thin-film and surface analysis," *Anal. Chem.*, vol. **62**, pp. 431–442, (1990).

[54] Q. Zhan and J. R. Leger, "High-resolution imaging ellipsometer," *Appl. Opt.*, vol. **41**, pp. 4443–4450, (2002).

[55] C. E. Giacomelli, M. J. Esplandiú, P. I. Ortiz, M. J. Avena, and C. P. D. Pauli, "Ellipsometric study of bovine serum albumin adsorbed onto Ti/TiO_2 electrodes," *J. Coll. Int. Sci.*, vol. **218**, pp. 404–411, (1999).

[56] S. M. Ma, D. L. Coleman, and J. D. Andrade, "Ellipsometry studies of albumin films on tantalum oxide and SiO_2," *Surf. Sci.*, vol. **56**, pp. 117–125, (1976).

[57] B. Lassen and M. Malmsten, "Competitive protein adsorption at plasma polymer surfaces," *J. Coll. Int. Sci.*, vol. **186**, pp. 9–16, (1997).

[58] H. Arwin, S. Welin-Klintström, and R. Jansson, "Off-null ellipsometry revisited: basic considerations for measuring surface concentrations at solid/liquid interfaces," *J. Coll. Int. Sci.*, vol. **156**, pp. 377–382, (1993).

[59] T. E. Tiwald, D. W. Thompson, J. A. Woollam, and S. V. Pepper, "Determination of the mid-ir optical constants of water and lubricants

using ir ellipsometry combined with an ATR cell," *Thin Solid Films*, vol. **313–314**, pp. 718–721, (1998).

[60] R. S. Moirangthem, Y. C. Chang, and P. K. Wei, "Local plasmonic resonance based biosensor for investigating dna hybridization using ellipsometry," in *Proc. SPIE 7757, Plasmonics: Metallic Nanostructures and Their Optical Properties VIII*, Aug. 2010. [Online]. Available: http://dx.doi.org/10.1117/12.862921

[61] R. M. Ostroff, D. Maul, G. R. Bogart, S. Yang, J. Christian, D. Hopkins, D. Clark, B. Trotter, and G. Moddel, "Fixed polarizer ellipsometry for simple and sensitive detection of thin films generated by specific molecular interactions: applications in immunoassays and DNA sequence detection," *Clin. Chem.*, vol. **44**, pp. 2031–2035, (1998).

[62] R. M. Ostroff, D. Hopkins, A. B. Haeberli, W. Baouchi, and B. Polisky, "Thin film biosensor for rapid visual detection of nucleic acid targets," *Clin. Chem.*, vol. **45**, pp. 1659–1664, (1999).

[63] W. Chegal, Y. J. Cho, H. J. Kim, H. M. Cho, Y. W. Lee, and S. H. Kim, "A new spectral imaging ellipsometer for measuring the thickness of patterned thin films," *J. J. of Appl. Phys.*, vol. **43**, pp. 6475–6476, (2004).

[64] U. Wurstbauer, C. Röling, U. Wurstbauer, W. Wegscheider, M. Vaupel, P. H. Thiesen, and D. Weiss, "Imaging ellipsometry of graphene," *Appl. Phys. Lett.*, vol. **97**, p. 231901, (2010).

[65] H. G. Tompkins, *A User's Guide to Ellipsometry.* Academic Press, (1993).

[66] W. Spottiswoode, *Polarisation of Light.* Macmillan & Co., (1874).

[67] E. Mach, *The Principles of Physical Optics.* Dover Publications, (1926).

[68] D. Brewster, *Treatise on Optics.* Longman, Rees, Orme, Brown and Green, (1831).

[69] W. Nicol, *Edinb. New Phil. J.*, vol. **6**, p. 83, (1828), as quoted in A. Johannsen, *Manual of Petrographic Methods*, Hafner, New York, 1968.

[70] P. Glan, *Carl's Report*, vol. **16**, p. 570, (1880).

[71] S. P. Thompson, *Phil. Mag.*, vol. **12**, p. 349, (1881).

[72] A. A. Kokhanovsky, *Light Scattering Reviews 4.* Springer, (2009).

[73] F. Moreno and F. Gonzalez, Eds., *Light Scattering from Microstructures.* Springer, (1998).

[74] S. N. Jasperson and S. E. Schnatterly, "An improved method for high reflectivity ellipsometry based on a new polarization modulation technique," *Rev. Sci. Instrum.*, vol. **40**, pp. 761–767, (1969).

[75] G. E. Jellison and F. A. Modine, "Optical constants for silicon at 300 and 10 K determined from 1.64 to 4.70 eV by ellipsometry," *J. Appl. Phys.*, vol. **53**, pp. 3745–3753, (1982).

[76] O. Acher, E. Bigan, and B. Drèvillion, "Improvements on phase modulation ellipsometry," *Rev. Sci. Instrum.*, vol. **60**, pp. 65–77, (1989).

[77] V. M. Bermudez and H. Ritz, "Wavelength-scanning polarization-modulation ellipsometry: some practical considerations," *Appl. Opt.*, vol. **17**, pp. 542–552, (1978).

[78] S. N. Jasperson, D. K. Burge, and R. C. O'Handley, "A modulated ellipsometer for studying thin film optical properties and surface dynamics," *Surf. Sci.*, vol. **37**, pp. 548–558, (1973).

Chapter 4

Designing guided modes of hyperbolic metamaterial slab waveguides

Hyperbolic metamaterials comprised of an array of plasmonic nanorods provide a unique platform for designing optical sensors and integrating nonlinear and active nanophotonic functionalities. In this work, the waveguiding properties and mode structure of planar anisotropic metamaterial waveguides are characterized experimentally and theoretically. While ordinary modes are typical guided modes of the highly-anisotropic waveguides, the extraordinary modes below the effective plasma frequency, exist in a hyperbolic metamaterial slab in the form of bulk plasmon-polaritons, in analogy to planar-cavity exciton-polaritons in semiconductors. They may have very low or negative group velocity with high effective refractive indices (up to 5) and have an unusual cut-off from the high-frequency side, providing a deep-subwavelength ($\lambda_0/6 - \lambda_0/8$ waveguide thickness) single mode guiding. These properties, dictated by the hyperbolic anisotropy of the metamaterial, may be tuned by

altering the geometrical parameters of the nanorod composite.

4.1 Introduction

Light interacts with a resonant medium by forming polaritonic waves. These are mixed excitations of the electromagnetic field (photons) with quasiparticles related to material resonances. These quasiparticles include phonons, excitons in semiconductors and plasmons in conductors [1] or atomic ensembles [2]. Exciton-polaritons are the most intensely studied having numerous applications in semiconductor lasers [3–6]. When electromagnetic fields propagate in resonant media, polaritonic waves are formed and their behaviour is governed by a specific dispersion determined by the material resonances and around which negative permittivity can be observed [1]. Both phonon-polariton and exciton-polariton can exist in bulk of the material and at the interface between their material and the adjacent medium as surface electromagnetic waves (surface polaritons). On the other hand, at frequencies lower than the electron plasma frequency, only surface plasmon polaritons (SPPs) have usually been considered, since electric fields do not significantly penetrate metals over more than the skin-depth [7].

In this Chapter, the behaviour of bulk plasmon-polaritons in a planar slab of metamaterial is studied both experimentally and theoretically. In a microscopic consideration of the plasmonic nanorod metamaterial studied here, these bulk plasmon polaritons arise from interacting cylindrical surface plasmons (CSP) supported by individual nanorods forming the metamaterial [8], but can also be observed in multi-layered metal-dielectric-metal metamaterials, where they arise from interacting smooth-film SPP modes [9–11]. It is found that such extraordinary modes exhibit low or negative

group velocity and low group velocity dispersion (GVD). Furthermore, a peculiar high-frequency cut-off for transverse magnetic (TM) polarized modes allows subwavelength single mode guiding with $\lambda_0/6 - \lambda_0/8$ waveguide thickness, in contrast to ordinary, transverse electric (TE) modes which behave as the mode of conventional transparent dielectric waveguide. Bulk plasmon-polaritons of an anisotropic plasmonic metamaterial slab can be considered in analogy to the exciton-polaritons in a semiconductor cavity. Such electromagnetic modes can be tailored by controlling the geometry of the metamaterial design, and their properties can be utilized in applications requiring sensitive control of both group and phase velocity dispersion such as waveguides [12], sensors [13] or nonlinear optical devices [14]. For example, decreasing group velocity, a phenomenon known as slow light, light-matter interaction can be enhanced in photonic crystal waveguides [15] greatly increasing sensitivity. Yet more applications can be found in communication networks where information is encoded with pulses. Network buffering, data synchronization and pattern correlation require pulse delays in a tunable environment that can be achieved via the manipulation of group velocity [16].

Plasmonic nanorod metamaterials possess unique optical properties [2] making them unrivalled for applications in imaging [17], sensing [18, 19], ultrasound detection [20], designing nonlinear optical properties [14, 21, 22] and controlling quantum optical processes [23, 24]. These metamaterials exhibit hyperbolic isofrequency surfaces in a spectral range where the real part of the diagonal components of the permittivity tensor, corresponding to ordinary and extraordinary axis, have opposite signs (read Section 3.1). We consider a planar metamaterial waveguide formed by a finite thickness slab of aligned Au nanorods as depicted in Fig. 4.1(a). The anisotropic geometry can be expressed through the Maxwell-Garnet (MG) approximation [25] as explained

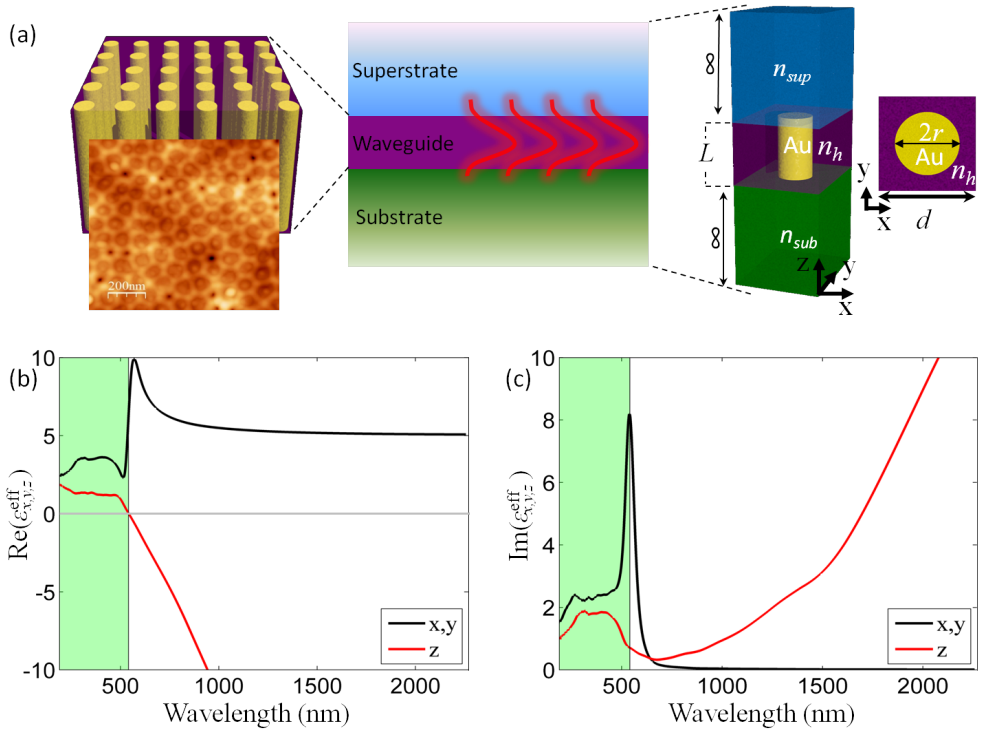

Figure 4.1: (a) Schematics of the planar metamaterial waveguide geometry consisting of an array of Au nanorods. Left: Schematic of the metamaterial's internal structure and top-view atomic force microscopy image of the metamaterial used in the experiment (topography variations is less than 10 nm). Center: effective medium representation of the metamaterial slab placed between a semi-infinite substrate (n_{sub}) and a superstrate (n_{sup}). Right: geometry and cross-section of the unit cell of the metamaterial used in the numerical simulations. (b) Real and (c) imaginary part of the effective permittivity of a Au nanorod metamaterial along different crystallographic directions for $p = 0.32$ and $\varepsilon_h = 2.56$. Marked regions show the spectral range over which hyperbolic dispersion of the metamaterial occurs.

in Section 3.5 leading to Eq. (3.136)-(3.137). For the purposes of this Chapter, it is more convenient to write the previous expressions in a more compact form as follows

$$\varepsilon_{x,y}^{eff} = \frac{p\varepsilon_{Au}\varepsilon_h + \varepsilon_h(1-p)\tilde{\varepsilon}}{p\varepsilon_h + (1-p)\tilde{\varepsilon}} \tag{4.1}$$

$$\varepsilon_z^{eff} = p\varepsilon_{Au} + (1-p)\varepsilon_h \tag{4.2}$$

where the embedding medium is porous alumina (AAO) of permittivity $\varepsilon_h = 2.56$ while nanorods are made of Au and have permittivity ε_{Au} [26]. Here $p = \pi(r/d)^2$ defines the nanorod filling factor, with d being the period of the array, r is the nanorod radius and $\tilde{\varepsilon} = (\varepsilon_{Au} + \varepsilon_h)/2$.

Depending on the geometrical parameters of the metamaterial and the wavelength range, either elliptical, with $Re(\varepsilon_{x,y}^{eff}) > 0$ and $Re(\varepsilon_z^{eff}) > 0$, or hyperbolic, with $Re(\varepsilon_{x,y}^{eff}) > 0$ and $Re(\varepsilon_z^{eff}) < 0$, dispersion can be achieved as shown in Fig. 4.1(b). By adjusting the filling factor, hyperbolic dispersion can be achieved throughout the visible and near-IR spectral ranges. For instance, for a low filling factor of $p = 0.03$ hyperbolic dispersion occurs above 1310 nm, while for a high filling factor of $p = 0.5$ it occurs above 500 nm. The spectral dispersion of the imaginary part of the permittivities follow the expected dispersive behaviour for a resonant dielectric and an electron plasma behaviour along x, y- and z- directions, respectively (Fig. 4.1(c)).

Let us introduce the effective plasma frequency of the metamaterial, for the characterization of the metal-like behaviour for TM-polarized field, via the free-electron Drude model [27] satisfying the condition $Re(\varepsilon_z^{eff}(\omega_p^{eff})) = 0$. Using effective medium parameters (Eq. (4.1), (4.2)), the effective plasma frequency can be derived as $Re(\varepsilon_{Au}(\omega_p^{eff})) = (1 - p^{-1})\varepsilon_h$. This expression can be simplified for the Drude-like permittivity of Au given by $\varepsilon_{Drude} = \varepsilon_\infty^{eff} - (\omega_p/\omega_p^{eff})^2$, where ε_∞^{eff} is the high frequency background (here $\varepsilon_\infty^{eff} = 6$) and ω_p is the free-electron plasma frequency of Au, leading to

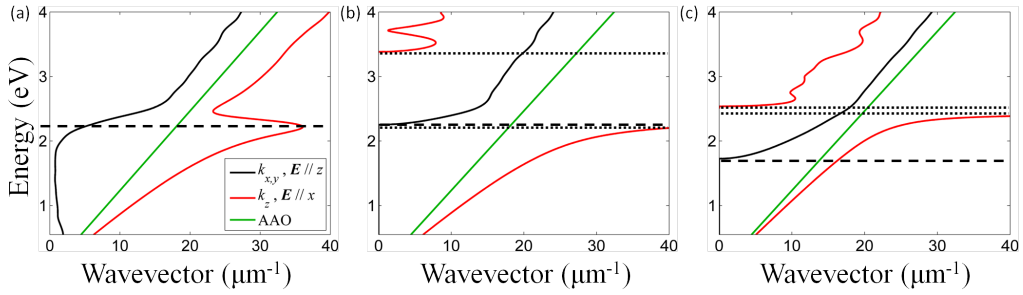

Figure 4.2: Dispersion of plasmon-polaritons in an infinite Au nanorod metamaterial along the ordinary (x, y) and extraordinary (z) directions: (a) the metamaterial parameters are as in Fig. 4.1, (b) the same as in (a) but with losses artificially reduces 100 times to show the asymptotic behaviour, (c) the same as in (b) but for $p = 0.13$. The light-line in AAO (green line) is also shown. The dashed line shows the effective plasma frequency for extraordinary waves. The EVL regime takes place between the dotted lines. Legend in (a) is the same for (b) and (c) as well. Dispersions are from MG approximation.

$$\omega_p^{eff} = \frac{\omega_p}{\sqrt{\varepsilon_\infty^{eff} + (p^{-1} - 1)\varepsilon_h}} \tag{4.3}$$

The aforementioned expression shows that the metamaterial's effective plasma frequency can be tuned by controlling the filling factor of nanorods, p, and the permittivity of the host medium, ε_h.

In the case of a spatially infinite anisotropic material, invariant in the z-direction, the electromagnetic wave dispersion can be plotted for both ordinary and extraordinary waves (read Section 3.2). For the ordinary scenario, applying Eq. (3.23) with $\theta = 90°$ we immediately get $n_{eff} = n_z^{eff}$ meaning that $k_{x,y} = k_0\sqrt{\varepsilon_{x,y}^{eff}}$, where k_0 is the wavevector of free space. Similarly for the extraordinary case, we have $\theta = 0°$ leading to $k_z = k_0\sqrt{\varepsilon_z^{eff}}$. Fig. 4.2(a) depicts the aforementioned wavevectors for an infinite Au nanorod metamaterial with $p = 0.32$. As expected, the ordinary wave has typical dispersion for

transparent dielectric lying to the right of the light-line in the AAO matrix since the effective refractive index is increased due to the presence of metal, with the resonance, the so-called epsilon-very-large (EVL) regime [28, 29], determined by the CSP excitation [8]. At the same time, the dispersion of extraordinary waves is that of a typical metal with an effective plasma frequency $\omega_p^{eff} = 2.2$ eV corresponding to the metamaterial's transition from the elliptic to the hyperbolic regime. It is instructive to consider a "gedanken" situation with reduced losses in Au that allows the nature of the dispersion properties of ordinary and extraordinary waves to be clearly revealed (Fig. 4.2(b)). In the low-loss case, there is a range of frequencies where $\varepsilon_{x,y}^{eff} < 0$ in the previously discussed EVL regime, where a bandgap opens in the TE-mode dispersion. This TE-mode bandgap and the effective plasma frequency for the TM mode can be tuned with the geometry of the metamaterial realization. While for low nanorod filling factor, at least one of the mode is always present and the metamaterial behaves either as an elliptic or as an hyperbolic medium, for higher filling factors ($p > 0.28$) and low loss, metallic behaviour can be observed in the frequency range where all diagonal components of the effective permittivity tensor are negative simultaneously, $\varepsilon_{x,y}^{eff} < 0$ and $\varepsilon_z^{eff} < 0$, resulting in the disappearance of bulk modes (Fig. 4.2(c)). This regime, however, takes place in the wavelength range and for loss parameters where nonlocal, spatial dispersion effects occur and that requires a different theoretical treatment [8, 30]. The propagation of extraordinary waves, in which electric field is solely polarized along the long axis of the rods, is prohibited below the effective plasma frequency (hyperbolic regime), as is expected for conductors. However, as a result of the anisotropy of the metamaterial, electrons plasma oscillation may still give rise to bulk plasmon-polaritons propagating in the metamaterial below the plasma frequency in directions

determined by the dispersion relation $k_x^2/\varepsilon_z^{eff} + k_y^2/\varepsilon_z^{eff} + k_z^2/\varepsilon_{x,y}^{eff} = (\omega/c_0)^2$, with c_0 being the speed of light.

4.2 Mode structure of a metamaterial slab

The modes supported by a metamaterial slab, when one (z-) dimension is taken to be finite, were studied for a metamaterial slab placed on a silica substrate ($n_{sub} = 1.5$) and with air as a superstrate ($n_{sup} = 1$). The slab

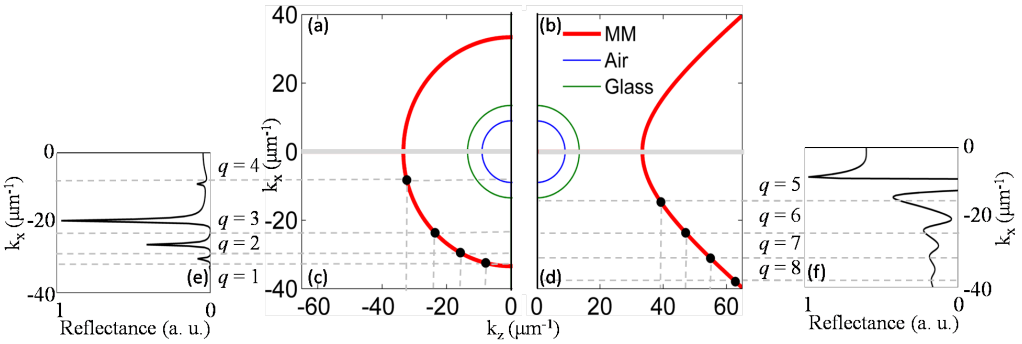

Figure 4.3: (a),(b) Isofrequency contours in the first Brillouin zone calculated for a frequency corresponding to a free-space wavelength $\lambda_0 = 700$ nm for an infinite Au nanorod metamaterial with $p = 0.5$ for (a) ordinary, TE, and (b) extraordinary, TM, modes. In the elliptic regime (a), the dispersion is bounded and corresponds to that of a typical anisotropic dielectric. The isofrequencies contours in superstrate (air) and substrate (glass) are also shown. (c),(d) The mode position of a metamaterial slab (400 nm thickness) shown as the dots corresponding to intersection of the isofrequency contours of the infinite metamaterial and the quantized values of $k_z = q(\pi/L)$, where $q = \pm 1, \pm 2, \pm 3, ...$ resulting from the finite size of the slab in the z-direction. (e),(f) Angular spectra of reflectance of the metamaterial slab as in (c),(d) for $\lambda_0 = 700$ nm calculated using TMM. The position of the modes obtained analytically is shifted to higher wavevectors due to the analytic model assumptions, influencing confinement of the modes.

geometry quantizes the z-component of the wavevector of the infinite metamaterial to values determined by the mode order and slab thickness, such as $k_z = q(\pi/L)$ [31]. This practically means the modal behaviour at a given frequency will be determined by the wavevectors satisfying both quantization condition and bulk metamaterial dispersion. To illustrate this, Fig. 4.3 depicts the infinite and finite slab (400 nm thickness) isofrequency contours for a free space wavelength of $\lambda_0 = 700$ nm and 0.5 filling factor. The isofrequency contours of the metamaterial dispersion for TE (elliptic), Fig. 4.3(a), (c), and TM (hyperbolic), Fig. 4.3(b), (d), modes show striking difference in allowed wavevector ranges at the same frequency, which determines dissimilar behaviour of these modes in both the infinite metamaterial as well as in a metamaterial slab. Concerning the finite slab scenario (Fig. 4.3(c), (d)), these solutions have an x-component $k_x(k_z, q)$ of the wavevector associated to each solution k_z corresponding to the propagation constant $\beta = k_x(k_z, q)$ of mode q in the slab. In this instance, the elliptic dispersion allows for one unbound mode with the solutions for the propagation constant within the isofrequency contour in superstrate and substrate, as well as three waveguided modes. The hyperbolic dispersion allows modes with $q \geq 5$, with limits eventually imposed by both losses and the geometry of the nanorod composite as the EMT breaks down for wavevectors near the boundary of the Brillouin zone. For the considered example (Fig. 4.3(d)), the modes are present both within the light lines (Fabry-Perot modes) and confined to the metamaterial (waveguided modes). The reflectance corresponding to the isofrequency contours and the mode quantization in the finite size slab is in a good agreement with the TMM simulations giving the same number of modes with a small discrepancy in their positions due to the overestimated mode confinement in the analytical simulations (approximated boundary conditions) as shown in

Fig. 4.3(e), (f).

Using TMM, the mode dispersion of a typical planar waveguide with thickness of 400 nm made of metamaterial comprised with 100 nm period and 40 nm radius nanorods was calculated via the evaluation of angular re-

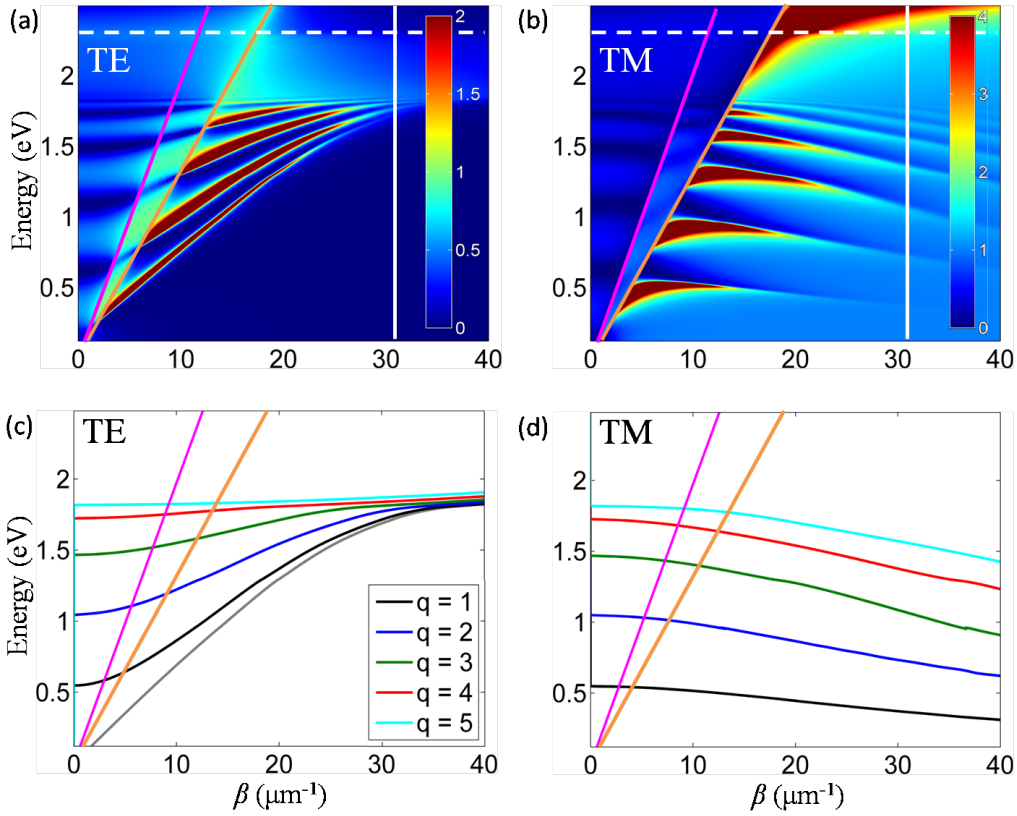

Figure 4.4: Hyperbolic waveguide dispersion depicting the first five modes ($q = 1 - 5$). The waveguide thickness is 400 nm with 100 nm period and 40 nm radius. TMM model for TE- (a) and TM-polarization (b). The dashed line indicates the effective plasma frequency. The vertical line corresponds to the first Brillouin zone limit of the metamaterial realization when considering a square lattice of nanorods. Analytic model for TE- (c) and TM-polarization (d). The air (magenta) and glass (orange) light lines are shown in all graphs. The grey line in (c) corresponds to the metamaterial light line.

solved reflection spectra (Fig. 4.4(a), (b)). The rich families of modes have been observed for both TE and TM-polarizations with distinctively different behaviour. The modes in the reflection dispersion correspond to the reflectance minima where incident light is coupled to the modes. The complex mode structure of the slab emerges as a consequence of spatial confinement of plasmon-polaritons in the slab and is associated with both cavity resonances and waveguided modes, above and below the light line in air, respectively. In the cavity regime, the TM-polarized dispersion reveals discrete modes with very low or negative group velocity. These unbound modes are not confined to the metamaterial slab, being accessible to plane waves in both the substrate and the superstrate. In this regime, the metamaterial slab simply acts as a Fabry-Perot (FP) cavity for bulk plasmon-polaritons resulting in the effects similar to those for cavity-polaritons in semiconductors. Between the light-lines in substrate and superstrate, the modes are coupled to radiating modes in the substrate (leaky modes), while being evanescent at the metamaterial/superstrate interface. Due to this coupling, the modes are "strongly bent" near the light lines and may have positive, negative, or vanishing values of the group velocity (Fig. 4.4(b)). The modes below the substrate-line are truly guided modes decaying exponentially in both substrate and superstrate. A similar analysis holds for the TE-polarized modes, but in this regime the metamaterial slab acts as a typical anisotropic dielectric waveguide due to the orientation of the electric field normal to the nanorod axes (ordinary direction) and does not support bulk plasmon-polaritons. The marked difference between TE and TM-modes is in the opposite sign of the group velocity. Neglecting a strongly dispersive behaviour in the vicinity of the light lines, the TM-modes always show either negative or vanishing group velocity (Fig. 4.4(b)) while the group velocity of the TE-modes is always positive (Fig.

4.4(a)).

In order to understand the observed mode structure, we adapted an analytic description of the dispersion of ordinary and extraordinary waves in a conventional anisotropic waveguide [32] to a hyperbolic metamaterial. Within this framework, a planar hyperbolic waveguide is considered in the xy-plane with phase-insensitive reflections at the metamaterial's boundaries. Given the 2D geometry of the waveguide, modes can be separated by TM- and TE-polarizations. The dispersions of TE and TM-guided modes can then be expressed as

$$\beta_{TE}^2 = Re(\varepsilon_{x,y}^{eff})k_0^2 - \left(\frac{q\pi}{L}\right)^2 \tag{4.4}$$

$$\beta_{TM}^2 = Re(\varepsilon_{z}^{eff})k_0^2 - \left(\frac{q\pi}{L}\right)^2 Re\left(\frac{\varepsilon_{z}^{eff}}{\varepsilon_{x,y}^{eff}}\right) \tag{4.5}$$

where β is the propagation constant for each polarization (i.e. $\beta = k_{x,y}$), q is a positive integer referring to the mode number and L is the thickness of the planar waveguide. To test the validity of Eq. (4.4) and (4.5), the first five ($q = 1 - 5$) waveguided modes are plotted in Fig. 4.4(c), (d) using the same geometry as in the TMM case. Comparing the analytical dispersions (Fig. 4.4(c), (d)) with the ones from TMM (Fig. 4.4(a), (b)) it is evident their very good agreement despite the assumptions.

At this point two limitations of the aforementioned models should be noted. a) In the epsilon near-zero (ENZ) regime, near the effective plasma frequency, a different treatment is needed to take into account non-local effects [8], and this case is not considered here. a) The effective permittivities extracted from Maxwell-Garnett approximation, are correct for the case of non-interacting nanorods (read Section 3.5). This practically means that any outcome that falls outside the first Brillouin zone (vertical line) cannot be

trusted unless it is compared with 3D numerical simulations.

Both TE and TM-guided mode dispersions are bound at a high-frequency side, converging, with the increasing mode number (q), to the effective plasma frequency of the metamaterial, above which bulk plasmon-polaritons do not exist. However, whilst TE-modes demonstrate conventional behaviour with a low-frequency cut-off determined by the mode order, the behaviour of the TM-modes is distinctly different. The TM-modes have a cut-off from the high-frequency side but no low-frequency cut-off with increasing propagation constant (β_{TM}), limited only by the metamaterial realization via the Brillouin zone. Thus, deep-subwavelength, hyperbolic metamaterial slabs may act as multimode waveguides, a behaviour that draws its origin in the inverse scaling law for hyperbolic metamaterial cavities [33].

Let us try to give a physical picture of group's velocity negative sign in hyperbolic media. It is known that group velocity is orthogonal to the isofrequency surfaces [34,35]. Due to the hyperbolic shape of the isofrequency, the z-components of the wavevector ($\mathbf{k}$) and group velocity ($\upsilon_{\mathbf{g}}$) will be anti-parallel (Fig. 4.5(a)) thus explaining the negative sign. Because the analytical model is in good agreement with the TMM, we can use Eq. (4.4) and (4.5) to mathematically investigate *why* the sign of group velocity changes between different polarizations. Since group velocity is given from $\upsilon_g = \partial\omega/\partial\beta$ we end up to the following expressions for each polarization

$$\upsilon_{gTE} = \frac{2\beta_{TE}}{\frac{\omega}{c_0^2}\left(\omega\frac{\partial\varepsilon_{x,y}^{eff}}{\partial\omega} + 2\varepsilon_{x,y}^{eff}\right)} \tag{4.6}$$

$$\upsilon_{gTM} = \frac{2\beta_{TM}}{\frac{2\omega}{c_0^2}\varepsilon_z^{eff} + \left(\frac{\omega}{c_0}\right)^2\frac{\partial\varepsilon_z^{eff}}{\partial\omega} + \left(\frac{q\pi}{L}\right)^2\frac{1}{\varepsilon_{x,y}^{eff}}\left(\frac{\varepsilon_z^{eff}}{\varepsilon_{x,y}^{eff}}\frac{\partial\varepsilon_x^{eff}}{\partial\omega} - \frac{\partial\varepsilon_z^{eff}}{\partial\omega}\right)} \tag{4.7}$$

The above expressions, especially for the TM-scenario, are complicated and

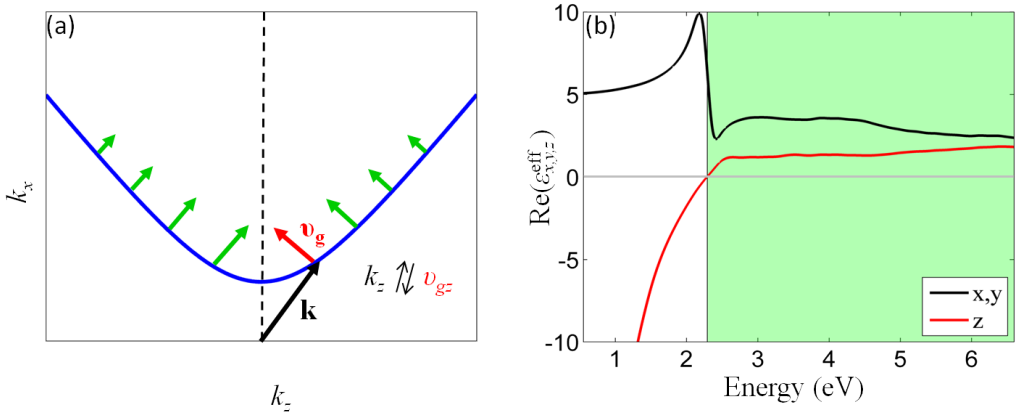

Figure 4.5: (a) Isofrequency diagram of a hyperbolic medium showing the sign difference between the z-components of the wavevector (black arrow) and group velocity (red arrow). The green arrows indicate group velocity at other points. Group velocity is proportional to the magnitude of arrows. (b) Real part of the effective permittivities for the inspection of group velocity. Filling factor is the same as in Fig. 4.1 ($p = 0.32$).

not very insightful at a first glance. It will be easier to interpret them if we examine the effective permittivities in terms of energy as demonstrated in Fig. 4.5(b). In the hyperbolic regime (white area) we have $\varepsilon^{eff}_{x,y} > 0$, $\varepsilon^{eff}_{z} < 0$ while the respective slopes are $\partial\varepsilon^{eff}_{x,y}/\partial\omega > 0$ and $\partial\varepsilon^{eff}_{z}/\partial\omega > 0$. Knowing these we immediately observe that Eq. (4.6) is always positive since the denominator cannot achieve negative values. For TM-polarization (Eq. (4.7)), all the denominator terms are negative apart from $(\omega/c)^2\partial\varepsilon^{eff}_{z}/\partial\omega$ which remains positive. However the negative terms are always greater than the positive one (in absolute values) as long as we remain in the hyperbolic regime and away from the resonance of $\varepsilon^{eff}_{x,y}$ located at the boundary between the elliptic and hyperbolic regimes. This gives us a mathematical explanation of the group velocity sign for each polarization. In the elliptic regime (green area) no general rule can be applied since both υ_{gTE} and υ_{gTM} can achieve

positive, negative or vanishing values. It is important to emphasize that for typical metamaterial geometries, the condition of negative group velocity is satisfied for all TM-mode orders (q) and any waveguide thickness (L).

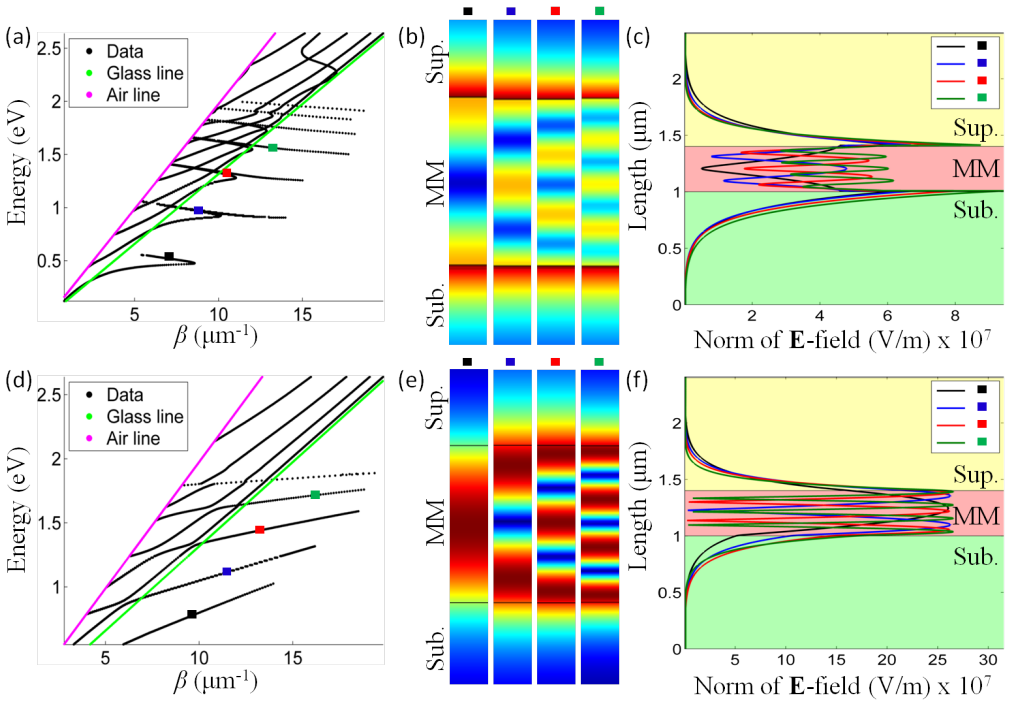

Figure 4.6: Eigenmode analysis for the 2D waveguide geometry of Fig. 4.9. (a),(d) Eigenmode simulations clearly showing the negative (positive) sign of group velocity for TM (TE) polarization. (b) Electric field distribution of the first four modes, marked with square in (a), and (c) the corresponding field cross-sections. (e),(f) Same as before but for TE-polarization. The magnitudes of the fields in (b) and (e) can be inspected from the field cross-sections as shown in (c) and (f), respectively.

To further support the aforementioned, eigenmode analysis was performed based on the structure of Fig. 4.4. The dispersion diagrams in Fig. 4.6(a), (d) clearly demonstrate the negative (positive) sign of group velocity for TM (TE) polarization. Fig. 4.6(b) and 4.6(c) depict the electric field distributions and the corresponding cross-sections of the first four ($q = 1 - 4$)

waveguided modes for TM-polarization. The same graphs, but this time for TE-polarization, are shown in Fig. 4.6(e), (f). As the mode number increases, the field distributions show an increasing number of maxima and minima (Fig. 4.6(b), (e)), which are typical of standing wave distributions inside the waveguide, as expected from the analytical calculations. Depending on the polarization, the waveguide acts either as a closed cavity with its field maximum close to the centre (TE-case) or as an open cavity with the field minimum at the centre (TM-case) of the slab waveguide. This is a direct consequence of boundary conditions due to the 1D confinement along the z-direction [31].

Taking into account the wavevector cut-off due to the metamaterial realization (the Brillouin zone) and the high-frequency cut-off of the TM modes, the wavelength range of around $2400 - 3100$ nm represents the single mode guiding regime for $p = 0.5$, corresponding to a waveguide thickness range of only $\lambda_0/6 - \lambda_0/8$. The energy confinement for the fundamental mode ($q = 1$) depends on operation frequency, but, when measured as the ratio between the power flow inside the waveguide to the total power flow of the mode, is on the order of 40% for an energy of 0.5 eV. This ratio increases for higher order modes, as TM-modes become increasingly confined to the waveguide. Numerical simulations show that losses for a given TM-mode number q reduce with increasing propagation constant. This behaviour is also captured through the analytical model showing its origin as from the complex interplay between the different components of the permittivity tensor (Fig. 4.1(b)) and the waveguide dimensions. For TE-modes, since normal modal dispersion is observed, losses increase with propagation constant. The dissipative nature of the hyperbolic waveguide results in increasing losses for higher order modes, as their confinement to the guide increases.

4.3 Non-monotonous shift of waveguided modes

A peculiar property of nanorod metamaterials in the hyperbolic regime is the non-monotonous change of the waveguided modes (leaky or purely waveguided) at increasing filling factors. To understand this phenomenon let us calculate the high cut-off frequency for the TM-polarization by solving Eq. (4.5)

$$\omega_{cut-off} = c_0 Re\left(\sqrt{\frac{\beta_{TM}^2}{\varepsilon_z^{eff}} + \left(\frac{q\pi}{L}\right)^2 \frac{1}{\varepsilon_{x,y}^{eff}}}\right) \tag{4.8}$$

so that for frequencies higher than $\omega_{cut-off}$, propagation along the hyperbolic slab waveguide for a given mode order q is prohibited as $\beta_{TM}^2 < 0$. To illustrate this, Fig. 4.7(a) shows the cut-off frequency dependence for the

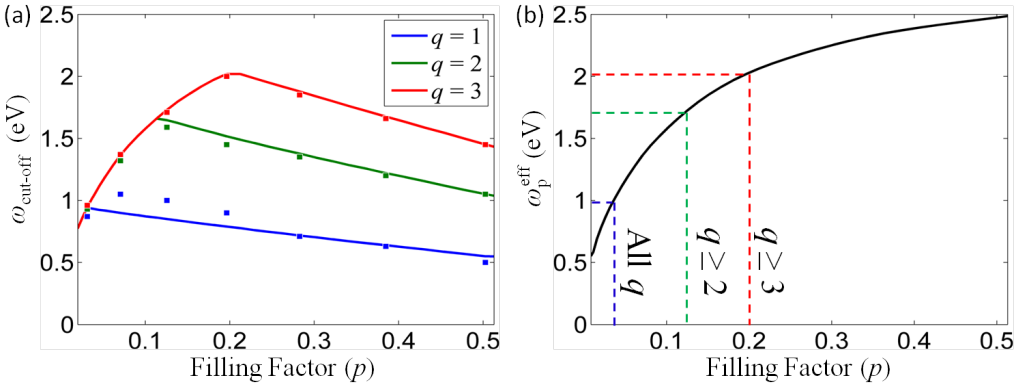

Figure 4.7: (a) The dependence of the high cut-off frequency TM-modes ($\omega_{cut-off}$) on nanorod filling factor, p, for $q = 1 - 3$ modes. The lines correspond to analytic model and squares to TMM simulations. (b) Effective plasma frequency, ω_p^{eff}, for the same filling factor range. The frequency threshold below which the effective plasma frequency determines mode cut-off is for $q \geq 3$ at $p = 0.2$, for $q \geq 2$ at $p = 0.13$, while for $p < 0.04$, the cut-off for all modes converges to the effective plasma frequency.

$q = 1 - 3$ TM-modes for various nanorod filling factors obtained analytically and with the TMM formalism. The mode cut-off frequency monotonously increases for $p > 0.2$ and then decreases for $p < 0.2$. The non-monotonous behaviour and, in particular, the decrease for smaller nanorod filling factors (smaller anisotropy of the metamaterial) is due to the decrease of the effective plasma frequency, ω_p^{eff}, which imposes the bound on the existence of bulk plasmon polaritons at the high frequency limit. For instance, when $p < 0.2$, $\omega_p^{eff} < \omega_{cut-off}$ pushing all the modes with $q \geq 3$ to lower frequencies (Fig. 4.7(b)). The mode density diverges as the frequency approaches the effective plasma frequency, the cut-off for modes of different orders eventually converge to a single value as ω_p^{eff} shifts to lower frequencies. The critical filling factor where *all* the modes converge to a single value is located at $p = 0.04$ corresponding to a plasma frequency of 1 eV approximately (Fig. 4.7(b)).

4.4 Experimental results

The metamaterial slab was fabricated on a silica substrate ($n_{sub} = 1.5$) and with air as a superstrate ($n_{sup} = 1$). The waveguide was fabricated as described thoroughly in [36]. Fig. 4.8(a) depicts a 3 x 3 μm^2 top-view of the waveguide measured via atomic force microscopy (AFM). The maximum height is close to 133 nm due to defects that occur during chemical etching (the 2 bright spots in Fig. 4.8(a)), however the RMS roughness is only 12.5 nm. To verify the smoothness of the waveguide, the dashed area of Fig. 4.8(a) (1 x 1 μm^2) is independently investigated in Fig. 4.8(b). Here, the maximum height is 49 nm and the RMS roughness is 4.8 nm. The same image also reveals that AAO pores are filled with Au. To make this clear, Fig. 4.8(c) shows an AAO porous structure with no Au inside (the black spots indicate

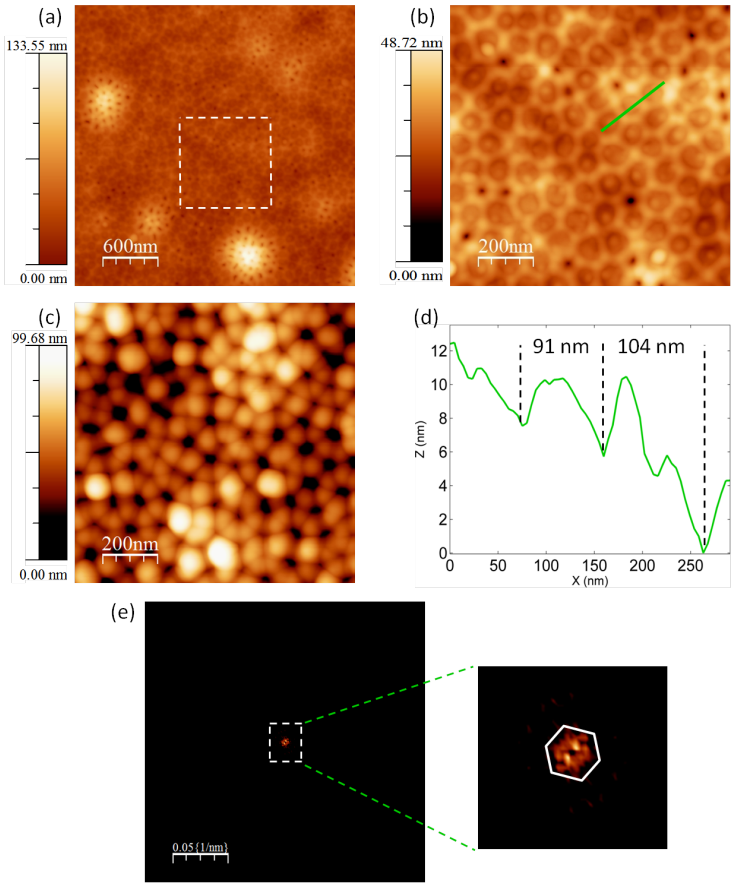

Figure 4.8: (a) AFM top-view of a 3 x 3 μm^2 periodic Au nanorod waveguide in AAO matrix. (b) Enlarged view of the dashed area (1 x 1 μm^2). (c) AFM top-view of a porous AAO waveguide to enable comparison with (b). (d) Example for the estimation of the average period. The cross-section is along the line in (b). (e) Fourier plane of (b) for the examination of the hexagonal shape of the structure.

the absence of Au). To estimate the average periodicity of the waveguide, the centre-to-centre distance was measured multiple times (> 50) at various locations on the structure. A typical cross-section for the determination of the average periodicity is shown in Fig. 4.8(d) depicting 2 periods measured along the line of Fig. 4.8(b). The measured average period was (98 $\pm$ 11) nm and, similarly, the average radius was (31 $\pm$ 4) nm. Consequently, the

filling factor was 0.32 ± 0.02. The thickness of the waveguide was (340 ± 10) nm (not shown). Finally, to measure how close to hexagonal formation the structure is, Fig. 4.8(e) shows the 2D-Fourier plane of Fig. 4.8(b). For comparison, a perfect hexagon is sketched around the plane. The structure has a hexagonal trend, but deviations occur due to different sizes and shapes of each hexagon.

The modal dispersion of the aforementioned waveguide was determined experimentally via reflectance measurements using the angular resolved spectrometer of Fig. 2.5. Given the 2D geometry of the waveguide, modes can be separated in TM- and TE-polarizations. The measurements for TM- and TE-polarizations are depicted in Fig. 4.9(a) and 4.9(c), respectively. Geometrical constrains in the experimental configuration determine the low-wavevector limit in the measured dispersions, while the high-wavevector limit is determined by the light line in the substrate. For that, the measured experimental angular range was $20° - 75°$ in the substrate.

To interpret the dispersions, the experimental results were compared with TMM simulations which are presented in Fig. 4.9(b) and 4.9(d). Starting from TM-polarization, the dispersions reveal both cavity resonances and waveguided modes, above and below the light line in air, respectively. More precisely, above the air light-line, the dispersion of TM-modes reveals discrete modes with negative group velocity (Fig. 4.9(a)). These modes are not confined to the waveguide, being accessible to plane waves in both the substrate and the superstrate. In this regime the metamaterial slab simply acts as a Fabry-Perot (FP) cavity. Between the light-lines in the superstrate and substrate, the modes are coupled to radiating modes in the substrate (leaky modes) while being evanescent at the metamaterial/air interface. Due to this coupling the modes (indicated with curved dashed lines in Fig. 4.9(a),

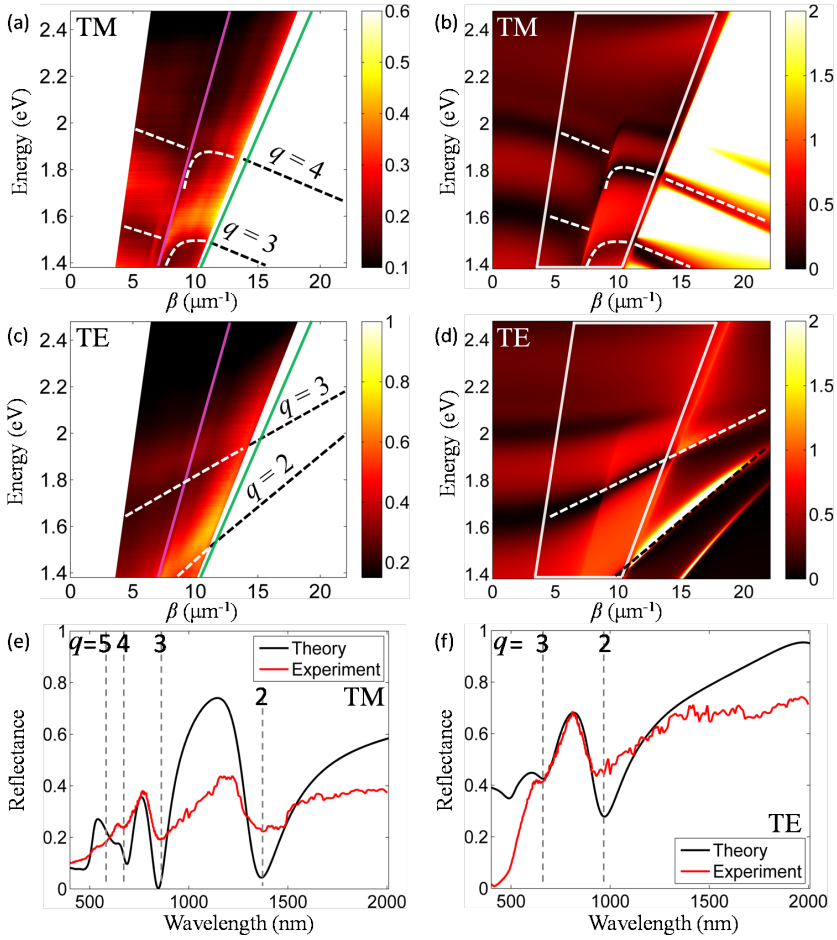

Figure 4.9: Experimentally measured (a),(c) and EMT simulated (b),(d) reflectance dispersions for a 340 nm thick metamaterial slab with $p \approx 0.32$ (the nanorod period is 100 nm and radius is 32 nm): (a),(b) TM, (c),(d) TE modes. The light-lines in substrate (glass, green) and superstrate (air, magenta) are shown. The Au nanorods are embedded in an AAO matrix. The modes with $q = 2 - 4$ are tracked with dashed lines as guide for the eye. The angular range measured in the experiment ($20° - 75°$ in the substrate) is indicated with the white boxes in (b) and (d). (e) Experimental and simulated reflectance spectra at the angle of 60° for TM-polarization as extracted from (a) and (b). The modes ($q = 2 - 5$) are indicated with dashed lines. (f) Same but for TE-polarization.

(b)) can have positive, negative, or vanishing small group velocity. The true waveguided modes below the light-line in the substrate are not accessible experimentally in the configuration used but had been examined analytically and numerically in Section 4.2. A similar analysis holds for the dispersion obtained for TE-modes (Fig. 4.9(c), (d)), but clearly only modes with positive group velocity are present in this case. For these modes, as was discussed above, the metamaterial slab acts as an anisotropic dielectric waveguide due to the orientation of the electric field along the y-axis only (normal to the nanorod axis) and bulk plasmon polaritons are not excited. It is thus possible to flip the sign of group velocity of the guided signal by altering polarization.

Based on the analytical model (Eq. (4.4) and (4.5)), we can now identify the modes in the experimental reflectance as modes $q = 2$ to $q = 5$ (Fig. 4.9). For the TM-modes, as the mode order increases, both the group velocity and group velocity dispersion decrease, with the $q = 4$ mode having negative group velocity even between the substrate and superstrate light-lines. In general, the experimental dispersions for the modes with $q = 2 - 4$ (Fig. 4.9(a), (c)) are in satisfactory agreement with the TMM modelled dispersions (Fig. 4.9(b), (d)), indicating that the EMT is still applicable for the metamaterial parameters and propagation constants considered and away from the effective plasma frequency. Fig. 4.9(e), (f) show the reflectance diagrams for TM and TE-polarization, respectively, for an angle of 60°. The experimental reflectance is in general lower to the theoretical one due to the increased scattering and losses that are not tracked by the EMT model. The resonant position for low-q modes is in good agreement with theory; it is important however to explain discrepancies that occur for higher mode orders. It is evident from Fig. 4.9(e) that the $q = 5$ mode is not observed in experimental reflectance. The reason is a combination of the higher losses and mode

density for increasing q's at increasing frequencies.

4.5 Impact of porous alumina on top of the waveguide

In Section 3.1 we briefly discussed the two-step anodization procedure for the fabrication of a Au nanorod array (more details can be found in [36]). Due to the nature of this process, a porous AAO overlayer remains on top of the hyperbolic waveguide that may be removed via Argon ion milling. Depending on application, the AAO layer can have minor or major contribution. Here it is shown, both theoretically and experimentally, that the AAO layer plays a critical role in group velocity as it drastically alters the slope of the modes. More precisely, when the AAO layer becomes comparable or thicker than the nanorod waveguide, group velocity between the substrate-superstrate light lines remains positive *regardless* the chosen polarization.

To understand this phenomenon, let us examine the TM-polarized optical response of a Au nanorod waveguide with and without a porous AAO overlayer as depicted in Fig. 4.10(a), (b) respectively. Both dispersions have exactly the same geometry with only difference the extra 300 nm AAO overlayer in Fig. 4.10(b). It is evident that all the guided modes ($q = 3 - 5$), observed below the air light line (solid line), switch from negative to positive group velocity when the AAO layer is added. The dashed lines correspond to the reflectance diagrams for three different incident angles as shown in Fig. 4.10(c), (d). These figures also demonstrate the transition of the modes from negative (red-shift) to positive (blue-shift) group velocity. It should be noted that when the thickness of the AAO layer is approximately lower that a third of the Au nanorod thickness, the group velocity retains its sign (i.e. remains

hyperbolic). The reason of this trend is the combination of the hyperbolic (Au nanorod array) and dielectric (porous AAO) waveguide. Since it is a two-layered system, the total refractive index depends on the effective re-

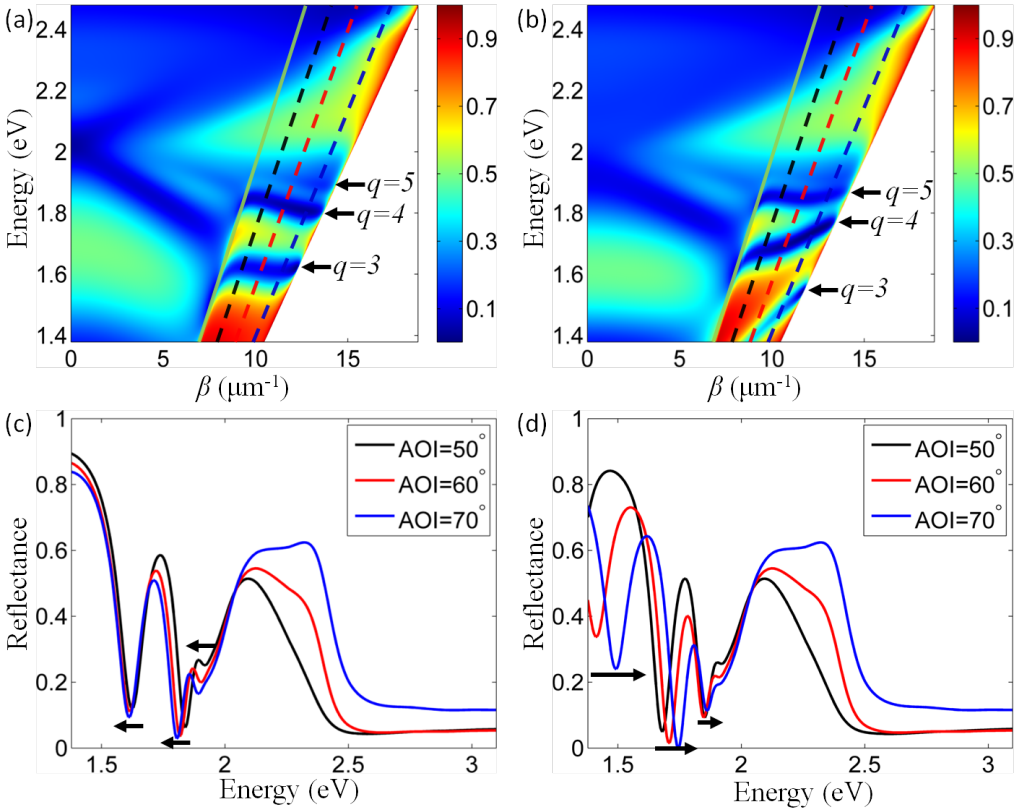

Figure 4.10: TM-polarized dispersion of a Au nanorod array without (a) and with (b) a porous AAO layer on top. Notice how the mode group velocity below the air light line (solid line) changes sign from negative to positive values. The dashed lines in (a) and (b) correspond to the cross-sections (Reflectance) at different angles as depicted in (c) and (d) respectively. When group velocity is negative the modes, shown with arrows, exhibit a red-shift contrary to the positive case in which a blue-shift is observed. The waveguide has 100 nm period, 25 nm radius and 300 nm thickness. The same geometry is considered also for the porous AAO. The angle of incidence (AOI) is measured from the substrate (glass).

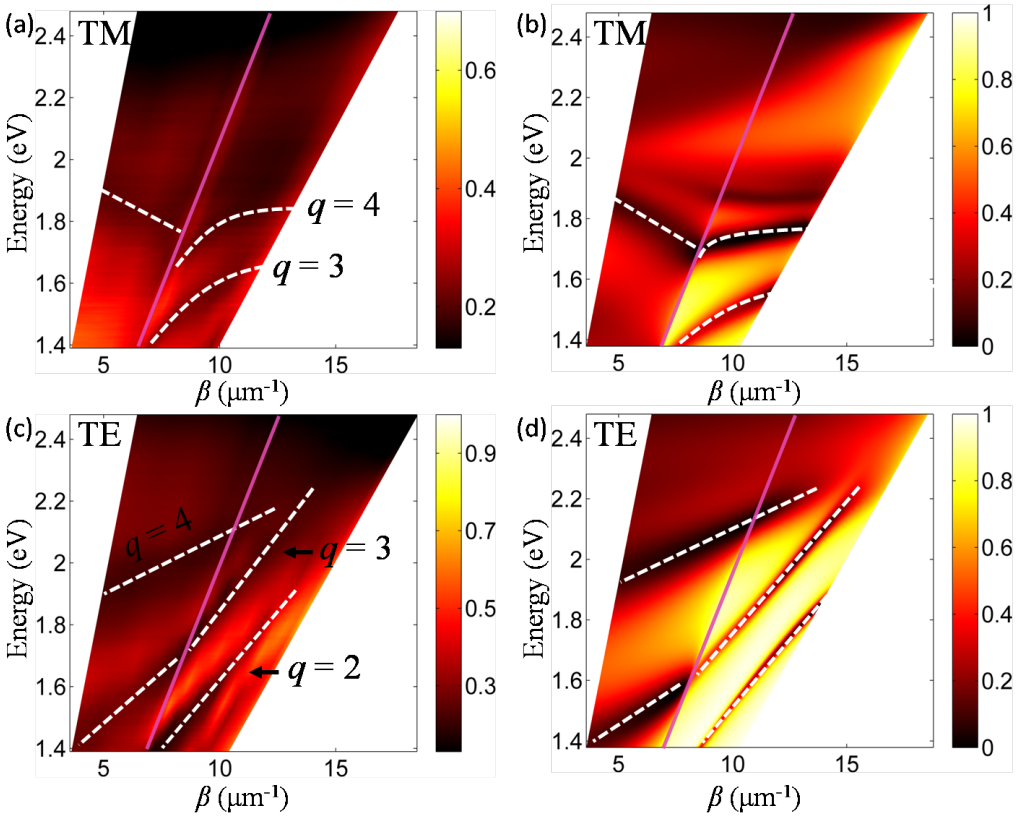

Figure 4.11: Experimental (a) and theoretical (b) dispersion of a Au nanorod waveguide with a porous AAO overlayer, for TM-polarization. (c),(d) Same as before but for TE-polarization. Notice how the group velocity below the air light line (solid line) remains positive regardless the polarization chosen. The waveguide, for both the experimental and simulated dispersions, has 100 nm period, 25 nm radius and 310 nm thickness. The same geometry is considered also for the porous AAO but with a thickness of 250 nm. The angular range is $20° - 80°$ from the substrate (glass). The modes $q = 2 - 4$ are tracked with dashed lines.

fractive indices of both layers. As the thickness of the porous AAO increases, the elliptic (dielectric) optical response dominates the hyperbolic one drastically affecting group velocity. It is thus possible to minimize group velocity (i.e. achieve slow light) in any dispersion position by carefully structuring

the porous AAO layer with respect to the Au nanorod waveguide.

To experimentally validate the aforementioned, a 310 nm Au nanorod waveguide with a 250 nm porous AAO overlayer was fabricated and characterized. The experimental and theoretical dispersions for TM-polarization are demonstrated in Fig. 4.11(a), (b), respectively, while the TE-case in Fig. 4.11(c), (d). Both polarizations have good agreement with theory and show three waveguided modes with mode numbers $q = 2 - 4$. The positive slope of the $q = 3$ and $q = 4$ modes, below the air line (solid line), can be clearly seen in Fig. 4.11(a) affirming the TE-like behaviour due to the porous AAO overlayer. These modes are more bent than the dielectric ones in Fig. 4.11(c) but definitely not flat or negatively sloped as the ones in Fig. 4.9(a) where no overlayer was considered (purely hyperbolic waveguide). Note however that above the air light line the structure retain its hyperbolic properties since the modes are not confined to the waveguide, being accessible to plane waves in both the substrate and the superstrate. In this regime the metamaterial slab simply acts as a Fabry-Perot (FP) cavity.

4.6 Summary

In conclusion, we have investigated bulk plasmon-polariton excitations in planar hyperbolic metamaterial waveguides. The most important outcomes can be summarized as follows

1. The spectral range of waveguided modes is limited by the effective plasma frequency of the metamaterial, below which conventional (like in a dielectric slab) TE and negative group velocity TM-waveguided modes exists. The negative group velocity as well as its dispersion can be controlled by varying anisotropy of the metamaterial. For the

nanorod metamaterial studied, these TM-modes are slow light modes with group velocity down to $-0.03c_0$ and have dispersion as low as 0.02 ps^2/mm. The low frequency cut-off of these mode is determined by the Brillouin zone related to a particular realization of the metamaterial, and single mode guiding can be achieved in the planar waveguides of $\lambda_0/6-\lambda_0/8$ thickness, depending on the anisotropy of the metamaterial.

2. TM-waveguided modes show a non-monotonous shift as filling factor increases. The critical filling factor that reverses the trend of *all* modes is close to 0.04; at this stage the effective plasma frequency is the upper frequency limit at which the modes are sustained by the waveguide. For even lower filling factors, the effective plasma frequency further decreases and the modes eventually converge towards each other. For increasing mode number, q, the critical filling factor is observed at higher values and eventually converges to $p = 0.34$ as $q \to \infty$.

3. Having an elliptical waveguide (like the porous AAO used here) on top a hyperbolic one (Au nanorod array) the effects of the later can be counteracted. This practically means that the negative group velocity of the modes, which is due to the hyperbolic metamaterial, can become positive if a dielectric layer is added on top. Using the ion milling technique, the thickness of the dielectric layer can be precisely controlled allowing the determination of group velocity as well. This way, group velocity can be minimized achieving slow light.

These properties of hyperbolic metamaterial waveguides are interesting for designing integrated deep-subwavelength sensors, quantum information processing, nonlinear and active nanophotonic devices and optical data storage components.

References

[1] V. M. Agranovich and D. L. Mills, Eds., *Surface Polaritons*. North-Holland, (1982).

[2] O. Firstenberg, T. Peyronel, Q.-Y. Liang, A. V. Gorshkov, M. D. Lukin, and V. Vuletić, "Attractive photons in a quantum nonlinear medium," *Nature*, vol. **502**, pp. 71–75, (2013).

[3] A. A. Khalifa, A. P. D. Love, D. N. Krizhanovskii, M. S. Skolnick, and J. S. Roberts, "Electroluminescence emission from polariton states in GaAs-based semiconductor microcavities," *Appl. Phys. Lett.*, vol. **92**, p. 061107, (2008).

[4] D. Bajoni, E. Semenova, A. Lemaître, S. Bouchoule, E. Wertz, P. Senellart, and J. Bloch, "Polariton light-emitting diode in a GaAs-based microcavity," *Phys. Rev. B*, vol. **77**, p. 113303, (2008).

[5] S. I. Tsintzos, N. T. Pelekanos, G. Konstantinidis, Z. Hatzopolulos, and P. G. Savvidis, "A GaAs polariton light-emitting diode operating near room temperature," *Nature*, vol. **453**, pp. 372–375, (2008).

[6] D. Bajoni, P. Senellart, E. Wertz, I. Sagnes, A. Miard, A. Lemaître, and J. Bloch, "Polariton laser using single micropillar GaAs-GaAlAs semiconductor cavities," *Phys. Rev. Lett.*, vol. **100**, p. 047401, (2008).

[7] A. V. Zayats, I. I. Smolyaninov, and A. A. Maradudin, "Nano-optics of surface plasmon polaritons," *Phys. Reports*, vol. **408**, pp. 131–314, (2005).

[8] B. M. Wells, A. V. Zayats, and V. A. Podolskiy, "Nonlocal optics of plasmonic nanowire metamaterials," *Phys. Rev. B*, vol. **89**, p. 035111, (2014).

[9] J. Schilling, "Uniaxial metallo-dielectric metamaterials with scalar positive permeability," *Phys. Rev. E*, vol. **74**, p. 046618, (2006).

[10] S. Ishii, A. V. Kildishev, E. Narimanov, V. M. Shalaev, and V. P. Drachev, "Sub-wavelength interference pattern from volume plasmon polaritons in a hyperbolic medium," *Laser & Phot. Rev.*, vol. **7**, pp. 265–271, (2013).

[11] S. V. Zhukovsky, O. Kidwai, and J. E. Sipe, "Physical nature of volume plasmon polaritons in hyperbolic metamaterials," *Opt. Express*, vol. **21**, pp. 14 982–14 987, (2013).

[12] W.-C. Lai, S. Chakravarty, Y. Zou, Y. Guo, and R. T. Chen, "Slow light enhanced sensitivity of resonance modes in photonic crystal biosensors," *Appl. Phys. Lett.*, vol. **102**, p. 041111, (2013).

[13] J. N. Anker, W. P. Hall, O. Lyandres, N. C. Shah, J. Zhao, and R. P. V. Duyne, "Biosensing with plasmonic nanosensors," *Nat. Mat.*, vol. **7**, pp. 442—453, (2008).

[14] G. A. Wurtz, R. Pollard, W. Hendren, G. P. Wiederrecht, D. J. Gosztola, V. A. Podolskiy, and A. V. Zayats, "Designed ultrafast optical nonlinearity in a plasmonic nanorod metamaterial enhanced by nonlocality," *Nat. Nano.*, vol. **6**, pp. 107—111, (2011).

[15] T. F. Krauss, "Slow light in photonic crystal waveguides," *J. Phys. D: Appl. Phys.*, vol. **40**, pp. 2666—2670, (2007).

[16] R. Ramaswami, K. N. Sivarajan, and G. H. Sasaki, Eds., *Optical Networks*. Elsevier, (2010).

[17] J. Yao, Z. Liu, Y. Liu, Y. Wang, C. Sun, G. Bartal, A. M. Stacy, and X. Zhang, "Optical negative refraction in bulk metamaterials of nanowires," *Science*, vol. **321**, p. 930, (2008).

[18] A. V. Kabashin, P. Evans, S. Pastkovsky, W. Hendren, G. A. Wurtz, R. Atkinson, R. Pollard, V. A. Podolskiy, and A. V. Zayats, "Plasmonic nanorod metamaterials for biosensing," *Nat. Mat.*, vol. **8**, pp. 867–871, (2009).

[19] M. E. Nasir, W. Dickson, G. A. Wurtz, W. P. Wardley, and A. V. Zayats, "Hydrogen detected by the naked eye: optical hydrogen gas sensors based on core/shell plasmonic nanorod metamaterials," *Adv. Mat.*, vol. **26**, pp. 3532–3537, (2014).

[20] V. V. Yakovlev, W. Dickson, A. Murphy, J. McPhillips, R. J. Pollard, V. A. Podolskiy, and A. V. Zayats, "Ultrasensitive non-resonant detection of ultrasound with plasmonic metamaterials," *Adv. Mat.*, vol. **25**, pp. 2351–2356, (2013).

[21] W. Dickson, G. A. Wurtz, P. Evans, D. O'Connor, R. Atkinson, R. Pollard, and A. V. Zayats, "Dielectric-loaded plasmonic nano-antenna arrays: a metamaterial with tuneable optical properties," *Phys. Rev. B*, vol. **76**, p. 115411, (2007).

[22] V. L. Krutyanskiy, I. A. Kolmychek, E. A. Gan'shina, T. V. Murzina, P. Evans, R. Pollard, A. A. Stashkevich, G. A. Wurtz, and A. V. Zayats,

"Plasmonic enhancement of nonlinear magneto-optical response in nickel nanorod metamaterials," *Phys. Rev. B*, vol. **87**, p. 035116, (2013).

[23] H. N. S. Krishnamoorthy, Z. Jacob, E. Narimanov, I. Kretzschmar, and V. M. Menon, "Topological transitions in metamaterials," *Science*, vol. **336**, pp. 205–209, (2012).

[24] M. Y. Shalaginov, S. Ishii, J. Liu, J. Liu, J. Irudayaraj, A. Lagutchev, A. V. Kildishev, and V. M. Shalaev, "Broadband enhancement of spontaneous emission from nitrogen-vacancy centers in nanodiamonds by hyperbolic metamaterials," *Appl. Phys. Lett.*, vol. **102**, p. 173114, (2013).

[25] J. Elser, R. Wangberg, V. A. Podolskiy, and E. E. Narimanov, "Nanowire metamaterials with extreme optical anisotropy," *Appl. Phys. Lett.*, vol. **89**, p. 261102, (2006).

[26] P. B. Johnson and R. W. Christy, "Optical constants of the noble metals," *Phys. Rev. B*, vol. **6**, pp. 4370–4379, (1972).

[27] C. Kittel, Ed., *Introduction to solid state physics*. John Wiley & Sons, (2005).

[28] S. Molesky, C. J. Dewalt, and Z. Jacob, "High temperature epsilon-near-zero and epsilon-near-pole metamaterial emitters for thermophotovoltaics," *Opt. Express*, vol. **21**, pp. A96–A110, (2013).

[29] J. T. Shen, P. B. Catrysse, and S. Fan, "Mechanism for designing metallic metamaterials with a high index of refraction," *Phys. Rev. Lett.*, vol. **94**, p. 197401, (2005).

[30] R. J. Pollard, A. Murphy, W. R. Hendren, P. R. Evans, R. Atkinson, G. A. Wurtz, A. V. Zayats, and V. A. Podolskiy, "Optical nonlocalities

and additional waves in epsilon-near-zero metamaterials," *Phys. Rev. Lett.*, vol. **102**, p. 127405, (2009).

[31] C. A. Balanis, Ed., *Advanced Engineering Electromagnetics*. John Wiley & Sons, (2012).

[32] J. A. Fleck and M. D. Feit, "Beam propagation in uniaxial anisotropic media," *J. Opt. Soc. Am.*, vol. **73**, pp. 920–926, (1983).

[33] X. Yang, J. Yao, J. Rho, X. Yin, and X. Zhang, "Experimental realization of three-dimensional indefinite cavities at the nanoscale with anomalous scaling laws," *Nature Phot.*, vol. **6**, pp. 450–454, (2012).

[34] B. Wood, J. B. Pendry, and D. P. Tsai, "Directed subwavelength imaging using a layered metal-dielectric system," *Phys. Rev. B*, vol. **74**, p. 115116, (2006).

[35] D. R. Smith and D. Schurig, "Electromagnetic wave propagation in media with indefinite permittivity and permeability tensors," *Phys. Rev. Lett.*, vol. **90**, p. 077405, (2003).

[36] P. Evans, W. R. Hendren, R. Atkinson, G. A. Wurtz, W. Dickson, A. V. Zayats, and R. J. Pollard, "Growth and properties of gold and nickel nanorods in thin film alumina," *Nanotechnology*, vol. **17**, pp. 5746–5753, (2006).

Chapter 5

Refractive index sensing with hyperbolic metamaterials

Metamaterials with hyperbolic dispersion based on metallic nanorod arrays provide flexible platform for design of bio- and chemical sensors and nonlinear devices allowing incorporation of index-dependent materials between and on top of the plasmonic nanorods. In this Chapter, we investigate the refractive index sensitivity of metamaterial's resonances in different regimes. We first start by comparing the dispersion and sensitivity of dispersion of a half-space metallodielectric pair with isotropic or anisotropic response and discuss the suitability of the later for sensing techniques. We then turn our attention to the more realistic case of a periodic metallic nanorod array, and investigate analytically and numerically the sensitivity of the mode response for small variations of the refractive index of the superstate, the host medium or metal itself. The results provide a general strategy for maximising refractive index sensitivity and can be used as the basis for the design of new ultra sensitive chemo- and biosensors outperforming both surface plasmons polaritons and localised surface plasmons based transducers.

5.1 Introduction to sensing with plasmonic metamaterials

The refractive index sensitivity of plasmonic and waveguided resonances forms the basis of commercial and newly emerging optical sensing techniques for label-free biosensing and chemical identification [1–4] as well as active nanophotonic components [5,6]. In the former class of applications, the presence of an analyte substance modifies the eingenmodes of the nanostructure, a change that can be detected by a shift of the resonant wavelengths of the structure or by changes of transmitted or reflected light intensity. In the latter, the refractive index changes are induced by external stimuli, such as temperature, acoustic pressure, external static electric or magnetic field, or indeed optical field via nonlinear effects in the surrounding dielectric or metal [6]. The strong modification of the optical response in plasmonic nanostructures arises from the strong confinement of the electromagnetic field near the metal/dielectric interface. Both sensing and active nanophotonic devices can make use of macroscopic thin metal films or nanostructured surfaces where surface electromagnetic waves called surface plasmon polaritons (SPPs) propagate, or nanoparticles and their assemblies supporting localised surface plasmons (LSPs) [2,3,7].

Surface plasmon resonance (SPR) biosensors use SPP waves for the detection of binding events, lifetime measurements or molecule concentration, based on the attenuated total internal reflection (ATR) configuration [1]. Due to a strong field confinement of SPPs, sensing limits are greatly enhanced, exceeding 3,000 nm per refractive index unit (RIU) [8] and can be even further boosted via phase-sensitive interferometry [9]. Nonetheless, SPP-based techniques have restrictions in detecting small molecule analytes, typically

smaller than 500 Da, making it problematic for modern nanoscale chemical and biochemical tasks [10]. An alternative route is to use LSP modes on plasmonic nanoparticles that provide an even stronger field confinement and, thus, more sensitive to smaller-size molecules [2,11]. However, the overall sensitivity provided by LSPs is typically orders of magnitude smaller than for SPPs, not exceeding $100 - 300$ nm/RIU [2,12].

Recently, plasmonic metamaterials have been demonstrated to provide the record refractive index sensitivity for biosensing, ultrasound detection and high effective Kerr-type nonlinearities [13]. In particular, the class of anisotropic metamaterials based on arrays of strongly interacting, aligned plasmonic nanorods exhibits hyperbolic dispersion, with one negative (ε_z) and two positive effective permittivity tensor components ($\varepsilon_{x,y}$), leading to a metamaterial with hyperbola-shaped isofrequency contours. This unique isofrequency surface enables a plethora of applications, from guiding and imaging beyond the diffraction limit [14,15] to enhanced nonlinearities [5,16] and chemo- and biosensing [5,6,17]. Additionally, selected resonances of plasmonic nanorod metamaterials have been shown to exhibit a strong sensitivity to the thickness change of the dielectric load [18], ultrasensitive detection of ultrasound [19], and ultrafast sub-ps response times due to optical nonlocality [16].

5.2 Differences of isotropic and anisotropic materials for sensing

The scope of this Section is to compare the sensing capabilities of isotropic and anisotropic media and show the advantages of the later based on some simple paradigms. We first inspect the dispersion relations for the half-space

media discussed in Section 2.3 and compare the derived expressions for the isotropic and anisotropic case. We then focus our attention on the sensitivity of dispersion for each scenario and explain why sensing is important, from the applied point of view, and why anisotropy plays a crucial role.

5.2.1 Comparison of dispersion

Based on the scheme of Fig. 2.2 and the calculations in Section 2.3, the SPPs dispersion between iso- and anisotropic media can be compared. Let us assume the material ε_1 to be Au following the Drude-Sommerfeld model. The material ε_2 can either be isotropic (Eq. (2.22)) or anisotropic (Eq. (2.19)). To examine these two cases, we can keep the permittivity component along one direction fixed and vary the other. Fig. 5.1(a) and 5.1(b) demonstrate the scenario where $\varepsilon_2^{iso} = \varepsilon_{xx}^{ani} = 4$ and ε_{zz}^{ani} varies from 1 to 9. An immediate observation is when $\varepsilon_{zz}^{ani} < \varepsilon_2^{iso}$ the SPP dispersion shifts to higher energies and vice versa. A similar shift is also true for the imaginary part of the dispersion as shown in Fig. 5.1(b). Thus tuning permittivity along a given direction the SPP resonance can be changed; this is not possible with isotropic materials since, by definition, the optical response for a given polarization remains unaffected along different axes. A more realistic case where ε_1 follows the experimental values from [20] is depicted in Fig. 5.1(c) and 5.1(d). Here the SPP dispersion shift along the energy axis is still valid but not so much distinct. The reason of the decreased energy shift is due to the interband transitions of Au that occurs close to 2.1 eV ($\omega/\omega_p = 0.23$). What is more pronounced is the change of the resonance along the ordinary axis. Note however that, although the SPP wavevector can be enhanced by choosing the appropriate anisotropic permittivity, the imaginary part is also increased thus losses become significant. The main outcome is that, regard-

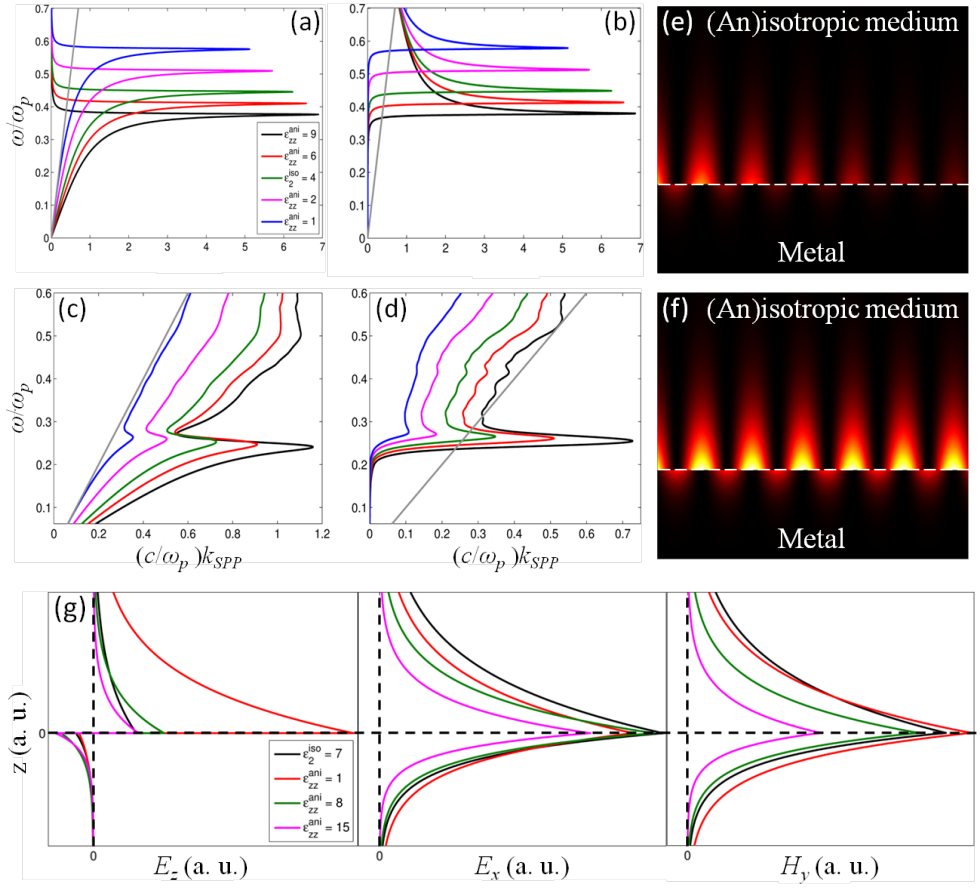

Figure 5.1: Comparison of SPP dispersion between isotropic and anisotropic media. Real (a) and imaginary part (b) of dispersion for the structure of Fig. 2.2. Material ε_1 follows the Drude-Sommerfeld model for Au ($\omega_p = 1.367 \times 10^{16}$ Hz). Material ε_2 has $\varepsilon_2^{iso} = 4$ for the isotropic case while the anisotropic one has $\varepsilon_{xx}^{ani} = \varepsilon_2^{iso}$ and ε_{zz}^{ani} varies from 1 to 9. (c), (d) Same as before but using the experimental values for Au taken from [20]. Note how the dispersion can be tuned by changing the anisotropic permittivity. (e), (f) Norm of the electric field showing the excitation of a SPP in a metal-(an)isotropic interface with and without losses, respectively. (g) Typical cross-sections of the electromagnetic field components at that interface for various ε_{zz}^{ani}. Notice that both E_x and H_y are continuous at the interface while E_z is not due to surface charge accumulation.

less of the theoretical or experimental approximation, the SPP dispersion can be tuned by carefully choosing the appropriate set of $(\varepsilon_{xx}^{ani}, \varepsilon_{zz}^{ani})$, a feature that is absent in isotropic media since they have no directionality.

To have a broader view of the validity of equations derived so far, we can examine the electromagnetic field distribution for the SPP excitation. Since the wavevectors are known, the fields for medium ε_1 will be (read Appendix B.1)

$$\left.\begin{aligned} \mathbf{H}_1(\mathbf{r},t) &= (0,H_0,0)^{\intercal} e^{i(k_x x - k_{z1} z - \omega t)} \\ \mathbf{E}_1(\mathbf{r},t) &= (-\frac{cH_0 k_{z1}}{\omega \varepsilon_1}, 0, -\frac{cH_0 k_x}{\omega \varepsilon_1})^{\intercal} e^{i(k_x x - k_{z1} z - \omega t)} \end{aligned}\right\} \tag{5.1}$$

and for material ϵ_2

$$\left.\begin{aligned} \mathbf{H}_2(\mathbf{r},t) &= (0,H_0,0)^{\intercal} e^{i(k_x x + k_{z2} z - \omega t)} \\ \mathbf{E}_2(\mathbf{r},t) &= (\frac{cH_0 k_{z2}}{\omega \varepsilon_{xx}^{ani}}, 0, -\frac{cH_0 k_x}{\omega \varepsilon_{zz}^{ani}})^{\intercal} e^{i(k_x x + k_{z2} z - \omega t)} \end{aligned}\right\} \tag{5.2}$$

where H_0 is a constant magnetic field amplitude and $k_x = k_{SPP}$. Note that for the case where $\varepsilon_{xx}^{ani} = \varepsilon_{zz}^{ani} = \varepsilon_2^{iso}$ it is simplified to the well known isotropic expression. Based on the aforementioned equations, the field distributions can be plotted. Fig. 5.1(e) and 5.1(f) show the norm of the electric field for a SPP travelling along a typical metallodielectric interface (either iso- or anisotropic) with and without losses, respectively. Note for the lossless case the SPP can travel infinitely along the surface (i.e. $L_p \to \infty$) while for the lossy case L_p is finite due to the small, but non negligible, imaginary part of the permittivity. Fig. 5.1(g) shows several cross-sections of the electromagnetic field components for different permittivity values. It is clearly shown that when ε_{zz}^{ani} increases the field components are more localized to the surface leading to high light confinement regardless of the fact that the permittivity along the x-direction is the same as in the isotropic case. The E_z component

has a discontinuity at the interface due to surface charge accumulation. Note however that the permittivities for the isotropic or anisotropic medium can not change arbitrarily with respect to the metallic medium; they both need to keep k_x real and k_z imaginary at all times as discussed in Section 2.3.

5.2.2 Comparison of sensitivity of dispersion

The examination of sensitivity, i.e. the change of the ordinary wavevector with respect to permittivity, of the SPP dispersion is another important factor that plays a critical role in applications that depend on small changes (typically $10^{-3} - 10^{-4}$) of the refractive index such as biosensors [2, 21–23]. As a consequence, having the ability to manipulate the sensitivity of the dispersion is a key factor. Based on Eq. (2.19) and (2.22), we can measure the derivative of the SPP dispersion with respect to permittivity, for the anisotropic and isotropic scenario, respectively. To compare these two cases, we follow the same recipe discussed before and keep the permittivity component along one the direction fixed while varying the other. Letting ε_1 be Au taken from Johnson and Christy [20], we set $\varepsilon_2^{iso} = \varepsilon_{xx}^{ani}$ and plot it for different values of ε_{zz}^{ani}. The results are shown in Fig. 5.2 for a typical wavelength of 600 nm ($\varepsilon_1 = -9.43 + 1.50i$).

Inspecting the figures, we clearly observe that both anisotropic sensitivities, $\partial k_x^{ani}/\partial \varepsilon_{xx}^{ani}$ and $\partial k_x^{ani}/\partial \varepsilon_{zz}^{ani}$, can be tuned in order to achieve resonances for a different ε_{xx}^{ani} range. Additionally, when $\varepsilon_{zz}^{ani} < \varepsilon_{xx}^{ani}$, the sensitivity with respect to ε_{zz}^{ani} has greater values than the one with respect to ε_{xx}^{ani} (Fig. 5.2(a)) while the opposite occurs when $\varepsilon_{zz}^{ani} > \varepsilon_{xx}^{ani}$ (Fig. 5.2(d)). Thus sensitivity can be altered with the appropriate set of permittivity components along different directions. The characteristic form of all sensitivities is due to the surface plasmon resonance discussed in Section 2.4. Close to this reso-

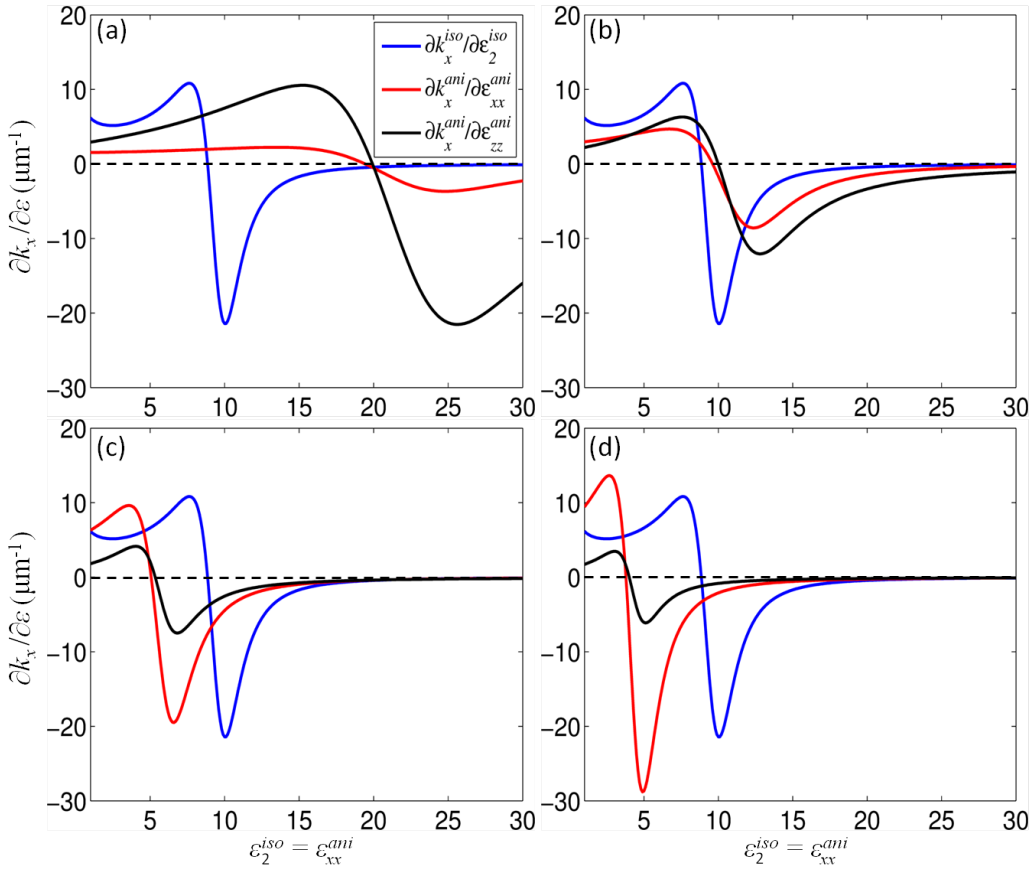

Figure 5.2: Sensitivity of SPP dispersion for a semi-infinite metallodielectric pair. The metal is considered Au taken from [20], while the dielectric is either isotropic or anisotropic. Figures (a) to (d) depict dispersion sensitivity for a broad range of $\varepsilon_2^{iso} = \varepsilon_{xx}^{ani}$ when ε_{zz}^{ani} is 4, 8, 15 and 20, respectively. Note how anisotropic sensitivity can be tuned along the permittivity plane contrary to the isotropic one which remains static since it is independent of ε_{zz}^{ani}. For all graphs the wavelength was 600 nm giving $\varepsilon_1 = -9.43 + 1.50i$.

nance there is a drastic increase of the slope, explaining the positive sensitivity peak, and then it sharply decreases for even higher permittivity values, affirming the negative slope. Lastly, anisotropic sensitivity along a certain

permittivity axis can be tuned with the appropriate permittivity components. For instance, Fig. 5.2(d) shows that sensitivity with respect to ε_{xx}^{ani} is superior to the one with respect to ε_{zz}^{ani}. This behaviour can be reversed by having $\varepsilon_{xx}^{ani} = 4$ and let ε_{zz}^{ani} vary (not shown). The main outcome is that anisotropy which is inserted through the tensorial form of permittivity can create various sensing dispersions and at the same time control the position where sensing is maximized through careful inspection of permittivity components at a given wavelength. Conversely, the isotropic sensitivity can only create a single sensitivity curve and remains static for variations of ε_{zz}^{ani} since it has no directionality.

To investigate sensitivity in a more thorough way, we can examine the dispersion along the anisotropic permittivity plane. Keeping the same configuration as before, Fig. 5.3 demonstrates both sensitivity dispersions, $\partial k_x^{ani}/\partial \varepsilon_{xx}^{ani}$ and $\partial k_x^{ani}/\partial \varepsilon_{zz}^{ani}$, for two typical wavelengths at 600 nm and 700 nm. A universal trend valid in all figures is the sign flip of sensitivity close to the resonance (red and blue curves). This has already been discussed and is connected with the surface plasmon resonance. The characteristic bending is due to the change of the resonance along the permittivity plane. Comparing Fig. 5.3(a), (b) with 5.3(c), (d) we observe that as wavelength increases, both anisotropic sensitivities need a higher set of $(\varepsilon_{xx}^{ani}, \varepsilon_{zz}^{ani})$ to satisfy the resonance condition. This means that sensing can but tuned either through wavelength or permittivity optimization. Although it is always easier to change the wavelength, there are times where the frequency range is limited (for example applications that function only in the visible spectrum), thus permittivity optimization is the only way. Here anisotropy has a crucial role since it allows us to change permittivity along different directions making it more flexible compared to the isotropic counterpart. Lastly, the two anisotropic sensitivities have a com-

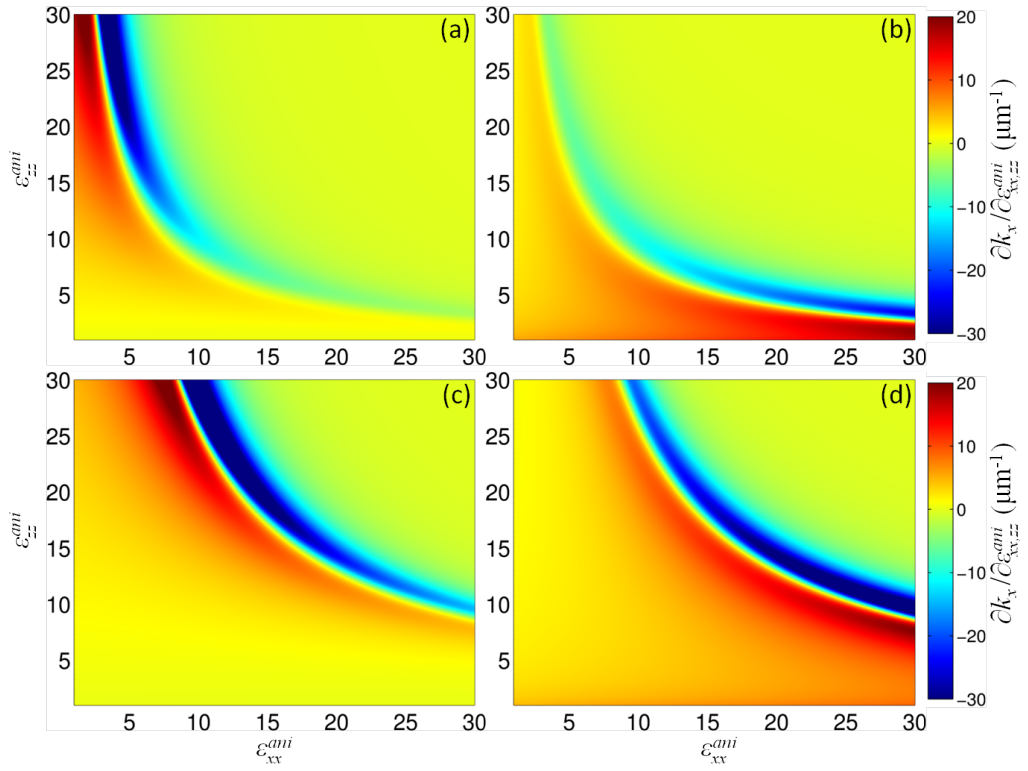

Figure 5.3: Anisotropic sensitivity dispersion with respect to ε_{xx}^{ani} (a) and ε_{zz}^{ani} (b) for a broad range of permittivities for a wavelength of 600 nm. (c), (d) Same as before but for 700 nm. Note the increase of sensitivity close to the surface plasmon resonance and the shift of it to higher $(\varepsilon_{xx}^{ani}, \varepsilon_{zz}^{ani})$ as wavelength increases.

plementary behaviour close to the resonance. This means that, for a given wavelength, if we need to achieve high sensitivity with respect to ε_{xx}^{ani} then ε_{zz}^{ani} should be increased while ε_{xx}^{ani} decreased and vice versa.

So based on some simple paradigms, we showed how anisotropy allows a more advanced manipulation of the SPP dispersion and at the same time a more flexible sensing configuration with respect to the isotropic scenario. However, the anisotropic permittivities were varied without any specific limitation, which is of course not the case in the real world. Consequently, in

the following Sections we investigate the refractive index sensitivity with metallic nanorod hyperbolic metamaterials and their impact in biosensing applications and nonlinear enhancement.

5.3 Numerical model

In this work, we present a comprehensive analysis of the anisotropic metamaterial's optical response to refractive index changes in order to develop strategies for optimising their sensing properties. We consider only the wavelength range of hyperbolic dispersion and study reflection, transmission, and total internal reflection modalities of operation, examining the role of perturbations of both the real and imaginary parts of the refractive index in the superstrate, host medium in which nanorods are placed, as well as the metal itself. All components of the permittivity tensor determine the formation of these modes and, thus, their refractive index sensitivities. We study the refractive index sensing capabilities of a metamaterial in several configurations when the anisotropic metamaterial slab is illuminated in both conventional and total internal reflection conditions and monitored the changes of the intensity and spectra of transmission and/or reflection upon modifications of the refractive index and absorption of the analyte as depicted in Fig. 5.4(a). The metamaterial is considered to be composed of an array of Gold nanorods arranged periodically (Fig. 5.4(a)). The thickness of the metamaterial slab (height of the nanorods) is l, and it is sandwiched between a substrate and superstrate with refractive indices of n_{sub} and n_{sup}, respectively.

The Maxwell-Garnett (MG) approximation (see Section 3.5) was followed to derive the tensor of the effective permittivity of the anisotropic metamaterial [24]. Considering an array of rods in the xy plane, the effective permit-

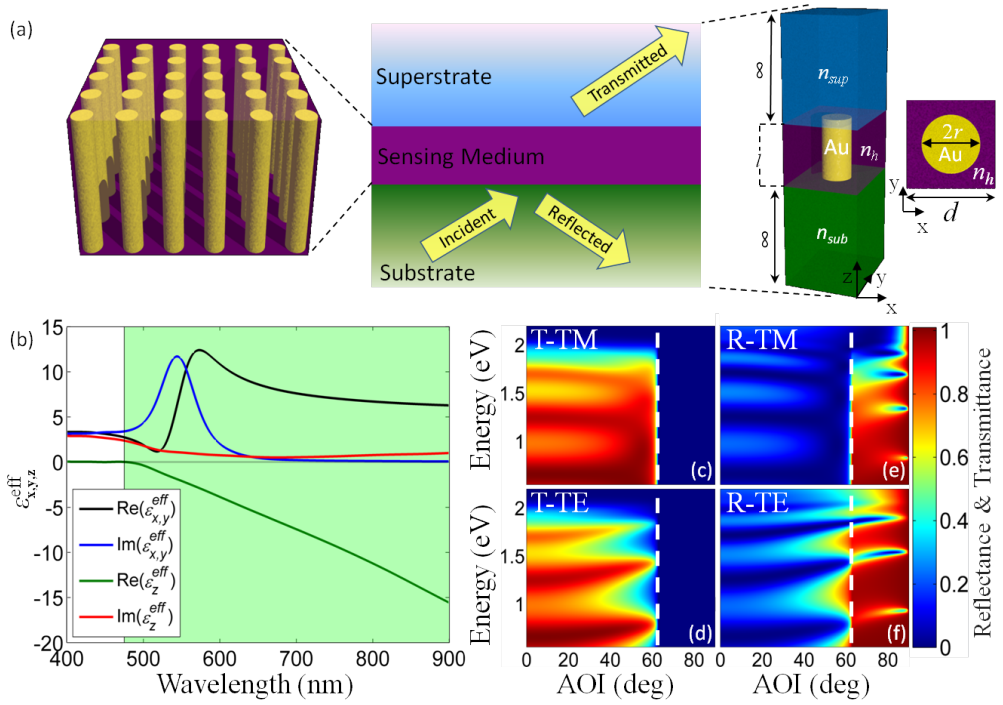

Figure 5.4: (a) Left: Schematic of the metamaterial transducer made of an array of Au nanorods embedded in a host environment (analyte); middle: Schematic of the typical experimental realization of refractive index sensing experiments in the reflection or transmission geometry; right: Schematics of the unit cell of the metamaterial. (b) Effective permittivities of the metamaterial in a water-like analyte ($n_h = 1.33$) with the nanorod period $d = 100$ nm and radius $r = 40$ nm. The green area shows the hyperbolic dispersion regime where $\varepsilon_z < 0$. (c-f) Transmittance and reflectance dispersions for (c),(e) TM- and (d),(f) TE-polarized light. Geometry is the same as in (b). The substrate is glass ($n_{sub} = 1.5$) and superstrate is water ($n_{sup} = 1.33$). Height of nanorods is $l = 400$ nm. In all dispersions the TIR occurs at an angle of incidence of 62.46° indicated with dashed line.

tivities for ordinary and extraordinary axes take the form

$$\varepsilon_{x,y}^{eff} = \frac{p\varepsilon_{Au}\varepsilon_h + \varepsilon_h(1-p)\tilde{\varepsilon}}{p\varepsilon_h + (1-p)\tilde{\varepsilon}} \tag{5.3}$$

$$\varepsilon_z^{eff} = p\varepsilon_{Au} + (1-p)\varepsilon_h \tag{5.4}$$

where $p = \pi(r/d)^2$ defines the nanorod filling factor, with d being the period of the array and r is the nanorod radius, ε_{Au} and ε_h are the permittivities of Au [20] and host medium, respectively, and $\tilde{\varepsilon} = (\varepsilon_{Au} + \varepsilon_h)/2$. Note that the same period is considered in both x and y directions, thus, $\varepsilon_x^{eff} = \varepsilon_y^{eff}$. The MG approximation breaks down for wavevectors close to the Brillouin zone boundary, however for a typical period of 100 nm considered here, the first Brillouin zone boundary is close to $k_x \approx 31\ \mu m^{-1}$, which is far from the investigated regime ($k_x < 17\ \mu m^{-1}$). Additionally, the wavelength range where $Re(\varepsilon_z^{eff})$ vanishes (ENZ regime) requires special considerations; the ENZ and elliptic dispersion regime will not be considered in this work [25,26].

To examine the refractive index sensitivity of the optical properties of the metamaterial, the effective permittivity has been designed to achieve hyperbolic dispersion throughout the visible spectral range. Fig. 5.4(b) shows the real and imaginary parts of the components of the effective permittivity tensor for a typical nanorod array parameters and a water-like permittivity for the host medium. For this geometry, ε_z^{eff}, the permittivity component for light polarized along the nanorod axis, is negative for wavelengths longer than approximately 475 nm (Fig. 5.4(b)), while the transverse permittivity $\varepsilon_{x,y}^{eff}$, for light polarized perpendicular to the nanorod axes, is always positive, exhibiting a resonant behaviour near a wavelength of 540 nm, where the imaginary part of the permittivity reaches a maximum. For wavelengths above 540 nm the transverse component of permittivity's imaginary part is small relative to its real counterpart and does not exhibit any resonances.

The reflectance and transmittance spectra of the metamaterial transducer

have been calculated for angles of incidence (AOI) $0° - 90^{\circ}$ using the transfer matrix method [27] and taking into account a glass substrate ($n_{sub} = 1.5$), a water superstrate ($n_{sup} = 1.33$), and Au nanorods of height $l = 400$ nm. Fig. 5.4(c), (e) and Fig. 5.4(d), (f) show the transmittance and reflectance dispersions for both TM and TE polarizations, respectively. Unbound modes that leak in both substrate and superstrate exist below the critical angle θ_c appear as maxima (minima) in the transmittance (reflectance), while "leaky" modes, homogeneous in the substrate, are only present above θ_c and their effect is most pronounced in the reflectance of the structure. These modes are quantized solutions of the wavevector (k_z) due to the 1D confinement of the metamaterial slab in the z-direction. For the glass/water (substrate/superstrate) interface, total internal reflection (TIR) occurs at $\theta_c = 62.46°$, above which there is no transmission, and thus transmission-detection sensing is possible only below TIR angles.

In order to compare the sensing capabilities of different transducers and geometries, it is convenient to introduce two figures of merit (FoMs): FoM_λ to characterize the spectral shift induced by the refractive index changes of an analyte and FoM_I to characterize induced intensity variations of the transmitted or reflected light. We define $\mathrm{FoM}_\lambda = (\Delta\lambda/\delta\lambda)/\Delta n$, where $\Delta\lambda$ is the resonance shift of a metamaterial resonance to a refractive index change Δn, and $\delta\lambda$ is the full-width at half maximum of the resonance [28]. This definition accounts simultaneously for both the wavelength shift of a given mode per refractive index change, and the sharpness of the resonance. For intensity measurements, $\mathrm{FoM}_I = (\Delta I/I_0)/\Delta n$, where ΔI is the change of the transmitted or reflected intensity corresponding to a refractive index change Δn, and I_0 is the initial intensity [28]. While intensity measurements are simpler to implement than the spectral shift measurements, in some cases the

later may provide better sensitivity [17]. We will use these FoMs to evaluate the sensing capabilities of the metamaterial in the numerical results obtained in the following Sections.

5.4 Analytical examination

Here the sensitivity of the effective permittivities along with the sensitivity of the mode frequency is examined. We begin by investigating the sensing dependence of $\varepsilon^{eff}_{x,y,z}$ in terms of the refractive index changes of the metamaterial's constituents and also the impact of geometry inserted via the filling factor (p). The mode frequency dependence on the refractive index of the constituents is discussed next, for both TE and TM polarizations.

5.4.1 Effective permittivity sensitivity to geometry and refractive index variations of constituents

We begin by examining the sensitivity of the effective permittivities $\varepsilon^{eff}_{x,y}$ and ε^{eff}_{z}, which determine the optical response of the metamaterial, on the refractive index changes of the metamaterial's constituents $n_h = \sqrt{\varepsilon'_h + i\varepsilon''_h}$ and $n_{Au} = \sqrt{\varepsilon'_{Au} + i\varepsilon''_{Au}}$, for the host medium and Au, respectively. The modification of the refractive index of the metal can be achieved for example in nonlinear optical experiments, when the metamaterial is under femtosecond optical excitation due to the Kerr-type third-order nonlinearity of Au, but can also be induced by environmental change in temperature or pressure [17, 26]. The refractive index of the host medium can be changed in sensing experiments when analyte is incorporated between the nanorods or if nonlinear or temperature effects are important in the host dielectric. To evaluate this sensitivity, we study the partial derivative of Eq. (5.3) and (5.4) with

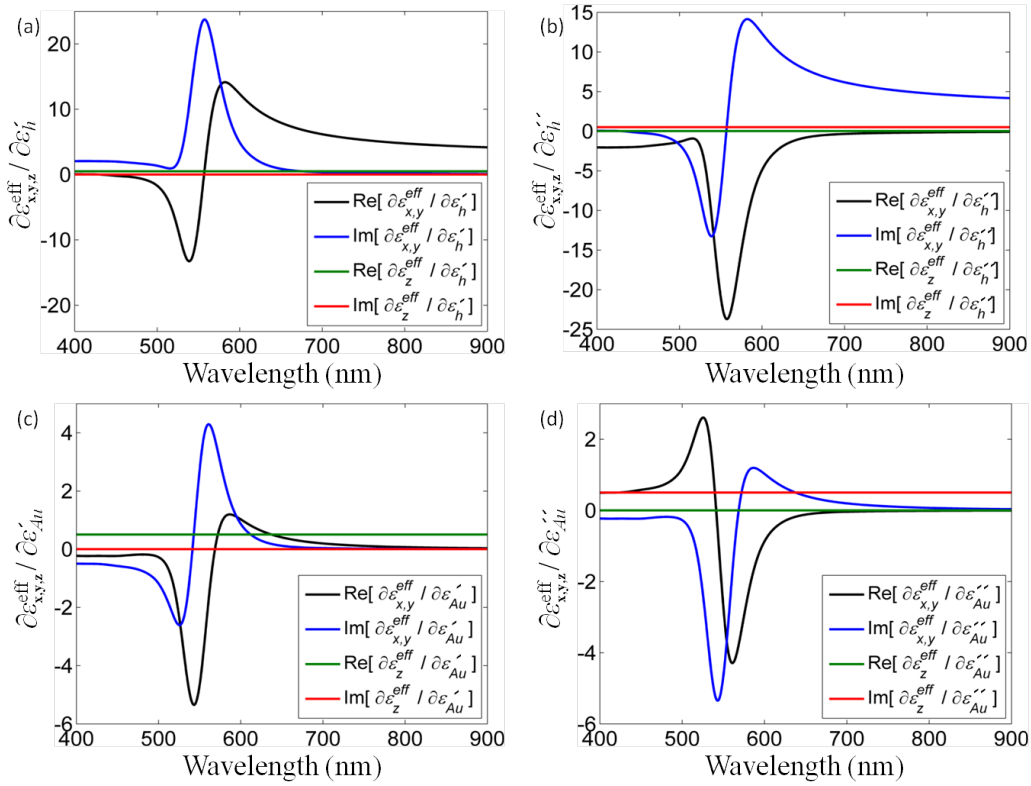

Figure 5.5: The spectral dependence of the derivative of the effective permittivity with respect to (a) ε'_h, (b) ε''_h, (c) ε'_{Au} and (d) ε''_{Au} modifications for a filling factor of $p = 0.5$.

regards to the permittivity components of each constituent, obtaining

$$\frac{\partial \varepsilon^{eff}_{x,y}}{\partial \varepsilon'_h} = -i\frac{\partial \varepsilon^{eff}_{x,y}}{\partial \varepsilon''_h} = \frac{P\varepsilon_{Au} + 2\varepsilon_h}{P\varepsilon_h + \varepsilon_{Au}} - P\varepsilon_h \frac{P\varepsilon_{Au} + \varepsilon_h}{(P\varepsilon_h + \varepsilon_{Au})^2} \tag{5.5}$$

$$\frac{\partial \varepsilon^{eff}_{x,y}}{\partial \varepsilon'_{Au}} = -i\frac{\partial \varepsilon^{eff}_{x,y}}{\partial \varepsilon''_{Au}} = \varepsilon_h \left[\frac{P}{P\varepsilon_h + \varepsilon_{Au}} - \frac{P\varepsilon_{Au} + \varepsilon_h}{(P\varepsilon_h + \varepsilon_{Au})^2}\right] \tag{5.6}$$

$$\frac{\partial \varepsilon^{eff}_{z}}{\partial \varepsilon'_h} = -i\frac{\partial \varepsilon^{eff}_{z}}{\partial \varepsilon''_h} = 1 - p \tag{5.7}$$

$$\frac{\partial \varepsilon^{eff}_{z}}{\partial \varepsilon'_{Au}} = -i\frac{\partial \varepsilon^{eff}_{z}}{\partial \varepsilon''_{Au}} = p \tag{5.8}$$

where $1 < P = (1+p)/(1-p) \leq 8.32$. The above expressions allow us to selectively track the response of the effective permittivities when either the real or the imaginary part of the constituents' permittivity changes. Fig. 5.5 illustrates this behaviour for the same metamaterial as in Fig. 5.4(b). The response of ε_z^{eff} to the refractive index modifications is extremely broadband and constant across the spectral range considered for both the real and imaginary parts (Fig. 5.5(a)-(d)), determined solely by the nanorod filling factor via p (Eq. (5.7) and (5.8)). On the other hand, $\varepsilon_{x,y}^{eff}$ exhibits the strongest changes close to its resonance at 540 nm (Fig. 5.4(b)) and strongly decreases for lower nanorod filling factors. Beyond the resonance at longer wavelengths, inspecting the dependence of $\varepsilon_{x,y}^{eff}$ on the host medium refractive index, one notices that it is always exceeds the sensitivity of ε_z^{eff} (Fig. 5.5(a), (b)), while both are similar at low nanorod filling factors. The ε_z^{eff} sensitivity to the refractive index of the plasmonic material dominates at long wavelengths, while the resonant behaviour of $\varepsilon_{x,y}^{eff}$ proves in general more strongly sensitive to the host medium refractive index.

To examine the impact of filling factor (p) more extensively, the dispersion diagrams of the derivative of $\varepsilon_{x,y}^{eff}$ with respect to ε_h' and ε_h'' are presented in Fig. 5.6. All refractive index sensitivity dispersions are dominated by a dispersive-shape resonance, which red-shifts and increases in magnitude with increasing nanorod filling factor. Both the dispersive behaviour and spectral shift observed in Fig. 5.6 can be linked to the spectral sensitivity of the resonance in $\varepsilon_{x,y}^{eff}$ shown in Fig. 5.4(b), which red-shifts with both an increase in ε_h and nanorod filling factor. It is important to note that Fig. 5.6(a), (c) are exactly the same; this is a direct consequence of the first equality of Eq. (5.5). The same calculations were repeated for ε_{Au}' and ε_{Au}'' showing a similar trend to Fig. 5.6, but with the resonant sensitivity approximately one order

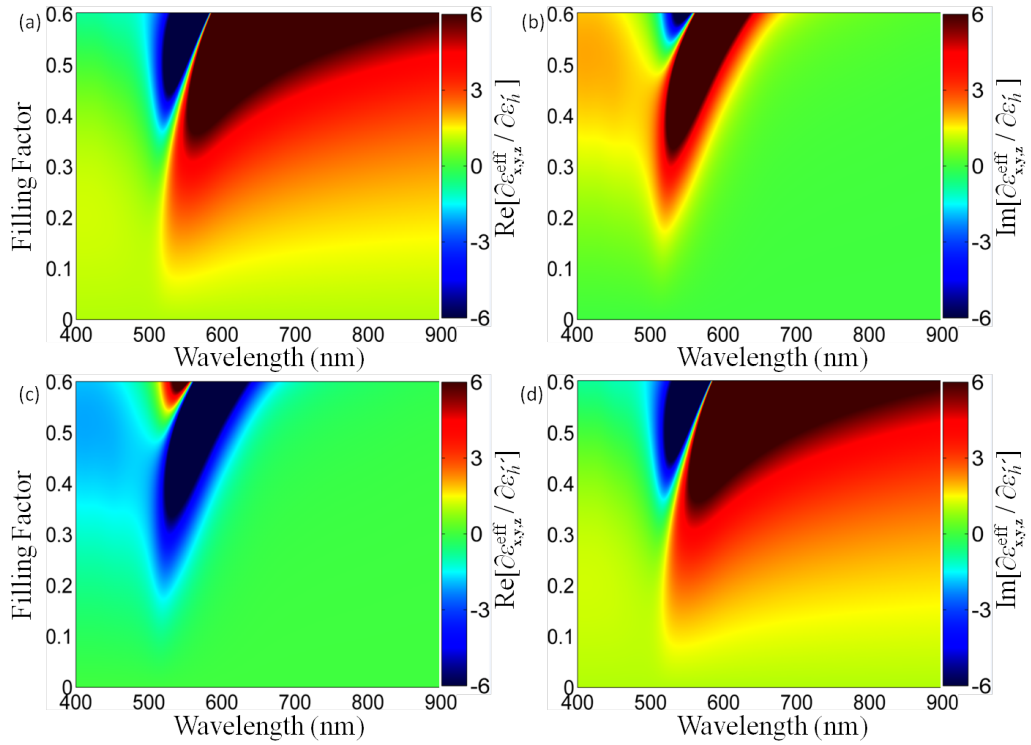

Figure 5.6: Real (a),(c) and imaginary (b),(d) derivatives of the effective permittivity maps with respect to (a),(b) ε'_h and (c),(d) ε''_h. Notice that (a) and (d) are the same; this is a consequence of Eq. (5.5).

of magnitude smaller (data not shown).

5.4.2 Mode frequency dependence on the refractive index of analyte

All the components of the effective permittivity tensor are important for defining the behaviour of TM modes of the metamaterial and, thus, their sensing capabilities. At the same time, only $\varepsilon^{eff}_{x,y}$ components define TE modes. To get better insight into the sensing properties of the unbounded, leaky, and waveguided modes of the metamaterial transducer, we consider the same an-

alytic model for the case of an anisotropic metamaterial layer as in Chapter 4. Neglecting phase shifts at the metamaterial's boundaries, we obtain a simple analytical approximation for the wavevector component k_x of TE and TM modes supported by the metamaterial slab as [15]

$$(k_x^{TE})^2 = \varepsilon_{x,y}^{eff} k_0^2 - \left(\frac{q\pi}{l}\right)^2 \tag{5.9}$$

$$(k_x^{TM})^2 = \varepsilon_z^{eff} k_0^2 - \left(\frac{q\pi}{l}\right)^2 \frac{\varepsilon_z^{eff}}{\varepsilon_{x,y}^{eff}} \tag{5.10}$$

where $k_0 = \omega/c_0$, and quantization $q\pi/l$ emerges from the transversal confinement of the wavevector component perpendicular to the metamaterial's interfaces with the integer $q > 0$ referring to the mode number. Unbounded, leaky, and waveguided modes then satisfy the condition $k_x^{TE,TM} < n_{sup}k_0$, $n_{sup}k_0 \leq k_x^{TE,TM} < n_{sub}k_0$, and $k_x^{TE,TM} \geq n_{sub}k_0$, respectively, with the mode frequency

$$\omega_q^{TE} = \frac{c_0}{\sqrt{\varepsilon_{x,y}^{eff}}} \sqrt{(k_x^{TE})^2 + \left(\frac{q\pi}{l}\right)^2} \tag{5.11}$$

$$\omega_q^{TM} = c_0 \sqrt{\frac{(k_x^{TM})^2}{\varepsilon_z^{eff}} + \left(\frac{q\pi}{l}\right)^2 \frac{1}{\varepsilon_{x,y}^{eff}}} \tag{5.12}$$

where the number of supported modes being determined by the sign of the permittivity components. For higher-order modes, it may be necessary to take into account deviations from the EMT due to spatial dispersion effects [25]. The sensitivity of the mode frequency $\omega_q^{TE,TM}$ to variations in ε_h, for a given q and $k_x^{TE,TM}$, immediately follows as

$$\frac{\partial \omega_q^{TE}}{\partial \varepsilon_h'} = -i\frac{\partial \omega_q^{TE}}{\partial \varepsilon_h''} = -\frac{\omega_q^{TE}}{2\varepsilon_{x,y}^{eff}} \frac{\partial \varepsilon_{x,y}^{eff}}{\partial \varepsilon_h'} = i\frac{\omega_q^{TE}}{2\varepsilon_{x,y}^{eff}} \frac{\partial \varepsilon_{x,y}^{eff}}{\partial \varepsilon_h''} \tag{5.13}$$

$$\frac{\partial \omega_q^{TM}}{\partial \varepsilon_h'} = -i\frac{\partial \omega_q^{TM}}{\partial \varepsilon_h''} = -\frac{c_0^2}{2\omega_q^{TM}}\left[\left(\frac{k_x^{TM}}{\varepsilon_z^{eff}}\right)^2 \frac{\partial \varepsilon_z^{eff}}{\partial \varepsilon_h'} + \left(\frac{q\pi}{l\varepsilon_{x,y}^{eff}}\right)^2 \frac{\partial \varepsilon_{x,y}^{eff}}{\partial \varepsilon_h'}\right]$$
$$= i\frac{c_0^2}{2\omega_q^{TM}}\left[\left(\frac{k_x^{TM}}{\varepsilon_z^{eff}}\right)^2 \frac{\partial \varepsilon_z^{eff}}{\partial \varepsilon_h''} + \left(\frac{q\pi}{l\varepsilon_{x,y}^{eff}}\right)^2 \frac{\partial \varepsilon_{x,y}^{eff}}{\partial \varepsilon_h''}\right] \quad (5.14)$$

and similarly for Au. Note the connection of the mode frequency with respect to the real and imaginary parts of permittivity; this is a direct consequence of Eq. (5.5)-(5.8). Eq. (5.13), (5.14), along with Eq. (5.3), (5.4) indicate the important interplay between the absolute values and variations in $\varepsilon_{x,y}^{eff}$ and ε_z^{eff} for determining shifts in mode frequencies, e.g. when one of the permittivity component becomes small. Their relative contributions also depend on the nanorod filling factor and wavelength.

The TM-mode position dependence with respect to the real part of the constituents' permittivities is plotted in Fig. 5.7 within the 1^{st} Brillouin zone to ensure EMT validity. As the mode number increases from $q = 1$ to $q = 5$ there is an order of magnitude increase in the sensitivity of the mode frequency to the host medium refractive index variations (Fig. 5.7(a)) and a two orders of magnitude increase to that of Au (Fig. 5.7(c)). The superior refractive index sensitivity of high-order modes is a consequence of their spectral position close to the resonance in $\varepsilon_{x,y}^{eff}$ (Fig. 5.4) and the increased field gradients inside the metamaterial for higher-order modes. These gradients are determined by the mode's spatial frequency $q\pi/l$, increasing with increasing q value or decreased sensor thickness l. Interestingly, this leads to an increase in the mode sensitivity as the mode shifts to shorter wavelengths, a trend opposite to that observed with conventional SPR or LSPR transducers. In particular, shifting the resonance frequency of the fundamental mode ($q = 1$) from 0.5 eV to 1.5 eV, by decreasing the metamaterial layer thickness from 500 nm to 130 nm, results in a 500% increase in sensitivity as monitored in both transmittance and reflectance at normal incidence. An increase in the

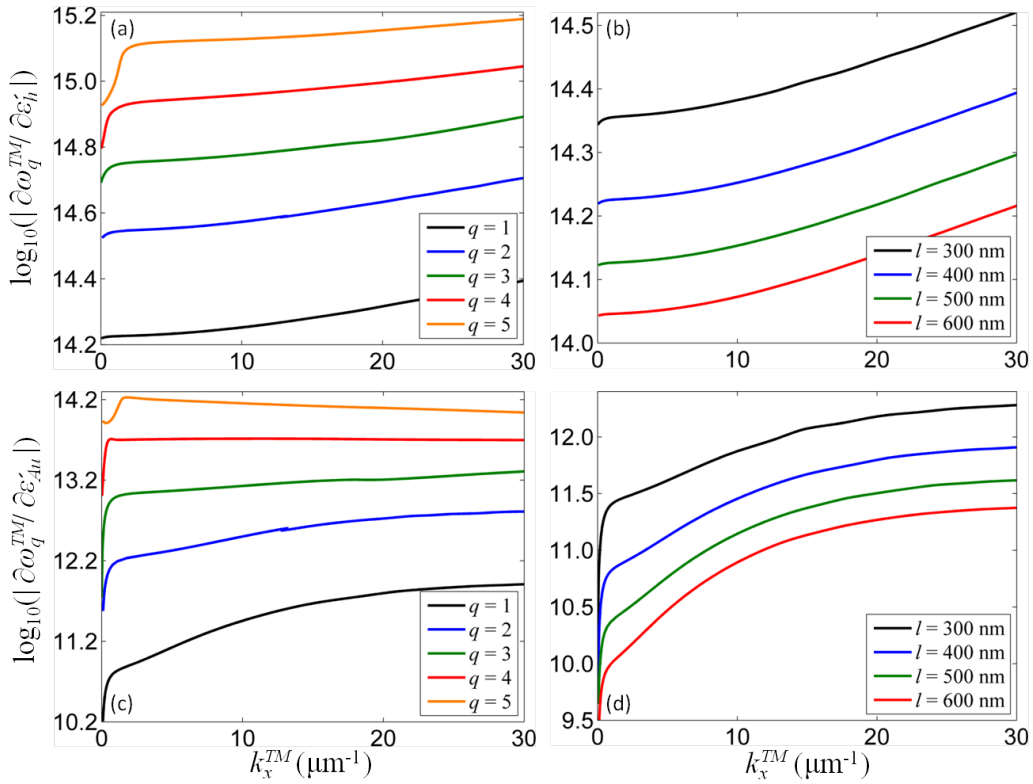

Figure 5.7: The TM-mode frequency shift with (a),(b) ε_h' and (c),(d) ε_{Au}' variations: (a),(c) the first five modes ($q = 1 - 5$) for $l = 400$ nm and (b),(d) the fundamental mode ($q = 1$) for various transducer thicknesses. Geometry is the same as in Fig. 5.4(b).

nanorod filling factor p, all other parameters being kept constant, leads to a decrease in the sensitivity of the mode position. Again, this is reminiscent of the increased mode delocalization within the metamaterial with decreasing frequency. Comparing Fig. 5.7(a) and 5.7(c) we can also observe that, for a given mode q, the rate of change of the resonance position is stronger with respect to changes in the real part of the host permittivity compared to changes in the real part of Au permittivity, $\partial\omega_q^{TM}/\partial\varepsilon_h' \gg \partial\omega_q^{TM}/\partial\varepsilon_{Au}'$. This is the result of the modal field distribution being mainly present in the host

medium.

The mode frequency sensitivity with respect to ε''_h and ε''_{Au} was also examined, giving a similar trend to Fig. 5.7(a), (c), but with a one-to-two orders of magnitude smaller sensitivity to the variations in either ε'_h or ε'_{Au} (not shown). This indicates that the real parts of both the host medium and Au will affect sensing more than the imaginary counterparts. Monitoring the analyte's refractive index changes at normal incidence provides the lowest sensitivity with regards to the modes' spectral shift (Fig. 5.7).

As a next step, the impact of the thickness of the metamaterial transducer, l, was examined. Fig. 5.7(b), (d) show the $q = 1$ mode frequency sensitivity with respect to ε'_h and ε'_{Au} as l varies from 300 nm to 600 nm. In both cases, as the waveguide thickness increases, the sensitivity drops, in agreement with the mode position shift to lower frequencies. A similar behaviour is observed for higher-order modes (not shown). This behaviour can be clarified more explicitly by examining the normal incidence behaviour of the mode resonance frequency, simplifying Eq. (5.14) to $\partial\omega_q^{TM}/\partial\{\varepsilon'_h, \varepsilon'_{Au}\} = -[c_0\pi(\varepsilon_{x,y}^{eff})^{-3/2}/2l]\partial\varepsilon_{x,y}^{eff}/\partial\{\varepsilon'_h, \varepsilon'_{Au}\}$, clearly showing the inverse proportionality of the mode resonance sensitivity to the metamaterial thickness l for unbound modes. Thus, for a given mode number, a thinner transducer will be more sensitive. This result has been verified using numerical simulations as long as the mode considered had a frequency not exceeding that corresponding to a free-space wavelength of 650 nm, or beyond the range of high losses due to $\mathrm{Im}(\varepsilon_{x,y}^{eff})$ (Fig 5.4(b)).

The same analysis, but this time when the TE-mode frequency varies, is presented in Fig. 5.8. The mode frequency range in Fig. 5.8(a), (c) is approximately the same as in TM-case (Fig. 5.7(a), (c)) meaning that the sensing capabilities between these 2 polarizations are comparable ($\partial\omega_q^{TM}/\partial\{\varepsilon'_h, \varepsilon'_{Au}\} \sim$

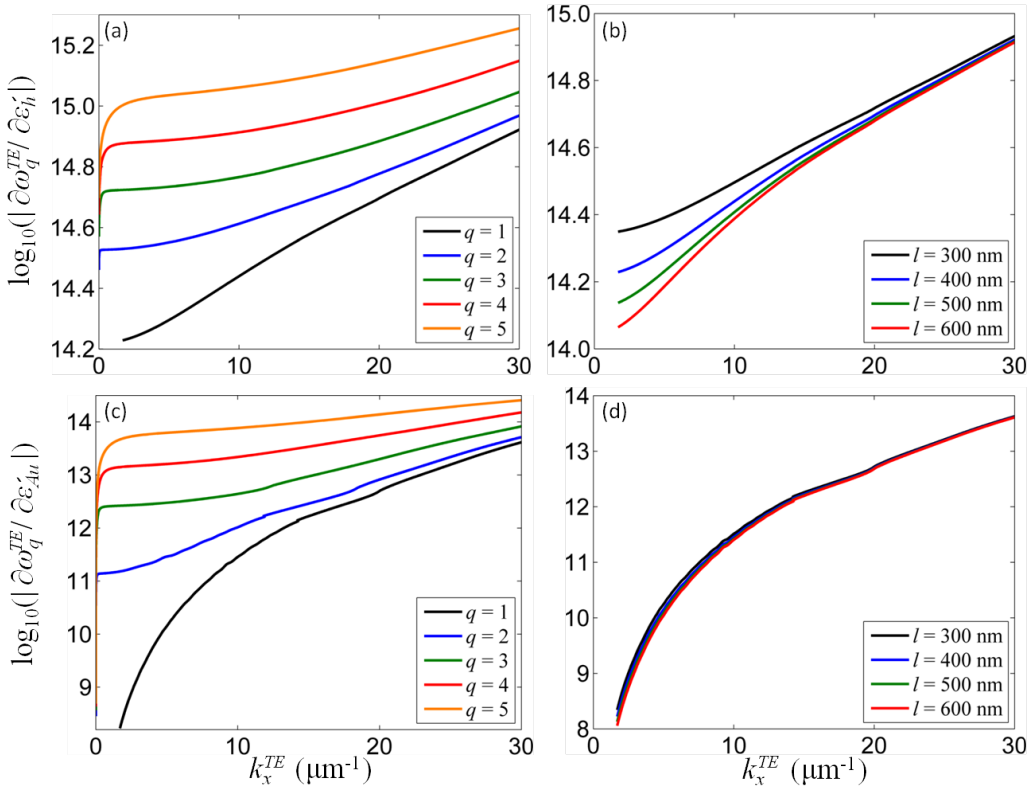

Figure 5.8: The TE-mode frequency shift with (a),(b) ε'_h and (c),(d) ε'_{Au} variations: (a),(c) the first five modes ($q = 1 - 5$) for $l = 400$ nm and (b),(d) the fundamental mode ($q = 1$) for various transducer thicknesses. Geometry is the same as in Fig. 5.4(b).

$\partial\omega_q^{TE}/\partial\{\varepsilon'_h, \varepsilon'_{Au}\}$). Only the fundamental mode ($q = 1$) has a different behaviour, with a mode frequency variation distinctively lower at low wavevectors; this is due to the absence of cut-off frequency of the fundamental mode for TE-polarization. It is important to note that TE-mode frequency variation is increasing faster at higher wavevectors, compared to the TM counterpart, and eventually all the modes converge at very high wavevectors. This phenomenon can be understood due to the positive group velocity of TE waveguided modes as explained in Chapter 4 and [15]. Similarly to TM-

scenario, the mode frequency sensitivity with respect to ε''_h and ε''_{Au} was also examined giving one-to-two orders of magnitude smaller sensitivity compared to ε'_h or ε'_{Au} (not shown).

Regarding the thickness of the metamaterial transducer (Fig. 5.8(b), (d)), TE-mode frequency variation has comparable values, with respect to the TM scenario, for low wavevectors ($k_x^{TE,TM} < 15\ \mu m^{-1}$) but becomes significantly higher as wavevector increases. A striking difference is the minor dependence of TE-mode frequency change as l increases from 300 nm to 600 nm (Fig. 5.8(b), (d)). To understand this phenomenon let us investigate the effects of TE polarization in the periodic nanorod array: The electric field ($\mathbf{E}$) will have only one component parallel to the interface, thus the electrons (e) will exhibit an oscillation force, $\mathbf{F} = e\mathbf{E}$, which will also be parallel to the interface. However the sensing medium is finite only along the extraordinary axis meaning that electrons can not sense changes in thickness, l. As a result the TE-mode frequency variation is expected to have lesser dependence in l with respect to TM-case.

5.5 Numerical examination

In order to show the complete pattern of the metamaterial behaviour with the refractive index modifications of its constituents, which are used to describe the sensing capabilities of the metamaterial and its active nanophotonic properties, we have also numerically studied the modification of the metamaterial resonances with changes of the complex refractive index of the superstrate, n_{sup}, and embedding medium, n_h. These changes may originate from an unknown analyte or a material with nonlinear or electro-optical properties used for switching/modulation purposes. It may also be represented by Au itself

as a source of nonlinearity for all-optical control or as temperature sensor. We examine how the latter two parameters translate into the sensitivity of the metamaterial transducer for the detection of the bulk refractive index changes of an analyte. We first consider a non-absorptive analyte (Section 5.5.1) for which only the real part of the refractive index changes. Then, the effect of changes in the absorption of analyte is studied (Section 5.5.2). Finally, the impact modifications of the refractive index of Au on the optical properties of the metamaterial is discussed in Section 5.5.3. For all simulations, the sensing geometry was kept the same as in Fig. 5.4(b) with a nanorod height fixed at 400 nm.

5.5.1 Sensing variations in the real part of the refractive index

We start with the nonabsorptive case, corresponding to the situation of an analyte consisting of nonresonant molecules. In this situation, changes in the refractive index may be induced through Kerr nonlinearities of the host medium or superstrate, electro-optical, thermo-optical or pressure effects. Fig. 5.9(a)-(c) show the reflectance sensitivity (FoM$_I$) for different wavelengths and angles of incidence for TM-polarization, when changes of the refractive index originate from either the superstrate (Δn_{sup}), host medium (Δn_h), or both simultaneously (Δn_b). The FoM$_I$ has a dispersive behaviour, changing sign in the vicinity of the mode resonances (Fig. 5.9(b), (c)). This behaviour is observed as a result of a simultaneous change in both the intensity (ΔI) and wavelength ($\Delta\lambda$) of the metamaterial modes. However, when ΔI has a dominating role, the FoM$_I$ retains its sign (for example, in Fig. 5.9(a) for the angular range between 0° and 50°). From Fig. 5.9(a), it is clear that the strongest variations of the optical response are observed in the

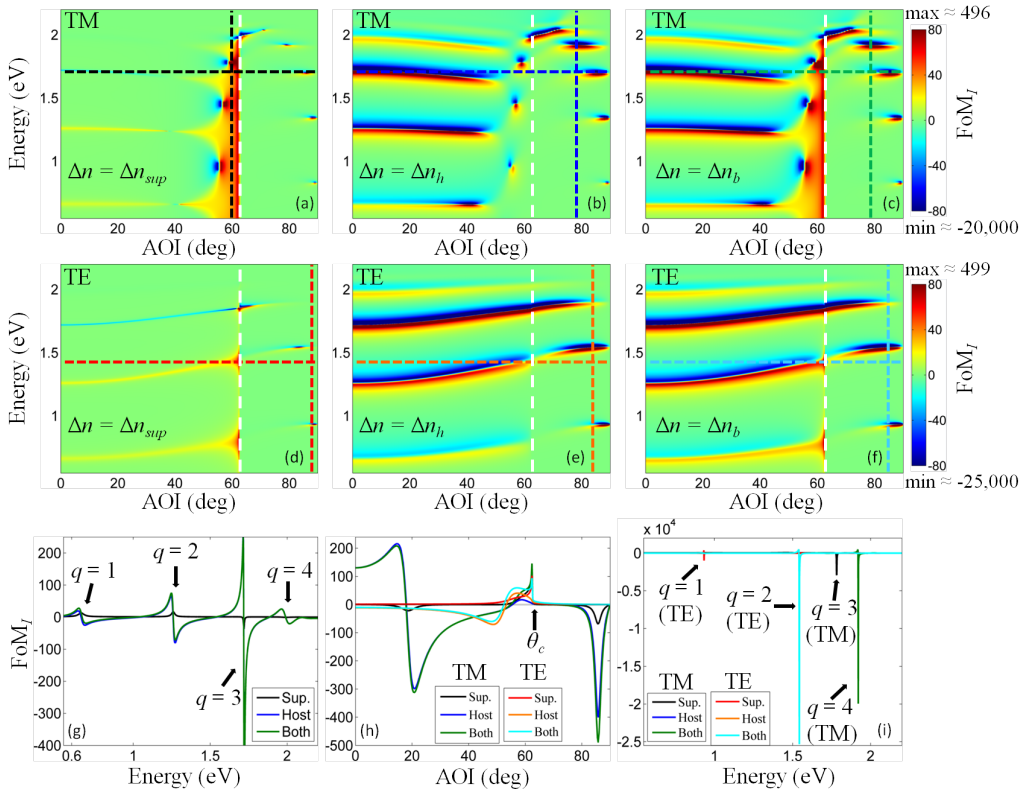

Figure 5.9: Spectral and angular dependencies of the intensity figure of merit (FoM$_I$) for the changes of the refractive index ($\Delta n = 0.002$) of superstrate (a),(d), host medium (b),(e) and both (c),(f) for (a)-(c) TM-polarization and (d)-(f) TE-polarization. Superstrate light line is also shown (white dashed line). Colour scale is the same to enable comparison. (g) Cross-sections of (a)-(f) at normal incidence. (h) Cross-sections of (a)-(f) tracking the $q = 3$ mode (horizontal dashed lines) at 1.7 eV for TM-polarization and $q = 2$ mode at 1.4 eV for TE-polarization. (i) Cross-sections of (a)-(f) at angles where highest sensitivity is observed (vertical dashed lines). All images were acquired from EMT approximation.

vicinity of the modes of the metamaterial transducer, but with a sensitivity maximised near the critical angle θ_c. The reason is that when the refractive index of the superstrate is changed by Δn_{sup}, the critical angle itself will

be affected leading to a strong sensitivity along the superstrate light line, the so-called near cut-off regime. This behaviour was also captured with 3D numerical analysis showing an order of magnitude higher sensing close to θ_c compared to lower angles.

A different behaviour is observed for the variations of the refractive index of the host medium Δn_h (Fig. 5.9(b)). In this case, the sensitivity of leaky modes is higher than that of unbound modes. When both the refractive index of the host medium and the superstrate change, a combination of the above individual cases is observed, although not just a simple addition of individual sensitivities since modes from the metamaterial layer are penetrating the superstrate medium (Fig. 5.9(c)). Not surprisingly, the results show that a small change in the refractive index of the superstrate affects the sensitivity only at angles very close to θ_c, while for any other incidence angle the host medium has a dominating role. Both TM (Fig. 5.9(a)-(c)) and TE (Fig. 5.9(d)-(f)) modes of the metamaterial transducer have comparable sensitivities if the analyte is incorporated between the rods. Full wave simulations confirmed this trend, but with TE modes exhibiting slightly lower sensitivity (not shown). This is not surprising giving the nature of the anisotropic waveguided modes determined by all components of the effective permittivity tensor. For low filling factors, the role of TM modes increases, when the $\varepsilon_{x,y}^{eff}$ sensitivity becomes smaller (not shown).

Fig. 5.9(g)-(i) shows the sensitivity for selected wavelengths and angles of incidence. The spectral dependence of FoM_I at normal incidence (Fig. 5.9(g)) reveals that the mode with the highest sensitivity ($q = 3$) reaches FoM_I exceeding 400, with the host medium being mainly responsible for this enhanced sensitivity. As mode number increases from $q = 1$ to $q = 3$, the FoM_I also increases in agreement with the analytical examination (Fig.

5.7(a)). However, the $q = 4$ mode, located close to 2 eV, shows a decreased sensing capability contrary to the analytical scenario. This is due to the increased absorption of $\varepsilon_{x,y}^{eff}$ (Fig. 5.4(b)) at wavelengths below 650 nm ($>$ 1.9 eV), which are not tracked with the analytical model discussed in Section 5.4. Fig. 5.9(h) examines the angular dependence of the sensitivity for the modes with the highest sensitivities: ($q = 3$) at 1.7 eV for TM-polarization and $q = 2$ at 1.4 eV for TE-polarization. These plots show a typical dispersive behaviour of the mode position, with high sensitivities observed on both sides of the resonance. As expected, the highest FoM_I is observed above θ_c for leaky modes. This behaviour is better observed in Fig. 5.9(i) which depicts the global maximum FoM_I for TM-polarization, for the $q = 4$ mode located at a wavelength of about 645 nm and for an angle of incidence of about 79°, above the critical angle. Similarly for the TE-case, the highest FoM_I is observed for the $q = 2$ mode for a wavelength close to 870 nm and at 84°. Only variations in the superstrate refractive index lead to high sensitivity which lies just below θ_c, at 58.8° for reasons already explained above. In the following sections, we will concentrate only on the sensing with TM modes, pointing out that in the case of absorption variation sensing TE-modes also have comparable but slightly lower FoM_I.

Regardless the polarization chosen, the $q = 1$ mode exhibits the highest resonant shift reaching almost 4,000 nm/RIU, while the highest $\mathrm{FoM}_\lambda \approx 167$ is observed for the mode $q = 3$, outperforming both SPR and LSPR sensors which have typical FoM_λ around 23 [2] and 8 [2, 29], respectively. The origin of such high FoM_λ is in the influence of the analyte not only directly on the electromagnetic mode properties, as usual for conventional sensors, but also on the effective permittivity of the metamaterial which is connected to the host medium refractive index (Fig. 5.5 and 5.6), on the microscopic

level, this is the result of plasmon-plasmon interactions within the nanorod array [18, 30, 31]. The intensity figure of merit (FoM_I) is proportional to $(\Delta R/R_0)/\Delta n$ and can be directly observed in Fig. 5.9. Depending on the wavelength and AOI, FoM_I can be as high as 25,000, significantly higher that any LSP- and SPP-based [28] sensors (Fig. 5.9(i)). Both FoM_I and FoM_λ can be further tailored and enhanced with geometrical parameters of the transducer, with FoM_λ reaching up to 300 has been experimentally demonstrated [16].

5.5.2 Sensing variations in the imaginary part of the refractive index

Turning to the impact of the absorption variations on the metamaterial transducer response, Fig. 5.10(a)-(c) show the reflectance variations for different wavelengths and angles of incidence for TM-polarized incident light with changes in the imaginary part of the refractive index of either the superstrate (Δn_{sup}), the host medium (Δn_h), or both simultaneously (Δn_b). Similar to changes in the refractive index (Fig. 5.9(a)-(c)), the sensitivity of the transducer originates from the modal dispersion of the metamaterial slab. Interestingly, an increase in the absorption leads to an increased reflection for some angles, while others behave oppositely. Again, an increased sensitivity is observed for higher mode order moving from $q = 1$ to 3, with the decreased sensitivity for the $q = 4$ mode due to losses (Fig. 5.10(d)).

Similarly to the nonabsorbing case, the mode with the highest FoM_I ($q = 3$) depicted in Fig. 5.10(d), showed a resonant shift of more than 700 nm/RIU, while the $q = 1$ mode exhibits the highest resonant shift reaching values close to 4,000 nm/RIU. Tracking the $q = 3$ mode at various AOI (Fig. 5.10(e)), its sensitivity is enhanced around both 20° and 85°, where the mode is leaky.

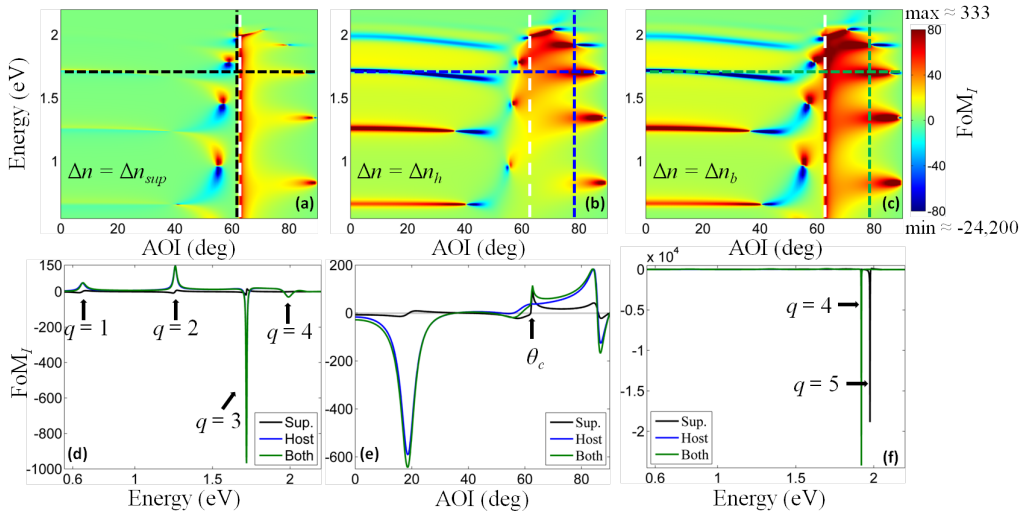

Figure 5.10: Spectral and angular dependencies of the intensity figure of merit (FoM_I) with the changes of the absorption ($\Delta n = 0.002i$) of superstrate (a), host medium (b) and both (c), for TM-polarization. Superstrate light line is also shown (white dashed line). Colour scale is the same to enable comparison. (d) Cross-sections of (a)-(c) at normal incidence. (e) Cross-sections of (a)-(c) tracking the $q = 3$ mode (horizontal dashed lines) at 1.7 eV. (f) Cross-sections of (a)-(c) at angles where highest sensitivity is observed (vertical dashed lines). All images were acquired from EMT approximation.

The FoM_λ of the $q = 3$ mode in Fig. 5.10(d) is close to 167, similar to the nonabsorbing analytes discussed in Section 5.5.1. However, its FoM_I reaches a value of almost 1,000, or at least twice higher than the corresponding one in Fig. 5.9(g) for the same mode ($q = 3$) since the influence of the imaginary part of the permittivity on reflection is stronger than the real one. The highest FoM_I in Fig. 5.10(f) exceeds 24,000, which is a significant 25% higher than the TM-FoM_I for sensing nonabsorbing analytes (Fig. 5.9(i)).

5.5.3 The effects of refractive index variations in Au

Lastly, the dispersive sensitivity of the metamaterial for refractive index variations of the Gold nanorods (Δn_{Au}) was investigated. These can be induced either optically, via the Kerr-type nonlinearity of the metal, or via thermo-optical effects. Fig. 5.11(a), (b) depict the reflectance variations when either the real or the imaginary part of the refractive index of Au varies. Note that the variations were set to be wavelength independent, which would correspond to different electronic/lattice temperatures at different wavelengths, to allow for comparison with the previous section but without altering the generality of the results. The sensitivity is smallest below the superstrate light line. More specifically, low-q modes exhibit lower sensitivities compared to high-q modes, located close to 2 eV. Again, material losses at higher frequency eventually limit the sensitivity of these modes as well. Interestingly, the sensitivity observed here is smaller than those resulting from changes in either host medium or superstrate discussed above. Examining again the mode with the highest sensitivity ($q = 3$) at normal incidence as shown in Fig. 5.11(c), (d), one can clearly see that FoM_I is approximately one order of magnitude less than for the scenarios in Fig. 5.9(g) and 5.10(d). The FoM_λ of the aforementioned mode to Au permittivity variations is 168, very close to FoM_λ observed for sensing of the analytes above. At the same time, the intensity figure of merit for Au permittivity modification is much smaller than for the sensing of analytes giving a maximum value of only 1,200 (Fig. 5.11(e)). It should be mentioned that the resonant shift per RIU is only a few nm regardless of the mode chosen; a result that applies for variations in both the real and imaginary part of the refractive index of Au.

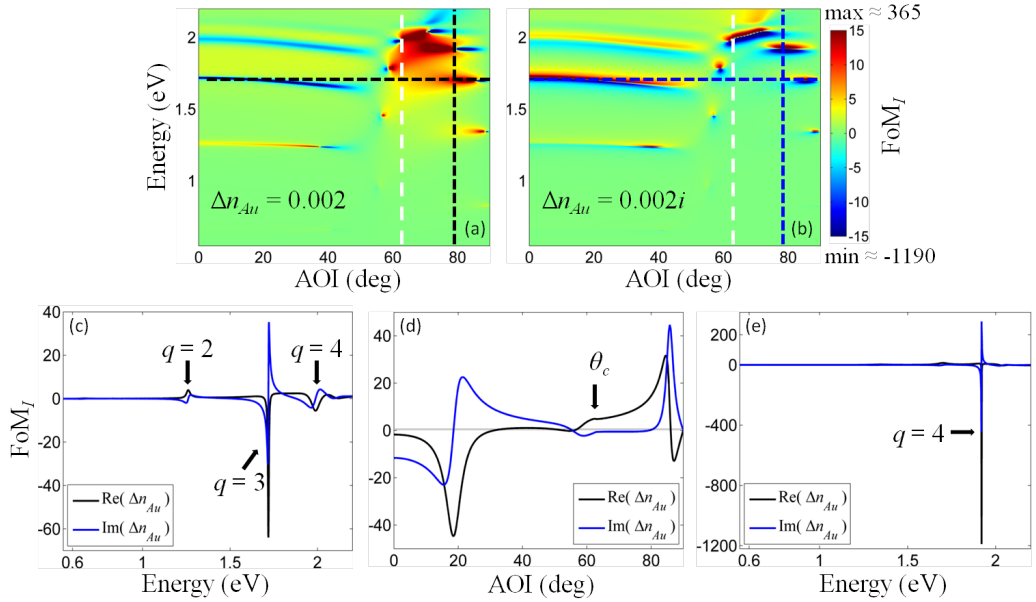

Figure 5.11: Spectral and angular dependencies of the intensity figure of merit (FoM$_I$) with the changes of (a) refractive index and (b) absorption of Au for TM-polarization. Superstrate light line is also shown (white dashed line). Colour scale is the same to enable comparison. (c) Cross-sections of (a)-(b) at normal incidence. (d) Cross-sections of (a)-(b) tracking the $q = 3$ mode (horizontal dashed lines) at 1.7 eV. (f) Cross-sections of (a)-(b) at angles where highest sensitivity is observed (vertical dashed lines). All images were acquired from EMT approximation.

5.6 Summary

In conclusion we have analysed, both analytically and numerically, the performance of a metamaterial transducer in sensing applications varying different geometrical and optical parameters such as the refractive indices of host medium, superstrate and Au as well as the filling factor and height of nanorods. The main results can be summarized as follows

1. The analytical model showed the increased refractive index sensitiv-

ities for higher-order modes (q) and decreasing thickness (l) of the transducer. The dependence in thickness for TE-polarization was less pronounced due to the absence of the extraordinary electric field component. The numerical model captured the same trend as long as the excited modes were away from the resonant absorption associated with ordinary modes of the metamaterial.

2. The sensitivity to the changes in the refractive index of a host medium was much stronger than that of the superstrate refractive index, confirming the important role of the interaction between plasmonic resonances of the nanorod assembly in the sensing performance of the metamaterial (Fig. 5.12). Furthermore, the sensitivity was increased when sensing changes in the analyte's absorption. The sensing capabilities of the metamaterial to changes in the refractive index of Au were shown to be more modest. Interestingly, in certain configurations, both TE (Fig. 5.12(a)) and TM (Fig. 5.12(b)) modes of the metamaterial transducer have comparable sensitivities, opening up opportunities for polarization multiplexing in sensing experiments.

3. Finally, the metamaterial transducer is shown to provide enhanced sensing performance compared to both SPP and LSP-based geometries presented in the literature to date, both in terms of $\mathrm{FoM}_{\lambda,I}$ and nm/RIU characteristics achievable. The above conclusions are valid in the hyperbolic dispersion regime and may be modified if the operating wavelength overlaps the ENZ regime of the metamaterial dispersion.

The results can be used as a design strategy to enhance flexibility of ultrasensitive transducers for bio- or chemical sensors or nonlinear photonic devices based on plasmonic hyperbolic metamaterials.

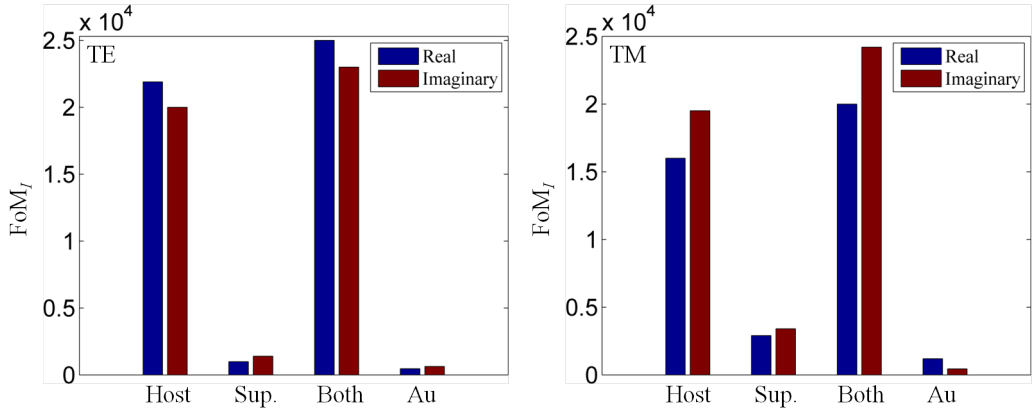

Figure 5.12: Highest FoM_I for the real and imaginary refractive index variations of the different materials considered in this Chapter, for (a) TE and (b) TM-polarization.

References

[1] J. Homola, Ed., *Surface Plasmon Resonance Based Sensors.* Springer, (2006).

[2] J. N. Anker, W. P. Hall, O. Lyandres, N. C. Shah, J. Zhao, and R. P. V. Duyne, "Biosensing with plasmonic nanosensors," *Nat. Mat.*, vol. **7**, pp. 442–453, (2008).

[3] M. E. Stewart, C. R. Anderton, L. B. Thompson, J. Maria, S. K. Gray, J. A. Rogers, and R. G. Nuzzo, "Nanostructured plasmonic sensors," *Chem. Rev.*, vol. **108**, pp. 494–521, (2008).

[4] B. Liedberg, C. Nylander, and I. Lundstrum, "Surface-plasmon resonance for gas-detection and biosensing," *Sensors Actuators B*, vol. **4**, pp. 299–304, (1983).

[5] M. Kauranen and A. V. Zayats, "Nonlinear plasmonics," *Nat. Phot.*, vol. **6**, pp. 737–748, (2012).

[6] A. V. Zayats and S. Maier, Eds., *Active Plasmonics and Tunable Plasmonic Metamaterials.* Wiley & Sons, (2014).

[7] S. Lal, S. Link, and N. J. Halas, "Nano-optics from sensing to waveguiding," *Nat. Phot.*, vol. **1**, pp. 641–648, (2007).

[8] M. Svedendahl, S. Chen, A. Dimitriev, and M. Käll, "Refractometric sensing using propagating versus localized surface plasmons: A direct comparison," *Nano Lett.*, vol. **9**, pp. 4428–4433, (2009).

[9] A. V. Kabashin and P. I. Nikitin, "Surface plasmon resonance interferometer for bio- and chemical-sensors," *Opt. Commun.*, vol. **150**, pp. 5–8, (1998).

[10] P. N. Prasad, Ed., *Introduction to Biophotonics*. Wiley-Interscience, (2003).

[11] S. Nie and S. R. Emory, "Probing single molecules and single nanoparticles by surface-enhanced raman scattering," *Science*, vol. **275**, pp. 1102–1106, (1997).

[12] A. J. Haes and R. P. V. Duyne, "A unified view of propagating and localized surface plasmon resonance biosensors," *Anal. Bioanal. Chem.*, vol. **379**, pp. 920–930, (2004).

[13] C. M. Soukoulis and M. Wegener, "Past achievements and future challenges in the development of three-dimensional photonic metamaterials," *Nat. Phot.*, vol. **5**, pp. 523–530, (2011).

[14] J. Yao, Z. Liu, Y. Liu, Y. Wang, C. Sun, G. Bartal, A. M. Stacy, and X. Zhang, "Optical negative refraction in bulk metamaterials of nanowires," *Science*, vol. **321**, p. 930, (2008).

[15] N. Vasilantonakis, M. E. Nasir, W. Dickson, G. A. Wurtz, and A. V. Zayats, "Bulk plasmon-polaritons in hyperbolic nanorod metamaterial waveguides," *Laser & Photonics Reviews*, vol. **9**, pp. 345–353, (2015).

[16] G. A. Wurtz, R. Pollard, W. Hendren, G. P. Wiederrecht, D. J. Gosztola, V. A. Podolskiy, and A. V. Zayats, "Designed ultrafast optical nonlinearity in a plasmonic nanorod metamaterials enhanced by nonlocality," *Nature Nanotech.*, vol. **6**, pp. 107–111, (2011).

[17] M. E. Nasir, W. Dickson, G. A. Wurtz, W. P. Wardley, and A. V. Zayats, "Hydrogen detected by the naked eye: optical hydrogen gas sensors based on core/shell plasmonic nanorod metamaterials," *Adv. Mat.*, vol. **26**, pp. 3532–3537, (2014).

[18] W. Dickson, G. A. Wurtz, P. Evans, D. O'Connor, R. Atkinson, R. Pollard, and A. V. Zayats, "Dielectric-loaded plasmonic nanoantenna arrays: A metamaterial with tuneable optical properties," *Phys. Rev. B*, vol. **76**, p. 115411, (2007).

[19] V. V. Yakolev, W. Dickson, A. Murphy, J. McPhillips, R. J. Pollard, V. A. Podolskiy, and A. V. Zayats, "Ultrasensitive non-resonant detection of ultrasound with plasmonic metamaterials," *Adv. Mat.*, vol. **25**, pp. 2351–2356, (2013).

[20] P. B. Johnson and R. W. Christy, "Optical constants of the noble metals," *Phys. Rev. B*, vol. **6**, pp. 4370–4379, (1972).

[21] T. Sannomiya, O. Scholder, K. Jefimovs, C. Hafner, and A. B. Dahlin, "Investigation of plasmon resonances in metal films with nanohole arrays for biosensing applications," *Small*, vol. **7**, pp. 1653–1663, (2011).

[22] H. N. Daghestani and B. W. Day, "Theory and applications of surface plasmon resonance, resonant mirror, resonant waveguide grating, and dual polarization interferometry biosensors," *Sensors*, vol. **10**, pp. 9630–9646, (2010).

[23] A. V. Kabashin, P. Evans, S. Pastkovsky, W. Hendren, G. A. Wurtz, R. Atkinson, R. Pollard, V. A. Podolskiy, and A. V. Zayats, "Plasmonic nanorod metamaterials for biosensing," *Nat. Mat.*, vol. **8**, pp. 867–871, (2009).

[24] J. Elser, R. Wangberg, V. A. Podolskiy, and E. E. Narimanov, "Nanowire metamaterials with extreme optical anisotropy," *Appl. Phys. Lett.*, vol. **88**, p. 261102, (2006).

[25] B. M. Wells, A. V. Zayats, and V. A. Podolskiy, "Nonlocal optics of plasmonic nanowire metamaterials," *Phys. Rev. B*, vol. **89**, p. 035111, (2014).

[26] K.-T. Tsai, G. A. Wurtz, J.-Y. Chu, T.-Y. Cheng, H.-H. Wang, A. V. Krasavin, J.-H. He, B. M. Wells, V. A. Podolskiy, J.-K. Wang, Y.-L. Wang, and A. V. Zayats, "Looking into meta-atoms of plasmonic meta-material," *Nano Lett.*, vol. **2014**, pp. 4971–4976, (2014).

[27] W. N. Hansen, "Electric fields produced by the propagation of plane coherent electromagnetic radiation in a stratified medium," *Opt. Soc. of America*, vol. **58**, pp. 380–390, (1968).

[28] J. Feng, V. S. Siu, A. Roelke, V. Mehta, S. Y. Rhieu, G. T. R. Palmore, and D. Pacifici, "Nanoscale plasmonic interferometers for multispectral, high-throughput biochemical sensing," *Nano Lett.*, vol. **2012**, pp. 602–609, (2012).

[29] H. Liao, C. L. Nehl, and J. H. Hafner, "Biomedical applications of plasmon resonant metal nanoparticles," *Nanomedicine*, vol. **1**, pp. 201–208, (2006).

[30] G. A. Wurtz, W. Dickson, D. O'Connor, R. Atkinson, W. Hendren, P. Evans, R. Pollard, and A. V. Zayats, "Guided plasmonic modes in nanorod assemblies: Strong electromagnetic coupling regime," *Opt. Express*, vol. **16**, pp. 7460–7470, (2008).

[31] G. A. Wurtz, P. R. Evans, W. Hendren, R. Atkinson, W. Dickson, R. J. Pollard, and A. V. Zayats, "Molecular plasmonics with tuneable exciton-plasmon coupling strength in j-aggregate hybridized au nanorod assemblies," *Nano Lett.*, vol. **7**, pp. 1297–1303, (2007).

Chapter 6

Optimizing Strontium Ruthenate thin films for near-infrared plasmonic applications

Several new plasmonic materials have recently been introduced in order to achieve better temperature stability than conventional plasmonic metals and control field localization with a choice of plasma frequencies in a wide spectral range. Here, we fabricated and studied low surface roughness (001) $SrRuO_3$ thin films suitable for plasmonic applications. The films of different optical parameters were obtained by pulsed laser deposition. The influence of different oxygen pressures (20 – 300 mTorr) during deposition on structural, electrical and optical properties of thin films was examined and elucidated the relationship between charge carrier dynamics and optical constants in the near-infrared spectral range. The obtained results indicate the suitability of $SrRuO_3$ thin films for plasmonic applications with controlled plasma

frequency and epsilon-near-zero wavelength in the 324 - 392 nm and 1.11 – 1.47 μm spectral range, respectively.

Note: This Chapter was a joint effort with Laurentiu Braic. Fabrication and electrical characterization was done by him.

6.1 Introduction

Plasmonic nanostructures and metamaterials open up unprecedented possibilities to control and manipulate light at the nanoscale [1]. Plasmonic phenomena originate from the collective oscillations of free electrons interacting with electromagnetic field near the surface and require materials with high concentration of free electrons and low loss, such as Ag and Au metals. Modern technological requirements on the physical and chemical properties of plasmonic materials, such as high temperature stability, compatibility with CMOS semiconductor processing to name but a few, have stimulated a search for alternative plasmonic media [2, 3]. Plasmonic properties of ITO and doped-ZnO conductive oxides and TiN nitrides have already been demonstrated [4, 5].

$SrRuO_3$ (SRO) is a material with perovskite crystal structure that exhibits orthorhombic symmetry at room temperature as demonstrated in Fig. 6.1(a). This results when the Sr-O bond length is less than two times the Ru-O one, allowing the rotation of the Ru-O_6 octahedra. It is the rotation of the Ru-O_6 octahedra which produces the orthorhombic unit cell of Fig. 6.1(a). At room temperature, the lattice constant is a = 5.5670 Å, b = 5.5304 Å and c = 7.8446 Å, along the [100], [010] and [001] crystallographic directions, respectively [8]. At higher temperatures the crystal lattice becomes more symmetrical achieving tetragonal and cubic formations at 547 °C and

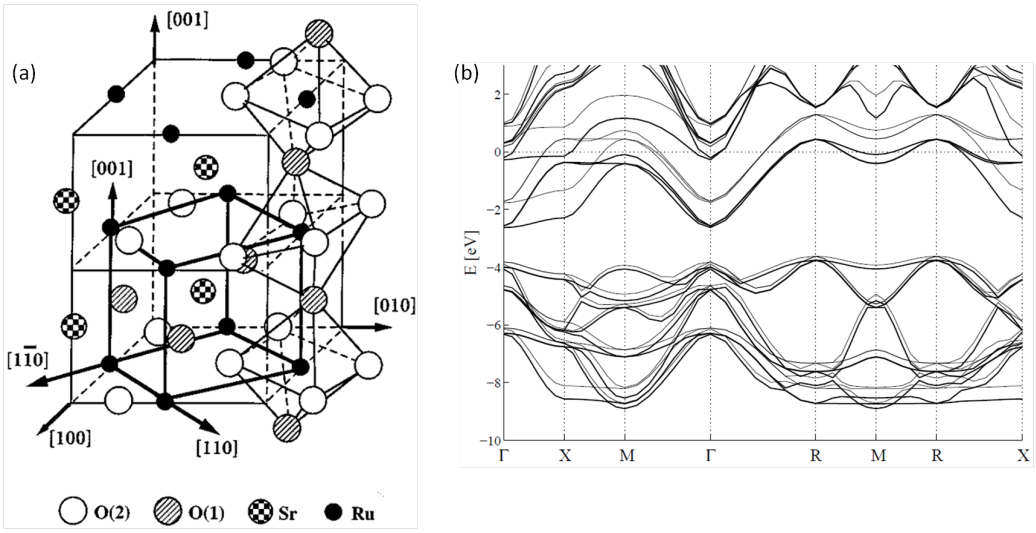

Figure 6.1: (a) Schematic presentation of the orthorhombic unit cell of $SrRuO_3$ at room temperature. The thick solid lines correspond to the pseudocubic unit cell. The lattice constant along the [100], [010] and [001] directions is 5.5670 Å, 5.5304 Å and 7.8446 Å, respectively. Adapted from [6]. (b) Band structure of SRO in a cubic perovskite crystal structure. The origin of the energy axis is the Fermi energy. Adapted from [7].

677 °C, respectively [9]. Fig. 6.1(b) demonstrates the band structure of SRO with cubic symmetry. The band structure is split into 3 regions; the Sr d orbital character above the Fermi energy (set at the origin of the energy axis), the Ru d orbital character around the Fermi energy, and the O p orbital character below the energy gap [7].

Although SRO properties are investigated for more than 50 years [10], the milestone manuscript that brought them to the fore was the fabrication of epitaxial single-crystal thin films by Eom *et al.* in 1992 [11]. After this, a plethora of fabrication methods have been proposed such as pulsed laser deposition (PLD) [12], magnetron sputtering [13], spin coating [14], or metal

organic chemical vapour deposition (MOCVD) [15] among others. Some of the most important characteristics of SRO are the high thermal and electrical conductivity, and high thermal and chemical stability (up to 1200 K in oxidizing or inert-gas atmospheres) [16]. For these reasons $SrRuO_3$ is widely used as electrode material for semiconductors and ferroelectric devices [17,18], and can be grown on Si substrates [19] or used as a standard substrate for the epitaxial growth of $SrTiO_3$ and other functional materials [20–23]. Additionally, It is used in heterostructure electronic devices as buffer layer for deposition of high-temperature superconductors and ferroelectric materials [18, 24]. It has also recently been shown how $SrRuO_3/SrTiO_3/SrRuO_3$ thin film capacitors can be a potential candidate for dynamic random access memory (DRAM) applications [25].

$SrRuO_3$ exhibits carrier dynamic similar to that of the cuprate superconductors [26–28]. The mid-infrared optical conductivity is a common feature of all ruthenium oxides, including $SrRuO_3$ [29–32]. In general, the experimental results for itinerant electron systems on the kinetic energy of the electrons, as derived from optical conductivity data are in good agreement with band-structure calculations with the deviations due to strong spin-orbit coupling, which are specific for many inter-metallic compounds with d and f electrons [33]. Considering the above described electronic properties, this Chapter examines the potential of $SrRuO_3$ thin films for plasmonic applications in the near-infrared spectral range, including optical telecommunication frequencies. Here, it is shown that the optical properties of the films can be controlled via growth conditions changing oxygen pressure during film deposition, and the epsilon-near-zero[1] (ENZ) condition can be controllably achieved

[1]Generally, the ENZ is used for anisotropic materials like the one examined in Ch. 4 and 5. Here SRO is isotropic so its ENZ corresponds to the critical point where the

in the wavelength range 1.11 - 1.47 μm, so that a negative permittivity and plasmonic behaviour are observed at longer wavelengths.

6.2 Experimental details

All $SrRuO_3$ thin films were deposited by PLD (Neocera Pioneer 120 system) from a sintered $SrRuO_3$ target on (001)-oriented single crystal MgO substrates (Crystal GmbH, Berlin). The thin film deposition process was optimized to manufacture films with the best crystalline structure and electrical conductivity [34]. Therefore, during the deposition the substrate temperature was kept at 700 °C, while the oxygen pressure was varied between 20 and 300 mTorr. Detailed description of the thin film deposition process can be found elsewhere [34]. All films were analysed ex-situ in open atmosphere, at room temperature.

A X-ray diffraction system (Brucker D2 Phaser), equipped with a graphite monochromator coupled with a scintillation counter detector using Cu K_α radiation (λ = 1.5405 μm) was used in the Bragg-Brentano mode in order to investigate the crystallographic structure and phase composition of the films. Atomic force microscopy (AFM) was performed on a Brucker INNOVA instrument. The film thickness of all samples measured using a Dektak 150 surface profiler was (100 ± 5) nm. The electrical resistivity and charge carrier concentration and mobility of the films were investigated by Ecopia HMS-3000 Hall measurement system with Van der Pauw geometry at 0.55 T magnetic field, using soldered indium contacts.

The optical characterisation of the films was done using a Horiba Jobin-Yvon Uvisel 2 ellipsometer (read Section 3.7.2). Phase-modulation reflection

isotropic permittivity crosses zero.

ellipsometry was used for all measurements at a 70° angle of incidence while the signal was acquired from an elliptical spot 2 mm x 0.7 mm in size. After the acquisition, the data were post-processed to determine optical parameters of the films in the wavelength range of 300 – 2000 nm. The MgO substrate optical constants [35] and thickness of $SrRuO_3$ were considered known and only the refractive index was fitted via the Levenberg-Marquardt minimization algorithm [36]. No pre-defined function (Drude, Tauc-Lorentz etc.) was used for the determination of the optical constants of $SrRuO_3$; they were all directly fitted to the experimental data via the "point-by-point" method.

6.3 Results and discussion

This Section describes the main outcomes from the electrical and optical characterization of SRO thin films under different oxygen pressures. We begin with AFM analysis to determine the mean roughness of the films and X-ray diffraction (XRD) for the inspection of inclusions. Subsequently, various electrical and optical characteristics are compared at different oxygen pressures, such as the change of carrier concentration, carrier mobility, permittivity and epsilon-near-zero (ENZ) energy. Lastly, the properties of SRO are compared with other standard metals to dictate the advantages/disadvantages of each one for plasmonic applications.

6.3.1 AFM and XRD analysis

Let us begin by investigating the roughness a 100 nm thick SRO film grown on MgO (001) substrate. Fig. 6.2(a) represents the AFM pattern of a 3 x 3 μm^2 SRO surface. The highest peak is 8.3 nm while the green line corresponds to the cross-section shown in Fig. 6.2(b). The root mean square (RMS) of the

surface is 0.92 nm. From the above, it is evident that the film is very smooth making it suitable for optical applications where the roughness needs to be minimal. The same results were reproduced many times, for different SRO films, with RMS never exceeding 3 - 4 nm (not shown).

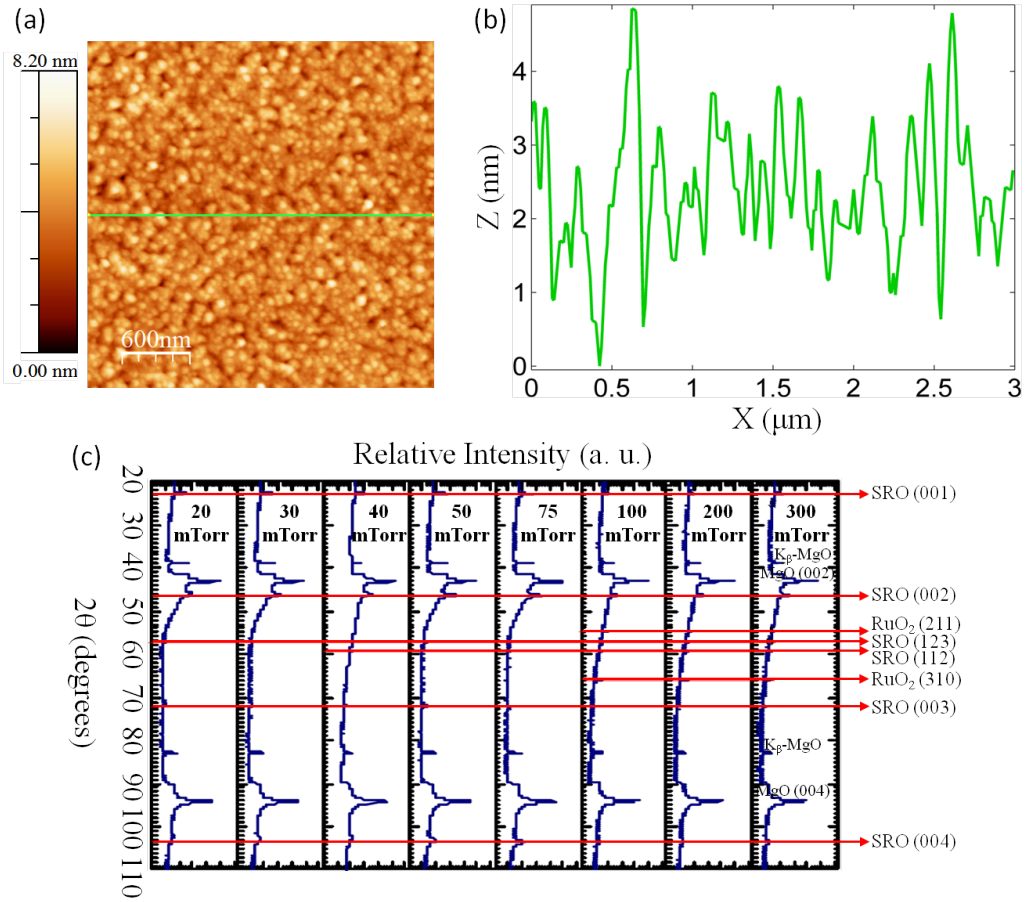

Figure 6.2: (a) AFM pattern showing the roughness of a 100 nm thick SRO layer. Analysed surface is 3 x 3 μm^2 while the RMS roughness is 0.92 nm. The green line corresponds to the cross-section shown in (b). (c) XRD diagrams of SRO films grown on MgO (001) substrates at oxygen pressures varying from 20 - 300 mTorr. Arrows show various crystallographic directions of SRO and RuO_2.

The XRD diagrams, for samples grown at oxygen pressures varying from 20 - 300 mTorr, are demonstrated in Fig. 6.2(c). The arrows show critical angles at which characteristic intensity peaks are observed due to SRO or RuO_2 contribution. All films exhibit a predominant (001) orientation; in the samples deposited at high oxygen partial pressures (100 – 300 mTorr) inclusions of SRO (112) and (123) are more pronounced while the formation of RuO_2 (211) and (310) can be observed. We thus conclude that low oxygen pressure samples (< 100 mTorr) have a better crystalline structure with less inclusions.

6.3.2 Electrical and optical characterisation of SRO

As already mentioned, the optical constants of $SrRuO_3$ films were determined via direct fitting to the experimental data. In order to understand the nature

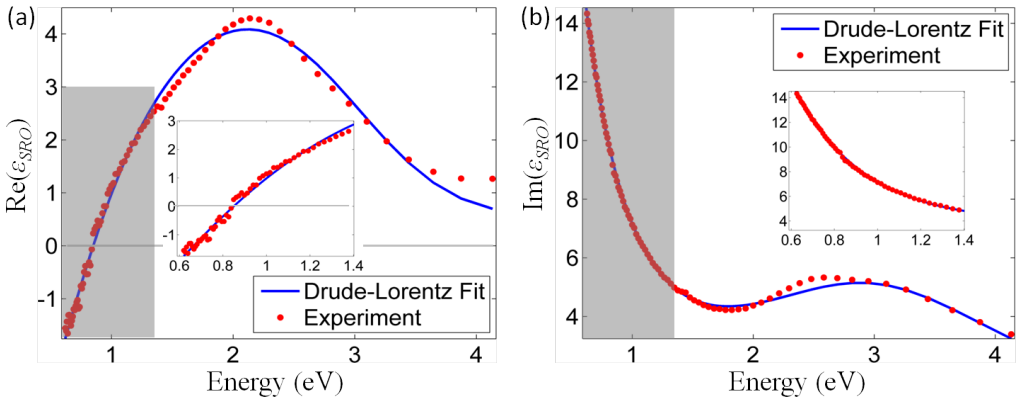

Figure 6.3: Real (a) and imaginary (b) permittivity of $SrRuO_3$ as obtained from 100 nm thick film on MgO substrate grown at 100 mTorr oxygen pressure. The data are fitted with the Drude-Lorentz oscillator of Eq. (6.1). Gray regions depict the NIR regime (< 1.4 eV). Insets show the NIR response corresponding to the greyed areas.

of the optical properties, the spectral dependence of the permittivity was fitted using the Drude model with a Lorentz-type oscillator to account for the interband transition in ruthenate materials [31]. The fitting expression will then have the form

$$\varepsilon_{SRO} = \varepsilon_b - \frac{\omega_p^2}{\omega^2 + i\omega\Gamma_1} - \frac{A^2}{\omega^2 - \omega_0^2 + i\omega\Gamma_2} \tag{6.1}$$

where high-frequency ε_b is the background permittivity, ω_p is the plasma frequency, ω_0 is the frequency of the interband transition, A is a constant, and Γ_1 and Γ_2 are the damping frequencies for the free and bound electrons, respectively.

The free parameters of the aforementioned equation were then fitted to the measured data. As an example, Fig. 6.3 shows the experimental and fitted optical constants for the film prepared at 100 mTorr oxygen pressure. The best fit (Fig. 6.3) was obtained for $\varepsilon_b = 2.67$, $\omega_p = 3.41$ eV, $A = 6.98$ eV, $\omega_0 = 3.38$ eV, $\Gamma_1 = 0.98$ eV and $\Gamma_2 = 3.23$ eV; the goodness of fit was $\chi^2 = 1.33$. The obtained spectral dependencies show that in the near infrared (NIR) regime (< 1.4 eV), the Drude part of the permittivity dominates, describing well the spectral behaviour of both the real and imaginary part of the SRO film dielectric constant (insets of Fig. 6.3). As wavelength increases, $\mathrm{Re}(\varepsilon_{SRO})$ reaches the ENZ frequency at 0.84 eV (1470 nm), so that for the photon energies below the ENZ frequency, $\mathrm{Re}(\varepsilon_{SRO})$ becomes negative in the measured spectral range up to 0.62 eV (2000 nm). Conversely, for the same wavelength range, losses (i.e. $\mathrm{Im}(\varepsilon_{SRO})$) increase monotonously. In the UV-VIS spectral range (> 1.4 eV), a non-monotonous behaviour is observed which is related to the interband transition resonance, in good agreement with [30]. The free parameters were re-evaluated for all the other films and showed a similar agreement with the optical response of Fig. 6.3. Appendix

D has the cumulative results of all the characterized films.

Continuing the investigation of SRO films, Fig. 6.4 depicts the corresponding electrical and optical measurements. All the studied films exhibit n-type conductivity and ohmic transfer function. The electron concentration (Fig. 6.4(a)) decreases with increasing pressure, hinting at the influence of trapped charges, produced by defects in the thin films or at the film/substrate interface. At the same time, the electron mobility (Fig. 6.4(b)) is the largest for the deposition pressures about 40 – 50 mTorr, while drops sharply for low oxygen pressures and slowly decreases for larger ones.

The plasma frequency extracted from the fitted experimental data (Fig. 6.4(c)) decreases with the pressure following the trend of the measured electron concentration. The slight fluctuations of the plasma frequency are probably related to the free-charge trapping on the defect states modified in different growth conditions. It is interesting to note that the charge carrier concentration in the studied SRO films is on average approximately 10 times higher than that of Au or Ag, while the carrier mobility is about 100 times lower. Comparing the electron concentrations and plasma frequencies of the SRO and plasmonic metals, one can notice the increased effective electron mass in SRO as should be expected [37, 38]. The crossover (ENZ regime) from dielectric (positive permittivity) to plasmonic (negative permittivity) behaviour takes place in the spectral range 0.84 – 1.12 eV, depending on the oxygen pressure (Fig. 6.4(c)). For all the studied films, plasmonic behaviour is observed in the infrared spectral range. In this spectral range, the absorption ($\mathrm{Im}(\varepsilon_{SRO})$) is comparable to that of Au for the films deposited at higher than 75 mTorr oxygen pressures.

The optical response corresponds well to the electric properties (Fig. 6.4(d)) with the decreased $\mathrm{Re}(\varepsilon_{SRO})$ for low pressures below 100 mTorr cor-

responding to the increased carrier concentration and, thus, stronger free-electron contribution in Eq. (6.1). The decrease in mobility (i.e. increased scattering) can be attributed to the increasing $\mathrm{Re}(\varepsilon_{SRO})$ for pressures lower than 40 mTorr. It should be noted that DC and optical-frequency scattering loss may not necessarily be the same. Nevertheless, the electron concentration is high enough to provide negative permittivity at infrared wavelengths

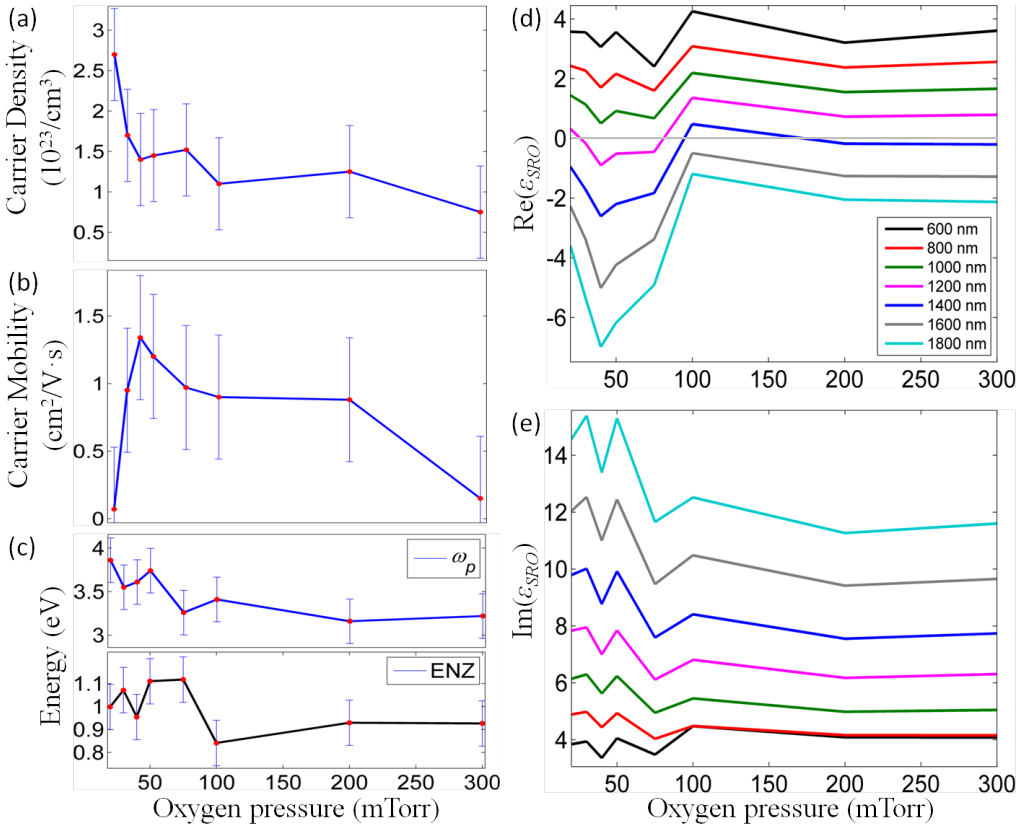

Figure 6.4: Dependence on oxygen pressure of (a) carrier concentration, (b) carrier mobility, (c) plasma frequency (ω_p) and ENZ frequency, (d) real and (e) imaginary parts of the dielectric constant of the 100 nm thick $SrRuO_3$ films. The standard deviation for carrier density, carrier mobility, ω_p and ENZ is 0.57, 0.46, 0.25 and 0.1 respectively.

for all deposition parameters. The optical losses (the imaginary part of the dielectric constant), have decreasing trend on the deposition pressure (Fig. 6.4(e)), again in agreement with the electron concentration and the Drude-Lorentz model (Eq. (6.1)). This behaviour is increasingly pronounced for longer wavelengths where the free-electron (Drude) part of permittivity becomes dominant.

6.3.3 Comparison of SRO with the optical constants of noble plasmonic metals

The motivation for this section is to compare the optical properties, discussed previously, with the optical constants of Au, Ag and Al which are the standard metals used in plasmonics. This will allow us to dictate the superiority/inferiority of each material for specific applications. In Section 6.3.2, it was shown that the best crystalline structure of SRO films can be achieved at oxygen pressures close to 75 mTorr, as a result the SRO permittivity at this pressure will be compared.

Let us start by plotting the real and imaginary parts of permittivity for each material. Fig. 6.5(a) shows that for all the wavelengths, especially far from the interband transition regime, $|Re(\varepsilon_{SRO})| \ll |Re(\varepsilon_{Au,Ag,Al})|$. Additionally, the absorption of Au and Ag has comparable values with SRO and only Al shows significantly higher absorbing behaviour (Fig. 6.5(b)). All these lead to the result that SRO does not have better optical properties due to the enhanced dissipation of plasmonic modes.

However, in order to have a broader view, it is important to investigate these materials in more detail. For that, the core characteristics of each material are summarized in Table 6.1. SRO is a less scarce material than Au or Ag which makes it cheaper. At the same time its weight is approximately

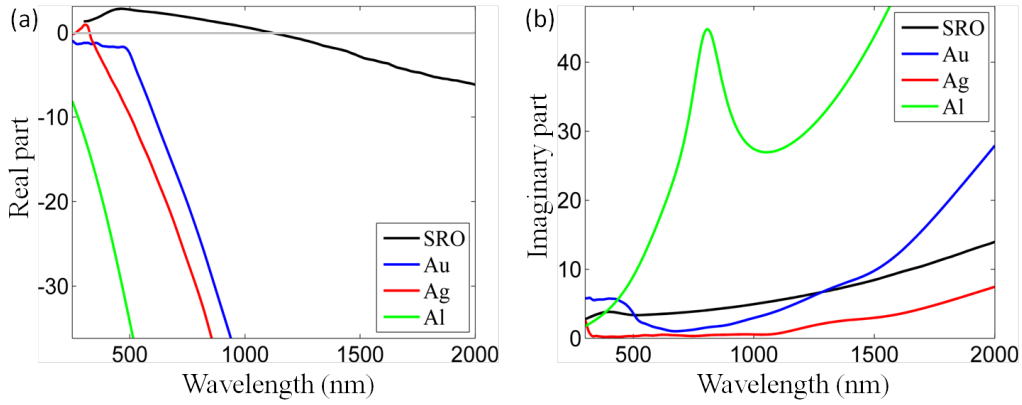

Figure 6.5: Real (a) and imaginary (b) permittivity of SRO, Au, Ag and Al. Notice that $|Re(\varepsilon_{SRO})| \ll |Re(\varepsilon_{Au,Ag,Al})|$ for pretty much all the wavelength range. At the same time absorption of Au and Ag is comparable to the one of SRO and only Al exhibits significantly higher values.

four times lighter than Au and 2 times lighter than Ag which might not be important when small structures are fabricated but will have an impact if mass production is taken into consideration. Another key-factor is the melting point; SRO's melting point is at 2302 °C [44] when Au, Ag and Al have a melting point varying from 660 °C to 1064 °C. Applications in which temper-

	SRO	**Au**	**Ag**	**Al**
Bulk melting point	2302 °C [39]	1064 °C [39]	962 °C [39]	660 °C [39]
Thin film melting point	-	600 °C [40]	527 °C [41]	550 °C [42]
Density	4.7 g/cm^3	19.3 g/cm^3	10.5 g/cm^3	2.7 g/cm^3
Price	Cheap	Expensive	Expensive	Cheap
Abundance	High	Low	Low	High

Table 6.1: General characteristics of SRO, Au, Ag and Al.

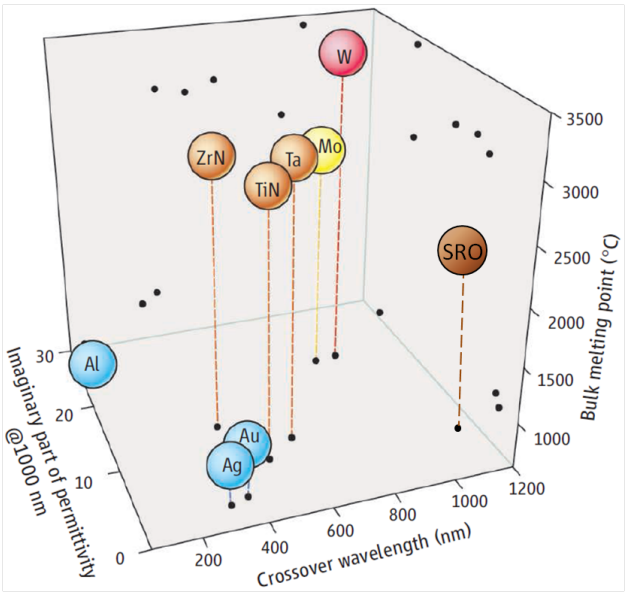

Figure 6.6: Comparison of refractory plasmonic materials with metals such as Au, Ag and Al. The crossover wavelength corresponds to ENZ where the material becomes plasmonic. Image adapted from [43]. The SRO has been manually added to enable comparison.

ature can locally reach very high values, such as nano-antennas, plasmonic metals will loose their thermal stability while SRO not. SRO is also compatible with and used in standard semiconductor technology and provides high temperature stability to up to 1200 K needed in many plasmonic applications, such as heat-assisted magnetic recording [45].

Over the last years, there has been a growing interest in the field of plasmonics for materials with high melting point and chemical stability, known as *refractory plasmonics* [43]. Fig. 6.6 demonstrates the melting point gap between refractory materials, with melting point higher than 2000 °C, and conventional metals (blue circles). SRO has approximately 700 °C lower melting point that other refractory materials but at the same time it has the smallest

imaginary part of permittivity at 1000 nm. Additionally it is the only material with such a high crossover (ENZ) wavelength that, as it is shown in this Chapter, can be adjusted all the way up to telecommunication frequencies.

6.4 Summary

In this Chapter, $SrRuO_3$ thin films on MgO (001) substrate were fabricated by pulsed laser deposition at different oxygen pressures. The influence of the oxygen pressure (20 – 300 mTorr) on structure, charge carrier dynamics and optical properties were investigated. The main results are the following

1. Atomic force microscopy showed minor roughness of films, with RMS never exceeding 4 nm, making them suitable for plasmonic applications. The X-ray diffraction revealed that the best crystalline structure, characterized by the absence of extra phases or directions of growth, was obtained at the oxygen deposition pressures below 100 mTorr.

2. The investigated films exhibit plasmonic behaviour in the near-infrared spectral range with the plasma frequency at 324 - 392 nm and epsilon-near-zero pattern at 1.11 – 1.47 μm, depending on the deposition conditions. Oxygen pressure of 100 – 200 mTorr provides best electronic and optical properties, in this range of deposition parameters, for plasmonic applications of the films.

3. The electron density decreases with the increasing pressure, hinting at the influence of trapped charges, produced by defects in the thin films or at the film/substrate interface. The impact of the defects can also be mapped in the optical constants of $SrRuO_3$ at various oxygen pressures.

4. The permittivity of $SrRuO_3$ is inferior to noble metals such as Au, Ag or Al meaning that the dissipation of optical modes is expected to be more pronounced. However, $SrRuO_3$ is a more abundant, cheaper and light material than most metals. Additionally, its melting point is 2302 °C which is at least 1000 °C higher than any noble plasmonic metal. It is this property which makes $SrRuO_3$ a better candidate for high temperature applications such as nano-antennas or heat-assisted magnetic recording.

References

[1] A. V. Zayats and S. A. Maier, Eds., *Active Plasmonics and Tuneable Plasmonic Metamaterials*. Wiley & Sons, (2013).

[2] A. Boltasseva and H. Atwater, "Low-loss plasmonic metamaterials," *Science*, vol. **331**, pp. 290–290, (2011).

[3] P. R. West, S. Ishii, G. V. Naik, N. K. Eman, V. M. Shalaev, and A. Boltasseva, "Searching for better plasmonic materials," *Las. & Phot. Rev.*, vol. **4**, pp. 795–808, (2010).

[4] G. V. Naik, J. Kim, and A. Boltasseva, "Oxides and nitrides as alternative plasmonic materials in the optical range," *Opt. Mat. Express*, vol. **1**, pp. 1090–1099, (2011).

[5] G. V. Naik, J. L. Schroeder, X. Ni, A. V. Kildishev, T. D. Sands, and A. Boltasseva, "Titanium nitride as a plasmonic material for visible and near-infrared wavelengths," *Opt. Mat. Express*, vol. **2**, pp. 478–489, (2012).

[6] Q. Gan, R. A. Rao, C. B. Eom, L. Wu, and F. Tsui, "Lattice distortion and uniaxial magnetic anisotropy in single domain epitaxial (110) films of $SrRuO_3$," *J. Appl. Phys.*, vol. **85**, pp. 5297–5299, (1999).

[7] G. Santi and T. Jarlborg, "Calculation of the electronic structure and the magnetic properties of $SrRuO_3$ and $CaRuO_3$," *J. Phys.: Condens. Matter*, vol. **9**, pp. 9563–9584, (1997).

[8] C. W. Jones, P. D. Battle, P. Lightfoot, and W. T. A. Harrison, "The structure of $SrRuO_3$ by time-of-flight neutron powder diffraction," *Acta Crystallogr. Sect. C*, vol. **45**, pp. 365–367, (1989).

[9] K. J. Choi, S. H. Baek, H. W. Jang, L. J. Belenky, M. Lyubchenko, and C.-B. Eom, "Phase-transition temperatures of strained single-crystal $SrRuO_3$ thin films," *Adv. Mat.*, vol. **22**, pp. 759–762, (2010).

[10] J. J. Randall and R. Ward, "The preperation of some ternary oxides of the platinum metals," *J. Am. Chem. Soc.*, vol. **81**, pp. 2629–2631, (1959).

[11] C. B. Eom, R. J. Cava, R. M. Fleming, J. M. Phillips, R. B. vanDover, J. H. Marshall, J. W. P. Hsu, J. J. Krajewski, and W. F. Peck, "Single-crystal epitaxial thin films of the isotropic metallic oxides $Sr_{1-x}Ca_xRuO_3$ $(0 \leq x \leq 1)$," *Science*, vol. **258**, pp. 1766–1769, (1992).

[12] C. L. Chen, Y. Cao, Z. J. Huang, Q. D. Jiang, Z. Zhang, Y. Y. Sun, W. N. Kang, L. M. Dezaneti, W. K. Chu, and C. W. Chu, "Epitaxial $SrRuO_3$ thin films on (001) $SrTiO_3$," *Appl. Phys. Lett.*, vol. **71**, pp. 1047–1049, (1997).

[13] N. Fukushima, K. Sano, T. Shimizu, K. Abe, and S. Komatsu, "Lattice deformation and magnetic properties in epitaxial thin films of $Sr_{1-x}Ba_xRuO_3$," *Appl. Phys. Lett.*, vol. **73**, pp. 1200–1202, (1998).

[14] A. J. Hartmann, M. Neilson, R. N. Lamb, K. Watanabe, and J. F. Scott, "Ruthenium oxide and strontium ruthenate electrodes for ferroelectric thin-film capacitors," *Appl. Phys. A*, vol. **70**, pp. 239–242, (2000).

[15] N. Okuda, K. Saito, and H. Funakubo, "Low-temperature deposition of $SrRuO_3$ thin film prepared by metalorganic chemical vapor deposition," *Jpn. J. Appl. Phys.*, vol. **39**, pp. 572–576, (2000).

[16] W. Bensch, H. W. Schmalle, and A. Reller, "Structure and thermochemical reactivity of $CaRuO_3$ and $SrRuO_3$," *Solid State Ionics*, vol. **43**, pp. 171–177, (1990).

[17] T. Morimoto, O. Hidaka, K. Yamakawa, O. Arisumi, H. Kanaya, T. Iwamoto, Y. Kumura, I. Kunishima, and S. Tanaka, "Ferroelectric properties of Pb(Zi, Ti)O_3 capacitor with thin $SrRuO_3$ films within both electrodes," *Jpn. J. Appl. Phys*, vol. **39**, pp. 2110–2213, (2000).

[18] C. B. Eom, R. B. vanDover, J. M. Phillips, D. J. Werder, J. H. Marshall, C. H. Chen, R. J. Cava, R. M. Fleming, and D. K. Fork, "Fabrication and properties of epitaxial ferroelectric heterostructures with ($SrRuO_3$) isotropic metallic oxide electrodes," *Appl. Phys. Lett.*, vol. **63**, pp. 2570–2572, (1993).

[19] T. Higuchi, Y. Chen, J. Koike, S. Iwashita, M. Ishida, and T. Shimoda, "Fabrication of pseudocubic $SrRuO_3$ (100) epitaxial thin films on Si by pulsed laser deposition," *Jpn. J. Appl. Phys*, vol. **41**, pp. L481–L483, (2002).

[20] K. Takahashi, T. Oikawa, K. Saito, S. Kaneko, H. Fujisawa, M. Shimizu, and H. Funakubo, "Effect of strain in epitaxially grown $SrRuO_3$ thin

films on crystal structure and electrical properties," *Jpn. J. Appl. Phys*, vol. **41**, pp. 5376–5380, (2002).

[21] Y. Z. Yoo, O. Chmaissem, S. Kolesnik, B. Dabrowski, M. Maxwell, C. W. Kimball, L. McAnelly, M. H.-Sheikh, and A. P. Genis, "Contribution of oxygen partial pressures investigated over a wide range to $SrRuO_3$ thin-film properties in laser deposition processing," *J. Appl. Phys*, vol. **97**, p. 103525, (2005).

[22] X. Fang and T. Kobayashi, "Characterization of $SrRuO_3$ thin film grown by laser ablation at temperatures above 400 °C," *J. Appl. Phys*, vol. **90**, pp. 162–166, (2001).

[23] X. Zhu, S. K. Lee, H. N. Lee, and D. Hesse, "Microstructure of (1 1 0)-oriented epitaxial $SrRuO_3$ thin films grown on off-cut single crystal YSZ(1 0 0) substrates," *Mater. Sci. and Eng. B*, vol. **118**, pp. 60–65, (2006).

[24] R. J. Bouchard and J. L. Gillson, "Electrical properties of $CaRuO_3$ and $SrRuO_3$ single crystals," *Mater. Res. Bull.*, vol. **7**, pp. 873–878, (1972).

[25] D. Popescu, B. Popescu, G. Jegert, S. Schmelzer, U. Boettger, and P. Lugli, "Feasibility study of $SrRuO_3/SrTiO_3/SrRuO_3$ thin film capacitors in DRAM applications," *IEEE Trans. Elec. Dev.*, vol. **61**, pp. 2130–2135, (2014).

[26] D. N. Basov and T. Timusk, "Electrodynamics of high-Tc superconductors," *Rev. Mod. Phys.*, vol. **77**, pp. 721–779, (2005).

[27] S. Dordevic and D. N. Basov, "Electrodynamics of correlated electron matter," *Ann. Phys.*, vol. **15**, pp. 545–570, (2006).

[28] D. N. Basov, R. D. Averitt, D. van der Marel, and M. Dressel, "Electrodynamics of correlated electron materials," *Rev. Mod. Phys.*, vol. **83**, pp. 471–541, (2011).

[29] A. V. Puchkov, M. C. Schabel, D. N. Basov, T. Startseva, G. Cao, T. Timusk, and Z.-X. Shen, "Layered Ruthenium oxides: From band metal to Mott insulator," *Phys. Rev. Lett.*, vol. **81**, pp. 2747–2750, (1998).

[30] J. S. Lee, Y. S. Lee, T. W. Noh, K. Char, J. Park, S.-J. Oh, J.-H. Park, C. B. Eom, T. Takeda, and R. Kanno, "Optical investigation on the electronic structures of $Y_2Ru_2O_7$, $CaRuO_3$, $SrRuO_3$, and $Bi_2Ru_2O_7$," *Phys. Rev. B*, vol. **64**, p. 245107, (2001).

[31] Y. S. Lee, J. J. Yu, J. S. Lee, T. W. Noh, T. H. Gimm, H. Y. Choi, and C. B. Eom, "Non-Fermi liquid behavior and scaling of low-frequency suppression in optical conductivity spectra of $CaRuO_3$," *Phys. Rev. B*, vol. **66**, p. 041104, (2002).

[32] P. Kostic, Y. Okada, N. C. Collins, Z. Schlesinger, J. W. Reiner, L. Klein, A. Kapitulnik, T. H. Geballe, and M. R. Beasley, "Non-Fermi-liquid behavior of $SrRuO_3$: Evidence from infrared conductivity," *Phys. Rev. Lett.*, vol. **81**, pp. 2498–2501, (1998).

[33] A. J. Millis, *Strong interactions in low dimensions*, D. Baeriswyl and L. Degiorgi, Eds. L. Kluwer Academic, (2004).

[34] B. Zou, P. K. Petrov, and N. M. Alford, "$SrRuO_3$ thin films grown on MgO substrates at different oxygen partial pressures," *J. Mater. Res.*, vol. **28**, pp. 702–707, (2013).

[35] W. J. Tropf, M. E. Thomas, and E. W. Rogala, *Handbook of optics, third edition volume IV: Optical properties of materials, nonlinear optics, quantum optics*, M. Bas, G. Li, and E. van Stryland, Eds. McGraw-Hill, (2009).

[36] K. Levenberg, "A method for the solution of certain non-linear problems in least squares," *Quarterly of Applied Mathematics*, vol. **2**, pp. 164–168, (1944).

[37] C. S. Alexander, S. McCall, P. Schlottmann, and J. E. Crow, "Angle-resolved de Haas–van Alphen study of $SrRuO_3$," *Phys. Rev.*, vol. **72**, p. 024415, (2005).

[38] D. E. Shai, C. Adamo, D. W. Shen, C. M. Brooks, J. W. Harter, E. J. Monkman, B. Burganov, D. G. Schlom, and K. M. Shen, "Quasiparticle mass enhancement and temperature dependence of the electronic structure of ferromagnetic $SrRuO_3$ thin films," *Phys. Rev. Lett.*, vol. **110**, p. 087004, (2013).

[39] M. Abdullah, S. Khairunnisa, and F. Akbar, "Zipper model for the melting of thin films." [Online]. Available: http://arxiv.org/abs/1506.08239

[40] P. Buffat and J.-P. Borel, "Size effect on the melting temperature of gold particles," *Phys. Rev. A*, vol. **13**, pp. 2287–2298, (1976).

[41] E. P. Kitsyuk, D. G. Gromov, E. N. Radichev, and I. V. Sagunova, "Specifics of low temperature melting and disintegration into drops of silver thin films," *Physico. Pro. at Inter.*, vol. **48**, pp. 256–261, (2012).

[42] S. L. Lai, J. R. Carlsson, and L. H. Allen, "Melting point depression of Al clusters generated during the early stages of film growth: Nanocalorimetry measurements," *Appl. Phys. Lett.*, vol. **72**, pp. 1098–1100, (1998).

[43] U. Guler, A. Boltasseva, and V. M. Shalaev, "Refractory plasmonics," *Science*, vol. **344**, pp. 263–264, (2014).

[44] S. Yamanaka, T. Maekawa, H. Muta, T. Matsuda, S. Kobayashi, and K. Kurosaki, "Thermophysical properties of $SrHfO_3$ and $SrRuO_3$," *J. Sol. St. Chem.*, vol. **177**, pp. 3484–3489, (2004).

[45] D. O'Connor and A. V. Zayats, "Data storage: The third plasmonic revolution," *Nat. Nano.*, vol. **5**, pp. 482–483, (2010).

Publications

N. Vasilantonakis, M. E. Nasir, W. Dickson, G. A. Wurtz and A. V. Zayats, "Bulk plasmon-polaritons in hyperbolic nanorod metamaterial waveguides," *Laser & Photonics Reviews*, vol. **9** (No 3), pp. 345-353, (2015).

N. Vasilantonakis, G. A. Wurtz, V. A. Podolskiy and A. V. Zayats, "Refractive index sensing with hyperbolic metamaterials: strategies for biosensing and nonlinearity enhancement," *Optics Express*, vol. **23**, pp. 14329-14343, (2015).

Laurentiu Braic*, **Nikolaos Vasilantonakis***, Bin Zou, Stefan A. Maier, Neil McN. Alford, Anatoly V. Zayats and Peter K. Petrov, "Optimizing Strontium Ruthenate thin films for near-infrared plasmonic applications," *Scientific Reports*, vol. **5** (No 9118), (2015).
*These authors contributed equally.

N. Vasilantonakis, M. E. Nasir, W. Dickson, G. A. Wurtz and A. V. Zayats, "Bulk plasmon-polaritons in hyperbolic nanorod metamaterial waveguides," Oral, CLEO Europe, Munich, (2015).

N. Vasilantonakis, M. E. Nasir, W. Dickson, G. A. Wurtz and A. V. Za-

yats, "Controlled modal dispersion in hyperbolic-metamaterial slab waveguides made of strongly interacting nanorod assemblies," Oral, Condensed matter in Paris, Paris, (2014).

N. Vasilantonakis, M. E. Nasir, J.-S. Bouillard, W. Dickson, G. A. Wurtz and A. V. Zayats, "Controlled plasmonic excitations in anisotropic media at visible wavelengths," Oral, European Optical Society Annual Meeting (EOSAM), Aberdeen (2012).

Conclusions and future work

Conclusions

This research work examined the optical behaviour of various plasmonic metamaterials with extreme anisotropy. Although the results cover a wide range of applications, from life to computer sciences, our guidance was not solely the applicability but mainly our scientific curiosity to explain and understand optical phenomena. The main results can be summarized as follows

- We theoretically proposed and experimentally verified the behaviour of bulk plasmon-polaritons in planar anisotropic metamaterial waveguides. Unlike to TE-polarized modes which have typical dielectric response, it was shown that the spectral range of TM-polarized hyperbolic waveguided modes is bound from the high-frequency side by the effective plasma frequency of the metamaterial. These modes have negative group velocity and unusual high frequency cut-off with no cut-off for high propagation constants, limited only by the Brillouin zone of the metamaterial realisation. The negative group velocity as well as its dispersion can be controlled by varying the anisotropy of the metamaterial. For the nanorod metamaterial studied here, TM modes exhibited slow light response with group velocity down to only 3% of the speed of light and had group velocity dispersion as low as 0.02 ps^2/mm.

- We examined geometry and refractive index sensing with hyperbolic matamaterials and provided general strategies for the optimization of the sensing response. Refractive index variations of the host medium resulted to at least 2 orders of magnitude increased sensing compared to superstrate variations. Additionally, sensing was more pronounced for higher-order unbound and leaky modes of the metamaterial sensor. The impact of the transducer's thickness showed a significant increased sensing for the thinner metamaterial layers as long as modes were supported by the structure and TM-polarization was considered. These results can be used as a general rule for the design and implementation of new ultrasensitive devices for chemo- and biosensors.

- We explored and optimized Strontium Ruthenate thin films for near-infrared plasmonic applications. The average roughness of such films was only 4 nm make them suitable for optical techniques. The best crystalline structure, characterized by the absence of extra phases, was acquired for oxygen pressures below 100 mTorr. All films exhibited tunable plasmonic behaviour in the near-infrared range with the plasma frequency at 324 - 392 nm and epsilon-near-zero pattern at 1.11 – 1.47 μm, depending on the deposition conditions.

Future work

Many of the research topics in the current thesis allow future work and analysis. The theoretical and experimental demonstration of low group velocity waveguided modes opens the possibility to achieve similar effects with other mode excitations. For example, when a porous AAO layer is structured on top of a thin Au slab, it is possible to control the SPP behaviour via ge-

ometry similarly to the work presented here. Regardless the case, achieving slow light in nanorod metamaterial waveguides opens new possibilities for deep-subwavelength sensors, high-speed optical processing, telecommunication networks and optical data storage components. Furthermore, the fact that ENZ becomes the upper cut-off frequency limit for low filling factors, forces all the modes to converge at a single frequency allowing multimode excitation and high density of states enhancing light absorption and emission.

The general approach of the sensing response with Au nanorod metamaterials was to provide a universal method for the optimization of the sensing capabilities with similar structures. The results can be used as a design strategy to enhance flexibility of ultrasensitive transducers for bio- or chemical sensors or nonlinear photonic devices based on plasmonic hyperbolic metamaterials. The outcomes shown that absorption plays an equally important role in sensing with respect to variations of the real part of the refractive index. This opens a new way to effectively manipulate the sensing response in such media. Additionally, both TE and TM-modes shown comparable sensitivities, opening up opportunities for polarization multiplexing in sensing experiments.

The optimization of Strontium Ruthenate (SRO) thin films showed their suitability for near-infrared plasmonic applications. The adjustable epsilon-near-zero (ENZ) makes SRO a promising ENZ component in the near-infrared spectral range which is difficult to achieve with conventional plasmonic metals. A significant advantage of SRO is the high melting point which categorizes it in the refractory plasmonics branch. As a result it is stable at very high temperatures close to 1200 K, where conventional metals like Au or Ag are not, making it attractive for metamaterial-based ideal absorbers, heat generating nanostructures or heat-assisted magnetic recording. We are cur-

rently working on another promising material which is TiN thin films. This material exhibits 2 ENZ, one in the far-visible and the other in infrared, which can both be controlled by deposition conditions. Similarly to SRO, it is stable at high temperatures so all the aforementioned applications are applicable here as well. The controllable double ENZ allows applications such as supercoupling effect, realization of delay lines and radiation directivity, to be selected in 2 optical regimes by switching the wavelength.

Appendix A

Drude–Sommerfeld model and interband transitions

This appendix examines the case of electrons bounded to the nucleus. The unbounded case is a simplified view and can be directly derived once the bounded solution is known. Apart form the force due to acceleration, there are three more forces contributing to electron's motion. Firstly, from the classical point of view, electron and nucleus have a spring-like connection obeying Hooke's law. Thus the restoring spring force will be $\mathbf{F}_H = -k\mathbf{r}$, where k is Hooke's constant which is proportional to the resonant frequency of spring $\omega_0 = \sqrt{k/m_e^*}$ (m_e^* is the *effective* electron mass). Secondly, it is assumed that electrons oscillate in a viscous fluid. As a result, there is a viscous force given from $\mathbf{F}_d = -m_e^*\gamma\boldsymbol{\upsilon}$, where γ is the damping coefficient due to radiative damping of electrons. Thirdly, the electric field creates an electric force of the form $\mathbf{F}_e = e\mathbf{E} = e\mathbf{E}_0 e^{-i\omega t}$, where $\mathbf{E}_0$ is the amplitude of the electric field. Taken all these forces into account, Newton's second law becomes

$$m_e^* \frac{\partial^2 \mathbf{r}}{\partial t^2} + m_e^* \gamma \frac{\partial \mathbf{r}}{\partial t} + m_e^* \omega_0^2 \mathbf{r} = e\mathbf{E}_0 e^{-i\omega t} \tag{A.1}$$

In order to find the total solution of Eq. (A.1) the homogeneous and inhomogeneous solutions must be found.

A.1 Homogeneous solution

The homogeneous solution is derived by solving Eq. (A.1) with the right hand side to be zero. The solution will be of the form $c_1 e^{\rho_1 t} + c_2 e^{\rho_2 t}$ where c_1, c_2 are free parameters found from problem's initial conditions and ρ_1, ρ_2 are the roots of equation $\rho^2 + \Gamma\rho + \omega_0^2 = 0$. The homogeneous solution is then given from

$$\mathbf{r}_{hom}(t) = c_1 e^{0.5(-\gamma + \sqrt{\gamma^2 - 4\omega_0^2})t} + c_2 e^{0.5(-\gamma - \sqrt{\gamma^2 - 4\omega_0^2})t} \tag{A.2}$$

Although this is a totally acceptable solution, it tends to zero very fast regardless the combination of c_1 and c_2. Its lifetime is typically in the range of few ps so the system is homogeneously relaxed for all times above that range.

A.2 Inhomogeneous solution

For the inhomogeneous case, we use the ansatz $\mathbf{r}(t) = \mathbf{r}_0 e^{-i\omega t}$. Replacing this to Eq. (A.1) we get

$$\mathbf{r}_0 = \frac{eE_0}{m_e^*(\omega_0^2 - \omega^2 - i\omega\gamma)} \tag{A.3}$$

and thus

$$\mathbf{r}(t) = \frac{eE_0 e^{-i\omega t}}{m_e^*(\omega_0^2 - \omega^2 - i\omega\gamma)} \tag{A.4}$$

If the number of the effective electrons per unit volume is n_e^*, then polarization will be $\mathbf{p} = en_e^*\mathbf{r}(t) = en_e^*\mathbf{r}_0 e^{-i\omega t}$. Taking into account that the electric field is $\mathbf{E} = \mathbf{E}_0 e^{-i\omega t}$ we can find the permittivity from $\varepsilon_{Lor} = 1 + \frac{p}{\varepsilon_0 E}$ giving eventually

$$\varepsilon_{Lor}(\omega) = 1 - \frac{\omega_p^{*2}}{\omega^2 - \omega_0^2 + i\gamma\omega} \tag{A.5}$$

where $\omega_p^* = \sqrt{\frac{n_e^* e^2}{\varepsilon_0 m_e^*}}$ is the *effective* plasma frequency.

In case we need to examine the unbounded electron model the restoring force should be omitted ($\omega_0 = 0$) while the effective mass of the electrons and the damping coefficient should now be replaced by the free electron mass (m_e) and the damping frequency (Γ), respectively. This leads to a simplified version of Eq. (A.5) known as Drude permittivity

$$\varepsilon_{Drude}(\omega) = 1 - \frac{\omega_p^2}{\omega^2 + i\Gamma\omega} \tag{A.6}$$

where $\omega_p = \sqrt{\frac{n_e e^2}{\varepsilon_0 m_e}}$ is the *free* plasma frequency.

Appendix B

Surface plasmon polaritons at plane interfaces

In the current appendix we derive the dispersion relation for an SPP between two semi-infinite planar materials. An electromagnetic wave, inside a material with relative dielectric constants (ε_1, μ_1), reaches the interface of another material with relative dielectric constants (ε_2, μ_2). Both polarizations are examined as shown in Fig. B.1.

B.1 TM-polarization

In this case, the material (ε_1, μ_1) is considered to be isotropic with $\mu_1 = 1$, while the material $(\widetilde{\varepsilon}_2, \mu_2)$ is anisotropic of the form $\widetilde{\varepsilon}_2 = (\varepsilon_{xx}, \varepsilon_{yy}, \varepsilon_{zz})^\intercal$ and $\mu_2 = 1$. The off-diagonal elements of permittivity tensor are zero. For TM-polarized waves, the fields of the two media $j = 1$ and $j = 2$ will be

$$\mathbf{E}_j = (E_{xj}, 0, E_{zj})^\intercal e^{i(k_{xj}x \mp k_{zj}z - \omega t)}, \quad j = 1, 2 \tag{B.1}$$

$$\mathbf{H}_j = (0, H_{yj}, 0)^\intercal e^{i(k_{xj}x \mp k_{zj}z - \omega t)}, \quad j = 1, 2 \tag{B.2}$$

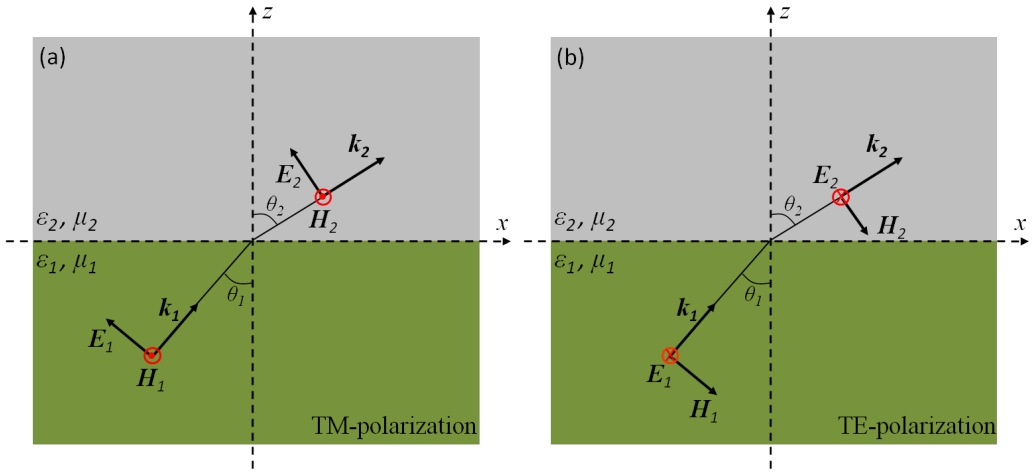

Figure B.1: An electromagnetic wave inside a material with relative dielectric constants (ε_1, μ_1) reaches the interface of a material with relative dielectric constants (ε_2, μ_2). The two possible polarized configurations for TM and TE are shown in (a) and (b), respectively. Both media are considered semi-infinite.

where the $\mp k_{zj} z$ term corresponds to the lower $(z < 0)$ or upper $(z > 0)$ material (see Fig. B.1).

We start from the macroscopic Maxwell's equations (in Gaussian units) with no charge $(\rho = 0)$ or current densities $(\mathbf{J} = 0)$

$$\nabla \cdot (\varepsilon_j \mathbf{E}_j) = 0, \quad j = 1, 2 \tag{B.3}$$

$$\nabla \times \mathbf{E}_j = -\frac{\mu_j}{c} \frac{\partial \mathbf{H}_j}{\partial t} = \frac{i\omega\mu_j}{c} \mathbf{H}_j, \quad j = 1, 2 \tag{B.4}$$

$$\nabla \cdot \mathbf{B}_j = 0, \quad j = 1, 2 \tag{B.5}$$

$$\nabla \times \mathbf{H}_j = \frac{\varepsilon_j}{c} \frac{\partial \mathbf{E}_j}{\partial t} = -\frac{i\omega}{c} \varepsilon_j \mathbf{E}_j, \quad j = 1, 2 \tag{B.6}$$

Applying Eq. (B.3) for material (ε_1, μ_1) we get

$$\varepsilon_1 \nabla \cdot \mathbf{E}_1 = 0 \Rightarrow E_{x1} \frac{\partial}{\partial x} (e^{i(k_{x1}x - k_{z1}z - \omega t)}) + E_{z1} \frac{\partial}{\partial z} (e^{i(k_{x1}x - k_{z1}z - \omega t)}) = 0$$

$$\Rightarrow \boxed{E_{x1} k_{x1} - E_{z1} k_{z1} = 0} \tag{B.7}$$

and for material $(\widetilde{\varepsilon}_2, \mu_2)$

$$\varepsilon_2 \nabla \cdot \mathbf{E}_2 = 0 \Rightarrow E_{x2}\varepsilon_{xx}\frac{\partial}{\partial x}(e^{i(k_{x2}x+k_{z2}z-\omega t)}) + E_{z2}\varepsilon_{zz}\frac{\partial}{\partial z}(e^{i(k_{x2}x+k_{z2}z-\omega t)}) = 0$$

$$\Rightarrow \boxed{\varepsilon_{xx}E_{x2}k_{x2} + \varepsilon_{zz}E_{z2}k_{z2} = 0} \tag{B.8}$$

Applying Eq. (B.4) for material (ε_1, μ_1) and knowing that H_1 is parallel to $\hat{\boldsymbol{j}}$ (unit vector of y-axis) we get

$$(\nabla \times \mathbf{E}_1) \cdot \hat{\boldsymbol{j}} = (\frac{\partial E_{x1}}{\partial z} - \frac{\partial E_{z1}}{\partial x})e^{i(k_{x1}x-k_{z1}z-\omega t)} \Rightarrow$$

$$E_{x1}(-\cancel{i}k_{z1})\cancel{e^{i(k_{x1}x-k_{z1}z-\omega t)}} - E_{z1}(\cancel{i}k_{x1})\cancel{e^{i(k_{x1}x-k_{z1}z-\omega t)}} = \frac{\cancel{i}\omega}{c}H_{y1}\cancel{e^{i(k_{x1}x-k_{z1}z-\omega t)}}$$

$$\Rightarrow \boxed{E_{x1}k_{z1} + E_{z1}k_{x1} = -\frac{\omega}{c}H_{y1}} \tag{B.9}$$

Following exactly the same steps for material $(\widetilde{\varepsilon}_2, \mu_2)$

$$E_{x2}k_{z2} - E_{z2}k_{x2} = \frac{\omega}{c}H_{y2} \tag{B.10}$$

Applying Eq. (B.6) for material (ε_1, μ_1) we have

$$\nabla \times \mathbf{H}_1 = -\frac{i\omega}{c}\varepsilon_1\mathbf{E}_1 \Rightarrow H_{y1}(-\frac{\partial}{\partial z}\hat{\boldsymbol{i}} + \frac{\partial}{\partial x}\hat{\boldsymbol{k}})e^{i(k_{x1}x-k_{z1}z-\omega t)} =$$

$$-\frac{i\omega}{c}\varepsilon_1(E_{x1}\hat{\boldsymbol{i}} + E_{z1}\hat{\boldsymbol{k}})e^{i(k_{x1}x-k_{z1}z-\omega t)} \Rightarrow H_{y1}k_{z1}\hat{\boldsymbol{i}} + H_{y1}k_{x1}\hat{\boldsymbol{k}} =$$

$$-\frac{\omega\varepsilon_1}{c}(E_{x1}\hat{\boldsymbol{i}} + E_{z1}\hat{\boldsymbol{k}}) \Rightarrow \boxed{H_{y1}k_{z1} = -\frac{\omega\varepsilon_1}{c}E_{x1}} \tag{B.11}$$

$$\boxed{H_{y1}k_{x1} = -\frac{\omega\varepsilon_1}{c}E_{z1}} \tag{B.12}$$

where $\hat{\boldsymbol{i}}$ and $\hat{\boldsymbol{k}}$ are the unit vectors along the x- and z-axis, respectively. Based on the same principle, material $(\widetilde{\varepsilon}_2, \mu_2)$ gives

$$H_{y2}k_{z2} = \frac{\omega\varepsilon_{xx}}{c}E_{x2} \tag{B.13}$$

$$H_{y2}k_{x2} = -\frac{\omega\varepsilon_{zz}}{c}E_{z2} \tag{B.14}$$

Assuming no surface charges or currents, the boundary conditions at the interface will give

$$(\mathbf{D}_2 - \mathbf{D}_1) \cdot \hat{\boldsymbol{n}} = 0 \Rightarrow D_{2z} = D_{1z} \Rightarrow \boxed{\varepsilon_1 E_{z1} = \varepsilon_{zz} E_{z2}} \tag{B.15}$$

$$\hat{\boldsymbol{n}} \times (\mathbf{E}_2 - \mathbf{E}_1) = 0 \Rightarrow \boxed{E_{x1} = E_{x2} \equiv E_x} \tag{B.16}$$

$$\hat{\boldsymbol{n}} \times (\mathbf{H}_2 - \mathbf{H}_1) = 0 \Rightarrow \boxed{H_{y1} = H_{y2} \equiv H_y} \tag{B.17}$$

where $\hat{\boldsymbol{n}}$ is the unit vector normal to the interface. Additionally, using Eq. (B.15) and (B.17) to Eq. (B.12) and (B.14) we can see that

$$k_{x1} = k_{x2} \equiv k_x \tag{B.18}$$

Dividing Eq. (B.11) with Eq. (B.13) we get

$$\frac{k_{z1}}{k_{z2}} = -\frac{\varepsilon_1}{\varepsilon_{xx}} \tag{B.19}$$

Replacing E_{z1} from Eq. (B.7) and H_y from Eq. (B.11) to Eq. (B.9)

$$k_{z1}^2 + k_x^2 = \left(\frac{\omega}{c}\right)^2 \varepsilon_1 \tag{B.20}$$

Replacing E_{z2} from Eq. (B.8) and H_y from Eq. (B.13) to Eq. (B.10)

$$k_{z2}^2 + \frac{\varepsilon_{xx}}{\varepsilon_{zz}} k_x^2 = \left(\frac{\omega}{c}\right)^2 \varepsilon_{xx} \tag{B.21}$$

Finally, dividing Eq. (B.20) with Eq. (B.21) and using the result of Eq. (B.19) we can derive the dispersion relation of k_x in terms of the dielectric functions of the two media

$$\left(\frac{k_{z1}}{k_{z2}}\right)^2 = \left(\frac{-\varepsilon_1}{\varepsilon_{xx}}\right)^2 = \frac{\left(\frac{\omega}{c}\right)^2 \varepsilon_1 - k_x^2}{\left(\frac{\omega}{c}\right)^2 \varepsilon_{xx} - \frac{\varepsilon_{xx}}{\varepsilon_{zz}} k_x^2}$$

$$\Rightarrow \boxed{k_x = \frac{\omega}{c} \sqrt{\frac{\varepsilon_{zz}\varepsilon_1(\varepsilon_{xx} - \varepsilon_1)}{\varepsilon_{xx}\varepsilon_{zz} - \varepsilon_1^2}}} \tag{B.22}$$

Note that for $\varepsilon_{xx} = \varepsilon_{zz} = \varepsilon_2$ it simplifies to the dispersion relation for isotropic media. The components k_{z1} and k_{z2} can be easily expressed in terms of permittivities by substituting Eq. (B.22) to Eq. (B.20) and (B.21) respectively.

Since the wavevectors are known, the electromagnetic fields can also be fully calculated. Let us consider the initial amplitude of the magnetic field to be $H_0(= H_y)$. Then from Eq. (B.11)-(B.14) the electric amplitudes E_{x1}, E_{z1}, E_{x2} and E_{z1} can be derived. Thus the total fields for material (ε_1, μ_1) will be

$$\left.\begin{aligned} \mathbf{H}_1(\mathbf{r},t) &= (0, H_0, 0)^\intercal e^{i(k_x x - k_{z1} z - \omega t)} \\ \mathbf{E}_1(\mathbf{r},t) &= (-\frac{cH_0 k_{z1}}{\omega\varepsilon_1}, 0, -\frac{cH_0 k_x}{\omega\varepsilon_1})^\intercal e^{i(k_x x - k_{z1} z - \omega t)} \end{aligned}\right\} \tag{B.23}$$

and for material (ε_2, μ_2)

$$\left.\begin{aligned} \mathbf{H}_2(\mathbf{r},t) &= (0, H_0, 0)^\intercal e^{i(k_x x + k_{z2} z - \omega t)} \\ \mathbf{E}_2(\mathbf{r},t) &= (\frac{cH_0 k_{z2}}{\omega\varepsilon_{xx}}, 0, -\frac{cH_0 k_x}{\omega\varepsilon_{zz}})^\intercal e^{i(k_x x + k_{z2} z - \omega t)} \end{aligned}\right\} \tag{B.24}$$

B.2 TE-polarization

Here, the material (ε_1, μ_1) is considered to be isotropic, while the material $(\varepsilon_2, \widetilde{\mu}_2)$ is anisotropic of the form $\widetilde{\mu}_2 = (\mu_{xx}, \mu_{yy}, \mu_{zz})^\intercal$ with zero off-diagonal elements. For TE-polarized waves, the fields of the two media $j = 1$ and $j = 2$ will be

$$\mathbf{E}_j = (0, E_{yj}, 0)^\intercal e^{i(k_{xj} x \mp k_{zj} z - \omega t)}, \quad j = 1, 2 \tag{B.25}$$

$$\mathbf{H}_j = (H_{xj}, 0, H_{zj})^\intercal e^{i(k_{xj} x \mp k_{zj} z - \omega t)}, \quad j = 1, 2 \tag{B.26}$$

where the $\mp k_{zj}z$ term corresponds to the lower ($z < 0$) or upper ($z > 0$) material (See Fig. B.1). Applying Eq. (B.5) for material (ε_1, μ_1) we get

$$\nabla \cdot \mathbf{B}_1 = 0 \Rightarrow \nabla \cdot \mathbf{H}_1 = 0$$
$$\Rightarrow H_{x1}\frac{\partial}{\partial x}(e^{i(k_{x1}x - k_{z1}z - \omega t)}) + H_{z1}\frac{\partial}{\partial z}(e^{i(k_{x1}x - k_{z1}z - \omega t)}) = 0$$
$$\Rightarrow \boxed{k_{x1}H_{x1} = k_{z1}H_{z1}} \tag{B.27}$$

and following the same procedure for material $(\varepsilon_2, \widetilde{\mu}_2)$

$$\boxed{k_{x2}H_{x2}\mu_{xx} = -k_{z2}H_{z2}\mu_{zz}} \tag{B.28}$$

Applying Eq. (B.6) for material (ε_1, μ_1) we find

$$\nabla \times \mathbf{H}_1 = -\frac{i\omega}{c}\varepsilon_1 \mathbf{E}_1$$
$$\Rightarrow \left(H_{x1}\frac{\partial}{\partial z} - H_{z1}\frac{\partial}{\partial x}\right) e^{i(k_{x1}x - k_{z1}z - \omega t)} = -\frac{i\omega}{c}\varepsilon_1 E_{y1} e^{i(k_{x1}x - k_{z1}z - \omega t)}$$
$$\Rightarrow \boxed{k_{z1}H_{x1} + k_{x1}H_{z1} = \frac{\omega}{c}\varepsilon_1 E_{y1}} \tag{B.29}$$

and for material $(\varepsilon_2, \widetilde{\mu}_2)$

$$\boxed{k_{z2}H_{x2} - k_{x2}H_{z2} = -\frac{\omega}{c}\varepsilon_2 E_{y2}} \tag{B.30}$$

Applying Eq. (B.4) for material (ε_1, μ_1) we get

$$\nabla \times \mathbf{E}_1 = \frac{i\omega\mu_1}{c}\mathbf{H}_1$$
$$\Rightarrow E_{y1}\left(-\hat{\boldsymbol{i}}\frac{\partial}{\partial z} + \hat{\boldsymbol{k}}\frac{\partial}{\partial x}\right) e^{i(k_{x1}x - k_{z1}z - \omega t)} = \frac{i\omega\mu_1}{c}(H_{x1}\hat{\boldsymbol{i}} + H_{z1}\hat{\boldsymbol{k}}) e^{i(k_{x1}x - k_{z1}z - \omega t)}$$
$$\Rightarrow \boxed{k_{z1}E_{y1} = \frac{\omega\mu_1}{c}H_{x1}} \tag{B.31}$$
$$\boxed{k_{x1}E_{y1} = \frac{\omega\mu_1}{c}H_{z1}} \tag{B.32}$$

and for material $(\varepsilon_2, \widetilde{\mu}_2)$

$$\boxed{k_{z2}E_{y2} = -\frac{\omega\mu_{xx}}{c}H_{x2}} \tag{B.33}$$
$$\boxed{k_{x2}E_{y2} = \frac{\omega\mu_{zz}}{c}H_{z2}} \tag{B.34}$$

Like in TM- scenario we assume no surface charges or currents, thus boundary conditions at the interface give

$$(\mathbf{B}_2 - \mathbf{B}_1) \cdot \hat{\boldsymbol{n}} = 0 \Rightarrow B_{2z} = B_{1z} \Rightarrow \boxed{\mu_{zz} H_{z2} = \mu_1 H_{z1}} \tag{B.35}$$

$$\hat{\boldsymbol{n}} \times (\mathbf{E}_2 - \mathbf{E}_1) = 0 \Rightarrow \boxed{E_{y2} = E_{y1} \equiv E_y} \tag{B.36}$$

$$\hat{\boldsymbol{n}} \times (\mathbf{H}_2 - \mathbf{H}_1) = 0 \Rightarrow \boxed{H_{x2} = H_{x1} \equiv H_x} \tag{B.37}$$

Plugging Eq. (B.35) and (B.36) to Eq. (B.32) and (B.34) we can verify the continuity of k_x

$$k_{x1} = k_{x2} \equiv k_x \tag{B.38}$$

Dividing Eq. (B.31) with Eq. (B.33) and using the result of Eq. (B.36) and (B.37) we get

$$\frac{k_{z1}}{k_{z2}} = -\frac{\mu_1}{\mu_{xx}} \tag{B.39}$$

Replacing H_x from Eq. (B.31) and H_{z1} from Eq. (B.32) to Eq. (B.29)

$$k_{z1}^2 + k_x^2 = \left(\frac{\omega}{c}\right)^2 \varepsilon_1 \mu_1 \tag{B.40}$$

Replacing H_x from Eq. (B.33) and H_{z2} from Eq. (B.34) to Eq. (B.30)

$$k_{z2}^2 + \frac{\mu_{xx}}{\mu_{zz}} k_x^2 = \left(\frac{\omega}{c}\right)^2 \varepsilon_2 \mu_{xx} \tag{B.41}$$

Finally, dividing Eq. (B.40) with Eq. (B.41) and using the result of Eq. (B.39) we find the dispersion relation of k_x as a function of the dielectric function of the two media

$$\left(\frac{k_{z1}}{k_{z2}}\right)^2 = \left(-\frac{\mu_1}{\mu_{xx}}\right)^2 = \frac{\left(\frac{\omega}{c}\right)^2 \varepsilon_1 \mu_1 - k_x^2}{\left(\frac{\omega}{c}\right)^2 \varepsilon_2 \mu_{xx} - \frac{\mu_{xx}}{\mu_{zz}} k_x^2}$$

$$\Rightarrow \boxed{k_x = \frac{\omega}{c} \sqrt{\frac{\mu_{zz}\mu_1(\varepsilon_2\mu_1 - \varepsilon_1\mu_{xx})}{\mu_1^2 - \mu_{xx}\mu_{zz}}}} \tag{B.42}$$

For the case where $\mu_{xx} = \mu_{zz} = \mu_2$ it simplifies to the dispersion relation for isotropic media. Additionally, if $\mu_1 = \mu_2$, k_x goes to infinity. This is the

reason why it is impossible to excite SPPs for materials with the same μ with TE-polarized waves.

Appendix C

Multiple reflections and transmissions inside a layer

To understand the physical meaning of multiple reflections and transmissions inside a layer we first need to find the time domain response of reflection and transmission coefficients. Let us start by reshaping Eq. (3.45). We can write the exponential term as $2k_1L_1 = \omega T$, where $T = 2L_1/\upsilon_1$ is the time the light needs to travel twice the thickness of the layer and υ_1 is the velocity inside that layer. This results to

$$\Gamma_1(\omega) = \frac{\rho_1 + \rho_2 e^{i\omega T}}{1 + \rho_1\rho_2 e^{i\omega T}}, \quad T = \frac{2L_1}{\upsilon_1} \tag{C.1}$$

Setting $z^{-1} = e^{i\omega T}$ we end up

$$\Gamma_1(z) = \frac{\rho_1 + \rho_2 z^{-1}}{1 + \rho_1\rho_2 z^{-1}} \tag{C.2}$$

We can break the previous expression into two terms of the form $\frac{A}{\rho_1} + \frac{B}{\rho^{-1}+\rho_2 z^{-1}}$ where A, B are unknowns (all these will become clear soon). If we set in Eq. (C.2) $z^{-1} = 1$ and $z^{-1} = 0$, we can derive two formulas giving $A = 1$ and $B = 1 - \rho^{-2}$. Thus Eq. (C.2) can be written as

$$\Gamma_1(z) = \frac{1}{\rho_1} - \frac{1-\rho_1^2}{\rho_1(1+\rho_1\rho_2 z^{-1})} \tag{C.3}$$

The resulted expression can be expanded in power series of z^{-1}. Having $x = z^{-1}$ and $\Gamma_1(z) = f(x)$ the Taylor expansion will be

$$f(x) = \sum_{m=0}^{\infty} \frac{f^{(m)}(0)}{m!} x^m \tag{C.4}$$

Let us try to apply Taylor expansion in Eq. (C.3).

For $m = 0$, $f^{(0)}(x) = \dfrac{1}{\rho_1} - \dfrac{1-\rho_1^2}{\rho_1(1+\rho_1\rho_2 x)}$, so $\dfrac{f^{(0)}(0)}{0!}x^0 = \rho_1$

For $m = 1$, $f^{(1)}(x) = \dfrac{(1-\rho_1^2)\rho_2}{(1+\rho_1\rho_2 x)^2}$, so $\dfrac{f^{(1)}(0)}{1!}x^1 = (1-\rho_1^2)\rho_2^1(-\rho_1^{1-1})x^1$

For $m = 2$, $f^{(2)}(x) = \dfrac{2!(1-\rho_1^2)(-\rho_1^{2-1})\rho_2^2}{(1+\rho_1\rho_2 x)^3}$, so $\dfrac{f^{(2)}(0)}{2!}x^2 = (1-\rho_1^2)\rho_2^2(-\rho_1^{2-1})x^2$

For $m = n$, $f^{(n)}(x) = \dfrac{n!(1-\rho_1^2)(-\rho_1^{n-1})\rho_2^n}{(1+\rho_1\rho_2 x)^{n+1}}$, so $\dfrac{f^{(n)}(0)}{n!}x^n = (1-\rho_1^2)\rho_2^n(-\rho_1^{n-1})x^n$

The ending result will then be

$$\Gamma_1(z) = \rho_1 + \sum_{n=1}^{\infty}(1-\rho_1^2)(-\rho_1)^{n-1}\rho_2^n z^{-n} \tag{C.5}$$

Reverting back to frequency domain through $z^{-1} = e^{i\omega T}$ and knowing that $\rho_1' = -\rho_1$, $\tau_1 = 1+\rho_1$ and $\tau_1' = 1+\rho_1' = 1-\rho_1$ the reflection will become

$$\Gamma_1(\omega) = \rho_1 + \sum_{n=1}^{\infty}\tau_1\tau_1'\rho_1'^{(n-1)}\rho_2^n e^{i\omega nT} \tag{C.6}$$

In order to calculate the time response of reflection we need to shift from frequency to time domain. Thus we have to perform an inverse Fourier

transform as follows

$$\Gamma_1(t) = \frac{1}{2\pi}\int_{-\infty}^{+\infty}\Gamma_1(\omega)e^{-i\omega t}d\omega$$

$$= \frac{1}{2\pi}\int_{-\infty}^{+\infty}\rho_1 e^{-i\omega t}d\omega + \frac{1}{2\pi}\int_{-\infty}^{+\infty}\sum_{n=1}^{\infty}\tau_1\tau_1'\rho_1'^{(n-1)}\rho_2^n e^{i\omega nT}e^{-i\omega t}d\omega$$

$$\Rightarrow \boxed{\Gamma_1(t) = \rho_1\delta(t) + \sum_{n=1}^{\infty}\tau_1\tau_1'\rho_1'^{(n-1)}\rho_2^n\delta(t-nT)} \tag{C.7}$$

Let us try to understand the significance of the above expression; for that Fig. C.1 will be of assistance. At $t = 0$ part of the initial light is reflected at the left interface giving a reflection coefficient of ρ_1. At the same time, the other part is refracted inside the layer with a transmission coefficient of τ_1. After $t = T/2$ the transmitted light is reflected on the right side of the slab giving $\tau_1\rho_2$, which can also be written as $\tau_1\rho_2\delta(t-T/2)$. This portion of light is then reflected backwards and reaches the left side of slab at $t = T$. The same process repeats and another portion of light is reflected/transmitted. This leads to a reflected pulse of $\tau_1\rho_2\rho_1'\delta(t-T)$ and a transmitted pulse of $\tau_1\tau_1'\rho_2\delta(t-T)$. Following the same process, the n^{th} pulse transmitted to the left will have the form $\tau_1\tau_1'\rho_1'^{(n-1)}\rho_2^n\delta(t-nT)$. Summing all the terms we end up to Eq. (C.7).

Following the same principle, the overall transmission can be derived. In this case the delta function will be shifted on the right side of the layer (i. e. $nT \to nT + T/2$). Based on the time progression of the transmission coefficient in Fig. C.1, the n^{th} coefficient will be $\tau_2\tau_1\rho_2^n\rho_1'^n\delta(t-nT-T/2)$. Thus the overall contribution will be the sum of all coefficients leading to

$$\boxed{T_1(t) = \sum_{n=0}^{\infty}\tau_2\tau_1\rho_2^n\rho_1'^n\delta(t-nT-T/2)} \tag{C.8}$$

Applying a Fourier transform, to move from time to frequency domain, we

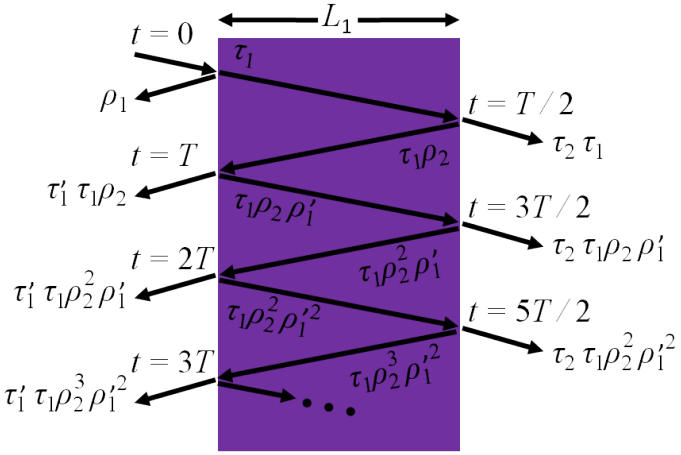

Figure C.1: Schematics of a beam that is reflected and transmitted multiple times in a layer.

get

$$T_1(\omega) = \sum_{n=0}^{\infty} \tau_2\tau_1\rho_2^n\rho_1'^n e^{i\omega nT} e^{i\omega T/2} \tag{C.9}$$

The previous expression must be equal to Eq. (3.50) which can also be written as

$$T_1(\omega) = \frac{\tau_2\tau_1 e^{i\omega T/2}}{1+\rho_2\rho_1 e^{i\omega T}} \tag{C.10}$$

So what we need to show is that

$$\sum_{n=0}^{\infty} \rho_2^n\rho_1'^n e^{i\omega nT} = \frac{1}{1+\rho_2\rho_1 e^{i\omega T}} \tag{C.11}$$

We can perform a Taylor expansion to the right side of the last equation. Let

$x = e^{i\omega T}$ and $f(x) = (1 + \rho_2\rho_1 x)^{-1} = (1 - \rho_2\rho_1' x)^{-1}$.

$$\text{For } m = 0,\ f^{(0)}(x) = \frac{1}{1 - \rho_2\rho_1' x),}\ \text{ so } \frac{f^{(0)}(0)}{0!}x^0 = 1$$

$$\text{For } m = 1,\ f^{(1)}(x) = \frac{\rho_2\rho_1'}{(1 - \rho_2\rho_1' x)^2},\ \text{ so } \frac{f^{(1)}(0)}{1!}x^1 = \rho_2\rho_1' x^1$$

$$\text{For } m = 2,\ f^{(2)}(x) = \frac{2!\rho_2^2\rho_1'^2}{(1 - \rho_2\rho_1' x)^3},\ \text{ so } \frac{f^{(2)}(0)}{2!}x^2 = \rho_2^2\rho_1'^2 x^2$$

$$\text{For } m = n,\ f^{(n)}(x) = \frac{n!\rho_2^n\rho_1'^n}{(1 - \rho_2\rho_1' x)^n},\ \text{ so } \frac{f^{(n)}(0)}{n!}x^n = \rho_2^n\rho_1'^n x^n$$

Summing all we eventually get

$$\sum_{n=0}^{\infty} \frac{f^{(n)}(0)}{n!}x^n = \sum_{n=0}^{\infty} \rho_2^n\rho_1'^n e^{i\omega nT} \tag{C.12}$$

Thus Eq. (C.11) is satisfied meaning that Eq. (C.9) and (C.10) are indeed the same. The results for both the overall time-dependant reflection and transmission response are important because they state that Eq. (3.45) and (3.50) are explicit formulas.

Appendix D

Table of SRO fitted permittivity parameters

Oxygen pressure (mTorr)	ε_b	ω_p (eV)	A (eV)	ω_0 (eV)	Γ_1 (eV)	Γ_2 (eV)
20	3.24	3.86	7.83	4.16	0.94	2.82
30	3.15	3.55	7.70	3.57	0.70	3.66
40	3.53	3.61	5.25	3.25	0.73	1.79
50	2.92	3.74	7.94	3.74	0.76	3.65
75	3.12	3.26	4.65	2.79	0.72	2.58
100	2.67	3.41	6.98	3.38	0.98	3.23
200	2.09	3.16	7.01	3.41	0.85	3.96
300	2.33	3.22	6.76	3.34	0.86	3.48

Table 1: Best fitted parameters of the Drude-Lorentz permittivity of Eq. (6.1) with SRO films grown at different oxygen pressures.